Dynamic magnetic susceptibility of systems with long-range magnetic order

by

Matthew Dano Vannette

A dissertation submitted to the graduate faculty

in partial fulfillment of the requirements for the degree of

DOCTOR OF PHILOSOPHY

Major: Condensed Matter Physics

Program of Study Committee:
Ruslan Prozorov, Major Professor
Paul C. Canfield
Jörg Schmalian
John Lajoie
R. William McCallum

Iowa State University

Ames, Iowa

2009

UMI Number: 3355540

INFORMATION TO USERS

The quality of this reproduction is dependent upon the quality of the copy submitted. Broken or indistinct print, colored or poor quality illustrations and photographs, print bleed-through, substandard margins, and improper alignment can adversely affect reproduction.
In the unlikely event that the author did not send a complete manuscript and there are missing pages, these will be noted. Also, if unauthorized copyright material had to be removed, a note will indicate the deletion.

UMI®

UMI Microform 3355540
Copyright 2009 by ProQuest LLC
All rights reserved. This microform edition is protected against unauthorized copying under Title 17, United States Code.

ProQuest LLC
789 East Eisenhower Parkway
P.O. Box 1346
Ann Arbor, MI 48106-1346

DEDICATION

This work is dedicated to Gabe, Chi, and Jennifer.

TABLE OF CONTENTS

LIST OF TABLES vi

LIST OF FIGURES vii

ACKNOWLEDGEMENTS xv

ABSTRACT xvi

CHAPTER 1. Magnetic Measurements 1

1.1 Introduction 1

1.2 Conventional Magnetic Measurements 2

1.2.1 Static Magnetic Moment and Susceptibility 2

1.2.2 AC Magnetic Susceptibility 3

1.2.3 Neutron Scattering 5

1.3 Radio–Frequency Susceptibility 5

1.3.1 Normal State Skin Effect 6

1.3.2 Energy Scales Associated With RF Fields 10

1.4 The Tunnel Diode Resonator 11

1.5 Measuring Changes in Magnetic Susceptibility 18

1.6 Representative TDR Data 21

1.7 Summary 23

CHAPTER 2. Local Moment Ferromagnets 25

2.1 Introduction 25

2.2 Basics of Magnetism 25

2.3 Materials Studied and Results 44

2.3.1 Multiple Magnetic Phases in CeSb 47
2.3.2 $CeVSb_3$ 50
2.3.3 $CeAgSb_2$ 54
2.3.4 $YTiO_3$ 57
2.3.5 GdPtIn 57
2.3.6 Ce_3Al_{11} 60
2.4 Evolution of $\chi_{TDR}(T)$ curves in applied field 63
2.5 Anisotropy in $CeVSb_3$ 69
2.6 Summary 71
CHAPTER 3. Failure of Critical Scaling Analysis of the Phase Transition . 73
3.1 Introduction 73
3.2 Experimentally Determining Scaling Exponents 77
3.3 Critical Scaling in $CeAgSb_2$ and $CeVSb_3$ 77
3.4 Scaling an Insulating Ferromagnet 88
3.5 Effect of Skin Depth Limit 91
3.6 Summary 98
CHAPTER 4. Itinerant Ferromagnets 99
4.1 Introduction 99
4.2 Stoner Theory 103
4.3 Spin Fluctuations 109
4.4 Semi-Phenomenological Model of Itinerant Ferromagnets 114
4.5 Materials Studied 119
4.5.1 $ZrZn_2$ 119
4.5.2 Y_9Co_7 121
4.5.3 Half-Band Ferromagnet NiMnSb 123
4.6 Analysis of $ZrZn_2$ and Y_9Co_7 125
4.7 Summary 128

CHAPTER 5. Magnetic Susceptibility of Selected Members of RT_2Zn$_{20}$ . . 129

5.1 Introduction 129

5.2 Data and Discussion 131

5.2.1 Parent Compounds 131

5.2.2 Cobalt doping 134

5.2.3 Aluminum doping 137

5.2.4 Discussion 139

5.3 Summary 141

CHAPTER 6. Conclusion and Future Directions 142

APPENDIX A. Design and Materials Considerations for the TDR 145

APPENDIX B. Thermal Response of Materials to the rf Probe Field 152

APPENDIX C. Shubnikov-de Haas Oscillations in Ce- & SmAgSb$_2$ 166

APPENDIX D. Multiferroic Compounds 174

BIBLIOGRAPHY 184

LIST OF TABLES

Table 1.1 Physical effects observable at radio frequencies. 6

Table 1.2 TDR Specifics 16

Table 1.3 Partial list of samples run in the TDR in the course of this work. . . . 17

Table 3.1 Critical exponents in various models from Fisher (1967). 75

Table 3.2 Characteristic fields from the analysis of peak amplitude with applied field. 88

Table A.1 TDR Specifics 149

Table A.2 Commercial electronics used in this work 151

LIST OF FIGURES

Figure 1.1 Schematic of skin depth effect in metals. 8

Figure 1.2 Tunnel diode I–V curve. 12

Figure 1.3 TDR circuit diagram. 13

Figure 1.4 TDR resonance shift due to thermal cycling. 15

Figure 1.5 Scaled comparison of Y–, Ce–, and $SmAgSb_2$ χ vs. T data. 22

Figure 2.1 Plot of Langevin function (dashed curve) and mean field magnetization at different temperatures (solid lines). Intersections of the lines with the curve correspond to simultaneous solutions of Eq. 2.21 and $M = H_{eff}/\lambda$. 30

Figure 2.2 Plot of RKKY function. 32

Figure 2.3 Geometry of uniaxial anisotropy energy expressed in Eq. 2.69. 43

Figure 2.4 Comparison of heat capacity (left axis, black circles) and TDR magnetic susceptibility (right axis, red squares) for $CeVSb_3$ measured along the magnetic easy axis. Peaks occur in both data sets at the ordering temperature. 45

Figure 2.5 Comparison of low frequency ac susceptibility (solid square) and TDR data (hollow hexagons) for $CeVSb_3$ with the probe field aligned with the magnetic easy axis. Both curves are normalized to 1 at the maximum. 46

Figure 2.6 Zero field cooled static susceptibility (left axis) and resistivity for current applied along the c and b crystal axes (right axis) for $CeVSb_3$. . . 48

Figure 2.7 χ_{TDR} for $CeVSb_3$ measured along the magnetic easy axis (crystallographic c-axis) in different static bias fields. The general behavior of a sharp zero field peak at T_C that suppresses in amplitude and shifts to higher temperatures is common to all measured local moment systems. The contribution from resistivity is evident. *Inset:* Peak amplitude (left axis) and temperature of peak (right axis) versus applied field. 49

Figure 2.8 χ_{TDR} vs. T for CeSb. 51

Figure 2.9 H–T phase diagram for CeSb. 52

Figure 2.10 Comparison of χ_{TDR} for two $CeVSb_3$ crystals of different sizes. 53

Figure 2.11 Zero field χ_{TDR} for $CeAgSb_2$. 55

Figure 2.12 χ_{TDR} near T_C in the labeled applied fields (in Oe) for $CeAgSb_2$. Note the extreme narrowness of the peak. 56

Figure 2.13 χ_{TDR} in cgs units for $YTiO_3$. 58

Figure 2.14 Susceptibility vs. temperature for GdPtIn in different applied fields. *Inset:* Peak suppression (left axis, filled circles) and temperature shift (right axis, hollow squares) as a function of field. 59

Figure 2.15 28 MHz susceptibility for GdPtIn near T_C in fields from 0-400 Oe in 100 Oe steps. Higher fields have lower amplitude maxima. *Inset:* Zero field susceptibility over entire measured temperature range. 60

Figure 2.16 χ_{TDR} vs. temperature for Ce_3Al_{11} in applied fields from 0 to 500 Oe. . 61

Figure 2.17 Detail of the para- to ferromagnetic phase transition in Ce_3Al_{11}. 62

Figure 2.18 Detail of the ferromagnetic to incommensurate structure in Ce_3Al_{11}. . 62

Figure 2.19 Heat capacity vs. temperature for Ce_3Al_{11}. 63

Figure 2.20 Temperature of the peak in χ_{TDR} vs. applied field for $CeVSb_3$ as measured along the c–axis. 67

Figure 2.21 Temperature of the peak in χ_{TDR} vs. applied field for Ce_3Al_{11} as measured along the c–axis. 67

Figure 2.22 Temperature of the peak in χ_{TDR} vs. applied field for GdPtIn as measured along the c–axis. 68

Figure 2.23 Comparison of zero field susceptibility for $CeVSb_3$ measured parallel and perpendicular to the magnetic easy axis. 69

Figure 2.24 χ_{TDR} measured perpendicular to the magnetic easy axis in different static bias fields. The amplitude of the maximum is much less than that measured along the easy axis. The fields required for suppression are also considerably larger. *Inset:* Peak amplitude (left axis) and temperature of peak (right axis) versus applied field. 70

Figure 2.25 χ_{TDR}^{max} normalized to the zero field value versus applied field for parallel and perpendicular to the easy axis for $CeVSb_3$. Dotted line marks a 90% suppression. 71

Figure 3.1 Difference in χ_{TDR} vs. T relative to a 1 kOe run for $CeAgSb_2$. *Inset:* Absolute χ_{TDR} vs. T for data in the main panel. 78

Figure 3.2 Peak amplitude (solid symbols, left axis) and inverse peak amplitude (hollow symbols, right axis) vs. applied field for $YTiO_3$. 79

Figure 3.3 (Color online) Inverse peak amplitude *vs.* applied magnetic field for $CeAgSb_2$ (a) and $CeVSb_3$ (b). Solid circles are data and the line is a linear fit. The H axis intercept (H^*) corresponds to the applied field at which the susceptibility would diverge. 80

Figure 3.4 (Color online) Scaled plots for $CeAgSb_2$ in the paramagnetic state neglecting H^* (a) and adding H^* to all applied fields (b). As $T \rightarrow T_C$, the plot extends off to right. Both plots use the same exponents. . . . 81

Figure 3.5 (Color online) Scaled plots for $CeVSb_3$ neglecting H^* (a) and adding H^* to all applied fields (b). Both plots use the same exponents. 83

Figure 3.6 Inverse peak amplitude vs. field for $CeVSb_3$ measured in the ^{4}He system at 28 MHz. 85

Figure 3.7 Inverse peak amplitude vs. field for $CeAgSb_2$ measured in the ^{4}He system at 28 MHz. 86

Figure 3.8 Plot of $H^*\mu_{sat}/\mu_B$ versus T_C for the magnets studied in this work. There is an obvious correlation between the energy associated with H^* and the Curie temperature. This suggests that H^* is related to the ordering mechanism in local moment ferromagnets. Dashed lines are guides to the eye. 87

Figure 3.9 Mean field scaling for $YTiO_3$. 89

Figure 3.10 2-D Ising scaling for $YTiO_3$. 89

Figure 3.11 3-D Ising scaling for $YTiO_3$. 90

Figure 3.12 3-D Heisenberg scaling for $YTiO_3$. 90

Figure 3.13 $\mu\rho$ vs. T for $CeAgSb_2$ as determined by $(1+4\pi\chi)^2$. *Inset:* Detail near T_C. 92

Figure 3.14 μ vs. T for $CeAgSb_2$ as determined by the method described in the text. *Inset:* Detail near T_C. 93

Figure 3.15 $\mathrm{Log}(\mu_{peak})$ vs. $\log(H)$ from the data presented in Fig. 3.14. 94

Figure 3.16 3-D Heisenberg scaling for μ data in $CeAgSb_2$. Solid symbols are for data with the resistivity contribution accounted for, while open symbols present data where ρ is still included. 95

Figure 3.17 Scaled χ_{TDR} data for $CeAgSb_2$ after accounting for the resistive component. 97

Figure 4.1 Comparison of χ_{static} in $CeAgSb_2$ and $ZrZn_2$. 100

Figure 4.2 Comparison of χ_{TDR} for $ZrZn_2$ and $CeAgSb_2$. 102

Figure 4.3 Calculated m^*, $1-m^*$, and dm^*/dh for the proposed itinerant magnetism model. 116

Figure 4.4 χ_{TDR} vs. T for YFe_2Zn_{20} andYCo_2Zn_{20}. 117

Figure 4.5 χ_{TDR} vs. T for $ZrZn_2$. 119

Figure 4.6 Arbitrary ρ vs. $T^{5/3}$ for $ZrZn_2$ in a 1.2 kOe applied field (solid line) and calculated $\rho_0 + AT^{5/3}$ (dashed line). *Inset:* ρ vs T up to 40 K. 121

Figure 4.7 χ_{TDR} vs. T for Y_9Co_7 in four applied fields. SC, FM, and PM denote the superconducting, ferromagnetic, and paramagnetic states, respectively. 122

Figure 4.8 Plot of χ_{TDR} vs. T for NiMnSb and the empty Inferno sample holder. 123

Figure 4.9 Magnetic susceptibility of NiMnSb with the sample holder contribution subtracted. 124

Figure 4.10 Fits of $ZrZn_2$ data to Eq. 4.72. 126

Figure 4.11 $ZrZn_2$ fit parameters with estimated errors. 126

Figure 4.12 Comparison of data (points) and fit (lines) for three applied fields in a polycrystalline sample of Y_9Co_7. 127

Figure 4.13 Y_9Co_7 fit parameters with estimated errors. 128

Figure 5.1 Zero field χ_{TDR} vs. T for $GdFe_2Zn_{20}$ and$GdCo_2Zn_{20}$. 133

Figure 5.2 Field dependent change in $\chi_{TDR}(T)$ for $GdFe_2Zn_{20}$. 134

Figure 5.3 Change in the measured susceptibility vs. temperature for five cobalt concentration ranging from x =0-0.75 in $Gd(Fe_xCo_{1-x})_2Zn_{20}$. 135

Figure 5.4 χ vs. T in different fields for the four Co concentrations studied here. Numbers next to each trace indicate the applied field in kOe. Strong local moment peaks are observed in all samples except for the 50% doping. 136

Figure 5.5 Magnetic susceptibility vs. temperature for five aluminum concentrations ranging from 0-4.9%. 137

Figure 5.6 χ_{TDR} vs. T in applied DC fields for the four Al doped samples studied. Only the 0.5% and 4.9% Al dopings show well–defined additional features. Numbers next to each trace indicate the applied field in kOe. 138

Figure 5.7 Comparison of published T_{mag} with TDR data in pure and doped $GdFe_2Zn_{20}$. 139

Figure A.1 Basic design of ^{3}He sample holder. 146

Figure A.2 Room temperature electronics for the tunnel diode. 150

Figure B.1 Magnetic field (solid line, left axis), sample temperature (filled circles, right axis), and magnetic susceptibility (half-filled pentagons, far right axis) vs. time for $Gd(Fe_{0.5}Co_{0.5})_2Zn_{20}$. The correlation between the sample temperature and susceptibility is clear. Vertical bars near 1250 seconds denote the time period where the field was held at a non-zero, constant value. 154

Figure B.2 Sample temperature (left axis, solid symbols) and TDR temperature (right axis, open symobls) vs. time for 1% Al doping in $GdFe_2Zn_{20}$. Initially the rf excitation field was off. At approximately 1 minute the circuit was set resonating and the temperature was allowed to reach a steady state. The rf field was turned off again at 4 minutes, and the temperature relaxed to the time=0 value. 155

Figure B.3 Circuit, 1-K pot, and sample temperature vs. time for a copper sample as the rf excitation field was cycled on and off. At time=0 the rf field was on. From a-e the rf field cycled between on, off, on, off, and on. Initial tests suggested the effect was small, so to mitigate any possible change in heat load due to the changing power dissipated in the circuit itself, the bias voltage on the diode was change very slowly. 158

Figure B.4 Response of the temperature of $YTiO_3$ with the rf field cycled between on-off-on (left axis, solid symbols) and the TDR temperature (right axis, open symbols). The effect is quite small, even with the heat pulse from rapidly changing the bias on the circuit. 159

Figure B.5 Temperatures of GdPtIn (left axis, solid squares) and the circuit (right axis, open circles) vs. time as the bias voltage was increased. At the time marked 'a' the circuit began resonating. At 'b' the resonance switched off due to overbiasing. 160

Figure B.6 Sample temperature vs. time for YFe_2Zn_{20} as the rf field was cycled on and off. 161

Figure B.7 Sample temperature for a 1 mm^3 single crystal of $CeVSb_3$ vs. time as the bias voltage is adjusted. The arrows labeled 1 and 2 are for increasing and decreasing bias voltages, respectively. The rf field was off at time=0. 162

Figure B.8 Sample temperature vs. resonant frequency for $CeVSb_3$. The arrow indicates the direction of decreasing bias voltage. 163

Figure B.9 Sample temperature (left axis, filled circles) and resonant frequency (right axis, hollow squares) vs. bias voltage for $CeVSb_3$. The lower and upper voltage points denote the resonance window. 164

Figure C.1 Comparison of ρ determined from TDR with 4–probe data for $SmAgSb_2$. 168

Figure C.2 Temperature variation of the resonant frequency oscillation amplitude in $CeAgSb_2$. 170

Figure C.3 Temperature variation of the oscillation amplitude in $SmAgSb_2$. Note the scale of $\Delta\rho$. 171

Figure C.4 Power spectrum of resistivity oscillations at three temperatures for $CeAgSb_2$. 172

Figure C.5 Power spectrum of the resistivity oscillations at 0.5 K for $SmAgSb_2$. The peak at 0.89 MG derives from a newly observed hole orbit. 173

Figure D.1 AC susceptibility of $HoMnO_3$ measured parallel to the c-axis in different static magnetic fields. Curves are offset for clarity. 176

Figure D.2 35 kOe temperature sweep for $HoMnO_3$ along the c-axis with features associated with phase changes marked by $T_1 - T_5$. 177

Figure D.3 Phase diagram for $HoMnO_3$ measured along the c-axis. Solid circles are phase changes detected with the TDR. Open red triangles are defined phase transitions digitized from Lorenz et al. (2005). Blue bowties are anomalies in dielectric constant digitized from Yen et al. (2005). Lines are guides to the eye, and labeled phases follow the convention of Lorenz et al. (2005). 178

Figure D.4 Low temperature detail of the phase diagram show in Fig. D.3. 179

Figure D.5 Full phase diagram for $HoMnO_3$ measured in the basal plane. 180

Figure D.6 χ vs. T for $DyMnO_3$ in five applied fields. The similarities between this compound and the holmium analogue are obvious. 180

Figure D.7 Phase diagram for hexagonal $DyMnO_3$. Filled black circles are TDR data and open red triangles are from Ivanov et al. (2006). Phases ITP and LTP are named following Nandi et al. (2008). Phases HT1 and INT are labeled as such under the assumption that they are similar to the other hexagonal rare earth manganites. 181

ACKNOWLEDGEMENTS

I want to thank the people who helped me accomplish all that I have in the past years. Of course, without the guidance of Ruslan Prozorov I would not have been able to complete my degree. The other members of the SMLT lab provided invaluable input, discussions, and advice throughout the course of this work.

To my friends and family, especially my parents, I extend a great thank you for taking the time to ask me to explain what it is I have been doing these past years. It has helped me better realize where there are holes in my understanding and pushed me to fill those holes.

I thank the members of my committee. Your patience and understanding is appreciated. I also thank you for the various discussions we have had regarding my research and physics in general. In particular, Paul Canfield worked beyond anything that could have been expected of him, and for that I will always be grateful.

Thank you to the physicists who designed interesting materials and offered samples to measure. Without their efforts, none of this work could have been accomplished.

I finally want to thank my wife, Jennifer, for her unwavering encouragement and support from the time we decided I would go back to school up through the completion of my degree. We've moved two times and over 2,000 miles in this process, and you always were there.

The United States Government has assigned the DOE report IS-T 2744 to this thesis. Notice: This document has been authored by the Iowa State University of Science and Technology under Contract No. DE-AC02-07CH11358 with the U. S. Department of Energy. The U. S. Government retains an non-exclusive, paid-up, irrevocable, world-wide license to publish or reproduce the published form of this document, or allow others to do so, for U. S. Government purposes.

ABSTRACT

The utility of the TDR as an instrument in the study of magnetically ordered materials has been expanded beyond the simple demonstration purposes. Results of static applied magnetic field dependent measurements of the dynamic magnetic susceptibility, χ, of various ferromagnetic (FM) and antiferromagnetic (AFM) materials showing a range of transition temperatures (1-800 K) are presented. Data was collected primarily with a tunnel diode resonator (TDR) at different radio-frequencies ($\sim$10-30 MHz). In the vicinity of T_C local moment ferromagnets show a very sharp, narrow peak in χ which is suppressed in amplitude and shifted to higher temperatures as the static bias field is increased. Unexpectedly, critical scaling analysis fails for these data. It is seen that these data are frequency dependent, however there is no simple method whereby measurement frequency can be changed in a controllable fashion. In contrast, itinerant ferromagnets show a broad maximum in χ well below T_C which is suppressed and shifts to lower temperatures as the dc bias field is increased. The data on itinerant ferromagnets is fitted to a semi-phenomenological model that suggests the sample response is dominated by the uncompensated minority spins in the conduction band. Concluding remarks suggest possible scenarios to achieve frequency resolved data using the TDR as well as other fields in which the apparatus may be exploited.

CHAPTER 1. Magnetic Measurements

1.1 Introduction

Interesting quantities to measure for magnetically ordered samples include the magnetic moment, M, the magnetic susceptibility χ, and the ordering wave vector $\vec{q}$. By determining these quantities and how they vary with temperature and applied magnetic field, information regarding the nature of the interaction between the magnetic ions is obtained. For example, suppose a sample of some material is cooled to low temperature in zero applied field. A small external field is applied and the moment is measured as temperature is increased. If the magnetic moment grows and then decreases again as the temperature increases, it is likely there is a phase transition in the temperature region where the moment changes. Field cooling through the transition while measuring the moment can provide hints to what type of order exists. The presence or absence of magnetic hysteresis also provides clues as to the magnetic structure. A feature in the magnetic susceptibility such as a peak, dip, or break in slope may provide other clues as to the nature of the magnetic order.

No single measurement will provide all the information necessary to fully characterize a sample. It is better to take a multifaceted approach and measure as many different properties as time, money, and interest permit. On rare occasions a new measurement technique is developed or an existing technique in one branch of physics is applied to a different phenomenon. In either case the data have a high probability of being novel. Such novel data are often confusing and require considerable effort to understand. The potential return is new insight into existing physical phenomena. An attempt to understand radio frequency, magnetic susceptibility data from a novel measurement technique is made in this work.

This chapter begins with a basic description of the more common measurements of mag-

netic moment, neutron scattering, and conventional AC susceptibility. It will proceed to a discussion of the various phenomena that may be explored with radio frequency susceptibility, placing emphasis on those phenomena that are most relevant to this work. A description of the technique used here (tunnel diode resonator) and representative data on five materials concludes the chapter.

1.2 Conventional Magnetic Measurements

Conventional measurements are defined here as those measurements performed on commercial equipment and common in the literature. There are a great many measurement techinques at the disposal of the experimentalist. However, there are three primary measurements by which pratically all magnetic information is gathered. These three are measurements of static magnetic moment, ac magnetic susceptibility, and neutron scattering. Supplementing these techniques are the slightly less common nuclear magnetic resonance (NMR), ferromagnetic resonance (FMR), electron paramagnetic resonance (EPR), Mössbauer spectroscopy, and microwave cavity perturbation. Each technique compliments the others and provides slightly different information regarding the macroscopic or microscopic magnetic nature of the sample under consideration.

Conventional measurements are extremely important because they offer data that are often well–understood within the confines of current theories. Interpreting these data is usually straightforward and allows for rapid and accurate comparison between different materials. When data from conventional measurements differ from those predicted by extant theories, it is an indication that some poorly understood physics might be at work.

1.2.1 Static Magnetic Moment and Susceptibility

Measurements of the static magnetic moment of a sample are the most common methods of characterizing the magnetic properties of a material. Typically measurements of magnetic moment are carried out in an applied static field. Static magnetic susceptibility, defined as $\chi = M/H$, is commonly reported for disordered samples. Through static moment measurements it

is possible to determine the paramagnetic moment per magnetic ion (via static susceptibility), saturation moment per ion, estimate the ordering temperature of the material, and evaluate the aniostropy in a single crystal sample. A drawback to static measurements is that a bias field is generally required for a measureable signal. In ferromagnetic materials at temperatures below T_C, the bias field acts to modify the domain structure so that a bulk moment is present in the sample. For temperatures above T_C in ordered materials or at any T is disordered materials, the bias field opposes thermal radomization which leads to zero moment in the paramagnetic state. A remenance measurement may be done in which a large bias field is applied and then taken to zero. Subsequently, the moment is measured a a function of a different parameter. Very often the additional parameter is temperature, but it could be any other controllable parameter that may affect the magnetic moment of the sample.

1.2.2 AC Magnetic Susceptibility

In a dynamic measurement of magnetic susceptibility, a time varying magnetic field is applied to the sample. The measured signal is obtained either through an induced voltage in a coil (conventional AC susceptometry) or a change in the natural resonant frequency of some portion of the measurement apparatus (microwave cavity perturbation and tunnel diode resonator).

Low frequency AC susceptibility measures the response of a sample to a time varying magnetic field which may be superimposed on a static magnetic field. Unlike static moment measurements, it is not necessary that a field be applied to collect the data. The measurement may be made in either a longitudinal or transverse mode. In a longitudinal measurement the ac and static fields are coaxial, whereas in a transverse measurement the two fields are perpendicular. Typically the AC field is limited in frequency to less than 100 kHz. The frequency limit is caused by issues with phase noise and the difficulty associated with driving a coil far from its resonant frequency. The amplitude of the alternating field may be anywhere from 0.1-10 Oe. The fairly large drive fields are needed to provide an adequate signal to noise ratio.

Measurements of AC susceptibility have been useful in determining critical indices associated with the second order para- to ferromagnetic phase change [Ho et al. (1981), Drobac (1996)]. A major drawback of these techniques is that the drive field is typically on the order of 0.1-10 Oe. Such a large probe field may overwhelm any fluctuations that exist, particularly in the vicinity of a phase transition. Further, the driven coil method places a relatively low upper limit on the frequency that can be used to test the system.

AC susceptibility may be carried out in either an amplitude domain or frequency domain fashion. In an amplitude domain measurement the magnitude of the output signal is measured. Usually the raw output signal is a voltage. The reliability of amplitude domain measurements is limited by the waveform of the output signal. If there is significant noise or distortion in the output signal, then there will be considerable uncertainty in the AC susceptibility. Frequency domian measurements are relatively insensitive to the waveform of the output signal. Since a frequency measurement is a counting of how often a particular event occurs in a given time period, as long as there is no noise in the vicinity of the counting condition, this source of uncertainty is removed.

Carrying out a frequency domain measurement requires precise knowledge of the natural resonant frequency of the measurement apparatus. The sample under consideration is placed in a cavity or coil. The sample properties under given field and temperature conditions determine the resonant frequency of the cavity or coil. Most frequency domain techniques (i. e. NMR or microwave cavity perturbation) rely on driving the oscillation with some external frequency source. The frequency of the applied power is swept in an effort to locate the resonance. The resonance is detected through a peak in the response of some detector vs. frequency. All oscillators manifest a finite width in the response peak which is inversely propotional to the quality factor of the system. To determine the resonant frequency via the sweeping method with precision requires very high quality factors which may be obtained only with considerable effort and expense. The gains inherent in a frequency domain measurement are offset by the cost and effort required to perform them and the experimenter must decide if the exchange is worthwhile.

1.2.3 Neutron Scattering

Neutron scattering is a very powerful technique for determining the microscoic magnetic structure of a magnetic material. The wavelength of low energy neutrons is on the order of angstroms, which is the typical spacing between ions in a solid. The fairly close match between neutron wavelength and ion spacing in a crystal permits the use of a beam of neutrons as a probe of crystal structure. Neutrons are unaffected by the charge on the electrons in the lattice and primarily scatter off the nuclei. The propensity for scattering off nuclei allows a neutron to probe deep into the bulk of the sample. The neutron also has a magnetic moment, and as such it is sensitive to magnetic structure. Through neutron scattering it is often possible to determine the magnetic structure of an ordered sample from the observation of different scattering profiles above and below the ordering temperature.

1.3 Radio–Frequency Susceptibility

Many physical phenomena are observable at radio frequencies, and some of these phenomena have been explored quite extensively. Almost all of the explored rf properties are resonance effects within the material. As such, they require frequency resolved measurements to determine a particular transition energy in the material. Useful data results from tracking how this transition energy shifts with some adjustable parameter like temperature, pressure, chemical doping, etc.

Increasing the frequency of the alternating field in ac susceptibility to 10 MHz allows for the exploration of several effects not accessible at lower frequencies. These effects include nuclear magnetic resonance, electron paramagnetic resonance, relaxation processes, domain wall resonance, as well as a probe of resistivity through the normal state skin effect. In conjunction with the normal state skin effect is the possibility of the rf field heating a metallic sample. Table 1.1 summarizes the various effects observable at radio–frequencies.

Table 1.1 Physical effects observable at radio frequencies.

Effect	**Typ. Freq. (MHz)**	**Reference**
NMR	10-100	Blundell (2001)
EPR	$\geq 10^3$	Blundell (2001)
spin–spin relaxation	10^4	Morrish (2001)
spin lattice relaxation	10^{-4}–1	Morrish (2001)
domain wall resonance	1–50	Saitoh et al. (2004)
skin effect	1-10^3	Jackson (1998)

1.3.1 Normal State Skin Effect

An oscillating electromagnetic field is attenuated when it penetrates a metal. The attenuation is due to the normal state skin effect. The characteristic length over which the attenuation occurs is called the skin depth and it is denoted by δ. The skin depth depends on the resisitivty (ρ) and permability (μ) of the metal, as well as on the frequency (f) at which the field oscillates. δ is related to the previous three parameters by the following equation [Jackson (1998)]:

$$\delta = \frac{c}{2\pi}\sqrt{\frac{\rho}{\mu f}}. \tag{1.1}$$

To see this, consider an oscillating electromagnetic field normally incident on a vacuum/metal interface. Maxwell's equations for this situation may be written as

$$\nabla \times \mathbf{B} = \frac{4\pi}{c}\mu\mathbf{J} \tag{1.2}$$

$$\nabla \cdot \mathbf{B} = 0 \tag{1.3}$$

$$\nabla \times \mathbf{E} + \frac{1}{c}\frac{\partial B}{\partial t} = 0 \tag{1.4}$$

$$\mathbf{J} = \sigma\mathbf{E} \tag{1.5}$$

where $\sigma = 1/\rho$ is the conductivity. We can replace $\mathbf{B}$ with the vector potential by setting $\nabla \times \mathbf{A} = \mathbf{B}$. This changes Eq. 1.4 to

$$\nabla \times \left(\mathbf{E} + \frac{1}{c}\frac{\partial \mathbf{A}}{\partial t}\right) = 0. \tag{1.6}$$

The immediate consequence of this is that

$$\mathbf{E} + \frac{1}{c}\frac{\partial \mathbf{A}}{\partial t} + \nabla\phi = 0. \tag{1.7}$$

Provided there are no free charges, it is appropriate to set $\phi = 0$, whence $\mathbf{E} = -\frac{1}{c}\frac{\partial \mathbf{A}}{\partial t}$. Further, by combining Eqs. 1.2, 1.5, and 1.7, and by exploiting the vector identity $\nabla \times \nabla \times \mathbf{A} = \nabla(\nabla \cdot \mathbf{A}) - \nabla^2 \mathbf{A}$ we arrive at

$$\nabla^2 \mathbf{A} = \frac{4\pi}{c^2}\mu\sigma\frac{\partial \mathbf{A}}{\partial t}. \tag{1.8}$$

If a plane wave magnetic field of the form $H_x(t) = H_0 \cos 2\pi f t$ is normally incident (in the z direction) on the metal in question, continuity conditions require the parallel component of H be conserved on crossing the boundary between the vacuum and the metal. Further, Eq. 1.8 requires that the magnetic wave in the medium have only an x component and travel in the z. Provided the conductivity is constant in space, $\mathbf{B}$ (as well as $\mathbf{H}$) will have the behavior of $\mathbf{A}$ in Eq. 1.8. Therefore, in the medium it is expected that

$$H_x(z,t) = h(z)\, e^{i\omega t} \tag{1.9}$$

and

$$\left(\frac{d^2}{dz^2} - \frac{4\pi}{c^2} i\mu\sigma\omega\right) h(z) = 0. \tag{1.10}$$

This problem has a common form with an expected solution $h(z) = h_0 e^{kz}$. Substituting this gives the condition

$$k = \pm(1+i)\frac{2\pi}{c}\sqrt{\mu\sigma f}. \tag{1.11}$$

In the above $f = \omega/2\pi$ is the frequency of the oscillating wave as measured in hertz rather than radians per second. k has the dimensions of inverse length and characterizes the decay of h in the medium. Consequently, we define $\delta = 1/k$, arriving at the skin depth of the metal as given in Eq. 1.1. Figure 1.1 is a schematic representing the decay of the magnetic field in the metal. From here we can proceed to the calculation of the ac susceptibility of a metal.

Within the metal, we can write the vector potential of the decaying field as

$$\mathbf{A} = -B\frac{\delta}{2}\frac{\sinh(2x/\delta)}{\cosh(2R/\delta)}\hat{z} \tag{1.12}$$

where $2R$ is the thickness of the metal. Equation 1.2 allows for a relation between $\mathbf{A}$ and $\mathbf{J}$, after exploiting the previously mentioned vector identity.

$$\nabla^2 \mathbf{A} = \frac{4\pi}{c}\mathbf{J} \tag{1.13}$$

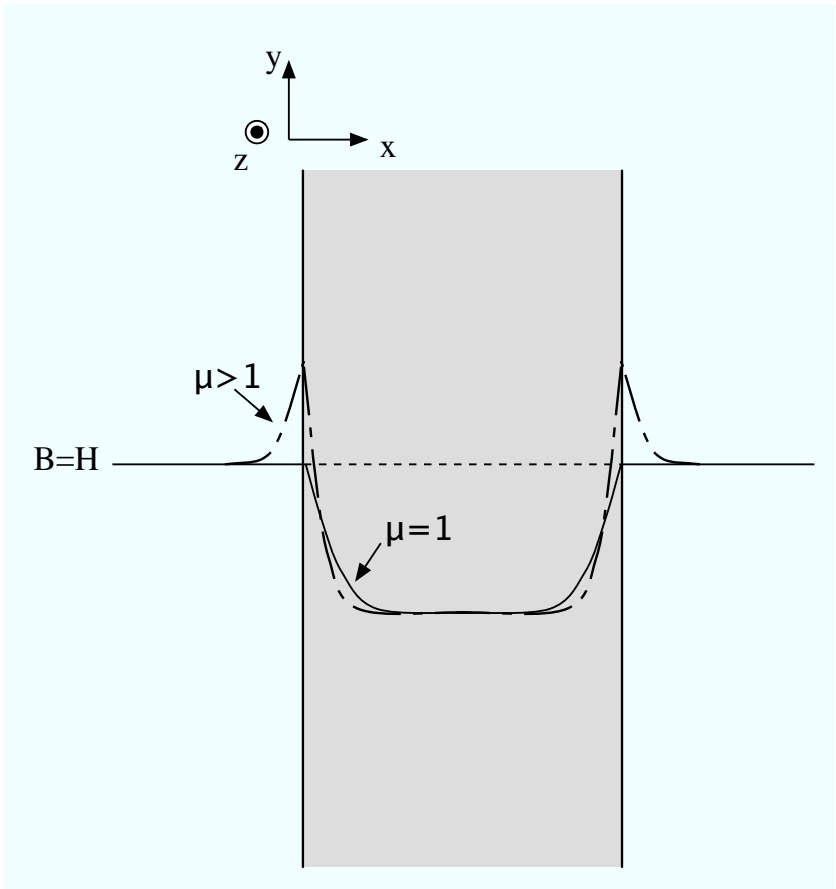

Figure 1.1 Schematic of decay of an oscillating magnetic field in a metal.

This gives the current density in the metal as a function of position, or depth, as

$$\mathbf{J} = B\frac{c}{4\pi}\frac{2}{\delta}\frac{\sinh(2x/\delta)}{\cosh(2R/\delta)}\hat{z} \tag{1.14}$$

The magnetic moment induced in the sample can be determined from

$$\mathbf{M} = -\frac{1}{2c}\int \mathbf{r}\times\mathbf{J}d^3r \tag{1.15}$$

Evaluating this over the limits 0 to R gives the following expression for the moment.

$$4\pi\mathbf{M} = \left(\frac{B\delta}{2R}\tanh\frac{2R}{\delta} - H\right)\hat{y} \tag{1.16}$$

Differentiating once with respect to H gives the susceptibility from the sample as

$$4\pi\chi = \frac{\mu\delta}{2R}\tanh\frac{2R}{\delta} - 1 \tag{1.17}$$

From Eq 1.17 we can extract some information that will be useful in analyzing the data. First, in magnetically static samples with permeability $\mu = 1$ the radio–frequency susceptibility will track the resistivity. This applies to field or magneto–crystalline anisotropy saturated magnetic samples wherein the ac–susceptibilitiy of the microscopic moments is essentially zero. That this is so is evident from Fig. 4.6 (below) where the unusual $T^{5/3}$ behavior of ρ at low temperatures in $ZrZn_2$ is recovered. This fact has been exploited in the past to probe the Fermi surfaces of metals [Coffey et al. (2000), Prozorov et al. (2006)] via the Shubnikov-de Haas effect [Shoenberg (1984)]. (See Appendix C.) In magnetically active samples, however, the situation is less clear due to the mixing of the magnetic permeability and resistivity through the product $\mu\delta$. There are two limiting cases. First, in the limit $2R << \delta$, the hyperbolic tangent goes to zero linearly and the susceptibility reduces to $4\pi\chi = \mu - 1$, which is the standard relation, valid when the magnetization in a sample is uniform. This is the insulating regime, and the resonator probes the response of the magnetic moments in the sample. In the other limit ($2R >> \delta$), the hyperbolic tangent term is very close to 1 and $4\pi\chi = (\mu\delta/2R) - 1$. This is a complicated case because there is a mixing of the permeability and the resistivity. Further, substitution of $1+4\pi\chi$ for μ is not valid as such a substitution requires the magnetization to be uniform in the sample. This clearly is not the case since the applied field decays exponentially

in the sample. This represents the skin depth limited regime, and here it can be argued that the resonator probes the changes in resistivity concomitantly with changes in the magnetic permeability. For ferromagnets that are far from the insulating regime, information regarding the response of the magnetic moments can be obtained provided the temperature is close to T_C. In this temperature range the susceptibility grows rapidly, formally diverging at T_C. Further, ρ remains finite. This implies the skin depth goes very small and the hyperbolic tangent term saturates to 1. In this case

$$4\pi\chi = \frac{c}{4\pi R}\sqrt{\frac{\rho}{f}}\sqrt{\mu} - 1. \tag{1.18}$$

This is seen by recognizing that the numerator of the coefficient on the hyperbolic tangent term is $\mu\delta$. Since $\delta \sim \sqrt{\mu^{-1}}$ the product $\mu\delta \sim \sqrt{\mu}$.

1.3.2 Energy Scales Associated With RF Fields

Any magnetic field (static or oscillating) gives rise to a Zeeman splitting in the energy levels of any magnetic moment. The amplitude of the Zeeman splitting is given by

$$U_{Zeeman} = \vec{mu} \cdot \vec{H} \tag{1.19}$$

where $\vec{mu}$ is the magnetic moment and $\vec{H}$ is the magnetic field. If μ is equal to one Bhor magneton and H is one tesla then $\mu H \approx 5.79 \times 10^{-5}$ eV. Comparing this to thermal energy ($k_B T$) gives an equivalent temperature of about 0.67 K. For small magnetic fields, on the order of 2.5 kOe or less, at temperatures above 2 K, the Zeeman energy is not expected to have a considerable effect unless the magnetic moments are on the order of $10\mu_B$ per ion as is the case for trivalent holmium and dysprosium.

In addition to the possibility of a Zeeman energy, an oscillating electromagnetic field has an energy associated with the frequency of oscillation. This is the energy of the photon associated with the wave. For a wave with a frequency of 10 MHz, the energy is on the order of 10^{-8} eV. Comparing the photon energy to thermal energy results in an equivalent temperature of approximately 10^{-3} K.

There is power dissipated in a metallic sample due to the screening from the normal skin effect. An estimate of the order of magnitude of this power can be made by considering the

energy density of the screened rf field. This is given by

$$\epsilon = \frac{B_{rf}^2}{8\pi}. \tag{1.20}$$

Without knowledge of the magnitude of the screened field, it is impossible to determine the energy density associated with the screening. However, the rf field used to measure χ in this work has a peak amplitude of about 5 mOe. This magnetic field has an energy density on the order of 1.5 pJ/cm^3. For the working frequencies (10^7 Hz) and typical sample sizes (1 mm^3=10^{-3} cm^3) here, the power dissipation is on the order of 0.01 pW in a magnetically dead sample. If there is significant magnetic permeability in the sample, this power can increase (Appendix B) provided the heat capacity of the sample is low enough.

1.4 The Tunnel Diode Resonator

In order to measure the magnetic susceptibility at 10's of MHz at tunnel diode resonator (TDR) was employed. The TDR is a self-resonating LC circuit driven by a tunnel diode (TD). The TD is a solid state diode with a heavily doped p-type terminal. The pn junction is of the order of 100 $\AA$, very narrow for a diode [Esaki (1976)]. The resulting device exhibits negative differential resistance when biased within a certain range of voltages (Fig. 1.2). When biased to this region, the TD can perform as a low current, alternating current power source. If we consider a simple LC tank circuit the frequency of the ac power delivered by the tunnel diode is determined by the frequency of the tank circuit. Indeed, it is this frequency matching that is exploited in the use of a TDR. The main advantage of making measurements this way is that inductance is placed on equal footing with capacitance. Commercial capacitance bridges are capable of attofarad resolution. However, determining small changes in inductance is not simple with commercial devices. By changing the measurement from a balance of inductances to a direct measurement of resonant frequency, the sensitivity to changes in L, and hence χ, is greatly improved. Further, the amplitude of the probe field is extremely small. The biasing of the TD creates a small static field in the probe coil on the order of 30 mOe in the resonators used here. Superimposed on this is a small ac ripple that is used as the probe field, the amplitude of which is determined by the excursions up and down the $I - V$ curve. The

deviations in current from the bias point are estimated to be $\leq 5\ \mu$A. The resulting ac field is then $\leq$6 mOe peak to peak. This is 1.5 orders of magnitude smaller than the typical excitation fields used in conventional low frequency ac-susceptibility.

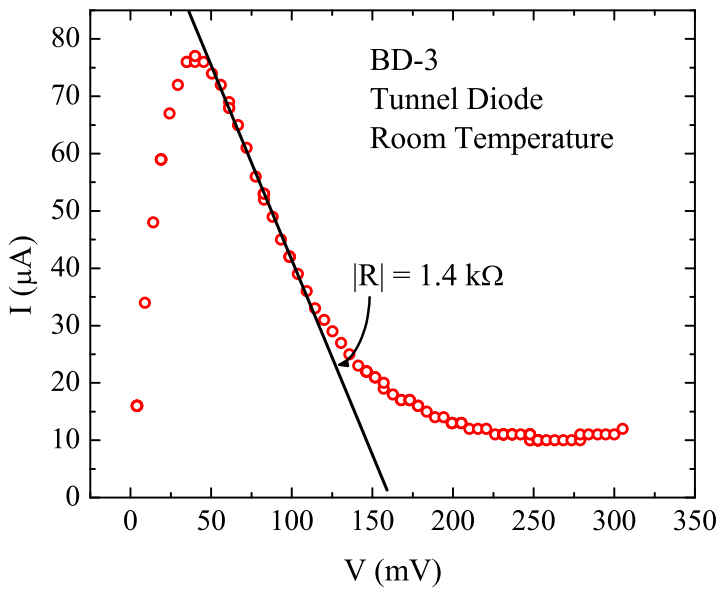

Figure 1.2 *I–V* curve for BD3 tunnel diode. Negative differential resistance is evident for bias voltages between 50 and 250 mV. Optimal biasing is for this particular diode is in the range 60-100 mV.

The TDR was developed in the 1970's. Many different groups constructed these devices and suggested measurements including NMR spectroscopy [Aslam and Weyhmann (1973)] and magnetic susceptibility [Clover and Wolf (1970), Habbal et al. (1975), Fox and Trefay (1975)]. The main development of the TDR as an ultraprecise scientific instrument was carried out by VanDegrift in the middle 1970's [VanDegrift (1975a)]. The primary use of the TDR in that work was in measuring dielectric constants. VanDegrift demonstrated that part per billion sensitivity could be achieved through careful design. To date, the apparatus has not been employed by many research programs. Those programs that do employ some version of the TDR are largely concerned with precise measurements of temperature dependent magnetic penetration depth

in various superconductors. A few other groups are concerned with measuring normal state magnetic effects, however their work is largely confined to thin films and nanoparticles. In the course of this work, the TDR has been employed to measure many different types of compounds and effects including ferromagnetic and antiferromagnetic conductors and insulators [Vannette et al. (2008d)], charge ordering effects in Ba_2NaOsO_6, spin glass behavior in LiV_2O_4 [Zong et al. (2008)], ferroelectric transitions, quantum oscillations in metals [Prozorov et al. (2006)], and the penetration depth in a host of superconductors (see Table 1.3). The main thrust of this work, though, was the study of the differential magnetic susceptibility ($\chi = \partial M/\partial H$) of magnetically ordered samples as functions of temperature and field in an attempt to extract information regarding phase changes and the different responses of local and non-local ferromagnets.

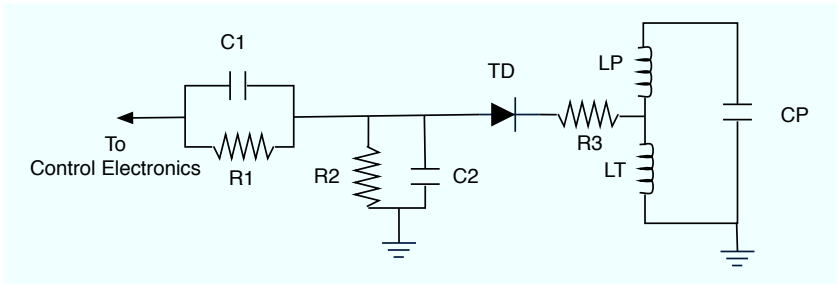

Figure 1.3 Schematic of the basic tunnel diode resonator circuit.

The basic tunnel diode resonator circuit is shown in Fig. 1.3. The primary inductor and capacitor are LP and CP respectively. The sample is placed in the bore of LP. Inductor LT is the tap coil, and it serves to shunt some of the power supplied by the diode to ground, thereby permitting extremely weak resonance. The weaker the resonance is, the fewer harmonics are present. Too many higher harmonics distort the waveform. If the harmonics are particularly strong, the wave distortion can be significant enough to lead to miscounts in the frequency measurement. The purpose of $C1$ and $C2$ are to decouple the tank circuit from the rest of the electronics. $C1$ is typically on the order of 50 pF while $C2$ is on the order of 10 nF. At 10 MHz the rf impedance of $C1$ and $C2$ are 340 Ω and 1.5 Ω. Thus, $C2$ is practically a short to ground for the rf signal and only a very small portion is passed back up the line by $C1$. $R1$ and $R2$

act as voltage dividers. $R3$ is termed the parasite resistor. It acts in concert with the tap coil to reduce unwanted oscillations. $R1$ has a typical value of 1.4 kΩ, $R2$ and $R3$ are 300 Ω. The primary coil is wound of 40 AWG enameled copper wire. It is on the order of 60 turns with one wire diameter space between each turn. This allows the coil to more closely approximate a pure inductance by limiting the stray capacity from adjoining turns. Primary coils are wound on a former (usually the chuck end of a drill bit) lightly coated with grease and wrapped in polyester flim. Once the coil is made, it is encased in Stycast 1266 epoxy (or similar) and after curing, is removed from the former. The polyester film is removed from the inside wall of the coil, and ideally the primary is just a coil of copper magnet wire suspended by an epoxy film. The tap coil is wound in a similar manner as the primary. The main difference being that the tap is left on a fused silica tube of the same outer diameter as the primary coil former. Also, the tap coil is not set in epoxy. Rather varnish is used to keep the turns of the tap glued to the tube. This allows for easy modification of the tap coil inductance. The ratio of LP:LT is about 3:1. For optimal performance this ratio must be tuned experimentally for each circuit by overtapping the circuit (i. e. intentionally making the tap coil too large) and then through successive cool downs, gradually unwinding the tap until the circuit spontaneously resonates only below about 40 K. TDR's will operate at room temperature, but the sensitivity drops from 0.001 ppm to about 1-10 ppm. This latter sensitivity is still quite good, but by operating at low temperatures with marginal oscillations, the greater sensitivity is achieved. The value of CP is chosen to keep the resonance less than 50 MHz. This range was chosen because amplifiers and filters that operate well at these frequencies may be easily acquired. Further, keeping the frequency below gigahertz limits problems associated with transmission line and connector size effects that may occur when the wavelength of the radiation approaches the typical dimensions these components. In principle, the TDR can be made to operate at higher frequencies, even into the GHz regime. This was not attempted here, but is a direction of future work (see Ch. 6). Thermal cycling of the circuit is expected to alter the resonant frequency of the circuit. The expansion and contraction of the coil, wires, solder joints, and commercial components all contribute to this effect. Fig. 1.4 plots the empty coil resonant frequency of the

^{4}He for nine consecutive runs over the course of two months. The uncertainty in the recorded empty coil resonance is on the order of 0.5 Hz for the system used here. The resonance stays constant to within about 0.5% (±50 kHz on 28 MHz) in this time period. Between the first run shown and the unshown zeroth run the coil had to be removed to recover a sample that had dropped off the sample holder. The empty coil resonance of this zeroth run was 27.76 MHz. Having to resolder these joints resulted in a change in the resonance on the order of 2%. This suggests that provided no modifications to the circuit are made, including fixing poor solder joints, the resonant frequency is very robust to thermal cycling. These variations come from

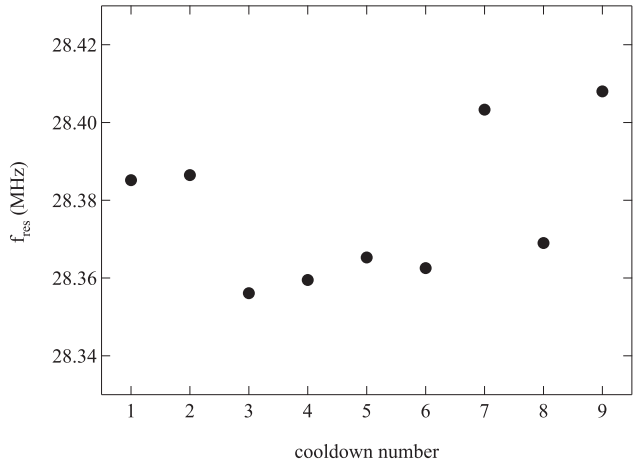

Figure 1.4 Empty coil resonance vs. thermal cycle count.

the binary state thermal cycling of the cryostat. During a given run the circuit is held at a constant, low temperature while the sample temperature is varied. Between runs the entire apparatus is warmed to room temperature. The cycling from high to low temperature results in small changes in the quality of the solder joints, the position of the coil, the parameters of the circuit elements, etc. leading to slightly different resonant frequencies during each run.

Three different TDR's were employed to collect data for this work. Specific details regarding design and construction can be found in Appendix A. Table 1.2 gives the name that is used in this work and presents the basic information for each system.

A gap in the accessible temperatures exists between 200-293 K. Due to the competing

Table 1.2 TDR Specifics

System	**Coil Volume (mm^3)**	f_{res} **(MHz)**	**Temp. Range (K)**
^{3}He	31	14	0.5-100
^{4}He	33	28	2-200
Inferno	250	36	293-800

requirements, this temperature window is particularly difficult to access with this technique. Chapter 6 discusses various modifications and improvements that may be attempted to gain access to more information regarding the radio frequency properties of materials.

The versatility of the TDR is evident from the material phase space that can be explored. Table 1.3 lists the samples measured in the course of this work. Most are unrelated to this dissertation, however the list is meant to demonstrate the breadth of application of the technique.

Table 1.3 Samples run in TDR during this project. $T_{char.}$ is a characteristic temperature for the sample.

Sample	$T_{char.}$	**Reference**
	Ferromagnets	
$CeAgSb_2$	9.8 K	Prozorov et al. (2006)
GdPtIn	68 K	Vannette et al. (2008a)
$CeVSb_3$	4.5 K	Vannette et al. (2008d)
$YTiO_3$	27 K	
EuS	16 K	
Gd	280 K	
$ZrZn_2$	28 K	Vannette and Prozorov (2008)
Ni	760 K	
$GdFe_2Zn_{20}$ (& dopings)	$\leq$86 K	Vannette et al. (2008d)
$Fe_{1/4}TaS_2$	160 K	Vannette et al. (2008e)
NiMnSb	730 K	
	Antiferromagnets	
$SmAgSb_2$	10 K	Prozorov et al. (2006)
MnSi	35 K	
FeGe	279 K	
	Multiple Transtitions	
CeSb	many	Vannette et al. (2008d)
Ce_3Al_{11}	6 & 3.8 K	Vannette et al. (2008d)
Y_9Co_7	6.7 K & 2.9 K	Gordon et al. (2008b)
	Superconductors	
MgB_2	38 K	Martin et al. (2008)
Re_3W	7.4 K	Zuev et al. (2007)
YNi_2B_2C	16 K	Prozorov et al. (2007)
$ErNi_2B_2C$	12 K & 6 K	Prozorov et al. (2008a)
$ErRh_4B_4$	10 K & 1.9 K	Prozorov et al. (2008b)
$TmNi_2B_2C$	10.2 K & 1.8 K	Prozorov et al. (2008a)
$Ba(Fe_{1-x}Co_x)_2As_2$	22 K	Gordon et al. (2008a)
Bi-2201	35 K	
OsB_2	2.1 K	Singh et al. (2007)
	Other Materials	
LiV_2O_4	2 K	Zong et al. (2008)
Ba_2NaOsO_6	6 K	
$HoMnO_3$	many	Vannette et al. (2008b)
$DyMnO_3$	many	Vannette et al. (2008b)
"Fe_8"	none	Engelhardt et al. (2007)
$Mo_{72}Fe_{30}$	1 K	Schroder et al. (2008)
$Mo_{72}Cr_{30}$	none	Schroder et al. (2008)
$CaFe_2As_2$	170 K	
Cu	none	

1.5 Measuring Changes in Magnetic Susceptibility

In exploiting a TDR the measurement of magnetic susceptibility is shifted from the amplitude domain to the frequency domain. As has been stated previously, amplitude domain measurements depend on the actual amplitude of the signal and, in AC measurements, the shape of the signal waveform. Frequency domain measurements are only concerned with counting how many times something happens in a given period. As such, frequency measurements are quite easy to do with very high precision. Since the TDR is a device that is locked onto the resonant frequency of the LC tank circuit, changes of the resonance can be linked directly to either the inductor (as is done here) or the capacitor. Careful design and good thermal stability can result in a circuit that resonates in the megahertz band with a stability of 0.05 Hz over hours to days. If field or temperature is varied, the resonant frequency shifts due to the changing properties of the sample. It is this shift in resonance that is measured to determine the dependencies of χ on these two parameters.

The frequency of oscillation for an inductor-capacitor circuit with inductance L and capacitance C is given by

$$f_0 = \frac{1}{2\pi\sqrt{LC}} \tag{1.21}$$

If the inductance changes a small amount to $L + \Delta L$ the new frequency can be written as

$$f_0 + \Delta f = \frac{1}{2\pi\sqrt{(L + \Delta L)C}} \tag{1.22}$$

Expanding this expression for small values of ΔL and canceling gives

$$\Delta f \approx -\frac{1}{2}\frac{\Delta L}{L} f_0 \tag{1.23}$$

From the definition of self inductance

$$L = \frac{d\Phi}{dI} \tag{1.24}$$

where Φ is the integrated magnetic flux in the coil and I is the current producing the flux. For an empty coil

$$\Phi = B_0 V_c \tag{1.25}$$

Here, V_c is the coil volume. In cgs units, the flux density B_0 is equal to the magnetic field H_0 in vacuum. Introducing a sample with zero demagnetization changes the flux density in the volume of the sample. This is accounted for by imagining the sample replaces the initial flux with a new value given by Φ' where

$$\Phi \rightarrow \Phi' = B_0 V_c + (B_s - B_0) V_s. \tag{1.26}$$

The flux density in the sample, B_s, is given by the usual relation

$$B_s = H_0 + 4\pi M_s \tag{1.27}$$

where M_s is the sample magnetization per unit volume. Substituting this results in the following expression for flux in the inductor:

$$\Phi' = H_0 V_c + 4\pi M_s V_s \tag{1.28}$$

Writing the derivative of Φ' with respect to current as

$$\frac{d\Phi'}{dI} = \frac{d\Phi'}{dH}\frac{dH}{dI} \tag{1.29}$$

allows the new inductance to be written as

$$L' = (V_c + 4\pi V_s \chi)\frac{dH}{dI} \tag{1.30}$$

The first term is the empty coil inductance and the second is the change caused by the sample. Returning to equation 1.23,

$$\frac{\Delta f}{f_0} \approx -\frac{1}{2}\frac{V_s}{V_c} 4\pi\chi \tag{1.31}$$

The above expression relates the measured change in frequency to the real part of the ac-susceptibility of the sample. Equation 1.31 shows that the change in frequency, Δf, is proportional to the base frequency, f_0. This means a larger signal is expected with higher base frequencies, all other things being equal. If there is non-zero demagnetization for the sample the true susceptibility (χ_t) may be written as

$$\chi_t = \frac{\chi_m}{1 + 4\pi N \chi_m}. \tag{1.32}$$

χ_m is the measured susceptibility as related to the measured frequency shift given above.

Thus, the change in resonant frequency is directly proportional to the dynamic magnetic susceptibility of any sample placed in the coil. An increase in magnetic susceptibility results in a decrease in resonant frequency and *vice versa*.

It is worth noting that this technique is not well suited to measuring the absolute value of χ_{TDR} in most samples. This is because a conversion from frequency shift to χ_{TDR} depends on accurate knowledge of the sample volume, sample demagnetization factor N, and the effective coil volume. Demagnetization factors may be estimated for each sample, but N is only analytically defined for ellipsoids. Effective coil volume is, in general, different from actual coil volume due to the effect of the materials required to mount the coil and sample in place. The main use is to measure *changes* in the properties relative to some arbitrarily chosen reference value. Thus, this technique is good for determining the general dependencies of ρ and χ on temperature and field. It is possible to determine the absolute value of the measured χ_{TDR}, but this value depends on the sample size, shape, and resistivity in addition to the response of the microscopic moments. Care must be taken when comparing the results of such measurements across different samples to choose samples that are of similar size and shape. Maintaining a consistent geometry across different samples maintains a consistent coefficient linking frequency shifts to susceptibility. This permits a more accurate comparision between samples of different compositions.

Bearing the preceeding paragraph in mind, it is possible to determine a figure for χ_{TDR} in real units by performing a pullout measurement. From Eq. 1.31 there are four quantities which must be known to allow for an estimate of the absolute value of χ_{TDR}. The sample and coil volumes can be determined by direct measurement. Determining the empty coil resonance, f_0, and the change in resonance caused by the sample, Δf, require extracting the sample from the coil while the circuit is held at the operating temperature. This can be done and the mechanism by which to do it was installed in one of the three systems used to collect data part way through this study. Since the derivation of Eq. 1.31 was carried out in cgs units, absolute values of χ_{TDR} will be determined in these units.

In practice one measures the difference, df, between the circuit frequency, f_{res} and a local oscillator, f_{LO} ($df = f_{LO} - f_{res}$). The local oscillator frequency is set higher than the circuit resonance ($f_{LO} > f_{res}$). In this way an increasing susceptibility is marked by an increasing df. Further, an increasing resistivity results in an increasing df since the skin depth increases with the resistivity resulting in decreased diamagnetic screening.

1.6 Representative TDR Data

Data on a set of rare–earth transition metal compounds (RAgSb$_2$, R =Y, Ce, Sm) are presented. These compounds were chosen based on their magnetic ordering properties. YAgSb$_2$ is not magnetically ordered. CeAgSb$_2$ manifests a canted antiferromagnetic order at 9.8 K. The canting of the Ce moments gives rise to a net magnetic moment, so it shows ferromagnetic order along a particular crystallographic axis. SmAgSb$_2$ manifests pure antiferromagnetic order at approximately 10 K. Data from these three related systems form a baseline to which other compounds will be compared.

Myers et al. (1999b) studied the tetragonal RAgSb$_2$ family of compounds. These compounds manifest a variety of magnetically ordered states. In particular, CeAgSb$_2$ shows a canted antiferromagnetism lying in the ab plane at approximately 9.8 K. The canting of the antiferromagnetic moments manifests itself as a ferromagnetic component along the c axis. SmAgSb$_2$ undergoes a transition to simple antiferromagnetic order at approximately 10 K. The non–magnetic YAgSb$_2$ allows for a study of how the presence of magnetic moments and/or magnetic order affect properties like resistivity and heat capacity. One sample of each of these three compounds was studied in the TDR to observe how the rf susceptibility differs across the three magnetic flavors (ferromagnetism, antiferromagnetism, and non–magnetic).

Figure 1.5 compares scaled susceptibility of Y–, Ce–, and SmAgSb$_2$ vs. temperature in the range 3–15 K as measured in the TDR. All thre data sets are shifted so that the low temperature data overlap. YAgSb$_2$ shows a monotonic behavior through the entire temperature regime. The yttrium data appears noisy compared to the other two data sets. In fact, all data sets have approximately the same level of noise. Due to the small variation in the measured susceptibility,

the yttrium data had to be magnified by a factor of approximately 100 so that the variation in χ with temperature could be discerned. $SmAgSb_2$ also manifests monotonic behavior through the entire temperature range. However, at approximately 9 K there is a sharp break in the slope of the χ vs. T graph. This temperature corresponds to the Nèel temperature, below which antiferromagnetic order sets in. In a magnetically ordered state conduction electrons can no longer scatter off ionic moments. The loss of this scattering mechanism generally leads to a decrease in the measured resistivity. Contrary to the other two compounds, $CeAgSb_2$ manifests non–monotonic behavior over the reported temperature range. At approximately 9.8 K a sharp peak in χ is observed. The peak in χ is associated with the increase in spin susceptibility due to strong ferromagnetic correlations. Below the ordering temperature the cerium compound exhibits a decrease in the measured susceptibility due to the loss of spin disorder scattering.

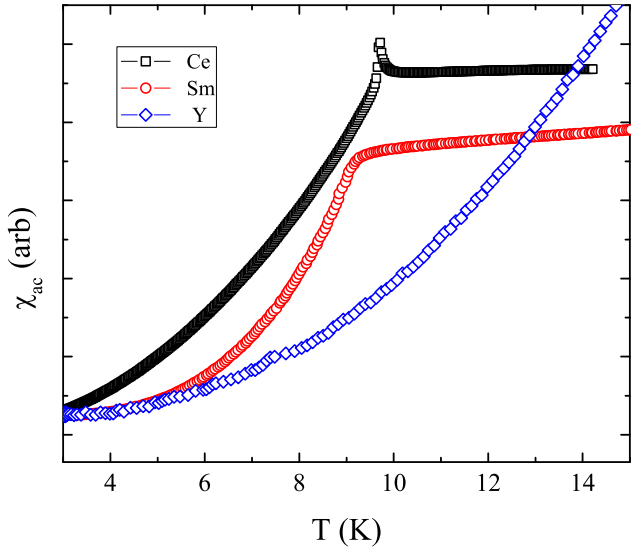

Figure 1.5 Scaled comparison of Y–, Ce–, and $SmAgSb_2$ χ vs. T data.

Static moment measurements of antiferromagnetic compounds show that the moment increases as the Néel temperature is approached. This is often reported as an increase in the

susceptibility of the compound. Similar increase in moment is observed in ferromagnetic materials as the Curie temperature is approached. However, the TDR data shows that the two different magnetic orders show different rf susceptibilities. The observed difference can be qualitatively understood based on the following argument. The perturbation field from the TDR coil is very small, being less than 5 mOe. The existence of magnetic order at a finite temperature implies an interaction between the moments in the sample. The strength of that interaction must be on the order of the thermal energy present at the ordering temperature. The perturbing field causes a change in the direction of a particular moment, tending to align the moment with the field. Near an ordering temperature the internal interactions between the perturbed moment and its neighbors dominates the response of the system. When the interaction is ferromagnetic neighboring moments have an energy advantage if they align with the perturbing field as well. This sets up a positive feedback, and the TDR sees a dramatic increase in the susceptibility of the material. Conversely, if the interaction is antiferromagnetic individual moments will tend to align so that there is no bulk magnetization in the sample. The TDR then sees no increase in χ, and the response through the transition is to follow the resistivity.

The differing measured susceptibilities across the three rare–earth silver diantimonides are taken as standards to which other results may be compared. Comparison with these standards will offer an initial interpretation of a given set of data. A sharp peak in χ at a particular temperature is associated with the onset of ferromagnetic order. A dramatic drop in χ at a particular temperature is associated with antiferromagnetic ordering in a metallic sample. Temperature dependent χ that manifests no obvious features will be taken to mean the sample shows no magnetic order.

1.7 Summary

Radio–frequency suscpetibility measurements provide data not accessible through other means, but the convolution of resistivity and magnetic spin responses in metals complicates the measurement and analysis process. It is possible to circumvent these problems through

careful choice of samples. The tunnel diode resonator is a method whereby extremely precise rf χ data may be collected. It was shown that there are stark differences between ferromagnetic, antiferromagnetic, and non–magnetically ordered metals. In the following chapters an attempt will be made to understand the differences in the measured χ of various samples.

CHAPTER 2. Local Moment Ferromagnets

2.1 Introduction

In this chapter the nature of local moment ferromagnets is explored. These are systems wherein the magnetic moment is strongly localized around a particular ion or particular ions in the crystal. Typically the $4f$ rare earth systems are considered local moment systems as the f electrons responsible for the atomic magnetic moment are buried deep in the core of the electron cloud.

2.2 Basics of Magnetism

Experimentally, it is known that the magnetic susceptibility, $\chi = \partial M/\partial H$, of a collection of non-interacting spins varies inversely with the temperature T of the system.

$$\chi = \frac{C}{T} \tag{2.1}$$

C is called the Curie constant and its magnitude depends on the strength and number of the individual moments in the system.

The genesis of this dependency is in the Zeeman energy for a free spin in a magnetic field, $U_Z = -\mu_B \mathbf{H} \cdot (\mathbf{L} + g_0 \mathbf{S})$ where $\mu_B = e\hbar/2m_e c$ is the Bohr magneton and $g_0 = 2(1 + \alpha/2\pi + O(\alpha^2) + ...) \approx 2$ is the electronic g-factor. α is the fine structure constant, given by $e^2/\hbar c \approx 1/137$. Due to the small size of μ_B ($\approx 5.8 \times 10^{-4}$ ev/T), this energy is usually small compared to all other energies under consideration. The problem may then be handled using perturbation theory. If the exact eigenstates for the system in the absence of the magnetic field are known, second-order perturbation theory may be used to determine the change in energy

due to the magnetic field [Ashcroft and Mermin (1976)].

$$\Delta U_n(H) = \mu_B \mathbf{H} \cdot < n|\mathbf{L} + g_0\mathbf{S}|n > + \mu_B^2 \sum_{n \neq n'} \frac{| < n|\mathbf{H} \cdot (\mathbf{L} + g_0\mathbf{S})|n' > |^2}{E_n - E_{n'}} \tag{2.2}$$

The second term in equation 2.2 is the Van Vleck paramagnetic susceptibility. If the second term is small compared to the first, then the ground state energy can be rewritten via the Wigner-Eckhart theorem as

$$< JLSJ_z|\mathbf{L} + g_0\mathbf{S}|JLSJ_z' >= g_J(JLS) < JLSJ_z|\mathbf{J}|JLSJ_z' > . \tag{2.3}$$

In the above, g_J is the Landé g-factor given by

$$g_J(JLS) = \frac{3}{2} + \frac{1}{2}\left[\frac{S(S+1) - L(L+1)}{J(J+1)}\right] \tag{2.4}$$

if $g_0 = 2$. Once the energy of the system is determined, the magnetization and magnetic susceptibility may be calculated from

$$M = -\frac{N}{V}\frac{\partial F}{\partial H} \tag{2.5}$$

and

$$\chi = \frac{\partial M}{\partial H} = -\frac{N}{V}\frac{\partial^2 F}{\partial H^2} \tag{2.6}$$

In equations 2.5 and 2.6, F is the free energy which can be calculated from

$$e^{-\beta F} = \sum_{J_z=-J}^{J} e^{-\beta g_J \mu_B H J_z} \quad , \ \beta = \frac{1}{k_B T}. \tag{2.7}$$

Using this, the magnetization may be written as

$$M = -\frac{N}{V} g_J \mu_B J B_J(\beta g_J \mu_B J H). \tag{2.8}$$

$B_J(x)$ is the Brillouin function [Blundell (2001)] with $x = \beta g_J \mu_B J H$.

$$B_J(x) = \frac{2J+1}{2J}\coth\left(\frac{2J+1}{2J}x\right) - \frac{1}{2J}\coth\left(\frac{x}{2J}\right) \tag{2.9}$$

The Brillouin function is a hyperbolic tangent for a spin-1/2 system and evolves to the Langevin function

$$L(x) = \coth x - \frac{1}{x} \tag{2.10}$$

for a classical, or infinite, spin system.

Often measurements are taken in the limit of small x, i. e. low field and high temperature. Under either condition of $J \to 1/2$ or $J \to \infty$ this results in a linear dependence of magnetization on field. Therefore, the magnetic susceptibility, χ, of non-interacting, free spins is given by Curie's Law:

$$\chi = \frac{C}{T} \tag{2.11}$$

where C is the Curie constant, given below.

$$C = N_A \frac{(g_J \mu_B)^2}{3} \frac{J(J+1)}{k_B} \tag{2.12}$$

In many magnetically active samples, a plot of $1/\chi$ vs. T gives a straight line with positive slope, C. Comparing the measured slope with the predicted response allows for the determination of an effective paramagnetic moment per ion or formula unit, p_{eff}, defined as

$$p_{eff} = g_J \left[J\left(J+1\right)\right]^{1/2} \tag{2.13}$$

Doing so allows Eq. 2.12 to be rewritten as

$$C = N_A \frac{p_{eff}^2 \mu_B^2}{3k_B}. \tag{2.14}$$

Usually, this form of the susceptibility is sufficient, however at low temperatures with sensitive measurements, it is useful to know the leading field correction to the free spin susceptibility. Purely physical intuition would suggest that the application of an external field should reduce the susceptibility at a given temperature. A Taylor series expansion of hyperbolic cotangent gives

$$\coth x \approx \frac{1}{x} + \frac{x}{3} - \frac{x^3}{45} + ... \tag{2.15}$$

Since the magnetization is proportional to $\coth(\alpha H)$, and the susceptibility is the first field derivative of magnetization, the leading correction to χ due to magnetic field is proportional to $-H^2$. It is therefore expected that the field dependent behavior of free spins will show an initial decrease in χ as the field is increased.

When interactions between magnetic moments are significant, magnetic order can result. Depending on the nature and strength of the interaction ferromagnetism (all moments aligning in the same direction), simple antiferromagnetism (individual moments lie on one of two antiparallel sublattices with each sublattice carrying the same moment), or other types of magnetic structures can be realized at sufficiently low temperatures. A second effect of the interactions is to modify the paramagnetic Curie law behavior in susceptibility (Eq. 2.11) to a Curie-Weiss type given below.

$$\chi = \frac{C}{T - \theta} \tag{2.16}$$

θ is a characteristic temperature that may be positive or negative. Positive values for θ generally give rise to ferromagnetic ordering, while negative values indicate antiferromagnetic order. The ordering temperature often is approximately equal to the absolute value of θ, however this is not always the case.

Ordering in local moment systems is usually modeled by an exchange interaction. The interaction of one moment with all of the others is assumed to be of a pairwise form with the energy of the interaction given by

$$U = -\Sigma J_{ij} \mathbf{S}_i \cdot \mathbf{S}_j \tag{2.17}$$

where the sum is taken for $i \neq j$. J_{ij} is called the exchange integral and its sign and magnitude determine the nature and strength of the interaction. For $J_{ij} > 0$ the energy is minimized when the moments are parallel and ferromagnetic ordering is preferred. If, only nearest neighbor interactions are considered then the problem is greatly simplified.

A second common simplification is the mean field approximation. In this model an individual moment interacts with an effective field produced by all of the other moments. The mean field model offers a simple method for explaining the Curie-Weiss law. If a magnetic field is applied to a sample of interacting magnetic moments, then within the mean field approximation the magnetization can be written as

$$M = \chi \left(H_{app} + H_{eff} \right). \tag{2.18}$$

The effective field is assumed to be proportional to the magnetization ($H_{eff} = \lambda M$). Substituting this for H_{eff} and replacing χ with a Curie law temperature dependence allows one to solve for $M(H,T)$.

$$M = \frac{CH}{T - C\lambda} \tag{2.19}$$

This magnetization leads to a mean field susceptibility of

$$\chi = \frac{C}{T - C\lambda} \tag{2.20}$$

The above equation for χ predicts that the susceptibility should diverge as $T \to C\lambda$. Comparing 2.16 with 2.20 it is seen that $\theta = C\lambda$. Hence, it is also possible to determine the magnitude of the mean field parameter, λ, from a measurement of the paramagnetic susceptibility.

A connection between the mean field expression in Eq. 2.19 and the Brillouin or Langevin equations (Eqs. 2.9 and 2.10, respectively) can be made [Spaldin (2003)]. Taking the Langevin case the magnetization of a paramagnet can be written as

$$\mathbf{M} = N\mathbf{m}L(x) \tag{2.21}$$

where $x = mH/k_BT = \beta g_J \mu_B JH$. However, under the assumptions of the mean field theory, the magnetization is also given by $M = H_{eff}/\lambda$. Further assuming that the field is given entirely by the molecular mean field implies the magnetization is a linear function of T. This follows from the expression for x which shows that $H_{eff} = xk_BT/m$. This allows the magnetization to be written as

$$M = \frac{H_{eff}}{\lambda} = \frac{xk_BT}{m\lambda} \tag{2.22}$$

These two equations may be solved graphically for a given temperature to determine what values of M are permitted. This is done for three different temperatures in Fig. 2.1. For all three temperatures, $M = 0$ is a solution. It is the only solution for high temperatures. When $T = T_C$ the slope of the linear mean field magnetization matches the initial slope of the Langevin paramagnetic function. For sufficiently low temperature, there are two solutions. The non-zero one is a result of the ordering. It is possible to relate the mean field parameter λ with the ordering temperature. If Eq. 2.10 is differentiated with respect to x it is seen that

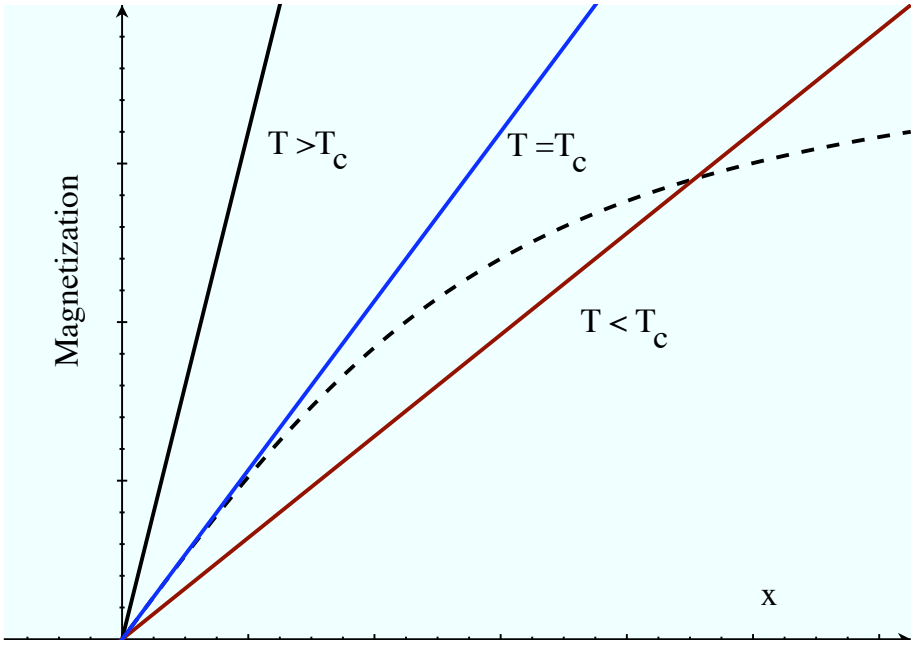

Figure 2.1 Plot of Langevin function (dashed curve) and mean field magnetization at different temperatures (solid lines). Intersections of the lines with the curve correspond to simultaneous solutions of Eq. 2.21 and $M = H_{eff}/\lambda$.

at $x = 0$ the slope of the curve is $Nm/3$, using the simplified x given above. When the slope of the linear curve matches this initial Langevin slope the temperature is T_C. Therefore, in the Weiss mean field approach the ordering temperature is given by

$$T_C = \frac{Nm^2\lambda}{3k_B}. \tag{2.23}$$

The resulting mean fields for realistic saturation moments and ordering temperatures are 10^4 kOe. At the time Weiss introduced his theory it was unclear how such large fields could be generated. Later, Heisenberg showed that the mean field does not really exist. Rather the ordering comes from a combination of quantum mechanical and electrostatic exchange interactions between the electrons. A very simple argument can be given to justify the existence of a magnetic ordering from electrostatic effects. As the electrons are fermions, the pairwise wavefunctions must be antisymmetric under exchange of the particle indices. Also, since each electron carries the same charge there is a repulsive force between them. The electrostatic energy is minimized by separating the electrons. An antisymmetric in space wave function is zero at the origin. Such a function tends to maintain a separation between the two electrons. To satisfy the overall antisymmetric nature of the paired wave function, the spin part must be the symmetric triplet state for two spin-1/2 particles. Therefore, electrostatic interactions combined with quantum mechanics allows for energy difference between magnetic states.

In metallic rare earth compounds exhibiting magnetic order the magnetic interaction is often mediated by the conduction electrons via the Ruderman-Kittel-Kasuya-Yoshida (RKKY) mechanism. In this interaction the local ionic moment polarizes the conduction electrons, and this polarization oscillates as a function of distance. In this model the interaction, J, between two local moments sitting at sites $\mathbf{R}_i$ and $\mathbf{R}_j$ is given by

$$J(\mathbf{R}_i - \mathbf{R}_j) \sim F(2k_F|\mathbf{R}_i - \mathbf{R}_j|) \tag{2.24}$$

In the above, k_F is the Fermi wavevector and $F(x)$ is given by

$$F(x) = \frac{x\cos x - \sin x}{x^4} \tag{2.25}$$

which is plotted in Fig. 2.2 .

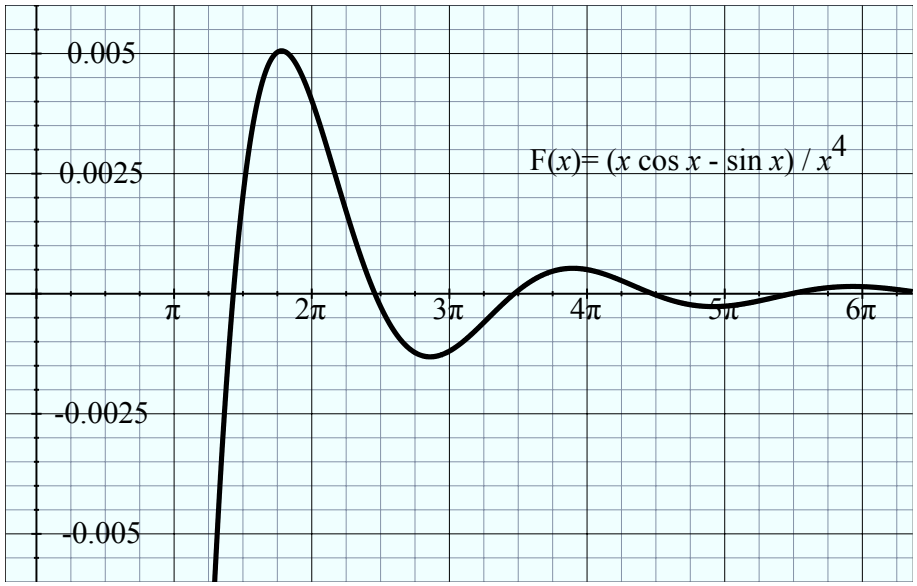

Figure 2.2 Plot of the RKKY function. Positive values correspond to ferromagnetic coupling while negative correspond to antiferromagnetic coupling.

In insulating compounds where there are no conduction electrons to mediate the exchange. One form of J_{ij} coupling is the so-called 'superexchange.' The superexchange is a method whereby two magnetic ions separated by a non-magnetic ion interact. Even though the compound under consideration is an insulator, if the valence electrons can 'hop' from one ion to another they delocalize and lower their kinetic energy. This reduction due to delocalization is reminiscent of the particle in a box where the energy levels vary inversely with the linear dimensions of the box. In general, superexhchange favors antiferromagnetism over ferromagnetism.

In ferromagnetically ordered samples application of a magnetic field of sufficient strength will saturate the moment. This occurs because all of the magnetic spins align with the field and there is no longer an increase in M with increasing H. The sample moment can be divided into moment per spin, that is

$$M = N\mu_s. \tag{2.26}$$

In strict local moment systems the saturated moment per ion will be the same as the effective

paramagnetic moment per ion ($p_{eff}/\mu_s = 1$). Rhodes and Wohlfarth (1963) pointed out that this is not the case for all ferromagnets and used it to categorize magnetic materials. Some magnets are known to have much smaller saturation moments when compared with their paramagnetic moments. These are the candidate itinerant magnets, discussed in Ch. 4.

In the absence of pinning effects, at zero kelvin a small bias field applied along the ordering axis is sufficient to completely saturate a ferromagnetic material as required by the third law of thermodynamics. In this case all of the local moments point in the same direction and the system is in its ground state. In an Ising system, if the temperature is raised slightly, the first change that occurs is one spin will flip so it points antiparallel to all other spins. This is presumed to be the first excited energy state as the flipped spin will result in an increase in exchange energy and it represents the lowest increase available. Each spin in the lattice will have an equal probability of being the one that is flipped, so the location of the flipped spin is expected to wander about the lattice. The most probable mechanism for this traveling spin inversion is from neighbor to neighbor as the exchange force aligns the reversed spin. This propagation is a spin wave and only certain wavelengths are permitted based on the boundary conditions of the crystal. These long wavelength, low energy collective excitations reduce the low temperature magnetic moment more effectively than through considering single particle effects alone. In principle the effects of spin waves may be observable in TDR data, particularly frequency resolved data, but this is not the goal here. The present discussion of spin waves is motivated by a desire to understand collective excitations in itinerant systems as described by the spin fluctuations theory.

Working in a spin-1/2 system with z nearest neighbors, and considering the Hamiltonian to consist of the exchange term only,

$$\mathcal{H} = -J \sum_{i \neq j} \mathbf{S}_i \cdot \mathbf{S}_j \tag{2.27}$$

where $\mathbf{S}$ are the Pauli matrices it is possible to determine the energy spectrum of the spin waves. It is convenient to introduce to raising and lowering operators $S^{\pm}$ defined by

$$S_i^{\pm} = S_{xi} \pm i S_{yi}. \tag{2.28}$$

If $|\xi_\alpha>$ represents the spin up state (with the z axis as the quantization axis) and $|\xi_\beta>$ the spin down it can be shown that

$$S^+|\xi_\beta>=|\xi_\alpha> \tag{2.29}$$

$$S^+|\xi_\alpha>=0 \tag{2.30}$$

$$S^-|\xi_\alpha>=|\xi_\beta> \tag{2.31}$$

$$S^-|\xi_\beta>=0 \tag{2.32}$$

$$S_z|\xi_\alpha>=\frac{1}{2}|\xi_\alpha> \tag{2.33}$$

$$S_z|\xi_\beta>=-\frac{1}{2}|\xi_\beta> \tag{2.34}$$

Therefore, the kets $|\xi_k>$ are not eigenkets of the raising and lowering operators. The Hamiltonian (Eq. 2.27) can be rewritten as

$$\mathcal{H}=-J\sum_{i\neq j}\left[\frac{1}{2}\left(S_i^+S_j^- + S_i^-S_j^+\right)+S_{zi}S_{zj}\right]. \tag{2.35}$$

Based on the assumed ground state, its eigenfunction can be written as

$$|\xi_0>=|\xi_{\alpha 1}\xi_{\alpha 2}\xi_{\alpha 3}\cdots\xi_{\alpha N}> \tag{2.36}$$

Applying the Hamiltonian in Eq. 2.35 to this ground state gives

$$\mathcal{H}|\xi_0>=-J\sum_{i\neq j}\left[\frac{1}{2}\left(S_i^+S_j^- + S_i^-S_j^+\right)+S_{zi}S_{zj}\right]|\xi_0>. \tag{2.37}$$

The effect of the first two terms it to flip a reversed spin. Since there are no reversed spins in the ground state, these terms contribute nothing. Only the third term gives a non-zero result:

$$\mathcal{H}|\xi_0>=-\frac{1}{4}NzJ|\xi_0>. \tag{2.38}$$

Moving to the first excited state, with one reversed spin allows for a determination of the reversal's behavior. If the reversed spin is located at the m-th atom, the first excited state may be written as

$$|\xi_m>=|\xi_{\alpha 1}\xi_{\alpha 2}\cdots\xi_{\alpha(m-1)}\xi_{\beta m}\xi_{\alpha(m+1)}\cdots\xi_{\alpha N}>. \tag{2.39}$$

Operating on $|\xi_m>$ with Eq. 2.35 shows that all terms contribute to the new energy.

$$\mathcal{H}|\xi_m>= -J\sum\left[\frac{1}{2}\left(S_i^+S_j^- + S_i^-S_j^+\right) + S_{zi}S_{zj}\right]|\xi_m> \tag{2.40}$$

The first two terms yield null vectors when operating on all spins except the mth and $(m+1)^{st}$. The last term has a nonzero contribution from the remaining $(N-2)$ spins given by

$$-J\sum S_{zi}S_{zj}|\xi_m>= -\frac{1}{4}Jz(N-2)|\xi_m> \tag{2.41}$$

where the z on the right hand side is the number of nearest neighbors. Taking the remaining spins with the first two terms in Eq. 2.40 gives

$$-J\sum_{i=1}^{z}\frac{1}{2}\left(S_m^+S_{m+1}^- + S_m^-S_{m+1}^+\right)|\xi_m>= -\sum_{i=1}^{z}J|\xi_{m+i}> . \tag{2.42}$$

The sum in the above equation is over the z nearest neighbors. The result is like this because the second term gives a null vector again, but the first term moves the reversed spin by one site. The $S_{zi}S_{zj}$ term contributes an energy of

$$\frac{1}{2}Jz|\xi_m> \tag{2.43}$$

when operating on the mth and $(m+1)^{st}$ spins. The net result is

$$\mathcal{H}|\xi_m>= \left(-\frac{1}{4}JNz + zJ\right)|\xi_m> -\sum_{i=1}^{z}J|\xi_{m+i}> . \tag{2.44}$$

It is obvious that $|\xi_m>$ is not an eigenfunction of $\mathcal{H}$. The effect of the hamiltonian is to move the reversed spin, allowing it to propagate through the lattice. Therefore an eigenfunction of $\mathcal{H}$ may be formed by a linear combination of the N functions represented by $|\xi_m>$, or

$$|\Xi>= \sum c_m|\xi_m> . \tag{2.45}$$

The coefficients c_m are given by

$$c_m = A_m e^{i\mathbf{k}\cdot\mathbf{R}_m} \tag{2.46}$$

where $\mathbf{R}_m$ is the position vector of atom m. Imposing periodic boundary conditions ($c_m = c_{m+N}$) the components of $\mathbf{k}$ are confined to particular values. This is analogous to the classic particle in a box problem with solutions of the sort

$$\frac{k_iN_ix_{mn}}{2\pi} = 0; \pm1; \pm2; \cdots \tag{2.47}$$

N_i is the number of lattice sites along the i direction and x_{mn} is the distance between those sites. The eigenfunctions have wavelike properties and operating on Eq. 2.45 with Eq. 2.35 gives

$$\mathcal{H}|\Xi >= E|Xi >= (E_0 + zJ)\,|\Xi > -J\sum e^{i\mathbf{k}\cdot\mathbf{r}}|\Xi > . \tag{2.48}$$

$\mathbf{r}$ is the vector between the reversed spin and one of its nearest neighbors, and the sum is taken over all nearest neighbors. The energy of the spin wave is

$$E - E_0 = J(z - \sum e^{i\mathbf{k}\cdot\mathbf{r}}). \tag{2.49}$$

For small k (low energy) this gives

$$E - E_0 = \frac{1}{2}J\sum(\mathbf{k}\cdot\mathbf{r})^2 . \tag{2.50}$$

For lattices with cubic symmetry this reduces to

$$E - E_0 = Jk^2a^2 \tag{2.51}$$

where a is the lattice spacing. Associating this with the usual quantum mechanical energy for a wave gives

$$\hbar\omega = Jk^2a^2 \tag{2.52}$$

Since the TDR measures the 'bulk' susceptibility, it is not feasible to try to map out spin-wave dispersion relations. However, if a material exhibits gaps in its spin wave spectra, then it may be possible to detect these gaps with frequency resolved measurements.

The free energy of a system is the difference between the internal energy and the entropic energy.

$$F = U - TS - \mathbf{M}\cdot\mathbf{H} \tag{2.53}$$

Various derivatives of the free energy correspond to different thermodynamic quantities. Entropy is the first derivative of the free energy with respect to temperature, and heat capacity is the second.

Of particular interest for magnetic systems is the magnetic energy $\mathbf{M}\cdot\mathbf{H}$. The negative of the first derivative of F with respect to H gives the magnetization, M.

$$-\frac{\partial F}{\partial H} = M \tag{2.54}$$

Taking the derivative of M with respect to H gives the magnetic susceptibility, χ.

$$\chi = \frac{\partial M}{\partial H} = -\frac{\partial^2 F}{\partial H^2} \tag{2.55}$$

Experimentally it is seen that certain thermodynamic quantities either grow very rapidly in the vicinity of a phase transition or have a step-wise change at T_c. The transition is classified based on which derivative (first, second, third, etc.) of the free energy manifests a discontinuity. The para- to ferromagnetic phase transition is usually second order, so the magnetic susceptibility is one of the diverging quantities. Application of a small field will tend to weakly align the moments in the direction of the field. As the temperature approaches T_C the exchange interaction grows in importance relative to the thermal randomization, and the alignment of a few moments in one direction will induce other moments to align as well. Thus, for a given applied field the response of the magnetization is amplified when compared to the non-interacting case. The mean field theory derivation of the magnetic susceptibility leading to the Curie-Weiss law accurately recreates this divergence. This is a tautology in some sense, as Weiss developed his theory to account for the magnetic order and rapidly growing susceptibility at the transition temperature.

Magnetic susceptibility is usually thought of as the zero field limit of dM/dH. Here the term susceptibilty refers to the local slope of the M–H curve, that is $\frac{dM}{dH}$ at a non–zero field. This suggests measuring χ in an applied magnetic field. Adhering to the ferromagnetic case, applying a magnetic field will suppress the growth of $\chi(T)$ near the phase transition, turning it into a local maximum near T_C. Further, the applied field shifts the maximum to higher temperatures. The static field adds an additional Zeeman energy to the problem which makes it easier for the moments to order resulting in the shift in temperature. Further, the energy splitting between the spins parallel and antiparallel to the field makes it more difficult for a perturbing field to induce a change in magnetization. This is what causes the field suppression of χ.

Landau developed a very simple model to show how a second order phase transition can occur [Landau (1937)]. He assumed there was a phase transition at some temperature, T_c, characterized by an 'order parameter.' The order parameter is some quantity that is zero

for $T > T_c$ and continuously grows from zero to some saturation value as the temperature is lowered below T_c. Associated with the order parameter is a conjugate field. In general terms, the response of an order parameter to changes in its conjugate field is termed the susceptibility. In ferromagnets the order parameter is the magnetization. The field conjugate to magnetization is the magnetic field, H. The response of the magnetization to changes in the applied field is the usual susceptibility, χ. If M_s is taken as the saturation value then the reduced order parameter, m, and the reduced temperature, t, can be defined as

$$m = \frac{M(T)}{M_s} \tag{2.56}$$

and

$$t = \frac{T}{T_c}. \tag{2.57}$$

For $t < 1$ the system is in the low symmetry, ordered phase, while for $t > 1$ it is in the high symmetry, disordered phase. If we are concerned with magnetization, the energy of the system cannot depend on whether m is positive or negative. These only indicate the direction the magnetization points relative to an arbitrary refrerence. Assuming the free energy can be expressed as a polynomial in m, symmetry requires that no odd powers of m appear. The free energy can then be written as

$$F(t, m) = F_0(t) + A(t)m^2 + \frac{1}{2}B(t)m^4. \tag{2.58}$$

The prefactor of 1/2 on the quartic term is placed for later convenience. $F_0(t)$ contains all temperature dependence not associated with the magnetization. In order to determine the equilibrium value of m, the free energy must be minimized with respect to m. Thus, $\partial F/\partial m = 0$ and $\partial^2 F/\partial m^2 > 0$.

$$\frac{\partial F}{\partial m} = 2A(t)m + 2B(t)m^3 = 0 \tag{2.59}$$

$$\frac{\partial^2 F}{\partial m^2} = 2A(t) + 6B(t)m^2 > 0 \tag{2.60}$$

From Eq. 2.59 $m = 0$ and $m^2 = -A(t)/B(t)$ are the two solutions. If $m = 0$, then Eq. 2.60 requires $A(t) > 0$ to assure a minimum. This corresponds to the case when $t > 1$. If $m \neq 0$ then substitution of $-A(t) = B(t)m^2$ into the second derivative shows that $A(t) < 0$ to assure

a minimum in F. This is the case when $t < 1$. Therefore, it is seen that as t is lowered through 1, $A(t)$ changes sign from positive to negative. Any functional form of $A(t)$ that satisfies this one condition will be sufficient to reproduce the phase change. Landau assumed a very simple temperature dependence for A,

$$A(t) = \alpha(t-1). \tag{2.61}$$

With this the magnetization for $T < T_c$ is given by

$$m = \pm\sqrt{\frac{\alpha(1-t)}{B(t)}}. \tag{2.62}$$

The $\pm$ indicates the isotropic nature of space. "Up" magnetization is equivalent to "down" in the absence of an applied field. Landau further assumed that $B(t) = B$ is constant with temperature. Under this assumption, the magnetization grows as $t^{1/2}$ near $t = 1$. This also allows the free energy to be expressed in terms of α and B.

$$F = F_0(t) - \frac{\alpha^2(t-1)^2}{2B} \tag{2.63}$$

From this expression for the free energy the magnetic contribution to the entropy and the heat capacity is easily computed. Landau's theory predicts a jump in heat capacity at $T = T_c$.

Since everything regarding the phase transition up to now has been derived in zero applied field, it is not possible to predict the behavior of the susceptibility as a function of temperature. This can be overcome by adding a small magnetic Zeeman term ($-mh$ where $h = H_{app}M_s$) to Eq. 2.58. The smallness of the Zeeman energy is ensured by keeping h very close to zero. The textbook approach in this case [Pathria (1996)] is to rewrite Eq. 2.58 including h, set the derivative of F with respect to m equal to zero and then solve for h.

$$h = 2A(t)m + 2Bm^3. \tag{2.64}$$

From here the inverse susceptibility $(1/\chi)$ is defined as $\partial h/\partial m$ which gives

$$\chi^{-1} = 2A(t) + 6Bm^2. \tag{2.65}$$

For $t > 1$, $m = 0$ and χ diverges like $1/t$ as $t \to 1^+$ if the form of $A(t)$ found in the zero field case holds. For $t < 1$, $m = \sqrt{\alpha(1-t)/B}$. Substituting this in for χ gives that the susceptibility

diverges as $1/t$ as $t \to 1^-$. The last bits of information gleaned from this procedure come from considering what happens to m if h is varied when $t = 1$. From Eq. 2.64 it is seen that $m \propto h^{1/3}$ in the low field limit. This in turn implies that at $t = 1$, that is at the actual zero field phase transition temperature, the susceptibility should vary with field like $\chi \propto h^{-2/3}$.

The most significant conclusion drawn from the Landau theory is that the physically measurable quantities m and χ vary with power law dependencies on t and h in the vicinity of the phase transition. Based on the temperature dependence of χ it is seen that the Landau theory of phase transitions is a mean field type of calculation. Therefore, any arguments derived from it are subject to the limitations of mean field theory.

The Heisenberg interaction, that models long range magnetic order, is isotropic (Eq. 2.17). However, in many magnetically ordered materials the spontaneous mangetization prefers to lie along particular crystallographic directions. This phenomenon is termed magnetocrystalline anisotropy (MCA). The most common manifestation of MCA is in the applied field required to saturate the measured magnetic moment of a sample. The direction that requires the smallest field for saturation is termed the "easy" axis. Other directions are called "hard" axes. The microscopic origins of MCA may be crystalline electric field effects, anisotropic coupling, or anisotropic moments.

Models of MCA are based around the idea that when the magnetization lies along the easy axis, the free energy of the system is minimized (if domain effects are neglected). The moment must be forced away from the easy axis which increases the energy in the sample. The connection between the energy increase and the displaced angle is made via anisotropy constants. Determining these constants can be accomplished in several ways. Commonly one measures the work required to saturate the magnetic moment of a sample along different directions. Then it is possible to extract the relative values of the constants. Another method exploits the fact that a moment placed in a perpendicular magnetic field will precess about the field with a characteristic frequency. If an alternating field with this frequency is applied perpendicular to the static field, there will be a coherent absorption of energy which manifests itself (among other ways) as a dramatic increase in the susceptibility of the sample. Such

transverse measurements have been shown to be useful in determining the anisotropy constants for thin films [Spinu et al. (2000)]. A third method is to fix H and measure M as a function of angle, rotating about symmetry axes in the sample. Then, fitting the data to an appropriate model will give the anisotropy constants.

Experimentally it is observed that the magnitude of anisotropy constants strongly depend on temperature [Morrish (2001)]. A major shortcoming of the typical techniques employed to measure the anisotropy constants is that a fairly large static field must be applied. Such a field can, and does, introduce considerable energy, especially at low temperatures and in samples with a large moment per ion. A 10 kOe field applied to a single Bohr magneton moment induces a Zeeman splitting on the order of 1 K. Especially along the hard directions, this field may not be sufficient to saturate the moments. Indeed, it is not uncommon that a 55 kOe field is insufficient to perform a saturation measurement at 2 K.

To develop a feel for the MCA, three itinerant ferromagnetic systems are considered, iron, nickel, and cobalt. Iron and nickel both possess cubic symmetry. The easy direction for iron is along the cube edge and for nickel it is the body diagonal. Cobalt is hexagonal and manifests uniaxial anisotropy with the c axis being the easy direction and anywhere in the hexagonal planes being (nearly) equivalent hard directions [Morrish (2001)]. These cases are studied because they illustrate the principle, but due to the high degree of symmetry many terms may be neglected. Deviations from the easy axis will increase the energy. It is convenient to express the anisotropy energy as a power series of trigonometric functions of the angles the magnetization direction makes with the crystal axes.

Beginning with the cubic systems, the direction cosines from the cube axes may be denoted as α_1, α_2, and α_3. The expression for the anisotropy energy must be independent of the sign of the α's. Hence, only even powers will appear. Cross terms of the type $\alpha_1\alpha_2$ are also not permitted. The first candidate is the term $k_1\alpha_1^2 + k_2\alpha_2^2 + k_3\alpha_3^2$. However, this term will not give any anisotropy energy as the expression must be independent of an interchange of any two α's which is a manifestation of the freedom in choosing two of the three directions in a right-handed coordinate system. Therefore, $k_1 = k_2 = k_3$. Since $\alpha_1^2 + \alpha_2^2 + \alpha_3^2 = 1$ there will be no

contribution to the anisotropy from this term. This means the lowest order term is the fourth degree term. Again, there is a simplification. Only the term containing $\alpha_1^2\alpha_2^2 + \alpha_1^2\alpha_3^2 + \alpha_2^2\alpha_3^2$ needs to be considered because it is equal to $\frac{1}{2} - \frac{1}{2}\left(\alpha_1^4 + \alpha_2^4 + \alpha_3^4\right)$. The next term will be of degree 6. Generally this is sufficient to explain the experimental results. Thus, the anisotropy energy for a cubic system may be written as

$$U_{aniso}^{cubic} = K_1\left(\alpha_1^2\alpha_2^2 + \alpha_1^2\alpha_3^2 + \alpha_2^2\alpha_3^2\right) + K_2\alpha_1^2\alpha_2^2\alpha_3^2. \tag{2.66}$$

Three typical cases are considered. First, if the magnetization lies along a cube edge, then two of the three α's are zero and the total energy is zero regardless of K_1 and K_2. Second, if the magnetization lies along a body diagonal, $\alpha_1 = \alpha_2 = \alpha_3 = \frac{\sqrt{2}}{2}$. The anisotropy energy in this case is given by

$$U_{aniso} = \frac{3K_1}{4} + \frac{K_2}{8}. \tag{2.67}$$

If K_1 is negative and $K_2 < -\frac{3K_1}{2}$ then the body diagonal will be the easy axis. Finally, if the magnetization lies along a face diagonal, then one of the α's is zero and the anisotropy energy is $\frac{K_1}{4}$. If $K_1 < 0$ and $K_2 > -\frac{3K_1}{2}$ then the face diagonal will be the easy axis. From the latter two cases, it may be seen that if $K_1 > 0$ then the cube edges will be easy directions.

For uniaxial symmetry, only one angle is needed. Specifically, if θ is defined as the angle between the magnetization and the easy axis then the anisotropy energy may be written as

$$U_{aniso}^{uni} = K_1' \sin^2\theta + K_2' \sin^4\theta. \tag{2.68}$$

Taking the uniaxial case, if a magnetic field is applied at an angle ϕ (Fig. 2.3) with respect to the easy axis, the magnetization will be deflected to that direction. Neglecting the fourth order term (small H) the total energy of the system is expressed as

$$U_{total} = K_1 \sin^2\theta - MH\cos\left(\phi - \theta\right). \tag{2.69}$$

The equilibrium condition is met when U_{total} is minimized, i. e. $dU/d\theta = 0$.

In general, this anisotropy should manifest itself in the measurement of magnetic susceptibility. Measurements of χ_{TDR} with the excitation field parallel to the ordering axis give a much stronger signal when compared to measuremenst perpendicular to the easy direction. This is discussed in more detail below.

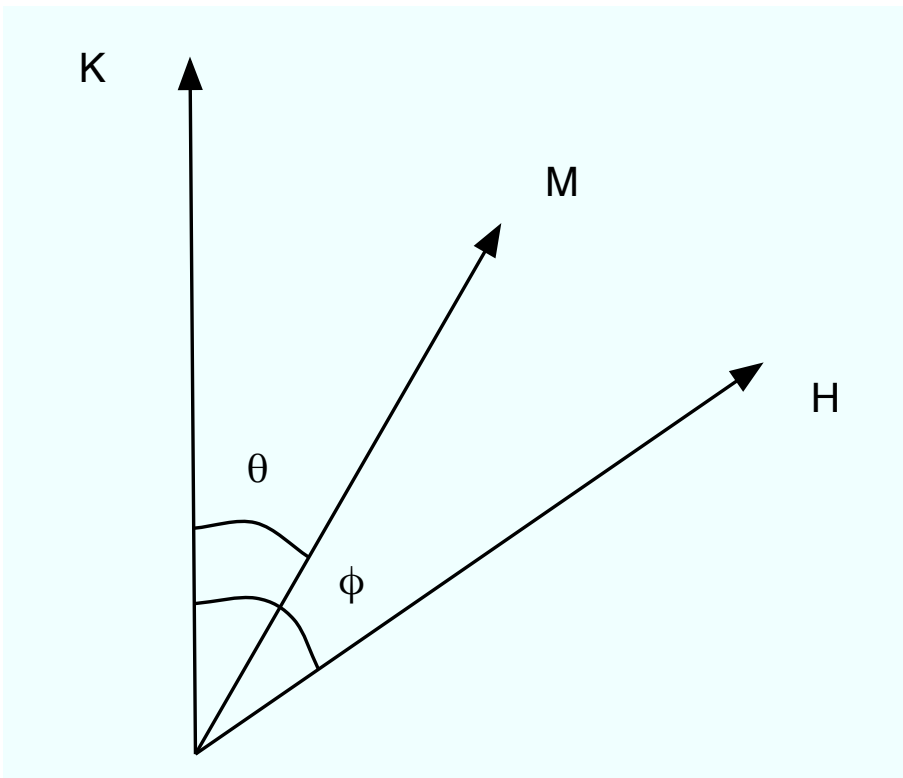

Figure 2.3 Geometry of uniaxial anisotropy energy expressed in Eq. 2.69.

2.3 Materials Studied and Results

Experimentally the TDR data on local moment ferromagnets in the vicinity of the phase transition show a narrow, well defined, peak in χ_{TDR}. Application of a static magnetic field suppresses this peak and shifts it to higher temperatures. In systems with significant magnetic anisotropy, the orientation of the crystal with respect to the rf probe field affects the behavior of the observed peak at and above T_C (Sec. 2.5). It is useful to compare these data with data collected from conventional measurements such as low field, static magnetization; low frequency ac susceptibility; resistivity; and heat capacity. To this end, single crystals of the ferromagnetic $CeVSb_3$ [Sefat et al. (2008)] with a Curie temperature of 4.6 K were studied using these more common techniques.

Figure 2.4 presents the heat capacity measured on a *Quantum Design* Physical Properties Measurement System (PPMS) and magnetic susceptibility as measured by the ^{4}He TDR (χ_{TDR}) in zero applied magnetic field for a single crystal of $CeVSb_3$ (Sec. 2.3.2). There is a clear lambda like anomaly in heat capacity at approximately 4.6 K. This coincides with a dramatic peak in χ_{TDR}. The coincident temperatures strongly suggest that the peak in χ_{TDR} is associated with the phase transition. The gradual decrease in measured susceptibility for temperatures less than 4.3 K or so is associated with a decrease in resistivity. The peak in χ_{TDR} should be contrasted with the response of antiferromagnetic $SmAgSb_2$ (Fig. 1.5). For the antiferromagnet there is no corresponding increase in χ_{TDR} at the Néel temperature. Rather there is just a decrease in resistivity due to a loss of spin disorder scattering as the samarium moments order. Figure 2.5 compares low frequency ac susceptibility available from a commercial ac susceptometer (*Quantum Design* Magnetic Properties Measurement System, or MPMS) with the same resonator data from Fig. 2.4. Both data sets are normalized to the maximum in measured χ for the respective technique. For both systems, this maximum corresponds to the same temperature to within 50 mK. The drive frequency from the commercial system was set at 333 Hz and the peak to peak amplitude of the probe field was 1 Oe. On the paramagnetic side, the normalized data from both systems follows the same temperature behavior. However on the ferromagnetic side the low frequency data drops off much slower than

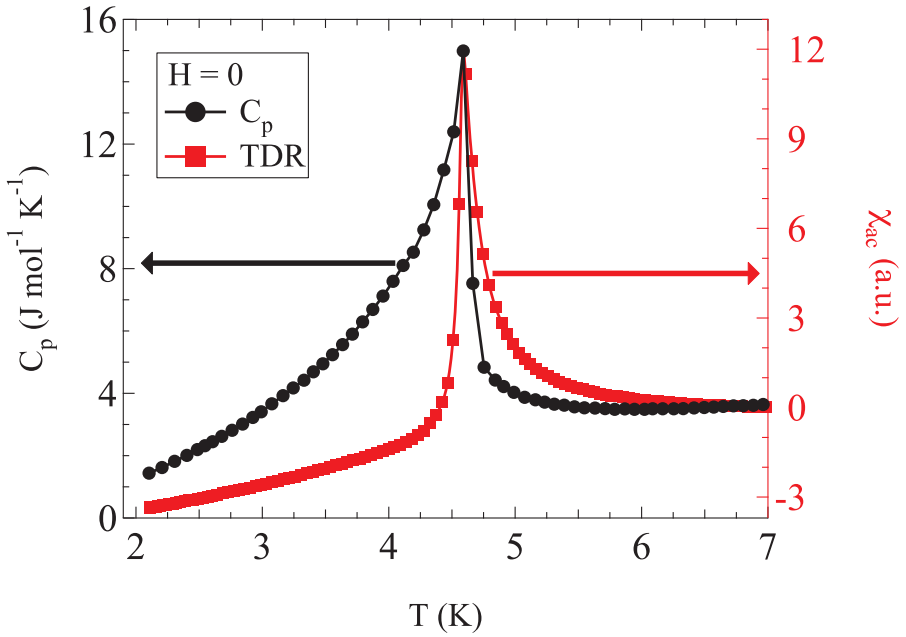

Figure 2.4 Comparison of heat capacity (left axis, black circles) and TDR magnetic susceptibility (right axis, red squares) for $CeVSb_3$ measured along the magnetic easy axis. Peaks occur in both data sets at the ordering temperature.

that from the resonator. This is due to a combination of the frequencies and the amplitudes of the probe fields. The TDR data are collected using a probe field $\leq$10 mOe which is at least 100 times smaller than the commercial system's. It is expected that correlation effects should dominate the response of the sample since the TDR provides such a weak perturbation. Also the much higher frequency from the TDR ($\sim 10^5$ times larger) cuts off the magnetic response of slower relaxation processes. This naïvely can be thought of as analogous to a simple harmonic oscillator. If the oscillator is driven far above its resonant frequency, then the response is very limited in amplitude. The oscillator is very 'stiff' at the high frequencies. Figure 2.6 shows

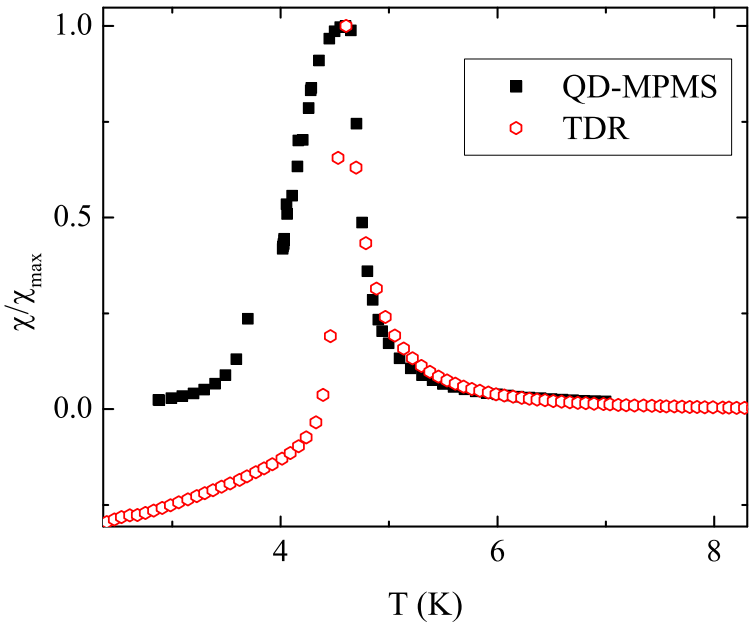

Figure 2.5 Comparison of low frequency ac susceptibility (solid square) and TDR data (hollow hexagons) for $CeVSb_3$ with the probe field aligned with the magnetic easy axis. Both curves are normalized to 1 at the maximum.

the zero field cooled-field warmed static susceptibility, as defined as magnetic moment divided by applied field, versus temperature in a 25 Oe field for $CeVSb_3$. The field is applied along the

magnetic easy axis. As this is a zero field cooled measurement, there are magnetic domains present. On warming in the applied field, thermal energy assists in domain wall motion allowing the moment parallel to the field to grow. At T_C thermal energy dominates the exchange interaction leading to order and the moment drops. The paramagnetic static susceptibility is qualitatively similar to both the low frequency ac susceptibility and the TDR data. Again, it is in the ferromagnetic state that these data differ dramatically.

Also shown in Fig. 2.6 are resistivity with the current parallel ($J||c$) and perpendicular to ($J||b$) the magnetic easy axis in zero field. Of particular importance is the lack of a peak in the resistivity at T_C. Comparison with the TDR data shows that below T_C the rf susceptibility is dominated by the resistivity, while above T_C there is a mixing of the spin susceptibility and the resistivity components. In the case where the TDR probe field is aligned with the crystallographic c axis, the resistivity in the ab-plane is simultaneously probed. The slightly convex nature of the b axis ρ for $T > T_C$ is masked in the TDR data by the increasing spin susceptibility as $T \rightarrow T_C^+$.

Several experimental facts are clear from these measurements on $CeVSb_3$. First, the TDR probes a combination of spin and resistive contributions to susceptibility as demonstrated by the decrease in χ_{TDR} below T_C in accordance with resistivity. Second, in the vicinity of a ferromagnetic phase transition the spin susceptibility dominates the change in measured χ_{TDR} as demonstrated by the sharp peak at T_C. Third, the peak in χ_{TDR} is associated with the magnetic ordering as evidenced by the matching ofT_C determined from the TDR, heat capacity, resistivity, and static and ac susceptibility data. Finally, the peak from the TDR data is much sharper than the low frequency commercial measurement of susceptibility. Applying a dc magnetic field suppresses χ_{TDR} in amplitude and shifts it to higher temperatures, as seen in Fig. 2.7.

2.3.1 Multiple Magnetic Phases in CeSb

As an example of the utility and sensitivity of the TDR the $H-T$ phase diagram of CeSb was determined solely from measurements of χ_{TDR} using the ^{3}He TDR. CeSb has been well studied

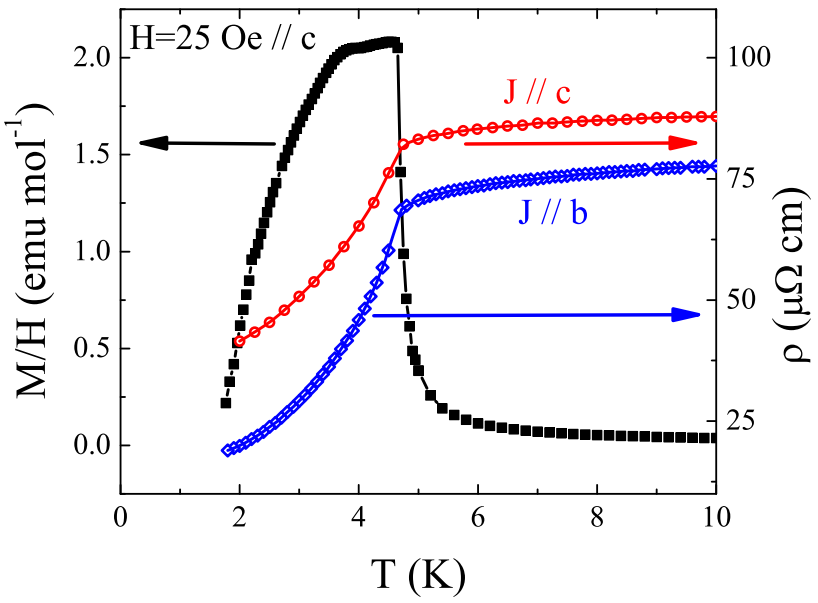

Figure 2.6 Zero field cooled static susceptibility (left axis) and resistivity for current applied along the c and b crystal axes (right axis) for $CeVSb_3$.

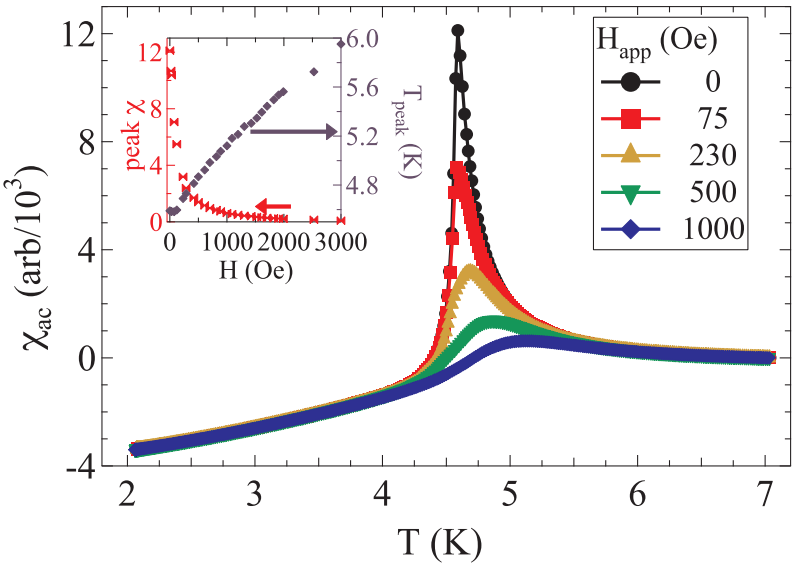

Figure 2.7 χ_{TDR} for $CeVSb_3$ measured along the magnetic easy axis (crystallographic c-axis) in different static bias fields. The general behavior of a sharp zero field peak at T_C that suppresses in amplitude and shifts to higher temperatures is common to all measured local moment systems. The contribution from resistivity is evident. *Inset:* Peak amplitude (left axis) and temperature of peak (right axis) versus applied field.

and is known to manifest a complex magnetic phase diagram. It forms a layered structure with magnetic ordering occurring in some of the layers while others remain paramagnetic as determined via heat capacity [Roussat-Mignod et al. (1980)] and neutron diffraction [Lebech et al. (1980)].

Figure 2.8 shows a temperature scan for the compound CeSb in zero applied field. This compound is well known to have multiple magnetically ordered phases in field-temperature space [Wiener and Canfield (2000)]. The TDR reproduces the phase diagram presented therein (see Fig. 2.9) as well as those reported previously [Bartholin et al. (1975), Meier et al. (1978), Roussat-Mignod et al. (1980), Escorne et al. (1981)]. Each transition into a new phase results in a kink in the measured susceptibility. This kink may originate in either the resistive or spin contributions to susceptibility. Either way, the transition would be observed.

The phase diagram developed by the TDR was generated by measuring χ_{TDR} parallel to the [100] axis of the sample. This means the resistivity in the <100> plane was probed. Further, only temperature sweeps were performed in constant magnetic field. These facts taken in tandem can account for the missed lines in the TDR data, however it does not account for the observed lines not seen in other data. The general nature of this difference was not explored, rather the measurement was performed as a check on the capabilities of the TDR. The strong similarities between the published and measured phase diagram clearly demonstrate that this apparatus can be used to study and resolve complex cascades of transitions.

2.3.2 CeVSb$_3$

CeVSb$_3$ is the only member of the RVSb$_3$ family to manifest ferromagnetic order [Sefat et al. (2008)]. The Curie temperature for this compound is 4.6 K (Fig. 2.4), and it has a saturated moment of 1.4 μ_B per cerium. It crystallizes in an orthorhombic structure with lattice parameters $a \approx 13.17\mathring{A}$, $b \approx 6.24\mathring{A}$, and $c \approx 6.02\mathring{A}$. The magnetic easy axis is the crystallographic c axis. Room temperature resistivity is on the order of 125 $\mu\Omega$ cm and decreases to less than 50 $\mu\Omega$ cm at 2 K. Assuming a temperature independent magnetic permability $\mu = 1$ and a measurement frequency of 10 MHz the corresponding skin depth for $\rho = 50$ $\mu\Omega$ cm is

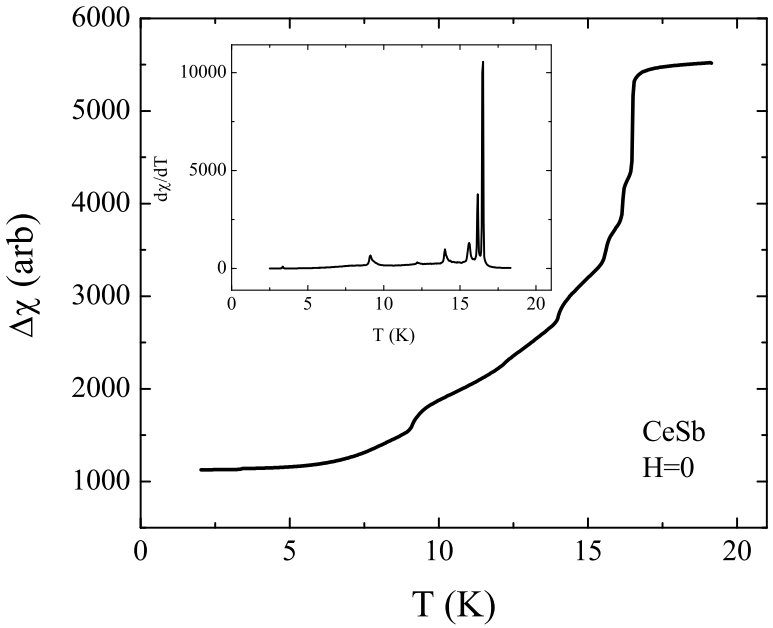

Figure 2.8 Plot of difference between TDR resonant frequency, f_{res}, and a fixed local oscillator, f_{LO} *versus* temperature in zero applied magnetic field. This difference is proportional to χ_{TDR}. Inset shows the derivative of the main plot. The small peak near 3 K in the derivative plot is from the superconducting transition of a small amount of tin flux left from the crystal growth.

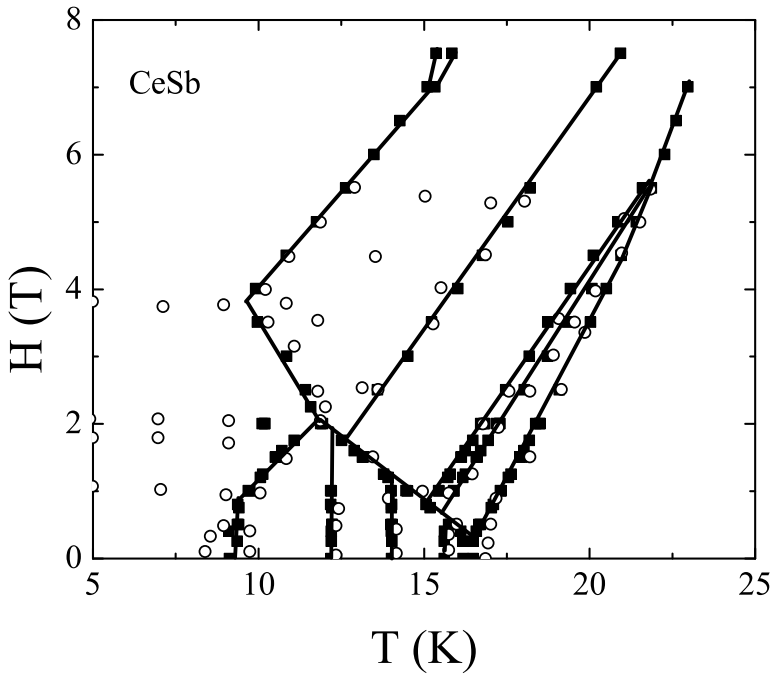

Figure 2.9 Phase diagram for single crystal CeSb. Hollow points are from Wiener and Canfield (2000) while solid points are TDR data.

approximately 200 μm calculated from Eq. 1.1. Therefore, unless the sample is reasonably large ($\geq$ 0.4 mm on a side), or the measurement frequency is increased, the measured χ_{TDR} should have at most a weak resistivity component. Data collected on two samples (one in the ^{3}He TDR and one in the ^{4}He TDR) do indeed show that for small samples this is true. The smaller, ^{3}He, sample had dimensions of 400×100 μm^2 perpendicular to the ac excitation field whereas the larger, ^{4}He sample had dimensions 1000×1000 μm^2 perpendicular to the ac excitation field. The larger ^{4}He sample used to study anisotropy gives a much larger low temperature suppression from the resistive component compared to the smaller ^{3}He sample as shown in Fig. 2.10. The smaller ^{3}He sample does show a slight resistive tail for $T < T_C$, but it is much reduced compared to the ^{4}He system.

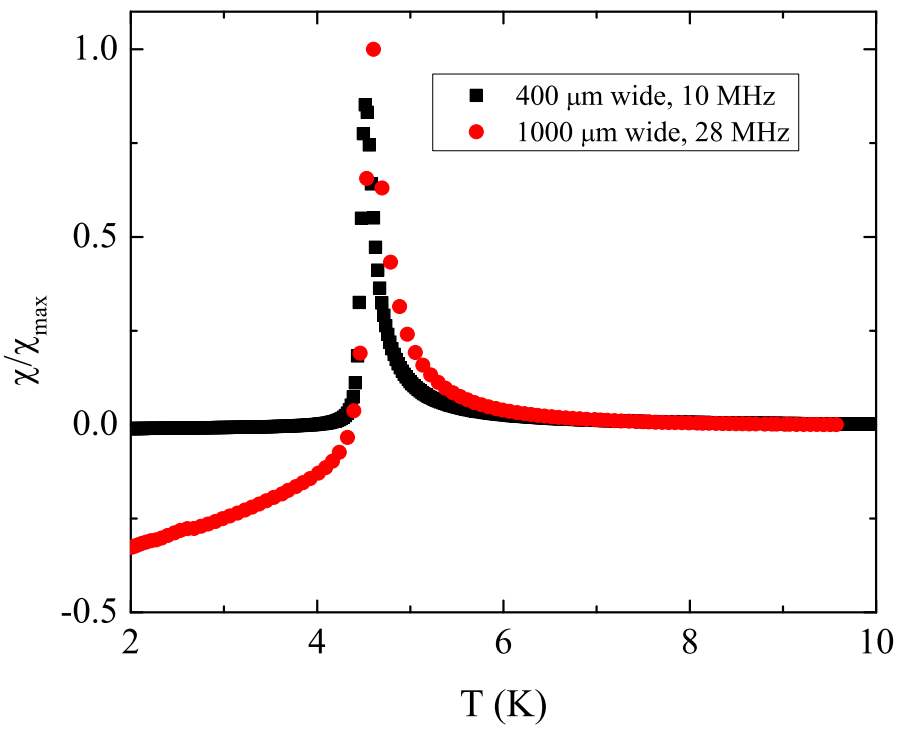

Figure 2.10 Comparison of χ_{TDR} for two $CeVSb_3$ crystals of different sizes. The smaller sample was measured in the ^{3}He system and the larger sample was measured in the ^{4}He system.

2.3.3 $CeAgSb_2$

$CeAgSb_2$ is a member of the tetragonal RAgSb$_2$ family. Published values of the lattice parameters obtained from the gadolinium member show that $a \approx 4.29\AA$ and $c \approx 10.49\AA$. It is know to order ferromagnetically along the c axis at 9.8 K with a saturated moment of 0.37 μ_B per cerium, which is greatly reduced from the paramagnetic effective moment of 2.26 μ_B per cerium [Myers et al. (1999b)]. The large ratio between p_{eff} and μ_{sat} would put this on the possible list of itinerant moments when compared with the Rhodes-Wohlfarth plot. However, in Myers et al. (1999b) it is shown that strong crystalline electric field effects constrain the moments of the other magnetic RAgSb$_2$ to the basal plane. Anisotropic magnetization data vs. applied field in the cerium compound suggests that there may be antiferromagnetic ordering in the plane with a cant of the moment out giving rise to the small observed c-axis saturation value.

In Fig. 2.11 the 28 MHz susceptibility is shown for $CeAgSb_2$ as measured in the ^{3}He. The low resistivity in the ordered state is evident from the decrease in χ_{TDR} as T drops. Absolute values of the zero field χ_{TDR} were determined via the method outlined in Sec. 1.5 at 28 MHz. Results presented in Fig. 2.11 show that the sample is still in the skin depth regime for $T > T_C$.

Fig. 2.12 is a detail of how the peak in χ_{TDR} suppresses with applied field. The full amplitude change in χ_{TDR} is less than 2×10^{-3} in cgs units for zero field. For the lower fields, the χ_{TDR} vs. T curves merge at a temperature just under 9.6 K. However, the 1 kOe curve shows an observably lower χ_{TDR} from 10 K and down. There are two possibilities as to what is causing the reduction in the observed susceptibility. The first is that the applied field is suppressing the spin fluctuations associated with the phase transition. While this is clearly the case, since the peak in χ_{TDR} marking T_C is caused by these fluctuations, this suppression is achieved by a field somewhat larger than 200 Oe. The second possibility is that there are ordered state magnetic fluctuations which are suppressed. This possibility was considered by Jobiliong et al. (2005). If this is the case, then the observed decrease in χ_{TDR} should be evident in ρ as well, as the effect of the fluctuations was to provide an additional scattering mechanism to allow for a unique resistivity curve. By applying the static bias field, the fluctations are

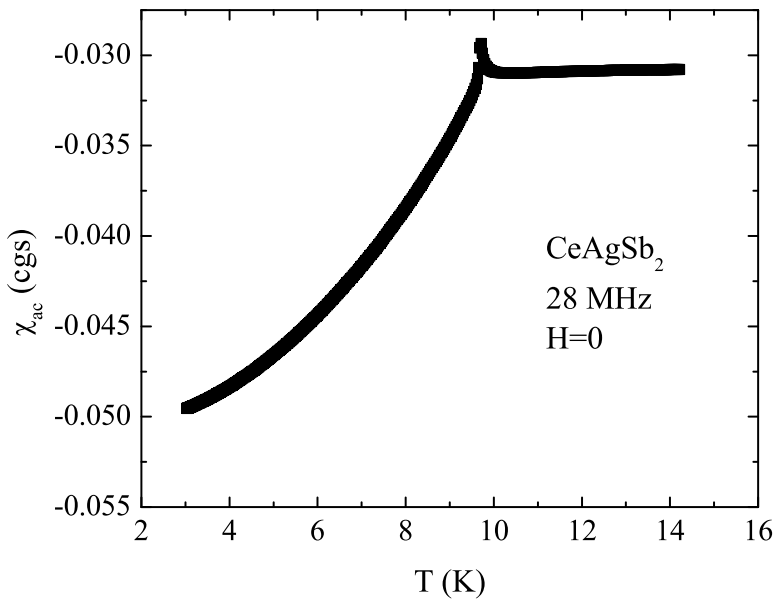

Figure 2.11 Zero field χ_{TDR} for $CeAgSb_2$ showing the magnetic transition at approximately 9.8 K and the decrease in resistivity due to loss of spin disorder scattering.

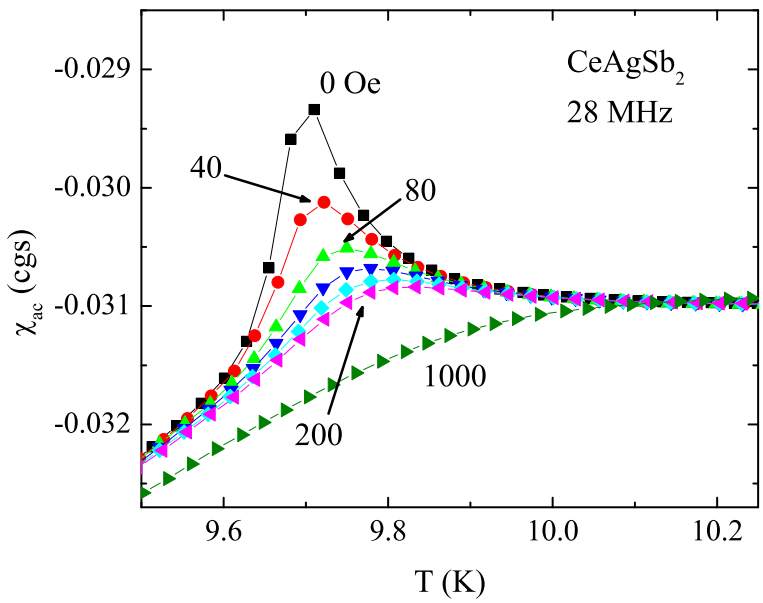

Figure 2.12 χ_{TDR} near T_C in the labeled applied fields (in Oe) for $CeAgSb_2$. Note the extreme narrowness of the peak.

suppressed and so is this scattering mechanism. Therefore, the observed χ_{TDR} data in higher fields should be reduced according to the reduction in ρ, as is seen.

2.3.4 $YTiO_3$

$YTiO_3$ is an insulating perovskite oxide that orders ferromagnetically at approximately 23.5 K. Each titanium ion carries a small moment of 0.85 μ_B [Garrett et al. (1981)]. The crystallographic c axis is the magnetic easy axis.

As an insulating magnetically ordered compound, it is expected that the measured susceptibility be positive through the transition. As has been presented previously, this is not the case for metallic ferromagnets wherein the resistive screening forces the measured χ_{TDR} to be negative even though the system is transitioning to the ordered state. Fig. 2.13 shows the measured susceptibility in absolute units obtained from the TDR. As expected, the observed χ_{TDR} is positive.

The difference in χ_{TDR} above and below T_C is curious and not well understood.

2.3.5 GdPtIn

This is an hexagonal metal with a magnetic ordering temperature of 68 K. It carries a moment of 7.55 μ_B per Gd and the magnetic easy axis is parallel to the c-axis [Morosan et al. (2005)].

The measured susceptibility at 14 MHz for GdPtIn is presented in Fig. 2.14. The metallic nature of the material is evident from the background decrease in χ_{TDR} as temperature decreases. The measured T_C is approximately 67.5 K which is consistent with the published value. Full suppression of the peak was not achieved as an applied field of 3 kOe resulted in the sample being pulled out of the frozen grease. The general behavior is still evident and consistent with the observed local moment behavior.

A second measurement at 28 MHz was made with the ^{4}He systems allowing for a pullout, and empty coil resonance to be determined. This permitted a determination of the absolute value of χ_{TDR}. Results of that measurement are presented in Fig.2.15. It is noteworthy that

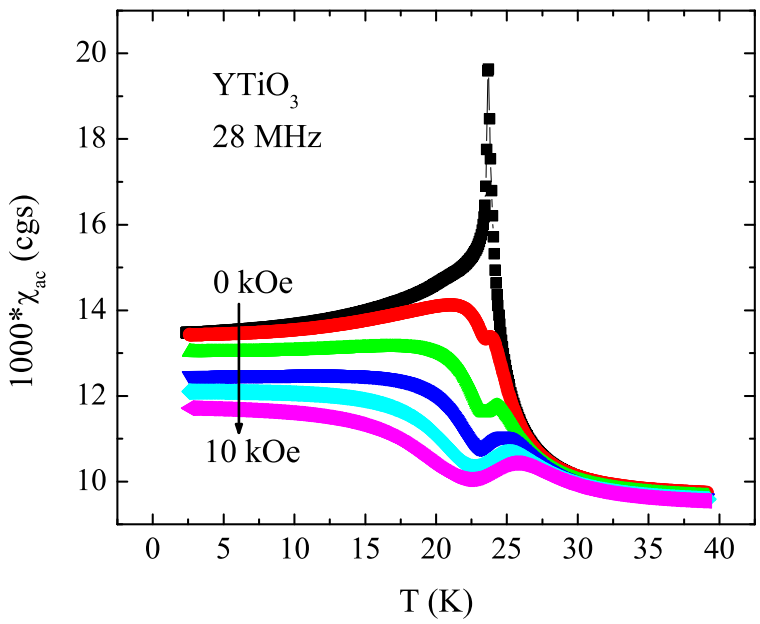

Figure 2.13 χ_{TDR} in cgs units for $YTiO_3$.

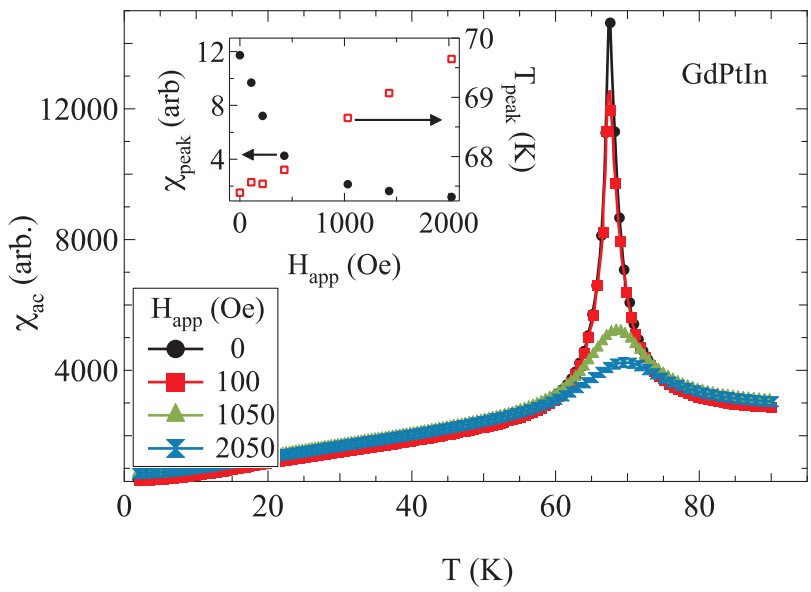

Figure 2.14 Susceptibility vs. temperature for GdPtIn in different applied fields. *Inset:* Peak suppression (left axis, filled circles) and temperature shift (right axis, hollow squares) as a function of field.

even at T_C the measured susceptibility is negative, and the sample is still skin depth limited. This suggests the divergence of χ_{TDR} at the ordering temperature may be suppressed by the finite frequency.

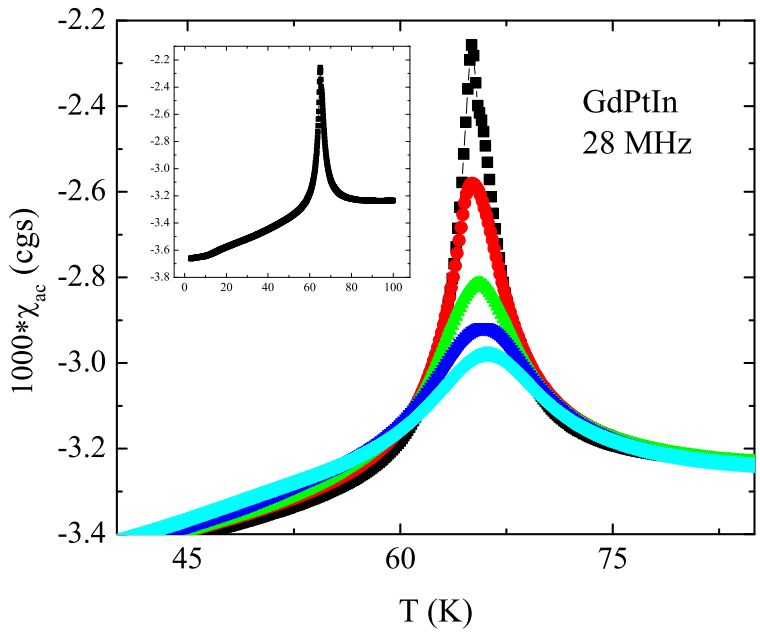

Figure 2.15 28 MHz susceptibility for GdPtIn near T_C in fields from 0-400 Oe in 100 Oe steps. Higher fields have lower amplitude maxima. *Inset:* Zero field susceptibility over entire measured temperature range.

2.3.6 Ce_3Al_{11}

Ce_3Al_{11} is a very good metal with ferromagnetic order setting in at 6.2 K. Upon further cooling, there is a transition to an incommensurate magnetic structure at 3.2 K [Boucherle et al. (1995)]. There are two distinct cerium sites in the lattice. One carries a moment of 1.27 μ_B while the other is 0.24 μ_B.

Both transitions are readily evident in the TDR data (Fig. 2.16). The para- to ferromag-

netic transition is consistent with the other local moment systems studied (Fig. 2.17). The ferromagnetic to incommensurate transition shows a strong mean field behavior in zero field, with a sharp step in χ_{TDR} (Fig. 2.18).

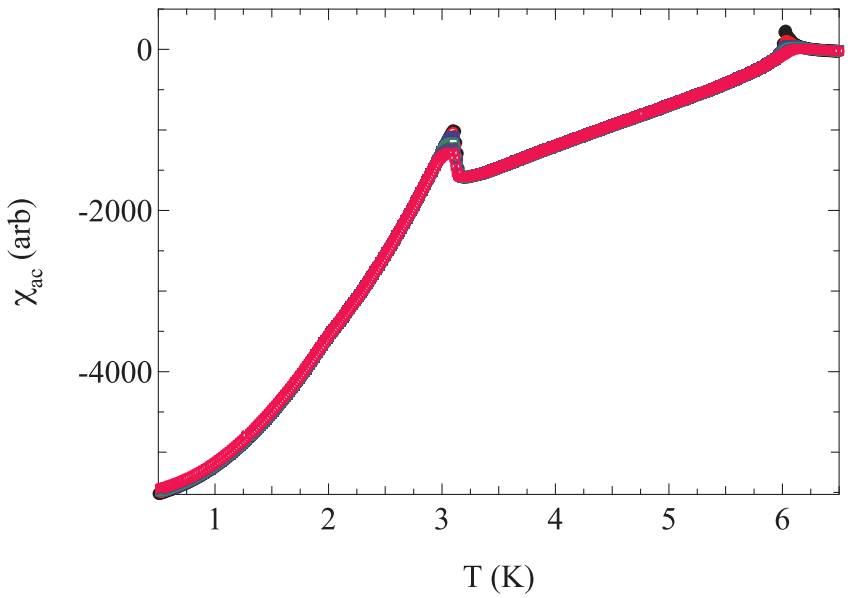

Figure 2.16 χ_{TDR} vs. temperature for Ce_3Al_{11} in applied fields from 0 to 500 Oe.

To further explore these transitions, heat capacity measurements were taken vs. temperature in six static fields on a larger sample. The static field was aligned with the magnetic easy axis when the sample was in the ferromagnetic state. Figure 2.19 displays the results of these measurements. The applied field was varied from 0-1 kOe in steps of 0.2 kOe. At first the low temperature feature looks very different from what is seen in susceptibility. There is a step-like change in c_P at the transition, but a second transition not seen in the rf susceptibility data is evident. At first this is somewhat confusing. However, these crystals were grown out a tin flux. The smaller sample used in the TDR measurements likely had no residual tin on its surface, thereby limiting the detection of the superconducting transition. Further, if there are tin inclusions in the sample then due to the excellent screening capabilities of Ce_3Al_{11}'s low resistivity, these inclusions would not be probed. Heat capacity does not suffer from this

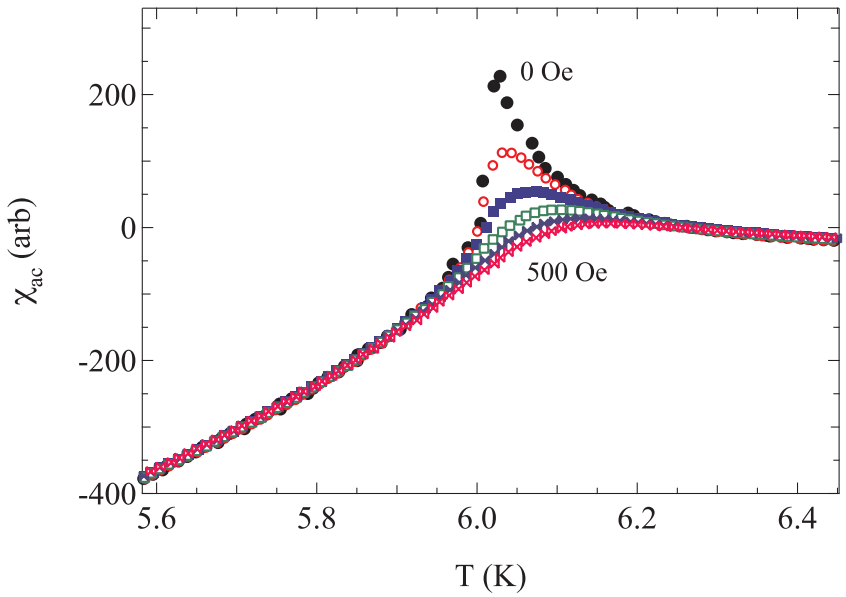

Figure 2.17 Detail of the para- to ferromagnetic phase transition in Ce_3Al_{11}.

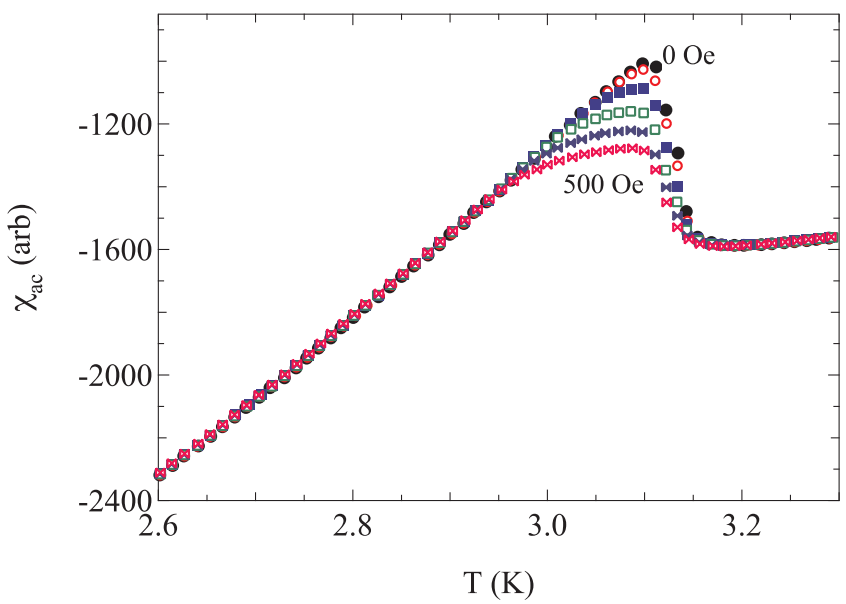

Figure 2.18 Detail of the ferromagnetic to incommensurate structure in Ce_3Al_{11}.

screening effect, and would detect included tin rather easily. If the second low temperature peak is ascribed to tin, then it is seen that the heat capacity suggests a mean field second order transition.

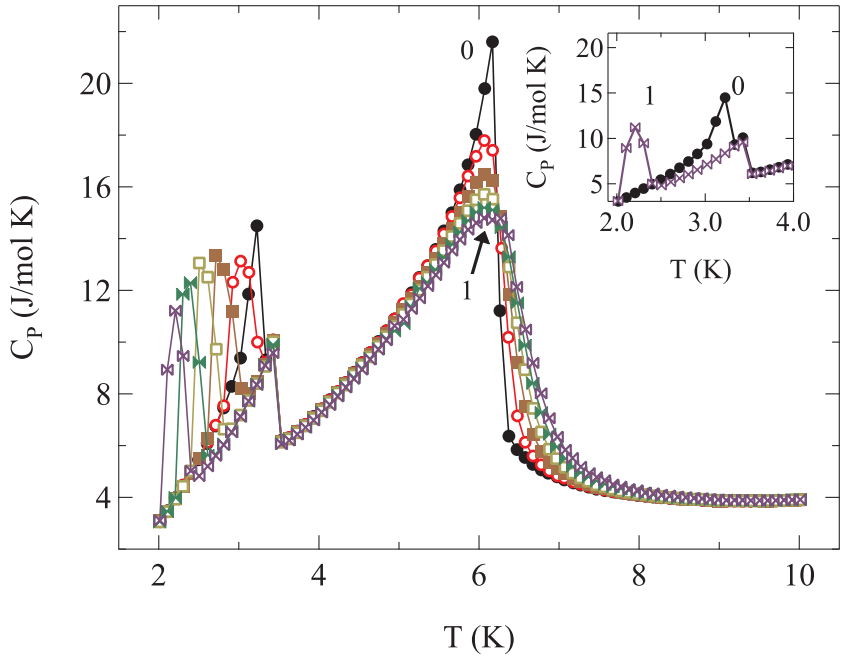

Figure 2.19 Heat capacity for Ce_3Al_{11} in six applied magnetic fields. Numbers indicate the extremes of applied magnetic field in kOe as described in the text. *Inset:* Detail of the low temperature transition for 0 and 1 kOe.

2.4 Evolution of $\chi_{TDR}(T)$ curves in applied field

Some common features have been seen in all local moment systems. First, there exists a well defined narrow peak at T_C in zero applied field. This peak is suppressed in amplitude and shifted to higher temperatures as the applied field is increased. This peak is clearly associated with the phase transition. An argument against a domain response is the observed fact of a rapid increase in χ for $T \rightarrow T_C^+$. In this temperature region, there are no domains because there is no long-range order.

This peak can be understood qualitatively by simple ferromagnetic exchange arguments. In zero applied static field, the individual moments respond to the rf excitation field and a bulk moment is induced. The total moment of the sample is the thermal average of the atomic moments in the sample. As the temperature is lowered close to the Curie point, the exchange energy becomes competitive with thermal fluctuation energy, $k_B T$. Therefore, the individual moments begin to respond in clusters, the linear dimension of which is on the order of the correlation length. For a given applied field there is a proportionately larger positive magnetic response of the sample and a larger measured χ. Upon crossing T_C the exchange interaction dominates the response of the sample. The small rf field is unable to induce a change in the sample moment because such a response requires the rotation of spins away from mutual parallel alignment. In effect, the atomic moments are 'frozen' in place with respect to the tank coil's ac field. This explains the rapid decrease in χ for temperatures just below T_C.

Application of a static bias field introduces a Zeeman splitting on the moments, giving a preferred orientation parallel to the applied field. When the static field direction coincides with the eventual ordering direction, it is easier for exchange interactions to overcome thermal randomization. So, the crossover that the maximum in χ marks can occur at a higher temperature. A second effect of this Zeeman splitting is to reduce the change in the sample moment induced by the rf field. This results in a reduced amplitude in χ as temperature is lowered.

If the effect of the static bias field is assumed to simply add an ordering energy term to the exchange, then it would be expected that the shift in the temperature of the maximum would be linear in field. Returning to the mean field model, one obtains

$$M(T,H) = M_0 \frac{\mu(H_{exch} + H_{app})}{k_B T}. \tag{2.70}$$

From Eqs. 2.19 and 2.20, however, it is unclear how the applied magnetic field will quantitatively effect the magnetic susceptibility. Recourse to the Brillouin expression for magnetization (Eq. 2.8), allows the leading correction to the susceptibility to be determined. However, an *ad hoc* introduction of the ordering temperature is needed. In one sense, such an artificial introduction of a parameter seems unjustified. Still, it could be argued that Landau developed his theory with just such an assumption, i. e. it is an experimental fact that there is an ordering

temperature. Boldly charging ahead, the magnetization for the spin-1/2 case is

$$M(t,h) = M_0 \tanh \frac{\mu_B h}{k_B t} \tag{2.71}$$

where $h = H_{app} + H_{int}$ is the sum of the applied field and the internal field from the moments, $t = T - T_C$, and $M_0 = -N g_J \mu_B J/V$the susceptibility can be determined by differentiation. This gives

$$\chi(t,h) = \frac{\mu M_0}{k_B t}\left(1 - \tanh^2 \frac{\mu_B h}{k_B t}\right). \tag{2.72}$$

Generally one would expand the hyperbolic tangent for small arguments. The validity of such an expansion must be justified since near the ordering temperature $t \approx 0$. In the zero applied field case, this can be dealt with by noting that above T_C the magnetization is zero (in the mean field theory). Application of a bias field forces the numerator to be finite. Concurrently the temperature of the maximum shifts higher so that t is finite as well. Therefore it seems reasonable that the argument in the hyperbolic tangent will stay small. The expansion of χ leads to

$$\chi(t,h) \approx \frac{\mu M_0}{k_B} \frac{t^3}{t^4 + (\mu_B h t/k_B)^2 + (\mu_B h/\sqrt{2} k_B)^4} \tag{2.73}$$

The temperature of the maximum in χ can be determined by taking the derivative with respect to t. This gives

$$\frac{\partial \chi}{\partial t} = \frac{-a t^6 + a(bh)^2 t^4 + (3a/4)(bh)^4 t^2}{\left(t^4 + (bht)^2 + (bh)^4/4\right)^2} \tag{2.74}$$

where $a = \mu_B M_0/k_B t$ and $b = \mu/k_B$. The condition for an extremum is met when the numerator is 0. Two of the six roots are 0, two are imaginary, and two are given by

$$t = \pm\sqrt{\frac{3}{2}}\frac{\mu_B h}{k_B}. \tag{2.75}$$

The positive root corresponds to the physically relevant situation. The shift in t is expected to be linear in h, confirming the physical argument given above. What is gained is, for a spin-1/2 system, the slope of a plot of t vs. H_{app} should be $\sqrt{3/2}\mu_B/k_B$. The temperature in Eq. 2.75 can be put back into Eq. 2.73 to get χ_{max} vs. H_{app}. Doing so gives

$$\chi_{max} = \frac{3}{8}\sqrt{\frac{3}{2}}\frac{M_0}{h} \tag{2.76}$$

and the expectation is that the maximum in susceptibility should be suppressed like $(Hex + H_{app})^{-1}$.

To generalize this to arbitrary spin, it is easier to return to Eq. 2.8 and expand it for small arguments.

$$M(t,h) \approx M_0 \left[\frac{hy}{12J^2 t} \left((2J+1)^2 - 1 \right) + \frac{y^3 h^3}{45(2J)^4 t^3} \left(1 - (2J+1)^4 \right) \right] \tag{2.77}$$

In the above M_0, h, and t have the same meaning as in Eq. 2.71 and

$$y = \frac{g_J \mu_B J}{k_B}. \tag{2.78}$$

Differentiating with respect to h results in

$$\chi(t,h) \approx M_0 \left[\frac{y}{12J^2 t} \left((2J+1)^2 - 1 \right) + \frac{y^3 h^2}{15(2J)^4 t^3} \left(1 - (2J+1)^4 \right) \right] \tag{2.79}$$

The susceptibility has a maximum at the temperature

$$t \approx + \frac{g_J \mu_B h}{k_B} \sqrt{\frac{3\left(1 + (2J+1)^2\right)}{20}} \tag{2.80}$$

Again, the temperature of the maximum in χ is expected to shift linearly with applied field. On substituting $J = 1/2$, equation 2.80 reduces to 2.75 apart from a factor of $1/\sqrt{2}$. Substituting back into Eq. 2.79 gives

$$\chi_{max}(h) \approx M_0 \frac{2J\,(J+1)}{9h} \sqrt{\frac{10}{3\,(2J^2 + 2J + 1)}} \tag{2.81}$$

Equation 2.80 predicts that a plot of $t = T - T_C$ vs. applied field should be linear with a slope, s, given by

$$s = \frac{g_J \mu_B}{k_B} \sqrt{\frac{3\left(1 + (2J+1)^2\right)}{20}}. \tag{2.82}$$

For a ferromagnet containing trivalent Ce ions, where $S = \frac{1}{2}$, $L = 3$, and $J = \frac{5}{2}$, and using Eq. 2.4 the preceding analysis predicts the slope should be 1.35×10^{-4} K/Oe regardless of the ordering temperature. Figure 2.20 shows a plot of t vs H_{app} for $CeVSb_3$ and a linear fit to these data. The fit gives a slope of 4.75×10^{-4} K/Oe which is about 3.6 times larger than the prediction. Similar data is presented in Fig. 2.21 for Ce_3Al_{11}. The resulting linear fit gives a slope of 3.13×10^{-4} K/Oe. This slope is about 2.3 times larger than the prediction.

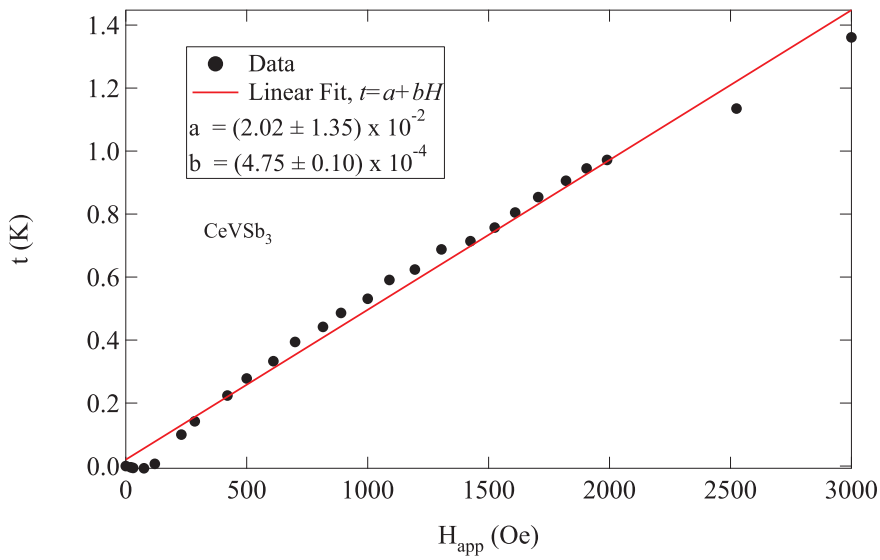

Figure 2.20 Temperature of the peak in χ_{TDR} vs. applied field for $CeVSb_3$ as measured along the c–axis.

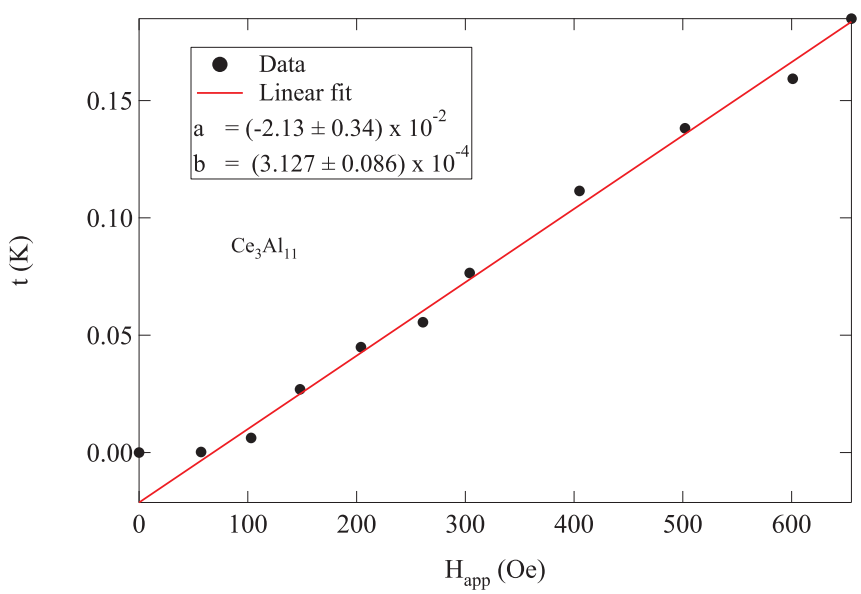

Figure 2.21 Temperature of the peak in χ_{TDR} vs. applied field for Ce_3Al_{11} as measured along the c–axis.

Turning to GdPtIn, Eq. 2.82 predicts a slope of 4.19×10^{-3} K/Oe for trivalent Gd ($S = \frac{7}{2}$, $L = 0$, $J = \frac{7}{2}$). From Fig. 2.22 a fit to the temperature of the maximum vs. applied field gives 1.15×10^{-3} K/Oe. The measured slope is almost 3.7 times smaller than what is predicted from this simple analysis.

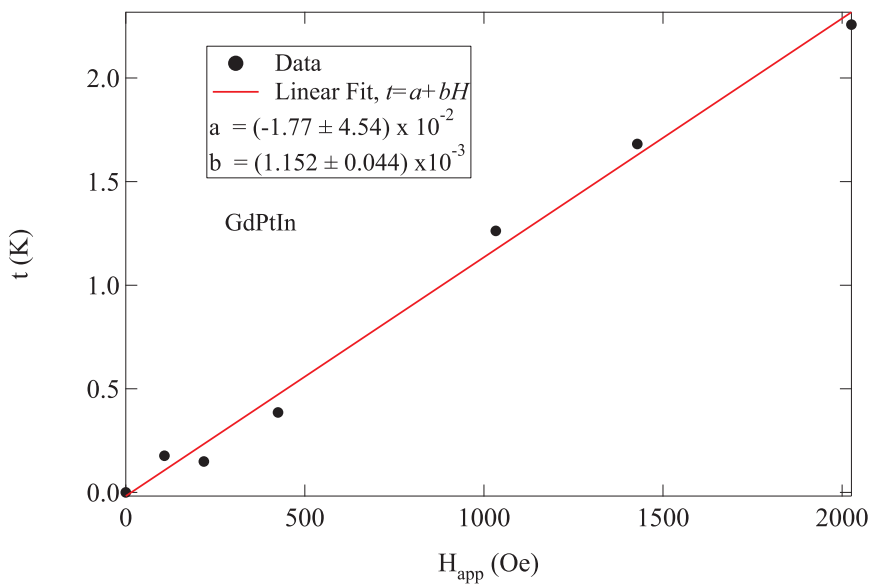

Figure 2.22 Temperature of the peak in χ_{TDR} vs. applied field for GdPtIn as measured along the c–axis.

Given the simplifications that have gone into this analysis, the match between the data and the predictions is quite good. It is seen in Ch. 3 that the amplitude of the maximum in χ_{TDR} does follow a $1/(H + H^*)$ type of behavior. The consequences of this observation for critical scaling are discussed in more detail there.

Quantitative analysis of the phase transition generally lies in the realm of scaling theory, and it will be addressed later. However, Sznajd (2001) presents an argument that the temperature evolution of the peak in χ with applied field is not associated with critical fluctuations at all. It is also stated that within the Landau mean-field theory of second order phase transitions this temperature should depend on applied field as a power law. Under this argument, the predicted thermal evolution for the peak in χ is it grows as h^2 while for cubic (essentially

isotropic exchange) it should grow like $h^{2/3}$.

2.5 Anisotropy in $CeVSb_3$

Asymmetry or anisotropy is common in Nature [McManus (1976)]. In this section, the anisotropic rf susceptibility in $CeVSb_3$ is studied. When χ_{TDR} is measured perpendicular to the magnetic easy axis, obvious differences in the data are seen (Fig. 2.23). First, the amplitude of the peak at T_C is approximately 40 times smaller. Also the field required to suppress the peak to 10% of the zero field value is nearly 11 times larger for the perpendicular orientation (Fig. 2.25). Finally, the temperature of the maximum is only weakly dependent on the applied field (inset of Fig. 2.24).

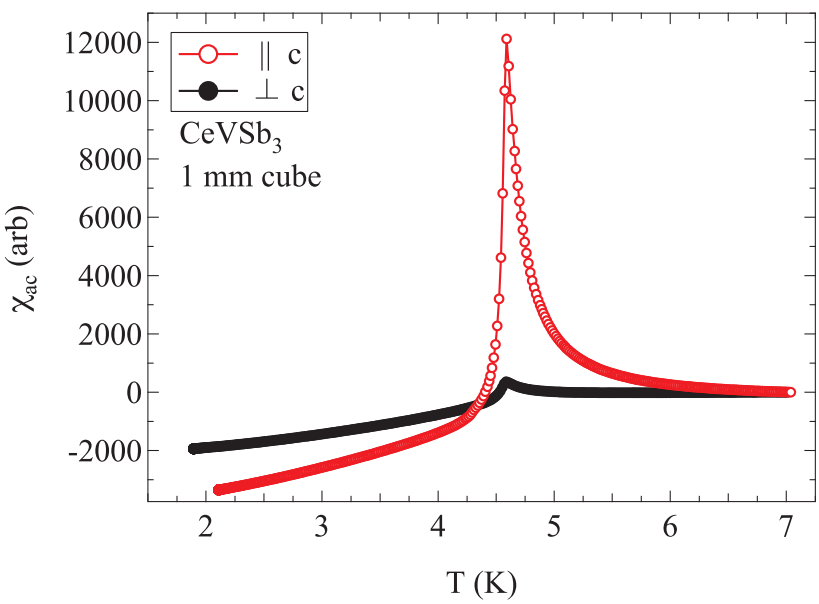

Figure 2.23 Comparison of zero field susceptibility for $CeVSb_3$ measured parallel and perpendicular to the magnetic easy axis.

The low temperature difference between the directions can be explained in two ways. First, the resistivity of this material along the c-axis is greater than along the b [Sefat et al. (2008)]. Since the rf field probes the resistivity perpendicular to it, when measuring χ_{TDR} along the c–axis ρ_b is probed and vice versa. An alternative possibility is that when χ_{TDR} is measured

perpendicular to the easy axis the rf field can tip the ordered moments coherently. While measuring χ_{TDR} parallel to the easy axis, the rf field is insufficient to flip the moments resulting in no change in magnetic moment. The deviation at higher temperatures is a direct result of the differing spin susceptibility, as the published resistivity along b is less than that along c. The screening in the ab plane (with the rf parallel to c axis) should be greater than the screening the in ac plane (rf parallel to b axis) and measured χ_{TDR} should be less. This is not observed.

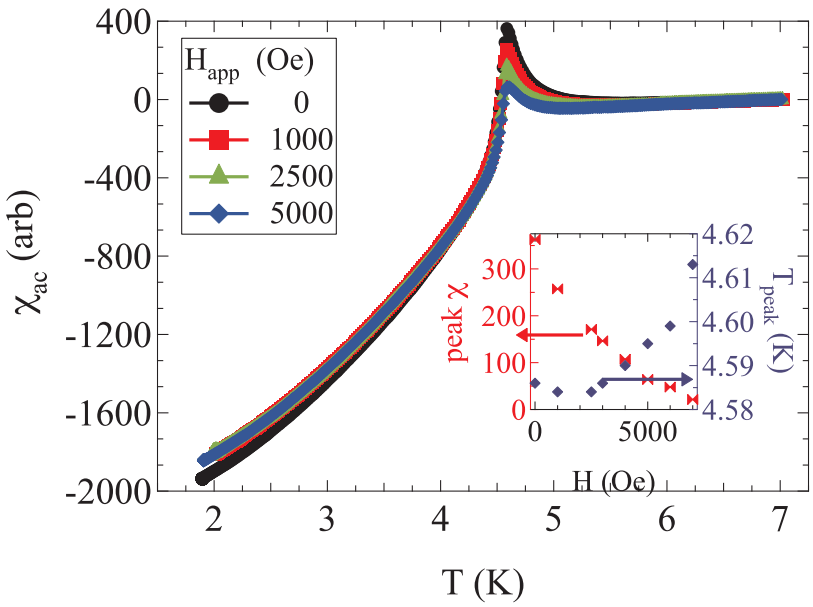

Figure 2.24 χ_{TDR} measured perpendicular to the magnetic easy axis in different static bias fields. The amplitude of the maximum is much less than that measured along the easy axis. The fields required for suppression are also considerably larger. *Inset:* Peak amplitude (left axis) and temperature of peak (right axis) versus applied field.

Fig. 2.24 shows χ_{TDR} vs. T for $CeVSb_3$ measured along the b axis in different applied static fields. Two features stand out when compared with the c axis data. First, the fields required to suppress the peak are much larger than the c axis case (6.5 kOe as compared to 0.5 kOe for a 90% suppression). Second, the temperature of the peak is basically unaffected

by the application of the magnetic field, increasing less than 40 mK with an applied field of 5 kOe. This is in stark contrast to the c axis data where the maximum shifts up by almost 2 K with an applied field of 3 kOe. Both of these behaviors are summarized in Fig. 2.25.

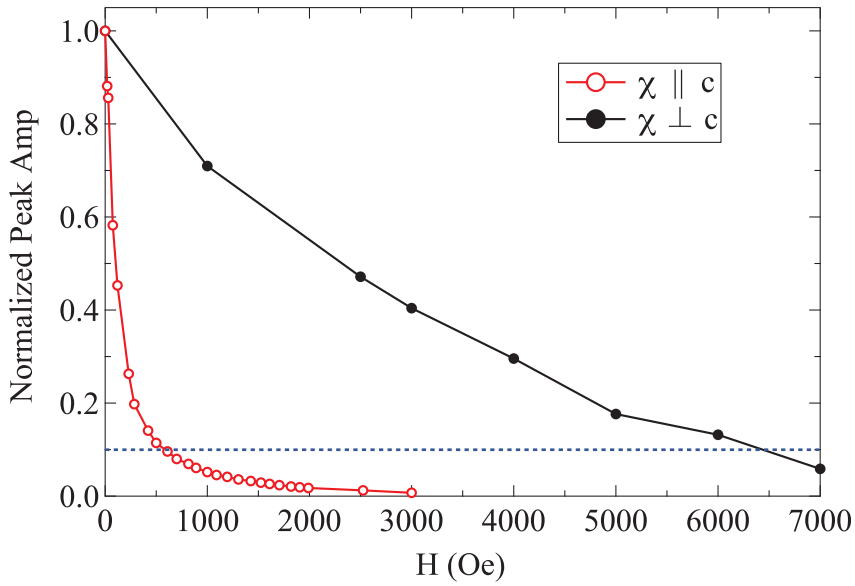

Figure 2.25 χ_{TDR}^{max} normalized to the zero field value versus applied field for parallel and perpendicular to the easy axis for $CeVSb_3$. Dotted line marks a 90% suppression.

2.6 Summary

The general features of radio–frequency magnetic susceptibility in local moment ferromagnets have been explored. The expected divergence in χ_{TDR} at T_C manifests as a sharp peak in zero applied field. Application of a static field suppresses the peak and shifts it to higher temperatures when the rf–field and static field are parallel with the magnetic easy axis in the crystal. In the case where both fields are perpendicular to the magnetic easy axis, a peak is still observed. However, the zero field amplitude of this peak is greatly suppressed relative to measurements along the easy axis. Applying a static field for a hard axis orientation does not appreciably shift the temperature of the peak. The fields required to suppress the hard axis

peak are much greater than those required to suppress the easy axis peak.

CHAPTER 3. Failure of Critical Scaling Analysis of the Phase Transition

3.1 Introduction

The quality of the data collected by the TDR suggests that it may provide information regarding the physics governing the phase transition. This physics falls under the subject of critical scaling analysis. An overview of the theory of critical scaling is provided first. Following, is application of this analysis to the systems $CeVSb_3$, $CeAgSb_2$, and $YTiO_3$. The failure of the TDR data to properly scale suggests that these data may lie on the boundary between the static and dynamic regimes.

Experimentally it is known that the behavior of the magnetization, heat capacity, and magnetic susceptibility near T_C are dominated by power law dependencies in field and temperature. The various exponents assigned to each are

$$C_P \sim \tau^{-\alpha} \tag{3.1}$$

$$m \sim \tau^{\beta} \tag{3.2}$$

$$m \sim h^{1/\delta} \tag{3.3}$$

$$\chi \sim \tau^{-\gamma} \tag{3.4}$$

where $\tau = |T - T_C| / T_C$ is the reduced temperature, and $h = \mu H / k_B T_C$ is the reduced field. The behavior of a system near a phase transition falls into the category of critical point analysis. The value of the particular thermodynamic variable driving the transition that sits on the boundary between the ordered and disordered phases is the critical point. Often this variable is temperature, but it may be field or pressure as well. The fundamental idea behind critical point analysis is that at the critical point the system has no intrinsic length scale over which correlations are established.

From a ferromagnetic standpoint, when the temperature is much higher than the Curie temperature the system is completely disordered and thermal fluctuations disrupt even nearest neighbor correlations. As the temperature decreases the ferromagnetic exchange interaction tends to align neighboring spins with one another. However, for any given spin there is a characteristic length, ξ, beyond which two spins are uncorrelated. This means that if a spin at point $\mathbf{r}$ points in some direction, then spins less than ξ away from $\mathbf{r}$ will tend to point in that same direction. Conversely, spins farther than ξ will not have any tendency to point in the same direction as the spin at a$\mathbf{r}$. The closer T is to T_C, the greater ξ is, until at $T = T_C$ ξ diverges. The divergence of ξ implies that there is no characteristic length in the problem. Therefore the free energy and its derivatives (magnetization, heat capacity, magnetic susceptibility, etc.) may be rescaled in some way provided the thermodynamic variables (field and temperature) are suitably scaled as well. Authoritative reviews of the subject are provided by Kadanoff et al. (1967) and Fisher (1967). Stanley (1999) offers a colloquial introduction to the concepts associated with these critical phenomena. Three basic ideas fall out of critical scaling theory. The first is the existence of relationships between the various exponents describing the behavior of the system as it approaches the phase transition. These are called scaling laws. The second idea is that of data collapse. Data collapse predicts that data collected on, say, magnetization vs. temperature in various fields, should all fall onto a single pair of curves that approach one another as $T \to T_C$ if the data are plotted appropriately. The proper way to plot susceptibility data will be extracted below.

A third, separate concept of scaling is that of universality [Stanley (1999)]. This is the observed fact that magnetically ordered materials usually fall into different classes based on the nature and dimensionality of the ordering. Each class has its own set of critical exponents (Table 3.1). For ferromagnets it is interesting to note that while there are widely varying values for β and δ, the product of the two (which is the relevant quantity for scaling susceptibility data) is always close to 1.5.

The free energy can be expressed as some unknown function of reduced temperature ($\tau = |T - T_C|/T_C$) and field ($h = \mu H/k_B T_C$) where T_C is the suitably defined zero field transition

Table 3.1 Critical exponents in various models from Fisher (1967).

Exponent	**2-D Ising**	**3-D Ising**	**3-D Heisenberg**	**mean field**
β	0.12	0.31	0.31	0.5
δ	15	5.0	5.2	3
$\beta\delta$	1.8	1.55	1.61	1.5
γ	1.75	1.25	1.33	1

temperature.

$$F = F\left(\tau, h\right) \tag{3.5}$$

T_C is taken as the temperature of the maximum in χ_{TDR} as measured in zero field. Under the scaling hypothesis if F is multiplied by an arbitrary factor then the function is unchanged provided the arguments are multiplied by the same factor to some power.

$$\lambda^D F(\tau, h) = F(\lambda^a \tau, \lambda^b h). \tag{3.6}$$

The power D on the prefactor refers to the dimensionality and reflects the fact that the free energy scales with the volume of the sample. Since the factor λ is arbitrary, it may be chosen for computational convenience. Taking $\lambda^a \tau = 1$ implies $\lambda = \tau^{-1/a}$. This allows a substitution into the free energy, recasting it as

$$F(\tau, h) = \tau^{D/a} F(1, \tau^{-b/a} h). \tag{3.7}$$

From here, the temperature dependence of the zero field heat capacity can be determined.

$$C_P = \frac{\partial^2 F}{\partial \tau^2} \sim \tau^{D/a-2}. \tag{3.8}$$

Examining the relationship from Eq. 3.1 shows that $\alpha = 2 - D/a$. This is the first scaling law, and it relates the divergence of the heat capacity directly to the dimensionality of the system. The exponent a is, as yet, undetermined. However, further work can be done to determine how the magnetization and susceptibility depend on temperature and field. This will allow for an elimination of a and b in favor of α, β, δ, and γ.

Eq. 3.7 can be differentiated once with respect to field to determine the temperature dependence of magnetization. Doing so gives

$$m \sim \tau^{(D-b)/a} \tag{3.9}$$

in the limit of zero field. Combining this result with Eq. 3.2 and the relationship between α, D, and a just found gives $\beta = 2 - \alpha - b/a$. Returning to Eq. 3.6 the choice $\lambda^b h = 1$ can be made. In this case the free energy is recast as

$$F(\tau, h) = h^{D/b} F(h^{-a/b}\tau, 1). \tag{3.10}$$

Now, at the critical point ($\tau = 0$) the magnetization depends on field as

$$m \sim h^{D/b-1}. \tag{3.11}$$

Again, comparison with the assigned labels for the critical indices shows that $\delta = b/(D - b)$. The free energy in Eq. 3.7 can be twice differentiated with respect to field to obtain the temperature dependence of the susceptibility. This gives

$$\chi \sim \tau^{(D-2b)/a} \tag{3.12}$$

which shows that $\gamma = (2b - D)/a$. Using the relationships between D, b, a, β, and δ it is possible to rewrite Eq. 3.7 eliminating the exponents b and a. Since $\beta = (D - b)/a$ and $\delta = b/(D - b)$ the product $\beta\delta$ is just b/a. This is the exponent on the reduced temperature in Eq. 3.7 (with a minus sign). Therefore, this form of the free energy may be rewritten as

$$F(\tau, h) = \tau^{D/a} F(1, h/\tau^{\beta\delta}). \tag{3.13}$$

Taking derivatives will alter the functional form of F, but it will not change the argument of that function. All changes are taken into account by moving them to the prefactor. What this implies is that the relation 3.12 may be rewritten as

$$\chi(\tau, h) = \tau^{-\gamma} G\left(\frac{h}{\tau^{\beta\delta}}\right). \tag{3.14}$$

Moving the factor $\tau^{-\gamma}$ to the left hand side shows that $\chi\tau^{\gamma}$ is a universal function of $h/\tau^{\beta\delta}$. If temperature dependent susceptibility data is collected in different fields, then a plots of $\chi\tau^{\gamma}$ vs. $h/\tau^{\beta\delta}$ should fall onto a single curve as the critical point is approached. This is termed 'collapse of the data.'

3.2 Experimentally Determining Scaling Exponents

Ho et al. (1981) have presented a method of determining the scaling exponents β and δ from measurements of the AC susceptibility in ferromagnets. The basis of their procedure is the simple fact that the derivative of a function is zero at a maximum of that function. They further exploit the idea that the derivative of a generalized homogeneous function is itself a generalized homogeneous function. γ can be determined from a log-log plot of the zero field susceptibility versus $T - T_C$ on the paramagnetic side.

For a fixed field, the susceptibility goes through a maximum at some temperature, τ_m near $\tau = 0$. At this temperature the derivative of the susceptibility with respect to temperature is zero, $d\chi/d\tau = 0$. This implies that G in Eq. 3.14 is independent of τ at the maximum which is satisfied if its argument is constant, i. e. $h/\tau^{\beta\delta} = const$. This leads to the conclusions that

$$\tau_m \sim h^{1/(\beta\delta)} \tag{3.15}$$

and

$$\chi_m(h, \tau_m) \sim h^{(1/\delta)-1}. \tag{3.16}$$

The Widom relation can be exploited to rewrite the exponent on τ_m as $1/\beta\delta = 1/(\gamma + \beta)$. Therefore, it should be possible to determine γ, δ, and the product $\beta\delta$ if χ_m and τ_m are plotted vs. H on log-log axes. These should be straight lines whose slopes are the exponents.

3.3 Critical Scaling in $CeAgSb_2$ and $CeVSb_3$

The scaling analysis developed in earlier sections is not applicable to all of the systems studied. Ce_3Al_{11} has two distinct cerium moments, and the assumptions going into the analysis of critical phenomena is that each magnetic site carries the same moment. Therefore, scaling in Ce_3Al_{11} is not expected to work. Further, some samples (Gd, YIG, , $Fe_{1/4}TaS_2$, and $Pr_2Fe_{14}B$) had obstacles to experimentally testing the critical phenomena. In the main, these problems were in the Curie temperatures of the samples. These temperatures were particularly difficult to reach without the addition of a considerable background signal and thermal lag. What this leaves for analysis are $CeVSb_3$, $CeAgSb_2$, $YTiO_3$ and GdPtIn. In this section, $CeAgSb_2$ and

$CeVSb_3$ are studied. The next section addresses $YTiO_3$. As there was never a field sufficient to suppress the maximum in χ_{TDR} fully for GdPtIn, this data is not scaled. However, certain analyses regarding the peak is attempted.

To account for the resistive background coming from the metallic samples, a high field temperature sweep is subtracted from the lower field runs. The chosen field is sufficiently large to completely suppress the peak at T_C. As an example of the results of this process the difference between the lower field data in $CeAgSb_2$ and a 1 kOe run is presented in the main plot of Fig. 3.1. The inset shows the raw χ_{TDR} vs. T for this same data.

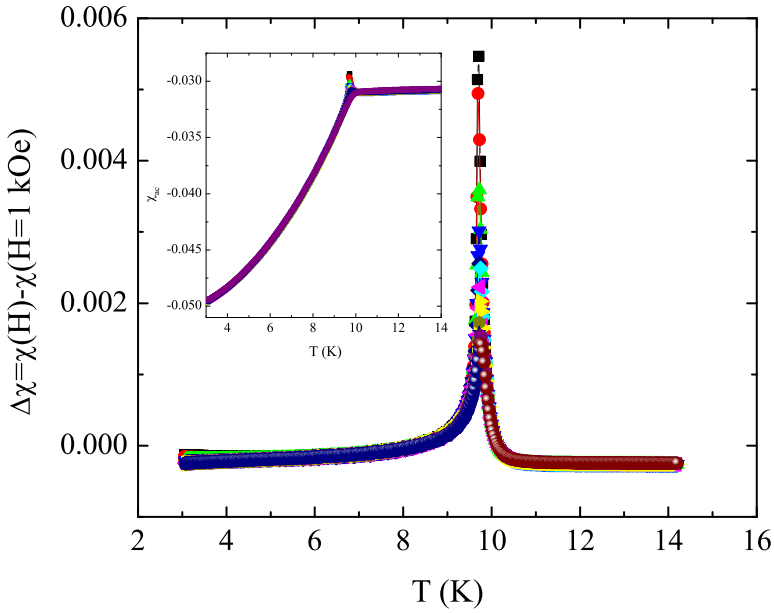

Figure 3.1 Difference in χ_{TDR} vs. T relative to a 1 kOe run for $CeAgSb_2$. *Inset:* Absolute χ_{TDR} vs. T for data in the main panel.

In the course of examining the data from the various local moment systems, it was noticed that the peak amplitude associated with the phase change was suppressed as H^{-1}. However, a plot of χ_{max} vs. H^{-1} deviates from linear for the lowest fields (see Fig. 3.2). This suggests that the true functional form is not $\chi_{max} \propto H^{-1}$, but rather that it is proportional to $(H + H^*)^{-1}$.

Indeed, a plot of χ_{max}^{-1} vs. H is linear. H^* is the effective applied field in which the magnetic susceptibility diverges for the sample. The general behavior of the susceptibility maximum with applied field has been observed before in many ferromagnetic systems. Further, Kunkel et al. (1988) have predicted similar behavior for paramagnetic systems with no interaction for $T \rightarrow 0$. In that work it is stated that such behavior from paramagnets provides evidence that the maximum is related to the static rather than the dynamic response of the system. This suggests that the systems are still in the static regime. However, if a comparison is made of similar measurements at different frequencies (14 and 28 MHz) it is seen that there are some differences in some of the samples [Vannette et al. (2008c)].

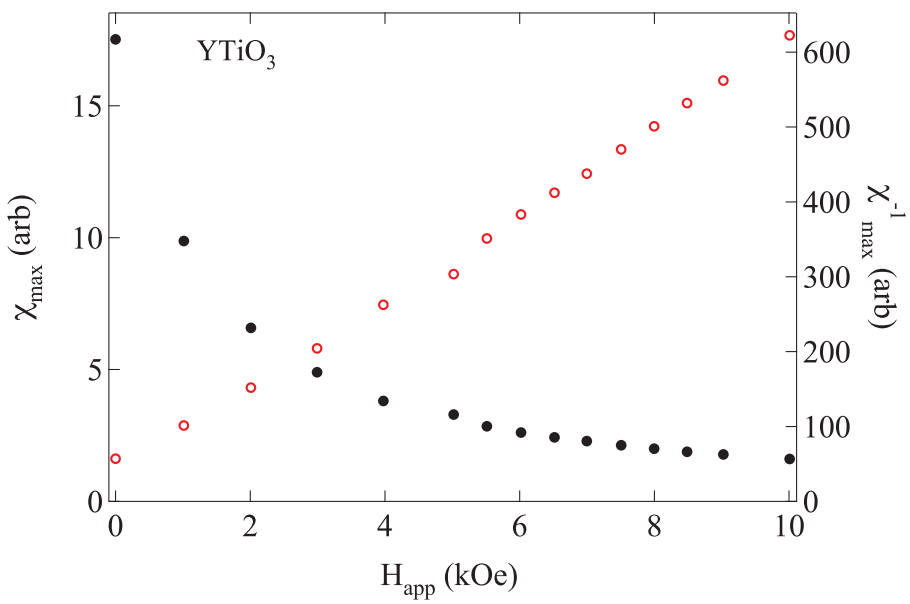

Figure 3.2 Peak amplitude (solid symbols, left axis) and inverse peak amplitude (hollow symbols, right axis) vs. applied field for $YTiO_3$.

Figure 3.3 shows plots of the inverse peak amplitude against applied magnetic field. Both compounds show a linear relationship with a negative H intercept, which is labeled H^*. This characteristic field represents the field at which the magnetic susceptibility would truly diverge.

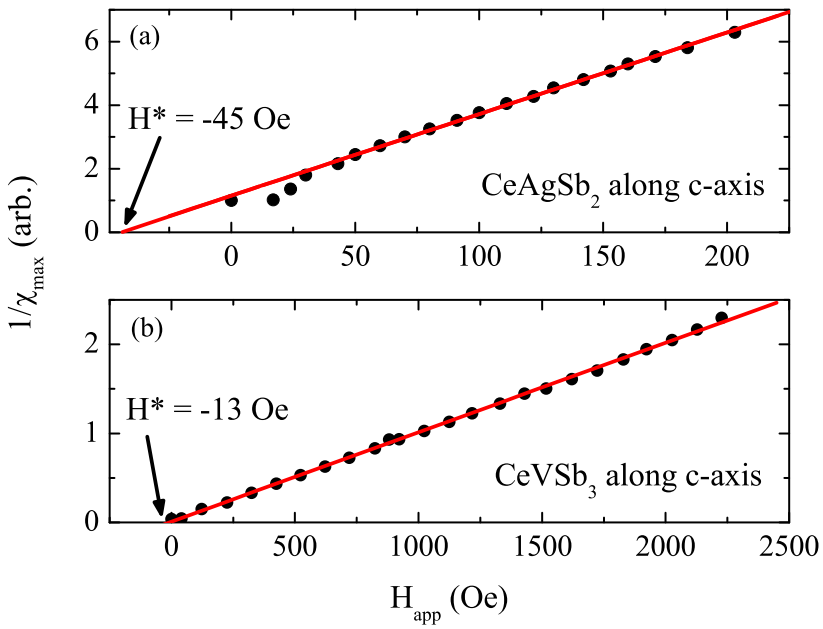

Figure 3.3 (Color online) Inverse peak amplitude *vs.* applied magnetic field for $CeAgSb_2$ (a) and $CeVSb_3$ (b). Solid circles are data and the line is a linear fit. The H axis intercept (H^*) corresponds to the applied field at which the susceptibility would diverge.

The linear relationship is also troubling for scaling analysis because it implies

$$\chi_m \sim h^{-1}. \tag{3.17}$$

In conjunction with Eq. 3.16 this suggests $1/\delta$ is zero and the value of δ is undefined. The absolute values of H^* for the two compounds are reasonably close. Comparison of H^* with the fields required to suppress the susceptibility maximum, however, indicates a significant difference. For $CeAgSb_2$ H^* is not quite a full order of magnitude below the suppression field. On the other hand, for $CeVSb_3$ H^* is nearly a factor of 100 smaller than the suppression fields.

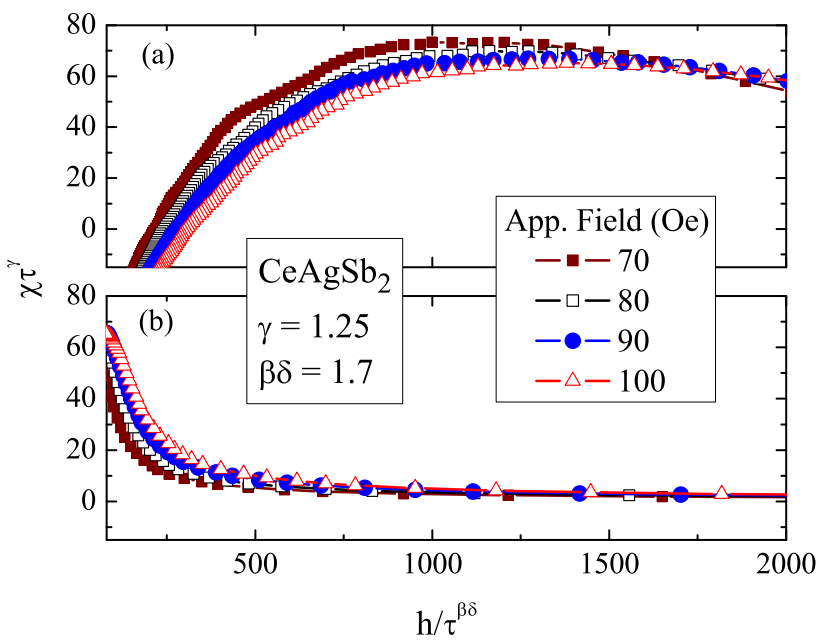

Figure 3.4 (Color online) Scaled plots for $CeAgSb_2$ in the paramagnetic state neglecting H^* (a) and adding H^* to all applied fields (b). As $T \to T_C$, the plot extends off to right. Both plots use the same exponents.

Scaling was attempted for $CeAgSb_2$. γ was estimated from a double log plot of the zero field susceptibility while the product $\beta\delta$ was treated as an adjustable parameter. Using values of the applied field without modification failed to produce any reasonable collapse of the data (Fig. 3.4(a)). However, if H^* determined from the plot of inverse peak amplitude versus applied

field is added to all applied fields the resultant collapse is much better (Fig. 3.4(b)). In order to determine the relative quality of the data collapse, χ^2 analysis was performed on data collected in the largest and smallest applied fields.

In comparing the two data sets it was seen that there was not a point by point match of the x values in the data. To combat the the data from the smallest field was parsed into seven point subsets, a midpoint and three points above and below the midpoint. Every point considered in the χ^2 analysis was treated as a separate midpoint. A fourth order polynomial was fit to each subset and the resulting fit parameters were used to interpolate the data so that a comparison between the largest and smallest field data could be made. Tests of this procedure on two identical cosine functions extending over 3 full periods, where χ^2 is expected to be 0, resulted in $\chi^2 \approx 2.5$. By reducing the test data sets to half period lengths the procedure reduced the χ^2 to 1.2. This lower value of χ^2 on a monotonic curve was taken as the ideal. Typical χ^2 values for the comparison of scaled data ranged from $> 10^5$ to < 2.

Figure 3.5 displays scaled plots for the $CeVSb_3$ data. As with $CeAgSb_2$, γ was estimated from a double log plot of the zero field susceptibility and $\beta\delta$ was treated as an adjustable parameter. In panel (a) H^* is neglected while in panel (b) H^* is added to all field values. Interestingly, for this sample the collapse of the data is somewhat better without considering H^*, however in both situations the collapse is very good.

The precise interpretation of H^* is difficult. At first, one might think of it as the demagnetizing field. This view has the problem that the demagnetizing field is proportional to the magnetization of the sample. Therefore, it should be recalculated for each applied field instead of being a single value. On the other hand, if this field is associated with the internal dipole field from the surrounding magnetic moments a separate complication is met. Using published values for structure and lattice parameters for $CeVSb_3$ [Sefat et al. (2008)] one can calculate the dipole field on one Ce ion from its neighbors. This is of the order of -800 Oe if one assumes a fully ordered lattice of 1.4 μ_B ions. It can be argued that near T_C, where the data is collected, the lattice is not fully ordered, so such a calculation is invalid. Indeed, at T_C the magnetization is formally zero and therefore the dipolar field should be zero. There

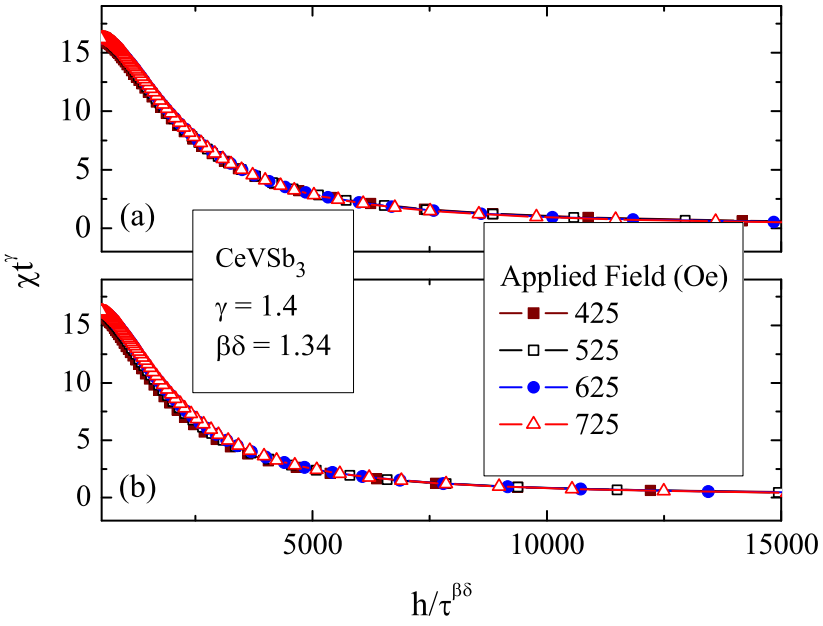

Figure 3.5 (Color online) Scaled plots for $CeVSb_3$ neglecting H^* (a) and adding H^* to all applied fields (b). Both plots use the same exponents.

exists the possibility that this field is somehow related to the imagined Weiss molecular field that leads to ordering in magnetic samples. Again, there is a problem in that the Weiss field is little more than an imaginary mechanism as its magnitude should be several orders larger than what is presented here. However, H^* represents the field that must be *applied* to result in true divergence in χ. Therefore, it can be considered as opposing some other field in the sample. Taking this stance suggests that H^* could be related to the exchange field leading to the magnetic order. Yet another interpretation is to consider H^* as an effective field originating with the finite frequency of the measurement. In this case, it would be expected that for fields less than $|H^*|$ the response would be frequency dominated and the linearity of the inverse peak amplitude would be more strictly adhered to. For larger fields it, the suppression should then evolve sublinearly in accordance with the exponent $\beta\delta$.

Two different frequencies were used to determine if this last idea is the case in $CeAgSb_2$ and $CeVSb_3$. The previously reported data was taken at 14 MHz. Fig. 3.6 shows the inverse of the peak in χ_{TDR} vs. applied field for $CeVSb_3$ as measured at 28 MHz. It is seen that H^* increases very slightly, but is the same as the 14 MHz data within the uncertainty. This notwithstanding, the observed linearity in the data points is striking, suggesting that the rf field is still in the static limit, if frequency effects are to be invoked. The 28 MHz data was collected on a cube shaped sample approximately 1 mm on edge. The demagnetization factor would be smaller for this sample than for the thinner piece used in the lower frequency measurement.

Similar data collected at 28 MHz on a larger sample $CeAgSb_2$ with nearly the same aspect ratio as the smaller sample suggests that this material is not in the static regime, as the measured H^* is approximately 50% larger when compared to the 14 MHz data (Fig. 3.7). This interpretation is in keeping with the previous observation that scaling in $CeAgSb_2$ could only be accomplished by considering the effect of this characteristic field. However, the puzzling fact that the inverse peak amplitude is linear in H up to 3 times H^* tends to suggest that this may not be the case. A possible explanation is that there are multiple terms (Weiss ordering field, frequency, and geometric) all combined to give the effective H^*. It would be expected that the Weiss term is constant across samples as this is an intrinsic quality. Given the similarities

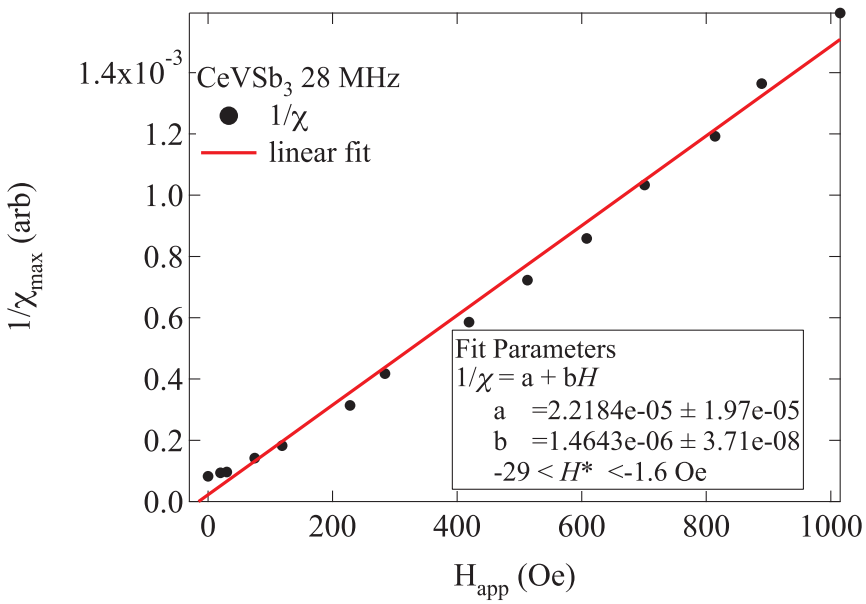

Figure 3.6 Inverse peak amplitude vs. field for $CeVSb_3$ measured in the ^{4}He system at 28 MHz.

of the shapes and aspect ratios of the samples, it is expected that the demagnetization effects would be the same. This leaves the main culprit as the frequency for inducing a change in H^*.

Similar analysis performed on a single sample of GdPtIn at both 14 and 28 MHz also shows that there is a different characteristic field for each frequency here as well. If $|H^*|\,\mu_{sat}/\mu_B$ is plotted against T_C for several local moment samples, there appears to be a strong correlation (Fig. 3.8) that depends on measurement frequency. This lends some credibility to the idea that H^* is tied to the exchange field, as there is a correlation between the magnetic energy associated with this characteristic field and the onset of long-range magnetic order. The higher frequency trend is very nearly linear while the lower frequency has some positive curvature for the samples studied. The $YTiO_3$ data at 14 MHz is considerably suppressed relative to the line joining $CeAgSb_2$ and GdPtIn at the same frequency.

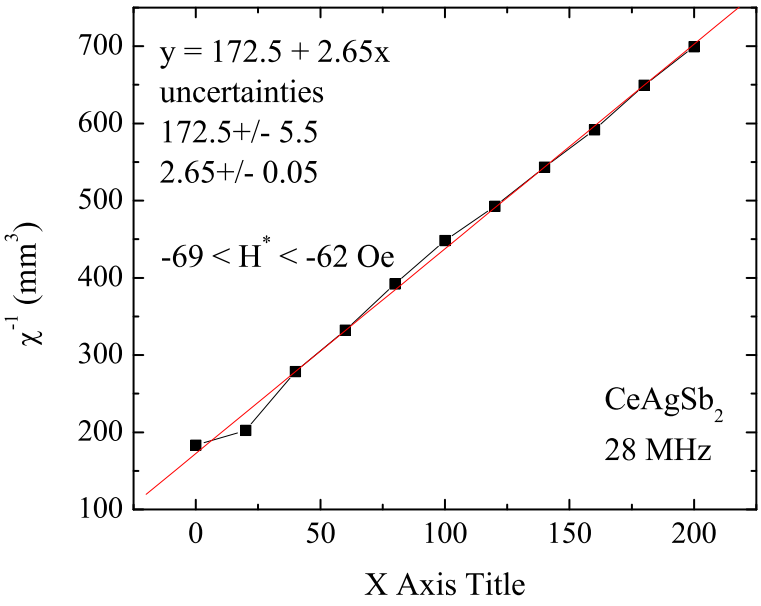

Figure 3.7 Inverse peak amplitude vs. field for $CeAgSb_2$ measured in the ^{4}He system at 28 MHz.

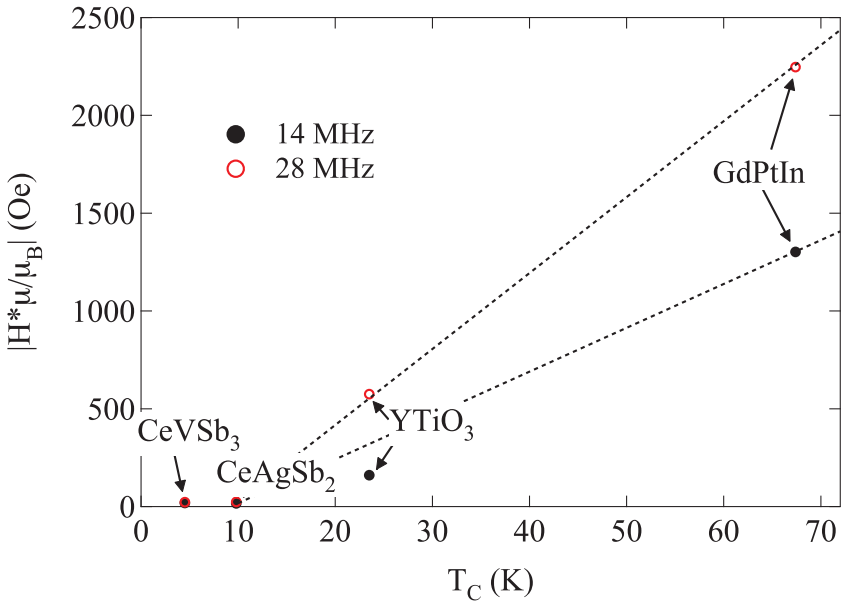

Figure 3.8 Plot of $H^*\mu_{sat}/\mu_B$ versus T_C for the magnets studied in this work. There is an obvious correlation between the energy associated with H^* and the Curie temperature. This suggests that H^* is related to the ordering mechanism in local moment ferromagnets. Dashed lines are guides to the eye.

Table 3.2 Characteristic fields from the analysis of peak amplitude with applied field.

Sample	μ_{sat} μ_B**/ion**	T_C **K**	**14 MHz** H^* **Oe**	**28MHz** H^* **Oe**
$CeVSb_3$	1.4/Ce	4.5	-13	-16
$CeAgSb_2$	0.37/Ce	9.8	-45	-65
$YTiO_3$	0.85/Ti	23.7	-189	-676
GdPtIn	7.55/Gd	68	-187	-321

3.4 Scaling an Insulating Ferromagnet

Since it appears that scaling works best when the H^* field is taken into consideration, presented scaled data on $YTiO_3$ immediately considers the effects of this field. Figs. 3.9–3.12 present the results of scaling in $YTiO_3$ using exponents from the models presented in Table 3.1. In all figures the lines marked '5%' and '10%' denote that fractional change in temperature from T_C. Since critical scaling is only valid close to T_C it is natural to expect the collapse of the data to be better as $T \to T_C$. Indeed this is the case for all models. (T_C is at $+\infty$ on the horizontal axis.)

The 'best' exponents for the scaling are taken to be those that result in a tighter collapse of the data farther from T_C as determined via the previously discussed χ^2 analysis. From the figures it appears that $YTiO_3$ falls into the 2-D Ising class of magnets. Caution must be exercised at this point, though, as the larger value of $\beta\delta$ in this model will stretch the horizontal axis considerably. This said, and considering the nature of the order giving rise to the ferromagnetic component (canted antiferromagnetism), there is little difference between the 3-D Ising and 3-D Heisenberg models.

An important aspect to note is that regardless of the values of the critical exponents, the gross features of the scaled data in $YTiO_3$ are expected for properly analyzed data. This material is an insulator which means the TDR measurement is only affected by the spin susceptibility. There is no resistive component to the data. Therefore, any modifications to the analysis, particularly as pertains to the handling of the skin depth component in the following section, will be judged by comparing the scaled data with the $YTiO_3$ results.

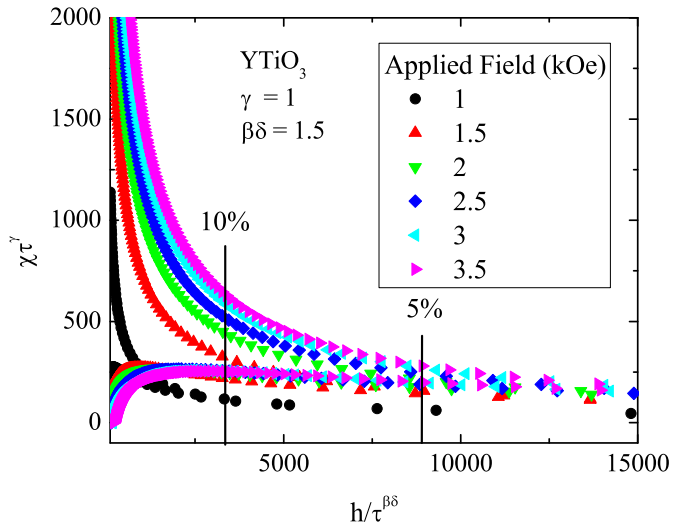

Figure 3.9 Mean field scaling for $YTiO_3$.

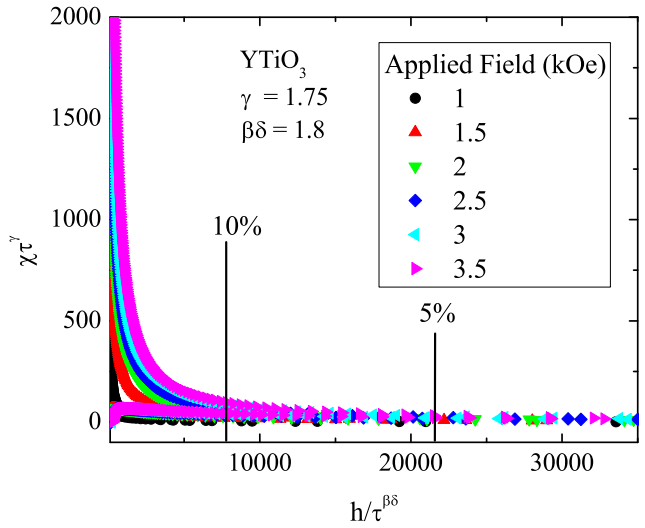

Figure 3.10 2-D Ising scaling for $YTiO_3$.

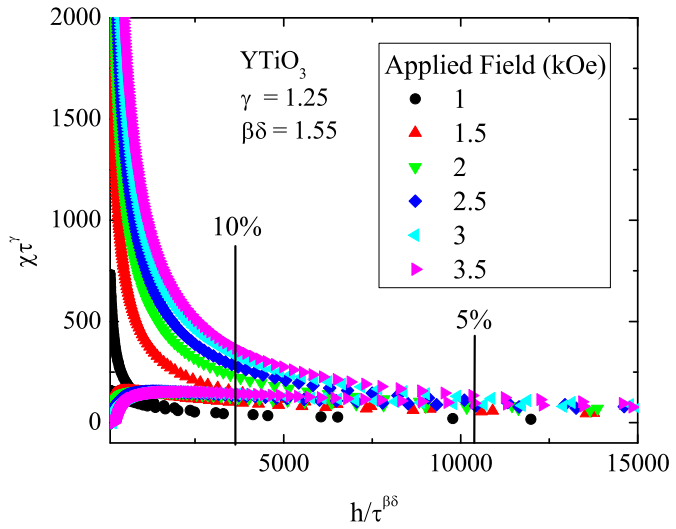

Figure 3.11 3-D Ising scaling for $YTiO_3$.

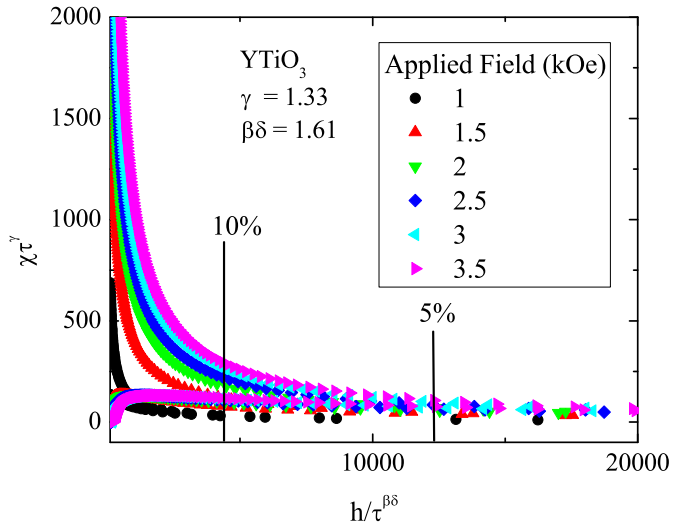

Figure 3.12 3-D Heisenberg scaling for $YTiO_3$.

3.5 Effect of Skin Depth Limit

Based on the analysis in Ch. 1, in the vicinity of a ferromagnetic phase transition, it is expected that the measured susceptibility be related to the magnetic permeability via Eq. 1.18

$$1 + 4\pi\chi = \sqrt{\mu}. \tag{3.18}$$

This neglects the contribution of the resistivity to the measured susceptibility. If this part is considered, from the previous analysis it is expected that Eq. 3.18 be modified so that $1 + 4\pi\chi = \sqrt{\mu\rho}$. If this is correct, then in skin depth limited samples true scaling should be attempted for μ instead of the measured χ_{TDR}. In some sense this is more reasonable as the critical scaling is supposed to be performed on materials using the internal field rather than the applied field. The definition of μ is dB/dH where B is the magnetic induction. In the sample, this amounts to the actual field present due to all effects. However, previously demagnetization was not considered. Ignoring demagnetization is justified based on the observed fact that the susceptibility does not show a saturation effect at $T \to T_C$. If such geometric/finite size effects were considerable, then the zero field χ_{TDR} would show a plateau near the Curie temperature. In fact, the peak in χ_{TDR} is extremely narrow and very sharp for all local moment systems studied. This tends to suggest the effects of demagnetization are not so important here.

Any dramatic deviations from the nature of Figs. 3.9-3.12 in the scaled data will be taken as indication that the consideration of the skin effect near T_C is not necessarily correct as previously derived. It is shown later that field saturation of the spin response leads to a reproduction of the behavior of the resistivity (Fig. 4.6 below). What remains in doubt is how the mixing of μ and ρ actually affect the data when χ formally diverges.

$CeAgSb_2$ is taken as the system under consideration here. The resistivity is low, so the sample is skin depth limited both above and below T_C. Further, the application of fields on the order of 1 kOe is sufficient to suppress the peak in χ_{TDR} at the transition. The previous scaling (Fig. 3.4) was accomplished by a simple subtraction of a 1 kOe run from the low field data sets. In what follows, a different method is used to attempt to account for the resistivity background.

Figure 3.13 presents the quantity $(1 + 4\pi\chi)^2$ vs. T for $CeAgSb_2$ as measured at 28 MHz in several applied fields. If the analysis of the skin depth limited regime is correct, then these curves represent the quantity $\mu\rho$. The inset to Fig. 3.13 is a detail of the ferromagnetic ordering. Qualitatively these curves are very similar to the as measured χ_{TDR} vs. T curves shown in Figs. 2.11 and 2.12. The main difference here is that the measured quantities are all positive.

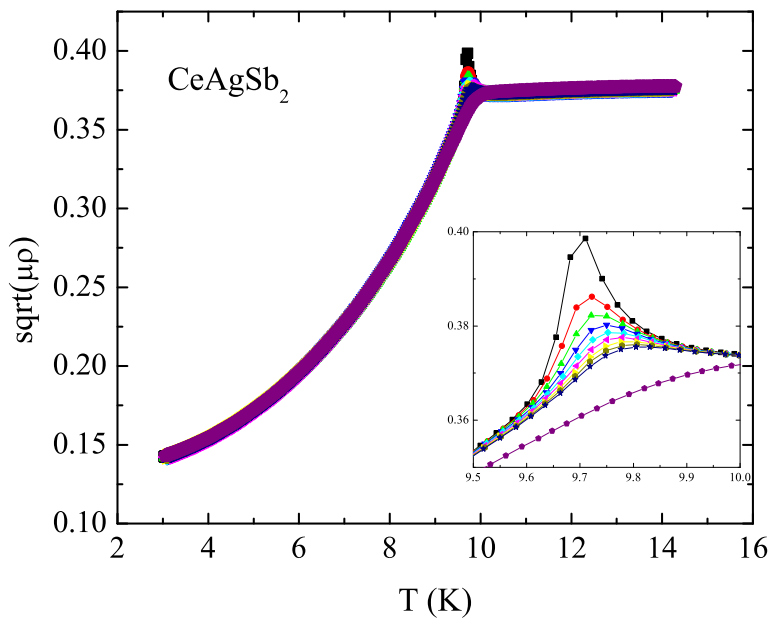

Figure 3.13 $\mu\rho$ vs. T for $CeAgSb_2$ as determined by $(1 + 4\pi\chi)^2$. *Inset:* Detail near T_C.

Under the assumptions that (1) Fig. 3.13 accurately represents the combination of magnetic spin and electrically resistive components, and (2) the application of a 1 kOe field does not dramatically alter the resistivity but suppresses the magnetic contribution, dividing the lower field data sets by the 1 kOe run should result in μ vs. T curves. Such curves are plotted in Fig. 3.14. It is evident that this is assumed to be the relative permeability.

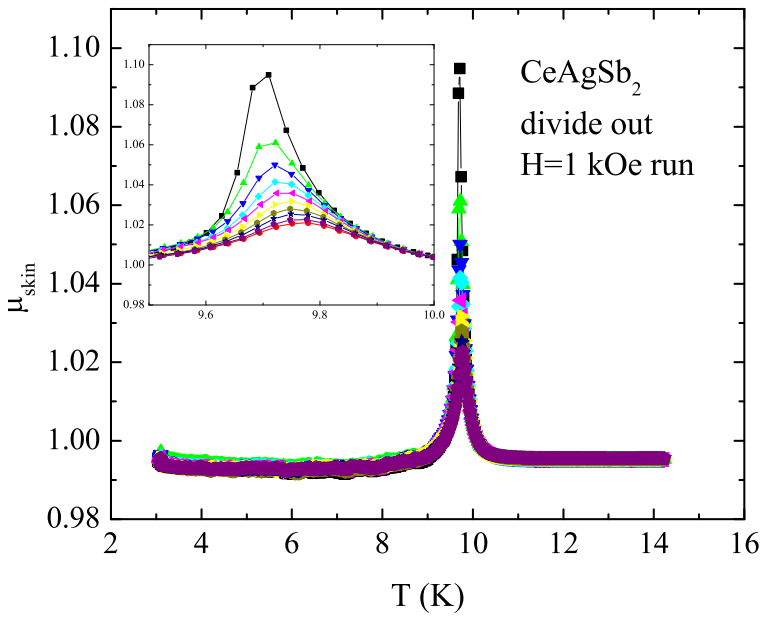

Figure 3.14 μ vs. T for $CeAgSb_2$ as determined by the method described in the text. *Inset:* Detail near T_C.

The analysis developed by Ho et al. (1981) is applied to the determined μ. Fig. 3.15 is a plot of $\log(\mu_{peak})$ vs. $\log(H)$ from 40-200 Oe. The data (with the exception of the 200 Oe point) all fall very close to a single line with slope -0.0248. This translates to a δ of 1.025. In some sense this is an improvement over the previous analysis where $\delta \rightarrow \infty$. The issue, though, is that the previous behavior of δ was observed in $YTiO_3$ as well. Further, the value of 1.025 is much too small for any model, mean field giving the smallest at $\delta = 3$. Failure to provide an appropriate value of δ does not preclude the possibility of scaling, though. As such, scaling was attempted for the μ data in $CeAgSb_2$. The results of the 3-D Heisenberg scaling are presented in Fig. 3.16 for three different fields. As there is no characteristic field derivable from this data, no field correction like what was done in Sec. 3.3 can be attempted.

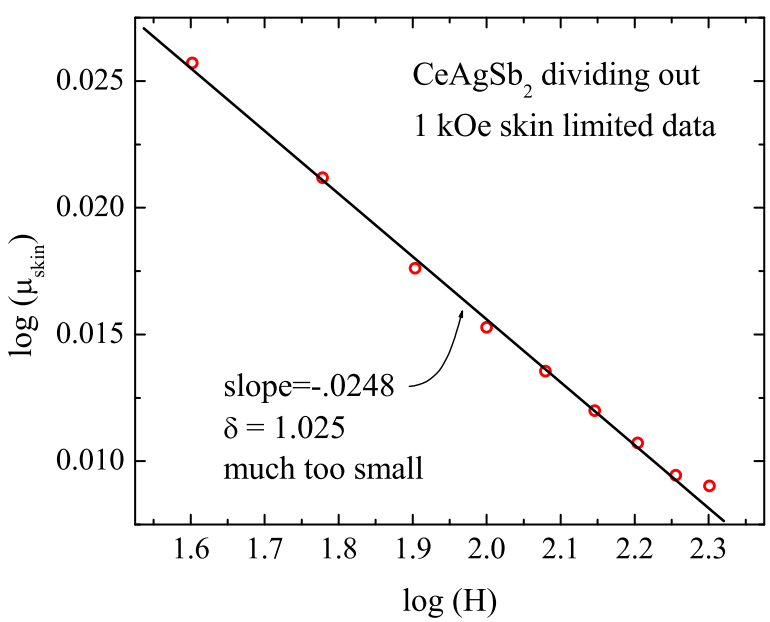

Figure 3.15 $\text{Log}(\mu_{peak})$ vs. $\log(H)$ from the data presented in Fig. 3.14.

It is evident that the compensation of ρ results in better collapse of the data. However, the fact that both above and below T_C data follow precisely the same curve for a given field is

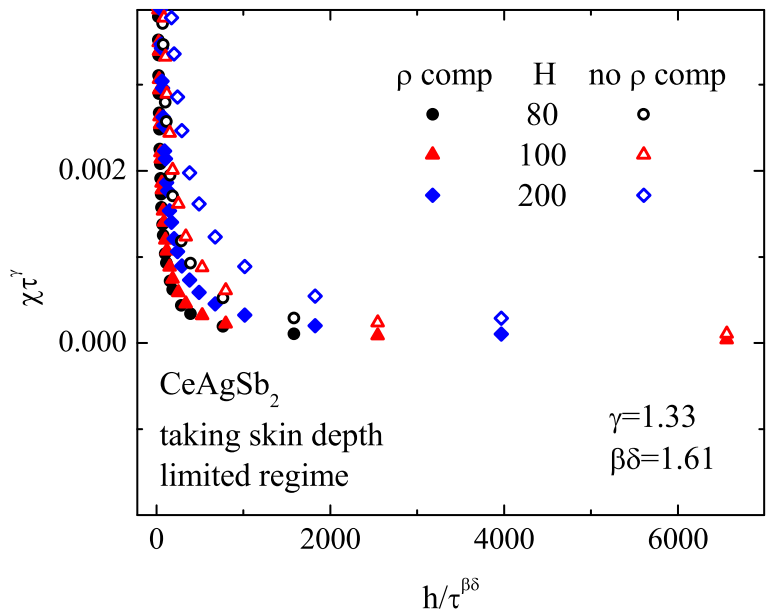

Figure 3.16 3-D Heisenberg scaling for μ data in $CeAgSb_2$. Solid symbols are for data with the resistivity contribution accounted for, while open symbols present data where ρ is still included.

troubling. In $YTiO_3$ the data above T_C curved down as temperature increased while the data below T_C curved up as temperature decreased. While the collapse of the data is quite nice with this method, it is unclear that the actual handling of the resistive component is better considering that the behavior of the scaled data far from T_C is dramatically different from the insulating compound.

It can be argued that since what was scaled was the relative permeability, while the scaling hypothesis deals with the susceptibility, the failure of the data to scale is due to a subtle mishandling of the analysis. It is apparent that the as derived μ (with ρ compensated for by division) is in SI units with the assumption that the 1 kOe run has the same ac spin susceptibility as vacuum. In principle this should be equivalent to the assumption that subtracting the high field data set from the lower fields adequately compensates for the resistivity while not affecting the spin susceptibility. If this is indeed the case, then it should be possible to convert the extracted permeability to susceptibility. The relation between μ and χ in SI units is $\chi = \mu - 1$. Taking this tack and converting μ to χ does change the results of critical scaling analysis (Fig. 3.17. However, that change amounts to reflecting the scaled μ data about the x-axis. Again the difference between these results and the insulating $YTiO_3$ is obvious and taken as evidence that this is not the correct way to handle the resistive contribution to the measured χ_{TDR}.

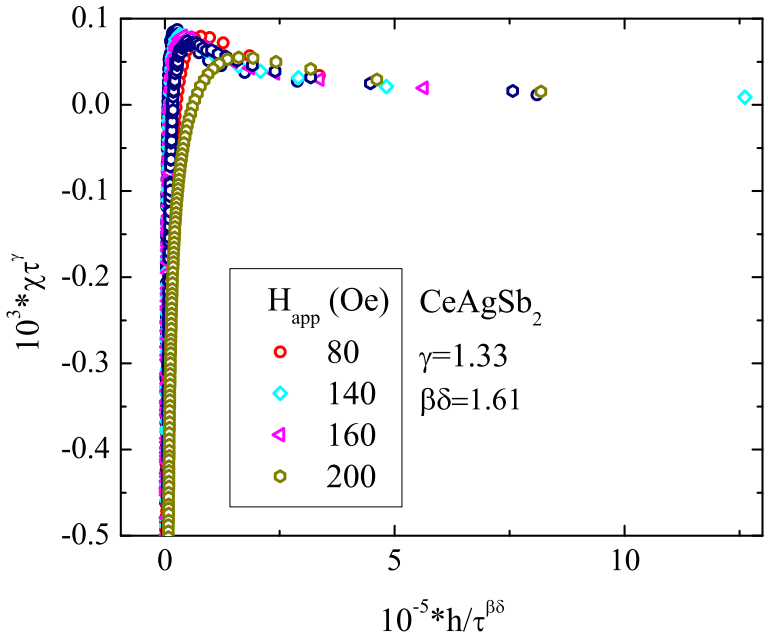

Figure 3.17 Scaled χ_{TDR} data for $CeAgSb_2$ after accounting for the resistive component.

3.6 Summary

The radio–frequency data collected via the TDR does not adhere to critical scaling analysis. Various attempts to account for the resistive component in metallic ferromagnets fail to produce scaled data that approximates the insulating $YTiO_3$ with the exception of a simple subtraction of measured χ_{TDR} vs. T data in fields large enough to suppress the peak associated with the phase transition. This suggests that the simple subtraction method is the most suitable way of dealing with the resistive component of the measured χ_{TDR}. Analysis of the peak in χ_{TDR} near T_C extracts a characteristic field H^*, the value of which depends on the measurement frequency. The frequency dependence of H^* implies that it may in fact be frequency taking on the roll of an applied field in suppressing the peak in χ_{TDR} at the phase transition. If this were the case then for fields larger than H^* a plot of $1/\chi_{max}$ vs. H_{app} should take on a curvature appropriate to the value of the critical exponent δ. That this is not observed suggests that if the finite frequency is acting as a field, then this frequency band may lie on the boundary between the static and dynamic regimes.

CHAPTER 4. Itinerant Ferromagnets

4.1 Introduction

In contrast to local moment ferromagnets, itinerant ferromagnets have a delocalized moment originating from their conduction band electrons. The fractional Bohr magneton moment of Ni and the discovery of ferromagnetism in $ZrZn_2$ [Matthias and Bozorth (1958)], of which neither constituent element displays magnetism, pushed the development of the theory of band ferromagnets.

Figure 4.1 compares temperature dependent static susceptibility for the local moment $CeAgSb_2$ with that for the itinerant $ZrZn_2$ as measured in a *Quantum Design* MPMS-5. Two different techniques were used to determine these susceptibilities. Panel (a) shows the usual χ_{static} where the magnetic moment is measured in a small applied field ($H = 20$ Oe) and M/H is calculated. This method is appropriate for temperatures well above T_C where magnetization is linearly dependent on field over a fairly large field range, it should be expected to fail in the ferromagnetic state because M is not necessarily linear in H all the way down to $H = 0$. Bearing this in mind, a delta measurement of χ_{static} was performed (results in panel (b)) as follows. Magnetic moment versus temperature was measured first in a 17 Oe field and then in a 22 Oe field. The difference in the resulting moment was divided by the 5 Oe difference in applied fields to determine $\Delta M/\Delta H$. The advantage of this method is that it only requires approximate linearity in $M(H)$ over the 5 Oe window defined by the upper and lower fields. Thus, it can be expected to approximate $\chi = \frac{dM}{dH}$ more closely. Obviously, a smaller H window is more likely to conform to the linear $M(H)$ approximation.

Whereas the delta measurement results in a lower susceptibility in both samples, both static techniques produce very similar $\chi(T)$ curves. This is to be contrasted with the results

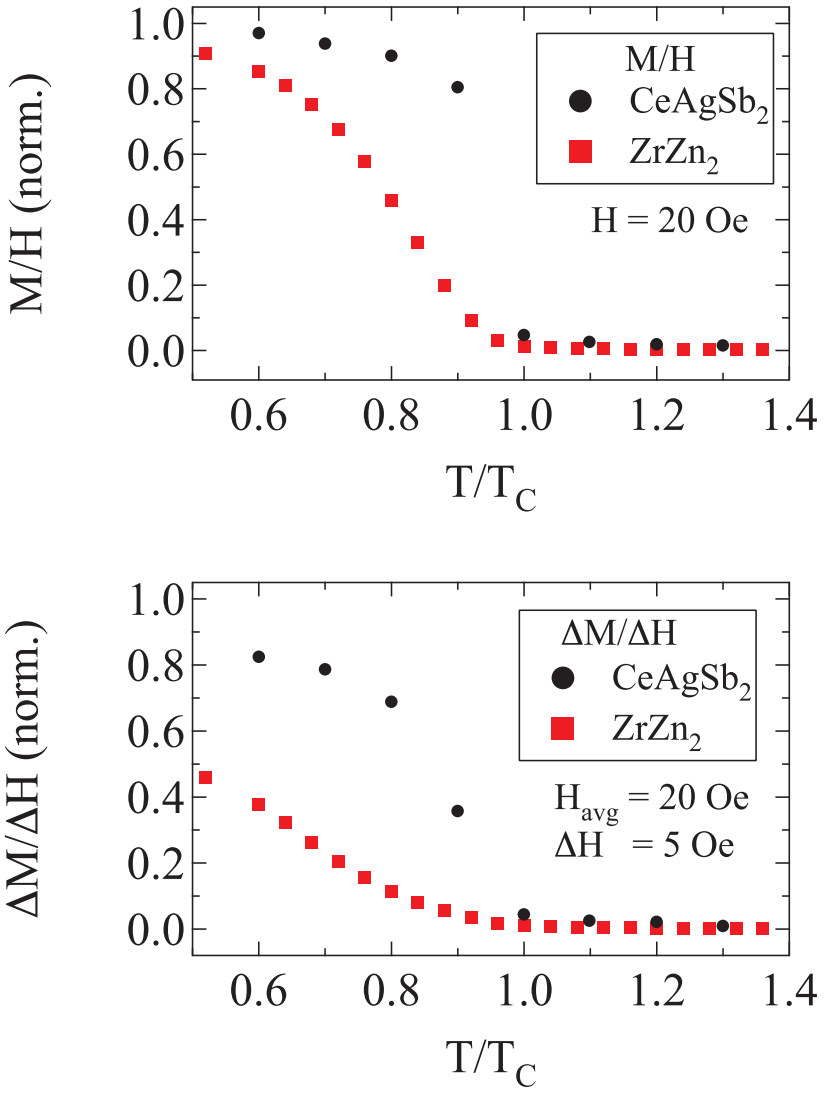

Figure 4.1 Comparison of two static measurements of magnetic susceptibility of $CeAgSb_2$ with $ZrZn_2$. Data are normalized to the M/H value for $CeAgSb_2$ at 5 K. T_C for $CeAgSb_2$ is approximately 9.8 K whereas for $ZrZn_2$ $T_C \approx 25$ K. Values of $M/H(T = 5\text{ K})$ for the two samples were $CeAgSb_2$. Static measurements do little to differentiate between the two types of ferromagnets.

of zero field radio frequency susceptibility versus temperature as shown in Fig. 4.2. Whereas the local moment system shows a sharp, well defined peak in χ_{TDR} at the Curie temperature, the itinerant system exhibits a broad maximum well below T_C.

The similarity in the static data in both systems is to be contrasted by the difference in the χ_{TDR} data in both systems. The sharp peak observed in χ_{TDR} in the local moment system is dramatically different from the static result, and more typical of ac susceptibility, albeit much sharper than what is seen in low frequency measurements. Contrary to this, χ_{TDR} in the itinerant system is qualitatively similar to that seen in the static case. The slow decay of χ_{TDR} below T_C in $ZrZn_2$ may even be explained as coming from a decrease in resistivity due to the decrease in T. This points to the possibility that the local moment system is in a dynamic measurement regime, and the itinerant is in a static measurement regime at these frequencies. Another argument for this may be made by considering the relaxation processes that might occur in these systems.

As local moment systems have their magnetic moments closely associated with particular ions in the lattice, it seems reasonable to assume these moments would have access to lattice vibrations, or phonons, as a method of dissipating energy. Conversely, in itinerant magnets the conduction band electrons are free to wander about the lattice, and therefore might be expected to interact less strongly with phonons. This may be important in this work because the spin–lattice interaction time scale is on the order of 10^{-3} s while the spin–spin interaction is on the order of 10^{-7} s. If spin–lattice interactions do dominate the local moment response, then these ferromagnets would be in a dynamic regime inasmuch as the system does not have adequate time to come to equilibrium with the probe field before that field changes. In a similar vein, if spin–spin interactions dominate the itinerant response then these ferromagnets would be in a static regime as the system has adequate time to come to equilibrium with the probe field before that field changes. This motivates a closer look at the theoretically predicted static response of itinerant magnets.

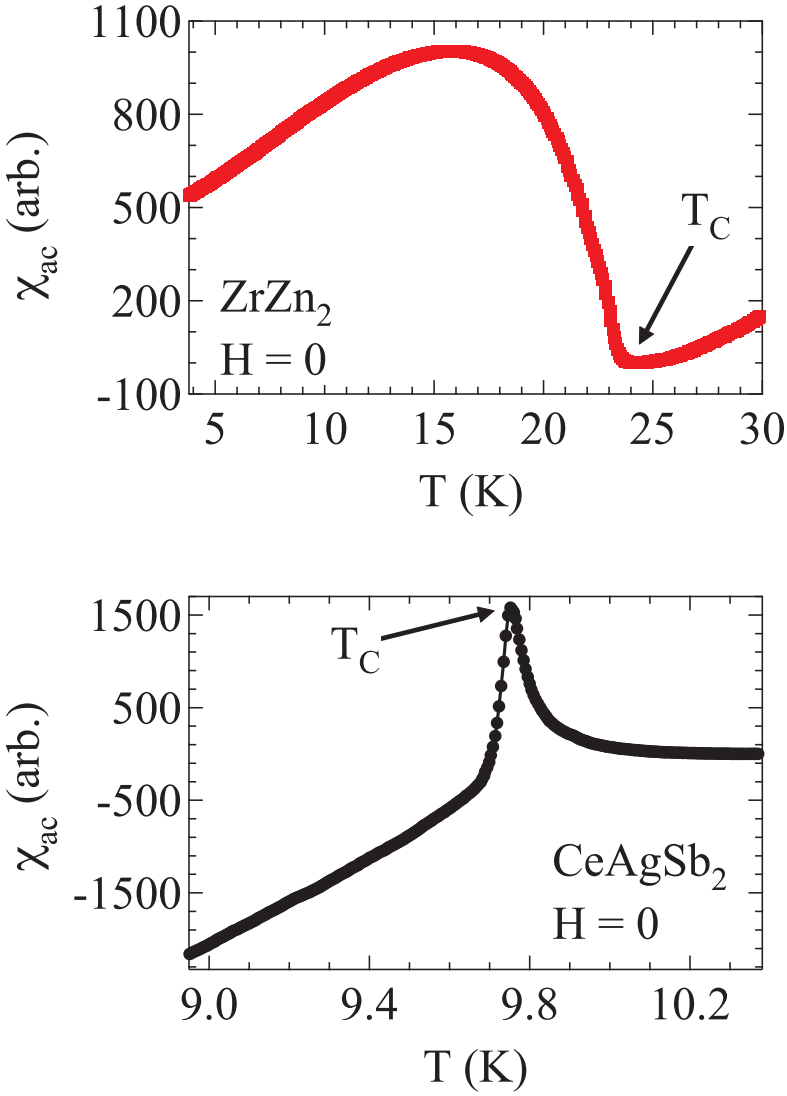

Figure 4.2 Comparison of the ac susceptibility of local moment $CeAgSb_2$ with itinerant $ZrZn_2$ in zero applied field. As was discussed in Chapter 2, the peak at T_C in $CeAgSb_2$ is associated with the critical fluctuations driven by the phase transition. The stark difference between the local and the itinerant response was the driving force behind this chapter.

4.2 Stoner Theory

The Stoner theory [Stoner (1938)] marked a major advancement in the understanding of itinerant electron magnetism. It offered, for the first time, a reasonable explanation for the fractional moment exhibited by certain ferromagnets, in particular nickel. Still, at the time there were recognized short-comings. Most glaring was the over-estimation of T_C and the lack of a Curie-Weiss type susceptibility seen in practically all ferromagnetic materials. The source of these problems lies in the total reliance on the Fermi function for the temperature dependence of the thermodynamic quantities. Still, despite its obvious flaws, the Stoner theory has become the basis for all major theoretical advancements in itinerant magnetism. This theory is a mean field approach to magnetic order. The main difference between the itinerant Stoner theory and the local moment Weiss theory begins with the Weiss assumption that the electrons are localized and occupy atomic m_J dependent energy levels. The Stoner theory considers the electrons to be delocalized, moving about in the periodic potential of the crystal lattice as part of the conduction band. The crystal fields quench the orbital moment of the conduction electrons and the good quantum numbers include the $\mathbf{k}$ and the spin.

Stoner theory is based on three postulates: 1) the magnetic carriers are unsaturated spins in the d-band, 2) effects of the exchange are treated in a mean field way, and 3) Fermi statistics must be followed. A simple explanation of the Stoner theory can be offered by considering a parabolic conduction band. The band can be split into two subbands each containing only one type of spin. If a mean field which incorporates all interactions is introduced, the strength per atom is given by

$$H_M = NM = NM_0\varphi \tag{4.1}$$

where $\varphi = M/M_0$, and M_0 is the satuartion magnetization of the material. Thus, φ is a measure of the magnetization of the sample. The energy shift due to the mean field is

$$\epsilon_m = -\mu_B H_M = -\mu_B N M_0 \varphi = -k_B \Theta \varphi. \tag{4.2}$$

This defines a temperature, Θ, which is characteristic of the material and equal to $\mu_B N M_0/k_B$. $k_B\Theta$ is a measure of the onsite electron–electron repulsion in the material. Realizing that the

field can be expressed as dF/dM allows the free energy contribution per electron of the mean field at $T = 0$ K (E_m/n) to be determined.

$$\frac{E_m}{n} = -\int HdM = -\frac{1}{2}k_B\Theta\varphi^2 \tag{4.3}$$

This is the energy reduction induced by polarizing the conduction band electrons. The different spin subbands are now split relative to one another. Due to the need to have an equal chemical potential for both spin directions (as they are in the same metal) causes the subband with a moment parallel to the applied field to have a larger population. Defining n^+ and n^- as the parallel and antiparallel moment populations respectively the following relations exist.

$$n^+ + n^- = n \tag{4.4}$$

$$n\varphi = n^+ - n^- \tag{4.5}$$

$$n^\pm = \frac{n}{2}\left(1 \pm \varphi\right) \tag{4.6}$$

The populations are given by

$$\frac{n}{2} = \int_0^{\epsilon_F} g\left(\epsilon\right) d\epsilon \tag{4.7}$$

$$\frac{n}{2}\left(1 \pm \varphi\right) = \int_0^{\epsilon^\pm} g(\epsilon)d\epsilon \tag{4.8}$$

The previous equation can be rewritten as two integrals

$$\frac{n}{2}\varphi = \int_{\epsilon_F}^{\epsilon^+} g(\epsilon)d\epsilon \tag{4.9}$$

and

$$\frac{n}{2}\varphi = \int_{\epsilon^-}^{\epsilon_F} g(\epsilon)d\epsilon \tag{4.10}$$

with the use of Eq. 4.7. In the parabolic band the density of states, $g(\epsilon)$, varies like $\sqrt{\epsilon}$ and the energy of the spin splitting is given by

$$\epsilon^\pm = \epsilon_F(1 \pm \varphi)^{2/3}. \tag{4.11}$$

The band energy change due to this splitting can be determined by integrating over occupied states to give

$$E_b = \int_{\epsilon_F}^{\epsilon^+} \epsilon g(\epsilon)d\epsilon - \int_{\epsilon^-}^{\epsilon_F} \epsilon g(\epsilon)d\epsilon. \tag{4.12}$$

If $\epsilon^{\pm}$ is given by Eqs. 4.9-4.11 then

$$E_b = \frac{3}{10} n\epsilon_F \left[(1+\varphi)^{5/3} + (1-\varphi)^{5/3} \right]. \tag{4.13}$$

This is the increase in energy caused by polarizing the conduction band electrons. Since the electrons are fermions, the polarization requires a promotion of antiparallel moments to the unoccupied, higher energies so that they may switch to a parallel orientation. The free energy is now given by

$$E = E_b + E_m = E(\varphi) = \frac{3}{10} n\epsilon_F \left[(1+\varphi)^{5/3} - (1-\varphi)^{5/3} \right] - \frac{1}{2} k_B \Theta \varphi^2 + E_0. \tag{4.14}$$

E_0 contains all other terms in the free energy not explicitly related to the mean field effects. An extremum for Eq. 4.14 is found by setting $dE(\varphi)/d\varphi$ equal to 0. Doing this gives

$$\epsilon^+ - \epsilon^- = 2k_B\Theta\varphi = \Delta E \tag{4.15}$$

ΔE is the band splitting, also referred to as the Stoner gap energy. It is the energy introduced by the mean field. The two extreme situations are $\varphi \to 0$ and $\varphi \to 1$. Combining Eqs. 4.11 and 4.15 the two limits on the magnetization can be explored.

$$\varphi = 0 \Rightarrow \frac{k_B\Theta}{\epsilon_F} = \frac{2}{3} \tag{4.16}$$

$$\varphi = 1 \Rightarrow \frac{k_B\Theta}{\epsilon_F} = \frac{1}{\sqrt[3]{2}} \tag{4.17}$$

These two results define three ranges of magnetic order. For the lower threshold where $\frac{k_B\Theta}{\epsilon_F} < \frac{2}{3}$ no magnetic order exists. This is the case for palladium. The intermediate range where $\frac{2}{3} < \frac{k_B\Theta}{\epsilon_F} < \frac{1}{\sqrt[3]{2}}$ there is magnetic order but the exchange is insufficient to saturate the spins and the system is weakly ferromagnetic. This corresponds to $ZrZn_2$. In the upper bound, for $\frac{k_B\Theta}{\epsilon_F} = \frac{1}{\sqrt[3]{2}}$, the system is strongly ferromagnetic as is the case for Ni.

Based on the free energy it is possible to calculate the inverse susceptibility $(1/\chi)$ as the second derivative of Eq. 4.14 with respect to φ. Doing so gives

$$\frac{n^2\mu_B^2}{\chi} = \frac{n^2}{4}\left(\frac{1}{g(\epsilon^+)} + \frac{1}{g(\epsilon^-)} \right) - nk_B\Theta. \tag{4.18}$$

If the free energy is to be a minimum, Eq. 4.18 must be positive which helps provide a criterion for spontaneous magnetic order. When $\varphi = 0$ the free energy must have a maximum so that as φ increases $E(\varphi)$ decreases and the moment bearing state is favored. In the non-magnetic case it is obvious that $g(\epsilon^+) = g(\epsilon^-) = g(\epsilon_F)$. As the spontaneous moment increases the inverse susceptibility must decrease. This gives rise to the so-called Stoner criterion for spontaneous magnetism

$$\frac{2}{n} g(\epsilon_F) k_B \Theta \geq 1. \tag{4.19}$$

In order to satisfy the Stoner criterion a system needs to have either a large density of states at the Fermi energy or a large interaction term, $k_B\Theta$. It turns out that the interaction term is an atomic property and is largely unaffected by chemistry, so the density of states in the metal is the dominant mechanism by which Eq. 4.19 is met. In practice a parabolic, free-electron like band will never have a density of states large enough for this to happen, so that assumption will have to be abandoned.

To determine the temperature dependence of the magnetization and the susceptibility the populations of the two subbands is written as

$$n^{\pm} = \int_0^{\infty} \frac{g(\epsilon)}{\exp\left(\frac{\epsilon - \eta^{\pm}}{k_B T}\right) + 1} d\epsilon \tag{4.20}$$

where $\eta^{\pm}$ is the sum of the chemical potential, interaction energy, and Zeeman energy from an externally applied field.

$$\eta^{\pm} = \mu \pm k_B \Theta \varphi \pm \mu_B H_{ext} \tag{4.21}$$

Combining Eqs. 4.6 and 4.20 allows for the calculation of the magnetization M given by

$$M = n \mu_B \varphi. \tag{4.22}$$

Doing this gives a magnetic moment of

$$M = 2\mu_B \left(\mu_B H_{ext} + k_B \Theta \frac{M}{n \mu_B} \right) \int_0^{\infty} g(\epsilon) \left| \frac{df(\epsilon)}{d\epsilon} \right| d\epsilon \tag{4.23}$$

with $f(\epsilon)$ being the Fermi function. This can be rather simply solved for M explicitly to give

$$M = \frac{2\mu_B^2 H_{ext} \int_0^{\infty} g(\epsilon) \left| \frac{df(\epsilon)}{d\epsilon} \right| d\epsilon}{1 - \frac{2k_B\Theta}{n}) \int_0^{\infty} g(\epsilon) \left| \frac{df(\epsilon)}{d\epsilon} \right| d\epsilon} \tag{4.24}$$

The (static, zero field limit) susceptibility can be found by taking $\chi = M/H_{ext}$. This gives

$$\chi = \frac{2\mu_B^2 \int_0^\infty g(\epsilon) \left|\frac{df(\epsilon)}{d\epsilon}\right| d\epsilon}{1 - \frac{2k_B\Theta}{n} \int_0^\infty g(\epsilon) \left|\frac{df(\epsilon)}{d\epsilon}\right| d\epsilon}. \tag{4.25}$$

The condition for spontaneous ferromagnetism is that the inverse susceptibility go to zero at a finite temperature. This condition is met when

$$\frac{2k_B\Theta}{n} \int_0^\infty g(\epsilon) \left|\frac{df(\epsilon)}{d\epsilon}\right| d\epsilon = 1. \tag{4.26}$$

The temperature dependence implied by the above equation is given by

$$2g(\epsilon_F)\frac{k_B\Theta}{n}(1 + aT_C^2) = 1. \tag{4.27}$$

The coefficient a is related to the characteristic Fermi dengeneracy temperature and is given by

$$a = \frac{\pi^2}{6}k_B^2 \left(\frac{g(\epsilon_F)''}{g(\epsilon_F)} - \left(\frac{g(\epsilon_F)'}{g(\epsilon_F)}\right)^2\right) \tag{4.28}$$

which comes from the Sommerfield expansion. If $T_C << T_F$ then Eq. 4.27 can be expressed as

$$k_B\Theta = \frac{n}{2g(\epsilon_F)}\left(1 + \frac{T_C^2}{T_F^2}\right). \tag{4.29}$$

To determine the behavior of the magnetization as temperature is varied the susceptibility from Eq. 4.18 is revisited and another Sommerfield expansion is done to pull out a magnetization dependence in χ.

$$\frac{n^2\mu_B^2}{\chi} = \frac{n^2}{2g(\epsilon_F)}\left(1 - c\varphi^2\right) - nk_B\Theta \tag{4.30}$$

The coefficient c is given by

$$c = \frac{1}{8}\frac{n^2}{g(\epsilon_F)^2}\left[\frac{g(\epsilon_F)''}{g(\epsilon_F)} - 3\left(\frac{g(\epsilon_F)'}{g(\epsilon_F)}\right)^2\right]. \tag{4.31}$$

For equilibrium

$$k_B\Theta = \frac{n}{2g(\epsilon_F)}\left(1 - \frac{1}{3}c\varphi^2\right). \tag{4.32}$$

If there is a minimum in χ for zero moment, then as the moment grows

$$\frac{2}{n}g(\epsilon_F)k_B\Theta \leq 1 - \frac{1}{3}c\varphi^2. \tag{4.33}$$

A negative value of c fulfills this condition for all values of φ. This occurs when the Fermi energy is at a maximum in the density of states. Under this umbrella

$$k_B\Theta = \frac{n}{2g(\epsilon_F)}\left(1 + \frac{1}{3}|c|\varphi^2\right) \tag{4.34}$$

Equating similar terms in Eqs. 4.29 and 4.34 allows for a determination of how the Curie temperature scales with magnetization. Equating like terms from both expressions gives

$$\varphi^2 = \frac{3}{|c|}\frac{T_C^2}{T_F^2} \tag{4.35}$$

This shows that in the Stoner model the Curie temperature scales linearly with the magnetization, and it is expected that systems with larger magnetizations will have higher Curie temperatures.

In the case of very weak itinerant ferromagnets ($0 < \varphi << 1$) it is possible to expand Eq. 4.20 in powers of φ. To first order at zero temperature this gives

$$\frac{2}{n}g(\epsilon_F)\left(k_B\Theta\varphi + \mu_B H_{ext}\right) = \varphi \tag{4.36}$$

Using the temperature dependencies of the coefficients a and c to substitute for the $T = 0$ value of φ leads to

$$\frac{2}{n}g(\epsilon_F)\left(k_B\Theta\varphi + \mu_B H_{ext}\right) = \varphi(1 - aT^2) - \frac{1}{3}c\varphi^3. \tag{4.37}$$

When c and a are both positive and using Eq. 4.35 where $a = T_F^2$ yields

$$\frac{2}{n}g(\epsilon_F)k_B\Theta\varphi = 1 + \frac{1}{3}|c|\varphi^3, \tag{4.38}$$

$$|a|T_C^2 = \frac{1}{3}|c|\varphi_0^3, \tag{4.39}$$

and

$$\chi_0 = \frac{3\mu_B^2 g(\epsilon_F)}{|c|\varphi_0^2}. \tag{4.40}$$

Substituting Eq. 4.22 for φ_0 the magnetic isotherms for weak itinerant systems take the form

$$\left(\frac{M(H,T)}{M(0,0)}\right)^3 - \frac{M(H,T)}{M(0,0)}\left(1 - \frac{T^2}{T_C^2}\right) = \frac{2\chi_0 H}{M(0,0)}. \tag{4.41}$$

In zero applied field the square of the magnetization is seen to decrease like T^2 as the temperature is increased.

$$M^2 = M(0,0)^2 \left(1 - \frac{T^2}{T_C^2}\right) \tag{4.42}$$

Rewriting Eq. 4.41 and taking dH/dM as the inverse susceptibility it is seen that

$$\frac{1}{\chi} = \frac{3M^2}{2\chi_0 M_0^2} - \frac{1}{2\chi_0}\left(1 - \frac{T^2}{T_C^2}\right). \tag{4.43}$$

For the paramagnetic case, the magnetization vanishes and

$$\chi = 2\chi_0 \left(\frac{T^2}{T_C^2} - 1\right)^{-1}. \tag{4.44}$$

This expression is sometimes written as

$$\chi = \frac{\chi_P}{1 - Z} \tag{4.45}$$

where χ_P is the Pauli paramagnetism and Z is the Stoner enhancement factor. The Stoner condition, i. e. $\varphi > 0$, may be expressed as $Z = 1$ when casting the susceptibility in this form. In the ferromagnetic case the temperature dependence of M must be considered. Doing this shows that the susceptibility in the ordered state varies like

$$\chi = \chi_0 \left(1 - \frac{T^2}{T_C^2}\right)^{-1}. \tag{4.46}$$

The factor of 2 reduction in the susceptibility in the ordered state when compared with the paramagnetic state is a reflection of the assumption that above T_C the magnetic moment vanishes completely. An applied field can be considered to create spins from a vacuum in the paramagnetic state. Below T_C, however, the field must flip a spin from (-) to (+) to induce a change in the moment.

4.3 Spin Fluctuations

The origin of the shortcomings in the Stoner model is its neglect of collective excitations. The only mechanism by which the magnetic moment can be destroyed is through single particle spin flips across the Stoner gap. As was seen in the previous section, in order to account for

the observed magnetization the resulting gap implies a very large Curie temperature. An attempt to rectify this problem is to try to consider how very low energy excitations in the magnetization might be accommodated, much like spin waves in local moments. The newly inherited problem is that without a lattice of moments it is much more difficult to establish the waves. To sidestep this problem and assumption of fluctuations of the spin density is made. It was first applied to itinerant ferromagnets by Moriya and Kawabata (1973). A particularly clear derivation of spin fluctuations is provided in Mohn (2003) which is followed here.

One definition of equilibrium is that the physical quantities which characterize the equilibrium are always very close to their average value. An alternative definition of an equilibrium state is one in which the entropy, S, is maximized. The probability of a given macrostate being realized may be written as

$$p(z) = Ae^{S(z)} \tag{4.47}$$

where z represents a quantity that characterizes the equilibrium and A is a constant. A constraint on z is that it must not be forced constant by a conservation law. Taking the equilibrium condition on z to be $z =< z >= 0$, if entropy is to be a maximum then

$$\frac{\partial S(z)}{\partial z} = 0 \tag{4.48}$$

and

$$\frac{\partial^2 S(z)}{\partial z^2} < 0. \tag{4.49}$$

With small z and the above two conditions on the first and second derivatives a Taylor expansion of S may be carried out and, up to second order

$$S(z) = S(0) - \frac{\nu}{2}z^2. \tag{4.50}$$

This implies, with Eq. 4.47, that

$$p(z)dz = Ae^{-\nu z^2/2}dz. \tag{4.51}$$

A may be calculated by requiring that $\int p(z)dz = 1$, that is the probability that the system is in some state is 1. Realizing that the probability is only significant for small values of z allows

the integral to be evaluated over the range $-\infty$ to $+\infty$. Carrying out this integral gives

$$A = \left(\frac{\nu}{2\pi}\right)^{\frac{1}{2}} \tag{4.52}$$

Therefore, Eq. 4.51 is now given by

$$p(z)dz = \left(\frac{\nu}{2\pi}\right)^{\frac{1}{2}} e^{-\nu z^2/2} dz. \tag{4.53}$$

This is a Gaussian distribution with a maximum a $z = 0$. With k equal to an integer

$$\left\langle z^{2k} \right\rangle = \left(\frac{\nu}{2\pi}\right)^{\frac{1}{2}} \int_{-\infty}^{+\infty} z^{2k} e^{\nu z^2/2} dz = \nu^{-k} (2k-1)!!. \tag{4.54}$$

This means that $\langle z^2 \rangle = \nu^{-1}$ and $\langle z^4 \rangle = 3\nu^{-2} = 3 \langle z^2 \rangle^2$, and all even higher order average can be expressed in terms of $\langle z^2 \rangle$. Armed with this knowledge, the fluctuations of the magnetic moment may now be explored.

Within a Landau theory of magnetic phase transitions the free energy can be written as

$$F = aM^2 + \frac{b}{2}M^4 \tag{4.55}$$

where $a = -\frac{1}{\chi_0}\left(1 - \frac{T^2}{T_C^2}\right)$ and $b = \frac{1}{\chi_0 M_0}$ recalling the Stoner result. It should also be noted that within the Stoner framework T_C is of the order of 10^3 K. This leads to a neglect of the temperature dependence of the a term. As in the local moment case, by symmetry only even powers of the magnetization may appear, and M is often treated as a scalar quantity. However, the inclusion of fluctuations requires that attention be given to the vector nature of both $\mathbf{M}$ and its fluctuations. Still, due to symmetry considerations the volume integral over odd powers in the fluctuations vanishes always. Setting $\mathbf{m}(r)$ as the locally fluctuating moment it is assumed

$$\frac{1}{V}\int (\mathbf{m}(r))^n \, dV = (m^n) \text{ for } n = 2k \tag{4.56}$$

while it is zero for $n = 2k + 1$.

For M pointing along some axis there will be two fluctuation directions perpendicular to and one along M. If M is taken parallel to the z-axis the three fluctuations may be written as $m_1 = m_x$, $m_2 = m_y$, and $m_3 = m_z$. The original order parameter in the free energy

(Eq. 4.55) can be replaced by the statistical average of the new order parameter, including the fluctuations.

$$\mathbf{M}^{2n} \rightarrow \left\langle \left(\mathbf{M} + \sum_{i=1}^{3} \mathbf{m}_i \right)^{2n} \right\rangle \tag{4.57}$$

Making this substitution, expanding, and setting the odd powers to zero gives

$$F = a\left(M^2 + 2\left\langle m_\perp^2 \right\rangle + \left\langle m_{||}^2 \right\rangle\right) + \frac{b}{2}\left(M^4 + M^2\left(6\left\langle m_{||}^2 \right\rangle + 4\left\langle m_\perp^2 \right\rangle\right) + 8\left\langle m_\perp^2 \right\rangle + 3\left\langle m_{||}^2 \right\rangle + 4\left\langle m_\perp^2 \right\rangle\left\langle m_{||}^2 \right\rangle\right) \tag{4.58}$$

In the above $m_\perp$ and $m_{||}$ denote the fluctuations perpendicular and parallel to M, respectively. In the limit of zero temperature the fluctuation amplitude is zero and this reduces to Eq. 4.55. Also, the dynamics of the fluctuations scale with the static susceptibility through the coefficients a and b. Keeping with the Landau theory of phase transitions, the Curie temperature corresponds to the temperature at which the susceptibility diverges (or the inverse susceptibility is zero). There is the additional constraint that $M = 0$ which implies there is no longer a difference between $\langle m_\perp^2 \rangle$ and $\left\langle m_{||}^2 \right\rangle$. The inverse susceptibility is calculated by $\chi^{-1} = \frac{\partial^2 F}{\partial M^2}$ with $M = 0$ giving

$$\chi^{-1} = 2a + 2b \times 10\left\langle m^2 \right\rangle = 0. \tag{4.59}$$

In the above, $T = T_C$ and $\langle m^2 \rangle$ is the fluctuation amplitude, keeping in mind that there is no preferred direction if the system is not ordered. At the Curie point the magnitude of the fluctuations is given by

$$\left\langle m_C^2 \right\rangle = \frac{M_0^2}{5} \tag{4.60}$$

Therefore, the amplitude of the fluctuations at the Curie temperature ($\langle m_C^2 \rangle$) is determined by ground state properties. Coupling Eq. 4.60 with the idea that the fluctuations must disappear for $T = 0$ the temperature dependence of the fluctuations can be determined. From the fluctuation-dissipation theorem classical fluctuations basically change linearly with temperature. Thus,

$$\left\langle m_{||}^2 \right\rangle (T) = \left\langle m_\perp^2 \right\rangle (T) \simeq \left\langle m_C^2 \right\rangle \frac{T}{T_C} = \frac{M_0^2}{5}\frac{T}{T_C} \tag{4.61}$$

is the approximate temperature variation in an isotropic system. From Eq. 4.58 $M(T)$ can be calculated directly by minimizing the free energy with respect to the magnetization. Setting

$\partial F/\partial M = 0$ and substituting the expressions for a and b given just after Eq. 4.55 gives

$$M^2 = M_0^2 - 3\left\langle m_{||}^2 \right\rangle + 2\left\langle m_{\perp}^2 \right\rangle. \tag{4.62}$$

If an isotropic system is assumed (Eq. 4.61) the resulting magnetization variation with temperature is

$$M^2(T) = M_0^2\left(1 - \frac{T}{T_C}\right). \tag{4.63}$$

The more rapid decrease in M as T increases when compared with the Stoner result derives from the consideration of low energy excitations.

Examining the temperature behavior of the order parameter defined in Eq. 4.57 shows another positive feature associated with these spin density fluctuations.

$$\left\langle \left(\mathbf{M} + \sum_{i=1}^{3} \mathbf{m}_i\right)^2 \right\rangle = M_0^2\left(1 - \frac{T}{T_C}\right) + 2\left\langle m_{\perp}^2 \right\rangle + \left\langle m_{||}^2 \right\rangle. \tag{4.64}$$

For temperatures less than T_C (in an isotropic system) this gives

$$M_0^2\left(1 - \frac{2}{5}\frac{T}{T_C}\right) \tag{4.65}$$

as the order parameter variation with temperature. For temperatures greater than T_C the right hand side of Eq. 4.64 is

$$M_0^2\frac{3}{5}\frac{T}{T_C}. \tag{4.66}$$

This last result shows that even in the paramagnetic state, the order parameter is locally non-zero even though globally it averages to zero. This recalls a Curie-Wiess-like behavior for $T > T_C$, which is commonly observed for many itinerant ferromagnets. This stands opposed to the Stoner result where the paramagnetic state is completely non-magnetic (other than as a usual metal).

From Eq. 4.59 it is possible to now determine an approximate temperature dependence for the susceptibility both above and below the ordering temperature.

$$\chi(T) = \chi_0\left(1 - \frac{T}{T_C}\right)^{-1} \text{ for } T \approx T_C, \tag{4.67}$$

$$\chi(T) = 2\chi_0\left(\frac{T}{T_C} - 1\right)^{-1} \text{ for } T \geq T_C. \tag{4.68}$$

A Curie constant can be extracted from this result as well which is

$$C = \frac{d\left(\chi^{-1}\right)}{dT} = \frac{1}{2\chi_0 T_C}. \tag{4.69}$$

This is seen not to vary with temperature as it did in the Stoner model. Therefore, it reproduces the linear behavior observed in χ^{-1} vs. T in the paramagnetic state.

The preceding work was developed for weakly ferromagnetic systems. Lonzarich and Taillefer (1985) extended this work to stronger ferromagnets and showed that in between the Stoner and spin fluctuations limits there is an intermediate strength where the temperature variation of the inverse susceptibility is like $T^{4/3}$ just below T_C. In all cases, though, the static magnetic susceptibility decreases as temperature decreases. This is in direct opposition to the experimentally observed results in the TDR data, indicating that, dispite the qualitative agreement between χ_{static} and χ_{TDR} in $ZrZn_2$, this material is not in a static regime at frequencies of a few 10's of megahertz.

4.4 Semi-Phenomenological Model of Itinerant Ferromagnets

The development of the Stoner theory [Stoner (1938)] was driven by a desire to understand how a fractional Bohr magneton magnetic moment could be created in nickel. The failures of Stoner theory, *i.e.* Curie temperatures that are too high and the lack of a Curie-Weiss susceptibility above T_C, were impetus for the development of the spin fluctuation theory of Moriya and Kawabata [Moriya and Kawabata (1973)]. Whereas spin fluctuation theory does predict a Curie-Weiss type paramagnetic state and largely correct the Curie temperatures, neither it nor the Stoner theory adequately describe the broad maximum seen in the rf data. Indeed, both theories derive a strictly zero field limit of χ just below T_C of the same form

$$\chi(T < T_C) = \chi_0 \left(1 - \left(\frac{T}{T_C}\right)^n\right)^{-1}. \tag{4.70}$$

The difference between the two theories is the value of n. For Stoner theory $n = 2$ while for spin fluctuations $n = 1$ [Mohn (2003)]. There is an intermediate regime where $n = 4/3$ [Lonzarich and Taillefer (1985)]. The Stoner theory does predict a nonzero χ at $T = 0$ and $H = 0$ [Wohlfarth (1968)].

A zero field limit calculation, however, is not representative of a ferromagnetic system below T_C. As the system begins to order there is a non-zero field in the sample from the ordered moments themselves. It is interesting that this internal field, which has been incorporated into the theory to account for the ordering is neglected in calculations of the magnetic susceptibility. In itinerant systems this mean field should continue to increase as T decreases and the fraction of spin polarized conduction electrons increases. To account for the self–field a modified Brillouin function for a spin-1/2 system in a magnetic field is proposed in Eq. 4.71 [Vannette and Prozorov (2008)]. A spin-1/2 system is chosen because in itinerant systems it is the single electron spin that is of interest.

$$m^*(t,h) = m_0^* \tanh \frac{h}{1-t^n}. \tag{4.71}$$

In the above equation, $t = \frac{T}{T^*}$ where T^* is a characteristic temperature not necessarily equal to T_C and h is a dimensionless field term. It should be noted that this form does not represent the magnetization of the sample. Rather, m^* may be taken as some measure of the unpolarized fraction of the conduction band. Differentiating with respect to h gives

$$\chi(t,h) = \frac{\chi_0}{1-t^n} \cosh^{-2} \frac{h}{1-t^n}. \tag{4.72}$$

In the limit $h \to 0$, this reduces to Eq. 4.70 if $T^* \to T_C$, even though we are not beginning with the proper form for the magnetization.

Figure 4.3 presents the calculated curves for m^* from Eq. 4.71, $1-m^*$, and χ from Eq. 4.72. The observed behavior of $1-m^*$ is qualitatively similar to the expected magnetization versus temperature curve. The susceptibility curve shows the basic features seen in the TDR data in the itinerant systems, as presented below.

As a test of the validity of the premise on which the proposed model is based, i. e. that the TDR measures the fluctuating component of the band magnetism, measurements on YFe_2Zn_{20} and YCo_2Zn_{20} were made. These compounds are part of the RT_2Zn_{20} family, some of which show extreme Stoner enhancement of the conduction band. Jia et al. (2007) showed that YFe_2Zn_{20} has a Stoner Z approaching the ferromagnetic limit while YCo_2Zn_{20} has a

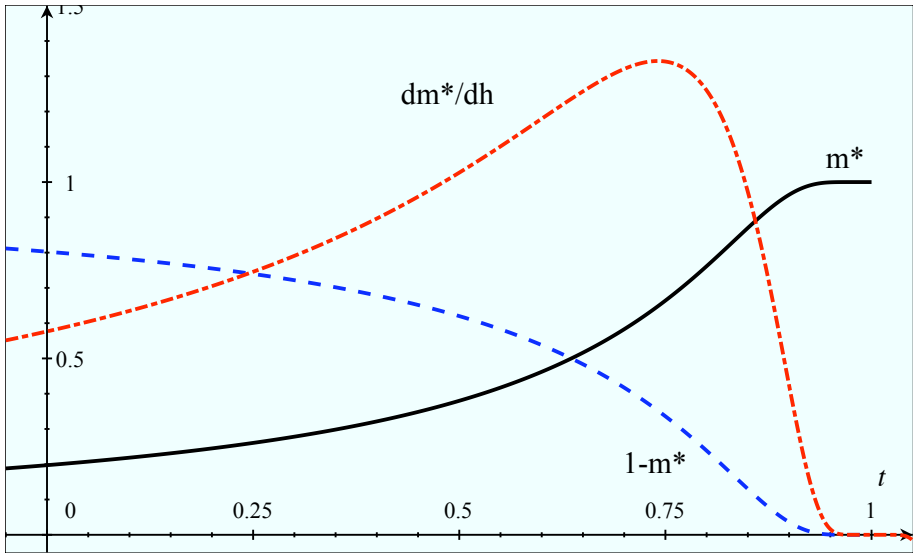

Figure 4.3 Calculation of m^* (solid line), $1-m^*$ (dashed line) and dm^*/dh (dotted-dashed line) for $h = 0.2$, $m_0 = 1$, and $n = 1$ plotted against t.

Z closer to that of copper. The small Z found in the cobalt compound suggests that TDR measurements of χ_{TDR} from YCo_2Zn_{20} should show a resistive signal, whereas the large Z in YFe_2Zn_{20} suggests that TDR measurements of χ_{TDR} should be resistive, with an enhancement due to the large fluctuations associated with proximity to ferromagnetic order. In order to facilitate a more accurate comparison between the two materials, samples of similar size and shape leading to similar filling factors were used. Figure 4.4 shows the measured change in susceptibility relative to 2 K for YCo_2Zn_{20} and YFe_2Zn_{20}. Both samples show a monotonic increase in χ_{TDR} consistent with the resistive behavior [Jia (2008)]. The inset to Fig. 4.4 shows the measured absolute change in χ_{TDR} for the same two samples.

Both samples exhibit a diamagnetic χ_{TDR} from 2–50 K. The observed susceptibility of YFe_2Zn_{20} is larger than that of YCo_2Zn_{20} by more than a factor of 4 over the entire temperature range. A fraction of the differences in χ_{TDR} between the two compounds may be accounted for by the different resistivities of each. From 2–300 K YCo_2Zn_{20} has a lower value of ρ than YFe_2Zn_{20}. At 50 K the resistivity of YFe_2Zn_{20} is approximately 10 $\mu\Omega$–cm while YCo_2Zn_{20} has

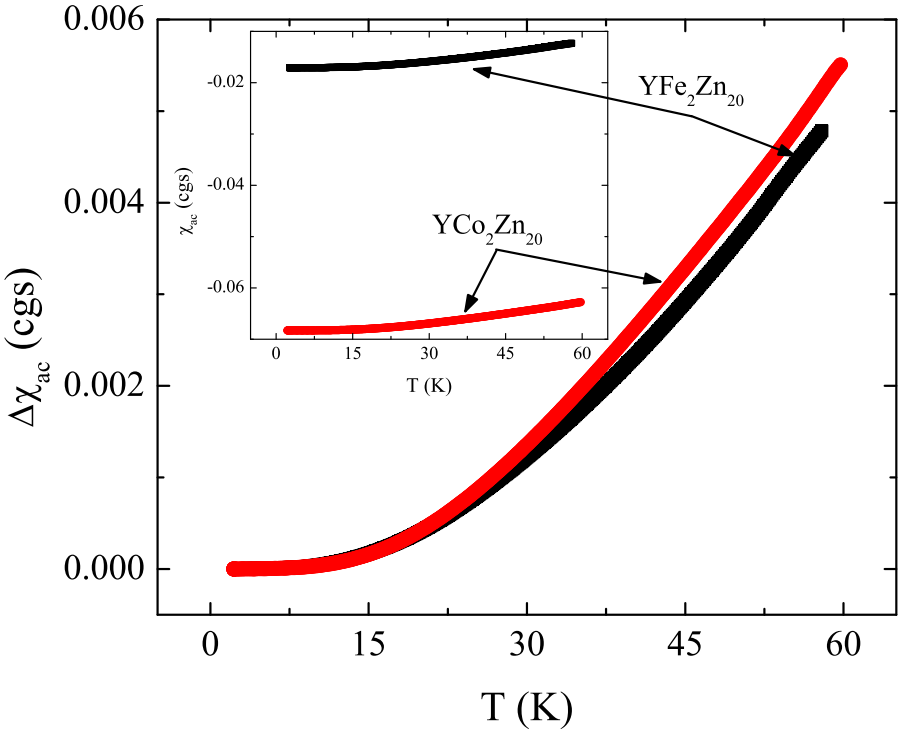

Figure 4.4 *Main panel*: Change in measured susceptibility for YFe_2Zn_{20} and YCo_2Zn_{20}. *Inset*: Measured susceptibility for the same two compounds on an absolute scale.

a resistivity of approximately 7 $\mu\Omega$–cm. The difference in ρ between the two samples decreases with decreasing temperature [Jia (2008)]. Based on these figures it is possible to estimate the difference in χ_{TDR} due to the difference in ρ between the two samples.

Define χ_1 (χ_2) as the measured susceptibility of sample 1 (2) with resistivity ρ_1 (ρ_2), permeability μ_1 (μ_2), geometric constant R_1 (R_2) measured at frequency f_1 (f_2). Provided $\delta_{1,2}$, given by Eq. 1.1 is much smaller than $R_{1,2}$, then Eq. 1.17 reduces to

$$4\pi\chi_{1,2} = 1 - \frac{\mu_{1,2}\delta_{1,2}}{2R_{1,2}}. \tag{4.73}$$

Under the conditions that $\mu_1 = \mu_2$, $R_1 = R_2$, and $f_1 = f_2$ Eq. 4.73 may be written as

$$4\pi\chi_{1,2} = 1 - c\sqrt{\rho_{1,2}}. \tag{4.74}$$

It is straightforward to show that

$$\left|\frac{\chi_1 - \chi_2}{\chi_1}\right| = \left|\frac{\sqrt{\rho_1} - \sqrt{\rho_2}}{\sqrt{\rho_1}}\right|. \tag{4.75}$$

Taking the iron compound as sample 1 and the cobalt compound as sample 2, at 50 K the right hand side of Eq. 4.75 is about 0.16. Using data collected with the TDR, the left hand side of Eq. 4.75 is about 4.23. Only about 4% of the observed difference in χ_{TDR} for YFe_2Zn_{20} and YCo_2Zn_{20} can be accounted for through differences in ρ. Allowing for variations in R and f between samples and runs respectively only accounts for another 5–10% of the observed difference. One of the assumptions leading to this conclusion must be wrong. All parameters in Eq. 4.73 have been accounted for with the exception of magnetic permeability. It was assumed that $\mu_1 = \mu_2$. Relaxing this condition allows for the majority of the observed difference in χ_{TDR} for these two materials to be attributed to the enhanced susceptibility of the conduction band in YFe_2Zn_{20}. The change in χ_{TDR} in YFe_2Zn_{20} is slightly greater than that for YCo_2Zn_{20}. Given the proximity to ferromagnetic order in YFe_2Zn_{20}, the magnetic susceptibility is expected to grow like T^{-1}, increasing the low difference in χ_{TDR} between the two compounds. That this behavior is not observed here is curious. A possible explanation is that in a low field, dynamic regime, the Stoner enhancement of the Pauli paramagnetism is equivalent to multiplication by a temperature independent constant, but it is not clear that this is the case. Frequency resolved measurements would help in clarifying this point.

4.5 Materials Studied

4.5.1 $ZrZn_2$

Ferromagnetism in $ZrZn_2$ was discovered Matthias and Bozorth in 1958 [Matthias and Bozorth (1958)]. It was a surprising development as this was the first transition metal compound to manifest magnetic order that did not contain Fe, Ni, Co, Cr, or Mn. The only mechanism that could be invoked for the observed small magnetic moment of 0.13 μ_B per formula unit was through conduction band polarization. Since the time of the discovery of ferromagnetic order samples and measurements have been refined and the saturated moment has shifted up to 0.17 μ_B per formula unit and the Curie temperature has shifted down to about 28 K [Yelland et al. (2005)]. The fields applied to measure the magnetic moment in the original paper are believed to be on the order of 5 kOe. The only notation is in the graph of the data where "H=3,900" and "H=10,800" are labels on the two magnetization curves. If the units are oersted then the large applied fields could easily shift the observed transition temperature up.

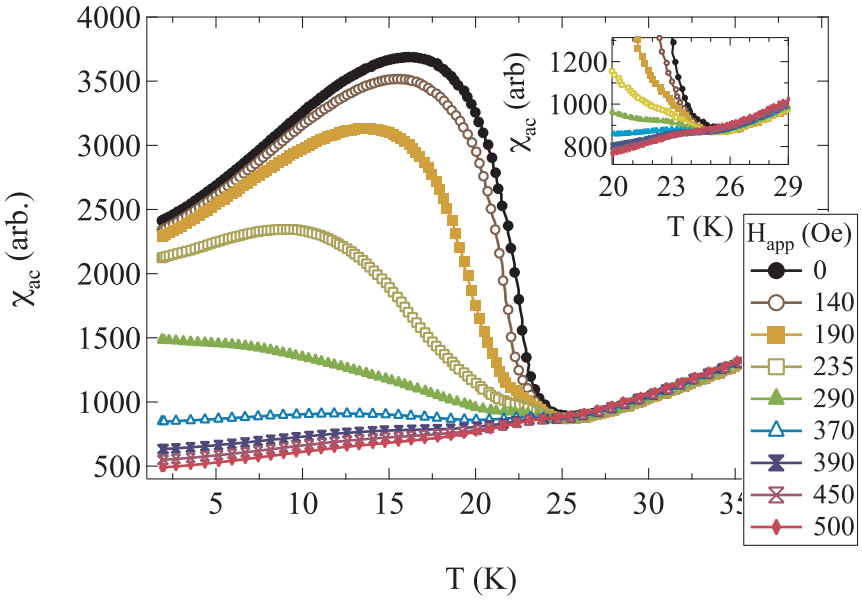

Figure 4.5 χ_{TDR} vs. T for the weak itinerant ferromagnet $ZrZn_2$ in various applied static fields. *Inset* Detail near phase transition region.

Figure 4.5 presents the rf susceptibility for single crystal $ZrZn_2$ in applied static fields. The behavior of χ_{TDR} at the radio frequencies stands in stark contrast to the accepted local moment systems (Ch. 2). Whereas the local moment systems manifest a strong, well-defined peak in χ_{TDR} at T_C which shifts to higher temperatures in applied fields, the itinerant system exhibits a broad maximum in χ_{TDR} below T_C which shifts to lower temperatures as field is applied. This difference was first reported in 2008 [Vannette et al. (2008d)]. The inset to Fig. 4.5 shows that at T_C a local maximum is absent.

There is a qualitative similarity between χ_{TDR} and χ_{ac} as determined from conventional measurements when applied to local moment ferromagnets. Both data sets manifest a peak in the measured susceptibility at the Curie temperature. This is to be contrasted with the difference between the static moment data and χ_{TDR} in the local moment magnets. Static moment shows an increasing magnetization with decreasing T below T_C. Contrary to this, there is a qualitative similarity between the static moment data and χ_{TDR} in $ZrZn_2$. Therefore, as stated previously, it is not unreasonable to at first assume itinerant ferromagnets are still in the static limit at measurement frequencies of 10-30 MHz.

The low temperature resistivity of $ZrZn_2$ exhibits unusual $T^{5/3}$ behavior [Yelland et al. (2005)]. Fig. 4.6 shows $(1 + 4\pi\chi)^2$ for $ZrZn_2$ in an applied field of 1.2 kOe vs. $T^{5/3}$. The solid line is the data and the dashed line is a calculated $\rho_0 + AT^{5/3}$ curve. The low temperature data are seen to fall on the calculated curve, showing that the measured χ_{TDR} in this field is a direct probe of the behavior of the resistivity with essentially no contribution from the spins. In this case, the spin component of the susceptibility has been suppressed below the level of detection. The inset to Fig. 4.6 is the full scale resistivity vs. temperature in the same field. The observation that the temperature dependence of the resistivity inferred from χ_{TDR} in this field is consistent with the zero field behavior will be of use in analyzing the spin component of the measured χ_{TDR}.

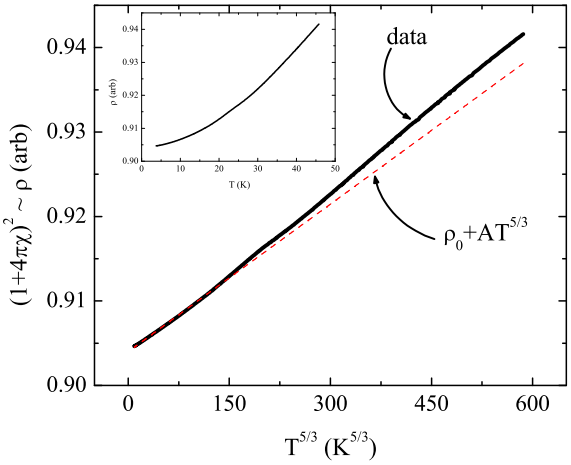

Figure 4.6 Arbitrary ρ vs. $T^{5/3}$ for $ZrZn_2$ in a 1.2 kOe applied field (solid line) and calculated $\rho_0 + AT^{5/3}$ (dashed line). *Inset:* ρ vs T up to 40 K.

4.5.2 Y_9Co_7

Y_9Co_7 has been reported to show itinerant ferromagnetism at 4.5 K with an extrapolated moment of 0.09 μ_B/f. u. as determined by heat capacity, low frequency ac susceptibility, and magnetization studies [Sarkissian and Grover (1982), Yamaguchi et al. (1984)]. Further, at approximately 3 K this material enters a superconducting state. There is one study [Rastogi and Coles (1985)] that suggests this compound is not truly ferromagnetic, however the consensus in the sparse literature is that long range ferromagnetic order does exist here, and the purity of the starting elements is a powerful indicator of whether or not the FM order is manifest. Qualitatively χ_{TDR} data are similar to that seen in $ZrZn_2$ (Fig. 4.7). These measurements suggest the itinerant ferromagnetism sets in at a much higher temperature ($T_C \approx 9$ K), if the data are assumed to be consistent with $ZrZn_2$ and the yet to be discussed $GdFe_2Zn_{20}$ pure and doped series of compounds.

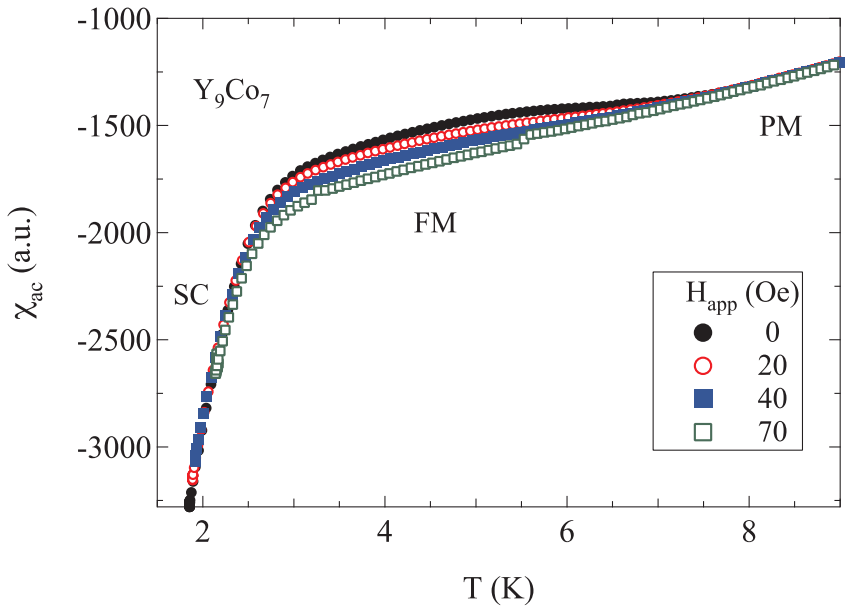

Figure 4.7 χ_{TDR} vs. T for Y_9Co_7 in four applied fields. SC, FM, and PM denote the superconducting, ferromagnetic, and paramagnetic states, respectively.

4.5.3 Half-Band Ferromagnet NiMnSb

NiMnSb is an example of the so-called half-band ferromagnets. These are materials that are supposed to exhibit complete polarization of the conduction band at low temperatures [de Groot et al. (1983)]. They are sometimes referred to as half-metallic systems as one spin-subband is metallic while the other is gapped at zero temperature. This material has a Curie temperature of approximately 730 K [Borca et al. (2001)]. A plot of χ_{TDR} of NiMnSb along with a measurement of the background due to the empty sample holder is presented in Fig. 4.8. On cooling, near the published ordering temperature a dramatic increase in χ_{TDR} is evident. It is difficult to envision a scenario whereby the resistance of a metal will dramatically increase with decreasing temperatures for $T > 700$ K. If χ_{TDR} at the highest temperature is

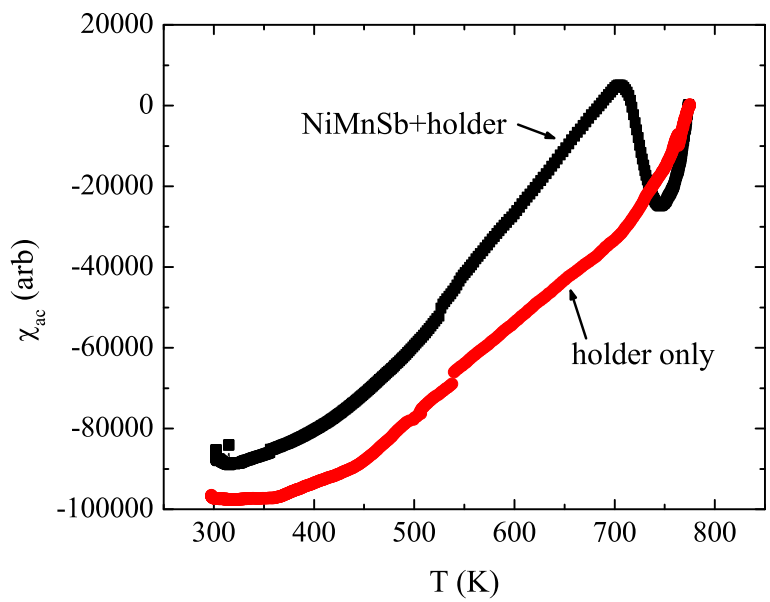

Figure 4.8 Plot of χ_{TDR} vs. T for NiMnSb and the empty Inferno sample holder.

dominated completely by the sample holder, then it is reasonable to set the values at this point in the two runs as equal and subtract the sample holder contribution. This approximation is

supported by the observation that the induced frequency shift from room temperature to 700 K is approximately the same for both the empty sample holder and the sample plus holder runs. Assuming the contributions of the two pieces simply add, we can subtract the frequency shift due to the holder from the NiMnSb run to get an idea of what the sample response is. This is presented in Fig. 4.9.

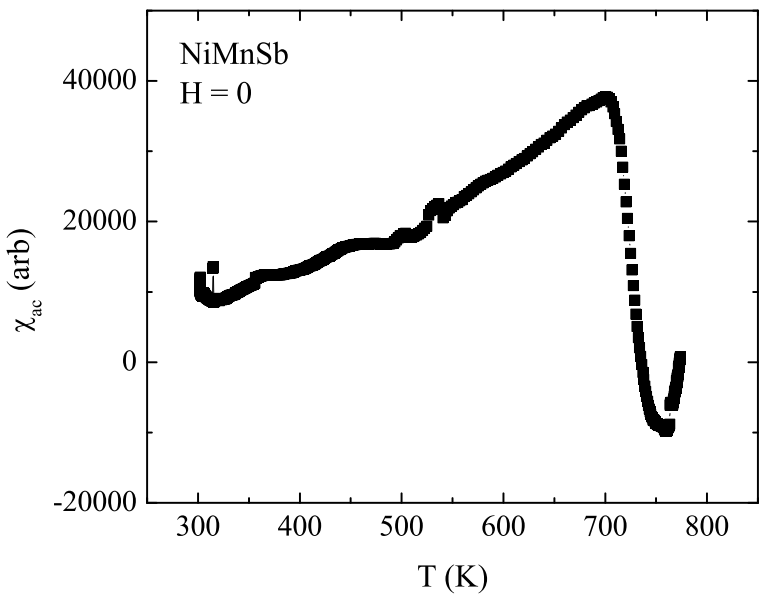

Figure 4.9 Magnetic susceptibility of NiMnSb with the sample holder contribution subtracted.

The behavior of NiMnSb stands in some contrast with the $ZrZn_2$ data in that the increase in χ_{TDR} below T_C is much sharper. This may be an artifact of the background subtraction process, or it may be a real effect hinting at the possibility that this material shows at least some local moment character. The contrast between NiMnSb and local moment systems at T_C is obvious, though. Whereas the local moments show a well defined peak, the half–band magnet only shows a rapid increase in χ_{TDR} followed by a gradual decrease. This is more consistent with χ_{TDR} data on $GdFe_2Zn_{20}$, presented in Ch. 5. Taken together, these data

suggest that there is a certain degree of localization in NiMnSb with the low tempearture behavior still manifests strong fluctuations.

4.6 Analysis of $ZrZn_2$ and Y_9Co_7

An attempt to fit the model developed to explain the data in itinerant systems is made. However, there is the problem that the as measured susceptibility contains a resistivity component. This must be dealt with in a reasonable manner in order to explore the magnetic effect. From Fig. 4.6 it is evident that the application of a 1.2 kOe field is insufficient to invoke a significant change in the $\rho(T)$ behavior in $ZrZn_2$, going so far as to recover the $T^{5/3}$ response. Therefore it is reasonable to assume that the resistivity will not be affected by lower fields.

To account for the resistivity contribution to the measured susceptibility in $ZrZn_2$, data collected in a static field of 1 kOe were subtracted from lower field runs. This field was sufficiently large to completely suppress the maximum in χ_{TDR} while being small enough that it is not expected to result in a significant magnetoresistance.

Data fits to the model were attempted for various values of n. It was found that $n = 1$, corresponding to the spin fluctuations theory, gave the best agreement. Figure 4.10 shows best fits of Eq. 4.72 to the TDR data for $ZrZn_2$. The best fit was determined by minimizing the sum of the squared differences between the data points and the fit curve at constant temperature. The resulting values of the fitting parameters are shown in Fig. 4.11. χ_0 decreases with applied H. T^* is constant within the errors and it is approximately equal to T_C. The value of h is approximately constant up to applied fields of about 125 Oe and thereafter grows monotonically as H is increased. Fields for which h increases are those where the fits become worse. Even though the higher field data are not well recreated by the model, the fact that the lower non-zero field data are fit reasonably suggests that this is a good direction to explore for understanding of this observation.

Similar fitting was done on the Y_9Co_7 sample in the ferromagnetic state. Results of those fits are shown in Fig. 4.12. Again, $n = 1$ was found to give the best fit for the data. Figure 4.13 shows the fit parameters for the Y_9Co_7 data. At the low temperature end, the superconducting

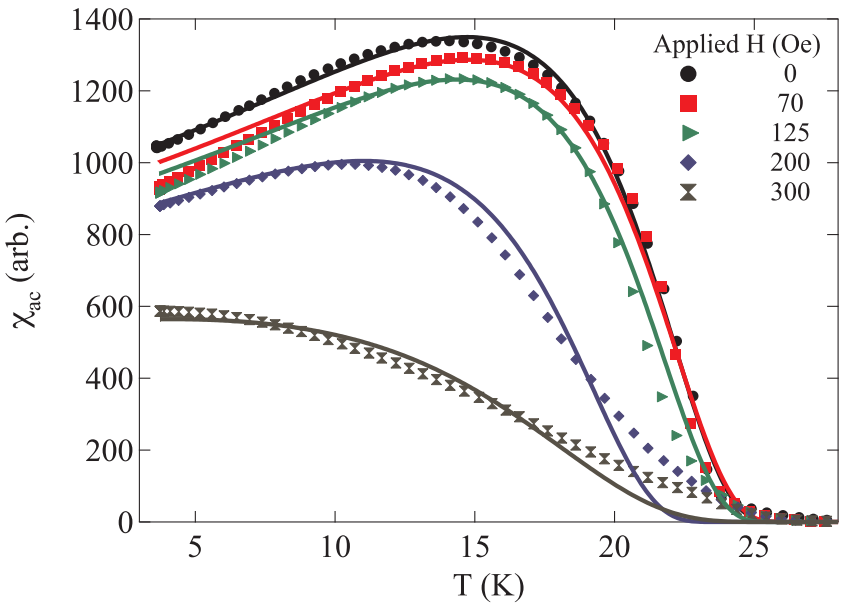

Figure 4.10 Fits of $ZrZn_2$ data to Eq. 4.72.

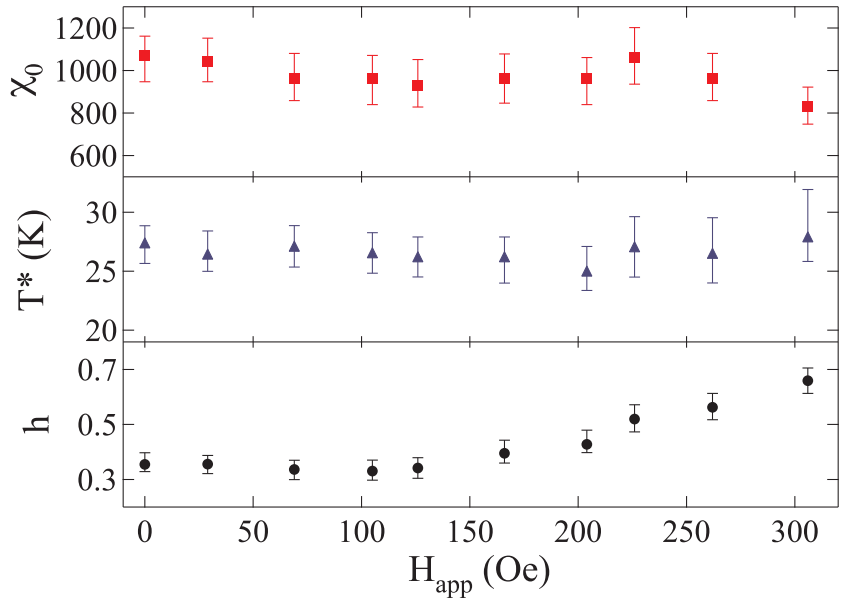

Figure 4.11 $ZrZn_2$ fit parameters with estimated errors.

state is beginning to compete more aggressively with the ferromagnetism, and the zero field data shows a strong deviation. This deviation is less pronounced as the applied field increases. Interestingly, if T^* is assigned the value of T_C as is apparently the case from the $ZrZn_2$ data, then this suggests that the Curie temperature for this compound is nearly 9 K. This is more than two times larger than what was previously thought. Curiously, even though both systems show strikingly different transition temperatures, and very different suppression fields, the effective fields from the fitting are approximately the same.

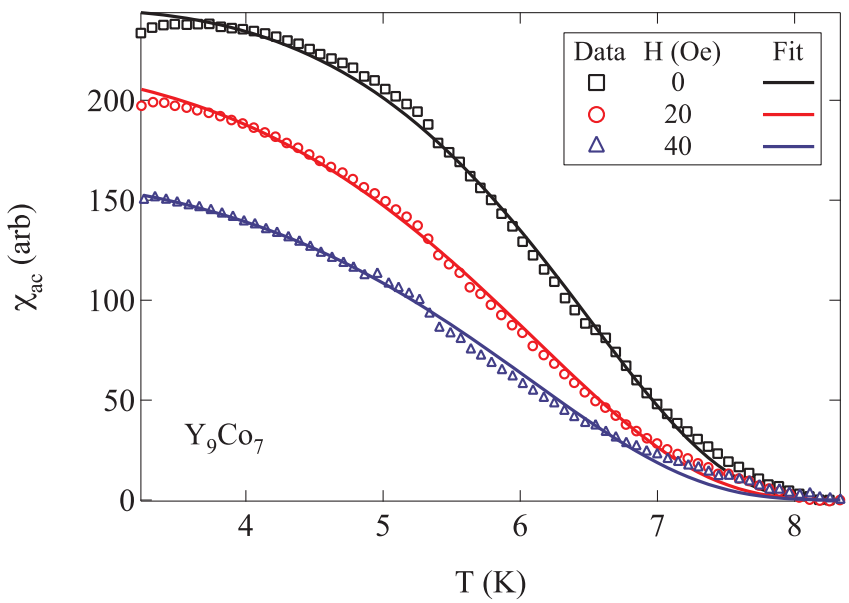

Figure 4.12 Comparison of data (points) and fit (lines) for three applied fields in a polycrystalline sample of Y_9Co_7.

Both systems that are fit to this model exhibit very large error bars (±10% or more). However, given that this behavior was not predicted by the successful theories on itinerant systems, the fact that the model comes this close is intriguing. It is likely that the true behavior is nothing like a hyperbolic cosine. This is only meant to serve as a starting point giving the general direction in which to look for solutions to this theoretical problem.

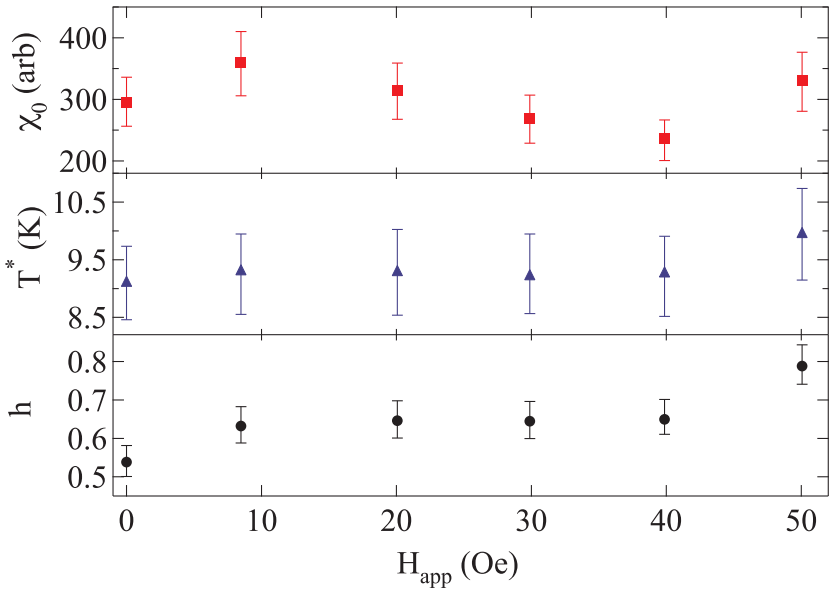

Figure 4.13 Y_9Co_7 fit parameters with estimated errors.

4.7 Summary

The sensitivity of TDR measurements to changes in χ_{TDR} has been applied to itinerant ferromagnetic systems. In contrast to local moment systems, the ordered state response of the magnetic susceptibility shows a broad maximum which suppresses in applied field and shifts to lower temperatures. Comparison with static measurements show that the observed response is not the result of residing in the static regime. Conventional theories do not adequately predict nor describe the observed effect. A model based on the presence of a fluctuating component of the conduction band was proposed and fits the data for $ZrZn_2$ and Y_9Co_7 reasonably well. The validity of the model is further confirmed by comparison of measurements of the non–magnetic, Stoner enhanced YFe_2Zn_{20} and non–magnetic, non–enhanced YCo_2Zn_{20} compounds.

CHAPTER 5. Magnetic Susceptibility of Selected Members of $RT_2\mathbf{Zn}_{20}$

5.1 Introduction

In metallic ferromagnets there is always the question of whether a particular system is itinerant or local in character. The absence of a theory that simultaneously explains both the local moment and itinerant magnetism is a long standing problem in condensed matter physics. A major step in the phenomology of local moment vs. itinerant magnetism was the Rhodes–Wholfarth (RW) theory [Rhodes and Wohlfarth (1963)]. Under this theory one plots the ratio of the paramagnetic moment per ion to the saturated moment per ion in the ordered state against transition temperature for any ferromagnet. Materials showing a large RW ratio are candidate itinerant systems, while those with RW ratios close to 1 are likely local moment systems. It is seen that most materials have moderate RW ratios, indicating that most materials manifest properties seen in both local moment and itinerant magnets. The experimentally observed relationship implied by the RW curve does not offer much insight into how the gap between intinerant and local moment physics might be crossed, however.

The first reasonably successful theory of itinerant magnetism may be attributed to Stoner [Stoner (1938)]. Improvements on the Stoner theory have been made, most notably the advent of the spin fluctuation theory [Moriya (1985)]. However, a discussion of whether or not a particular material manifests itinerant magnetism may be carried out under the terminology of the Stoner theory. By considering the effect of onsite electron–electron (e–e) repulsion, Stoner showed that under certain conditions it is energetically favorable for the conduction band in a metal to spontaneously spin polarize to a some degree. This polarization is responsible for the observed magnetic moment in itinerant ferromagnets. Even in the absence of a finite temperature conduction band polarization (i. e. a finite Curie temperature) the magnetic susceptibility,

χ, is enhanced due to the e–e interactions. The enhancement of χ often is described by the so–called Stoner Z factor. The susceptibility enhancement is in comparison to the calculated susceptibility as determined by band structure calculations, for example, with e–e interactions switched off. The relationship between the enhanced χ and the unenhanced χ_0 is given by

$$\chi = \frac{\chi_0}{1 - Z} \tag{5.1}$$

where χ_0 is given by $\mu_B g\,(E_F)$. $Z = 1$ is taken as the Stoner criterion for the onset of itinerant ferromagnetic order.

It would be beneficial to have a system whereby the itinerant component of the magnetism could be tuned from the Stoner limit to nearly pure local moment physics. Recently a series of dilute rare earth–transition metal compounds RT_2Zn_{20} was shown to have just such this tunable property [Jia et al. (2007)].

The properties of YFe_2Zn_{20}, YCo_2Zn_{20}, and $Gd(Fe_xCo_{1-x})_2Zn_{20}$ have been studied in detail [Jia et al. (2007), Jia et al. (2008)]. YFe_2Zn_{20} is a highly Stoner enchanced paramagnet ($Z \approx 0.89$) while the isostructural YCo_2Zn_{20} is only weakly paramagnetic. High field (50 kOe) M/H vs. T data coupled with low temperature specfic heat measurements suggest that by titrating Co into YFe_2Zn_{20} it is possible to continuously tune the Stoner Z from a value greater than that for Pd ($Z \approx 0.83$) to a value comparable to Cu ($Z \approx 0.29$). Substituting Gd for Y in either compound leads to long range magnetic order. In the case of $GdFe_2Zn_{20}$ the Gd ions order ferromagnetically with a mixed local moment/itinerant Fe flavor at an astonishingly high 87 K, while for $GdCo_2Zn_{20}$ the Gd ions settle into a local moment antiferromagnetic order at a more reasonable 5.7 K. The FM ordering temperature in $GdFe_2Zn_{20}$ is surprising because the Gd–Gd separation is approximately 6 $\AA$ [Nasch et al. (1997)]. Such a large separation normally implies very weak coupling between the rare earth ions. However, it was found that the highly Stoner enhanced conduction band measured in YFe_2Zn_{20} leads to a enhances the RKKY interaction allowing for the high ordering temperature [Jia et al. (2007), Jia et al. (2008)]. Since the cobalt containing analogue lacks the greatly enchanced conduction band, the ordered state sets in at a more conventional temperature.

Similar to the yttirum compounds, it is possible to titrate cobalt into the $GdFe_2Zn_{20}$ host to

study how the transition to $GdCo_2Zn_{20}$ progresses. Previous static measurements have shown that (a) the transition from FM to AFM order occurs only for fairly large Co concentrations ($\geq$75%), (b) the transition temperature decreases monotonically with increasing Co, and (c)

Cobalt doping directly affects the magnetic sublattice by replacing iron atoms and simultaneously contributes one extra valence electron per formula unit. Since the details of the Stoner enhancement depend both on the conduction electron density of states and on the ion type, finding a method to affect the conduction band without directly influencing the magnetic sublattice would be beneficial. Aluminum doping on the zinc sites allows for just such a modification. Each aluminum ion replacing a zinc ion contributes one extra valence electron per formula unit, just as in Co doping. However, since the Zn appears to be a spectator in the magnetic order, Al doping is not expected to directly affect the magnetic Fe sublattice. A comparison of the two types of doping (Co→Fe and Al→Zn) elucidated the different roles played by the conduction band and the magnetic sublattice in the order [Ni et al. (2008)]. Any measurement of a magnetic property will be a convolution of both the local moment rare earth and the itinerant transition metal, however. What is required is a method to deconvolve the two contributions.

5.2 Data and Discussion

To facilitate comparison of χ_{TDR} across the different compounds, samples of similar size and shape were chosen. $Gd(Fe_xCo_{1-x})_2Zn_{20}$ samples with x =0.12, 0.25, 0.5, 0.75, and 1 and $GdFe_2(Zn_yAl_{1-y})_{20}$ samples with y =0.005, 0.017, 0.021, and 0.049 were studied here. In addition pure $GdFe_2Zn_{20}$ was measured as well.

5.2.1 Parent Compounds

Fig. 5.1 presents χ_{TDR} vs. T for pure $GdFe_2Zn_{20}$ and $GdCo_2Zn_{20}$ in zero applied static field. The gadolinium ions order ferromagnetically in $GdFe_2Zn_{20}$ at T_C =87 K [Jia et al. (2007), Jia et al. (2008)]. Below this temperature χ_{TDR} exhibits a large increase followed by a slow decrease. $GdCo_2Zn_{20}$ does not manifest any increase in χ_{TDR} at T_N $\approx$5.7 K where

the gadolinium ions order antiferromagnetically [Jia et al. (2008)]. Rather it shows a rapid decrease in the measured susceptibility upon cooling into the antiferromagnetic state. The difference in χ_{TDR} is explained by the extremely weak perturbation field used here. Magnetic susceptibility is a measure of how the magnetic moment of a sample changes in response to a change in magnetic field. In ferromagnetic materials the exchange interaction favors parallel alignment of neighboring spins. Perturbations of one moment via an external field are transferred to neighboring moments through the exchange interaction. It is energetically favorable for the bulk moment of the sample to change in response to the applied field, in this case the rf field from the coil. Conversely, in antiferromagnets exchange interactions lead to antiparallel alignment of spins (in some configuration) giving rise to no net moment in the sample. If a particular localized moment is gently perturbed, the exchange interaction will dominate and no change in the bulk moment of the sample will occur. In the vicinity of an ordering temperature exchange energy and thermal energy are on equal footing. It is very easy to change the orientation of a given spin through the application of a magnetic field. In ferromagnets, this leads to an enhanced rf susceptibility as $T \rightarrow T_C$. In antiferromagnets, however, it is energetically favorable for the spins to order without a bulk moment. Therefore the rf susceptibility experiences no enhancement as $T \rightarrow T_N$. The decrease in the measured χ_{TDR} is associated with a decrease in resistivity due to a loss of spin disorder scattering.

The large value of χ_{TDR} in the ordered state for $GdFe_2Zn_{20}$ has been attributed to the enhanced susceptibility of the conduction band [Vannette et al. (2008d), Vannette and Prozorov (2008)]. Such a conclusion is supported by the data on YFe_2Zn_{20} andYCo_2Zn_{20} presented in Ch. 4.

Figure 5.2 presents field dependent $\chi_{TDR}(T)$ data for $GdFe_2Zn_{20}$. Applying a static bias field to $GdFe_2Zn_{20}$ suppresses the amplitude of the broad maximum below T_C and shifts it to lower temperatures. The inset of Fig. 5.2 shows that a small amplitude local maximum slightly below the published ordering temperature emerges in applied field. The small amplitude maximum shifts to higher temperatures and is suppressed in amplitude in applied field. The behavior of the low temperature maximum is consistent with what is observed in itinerant

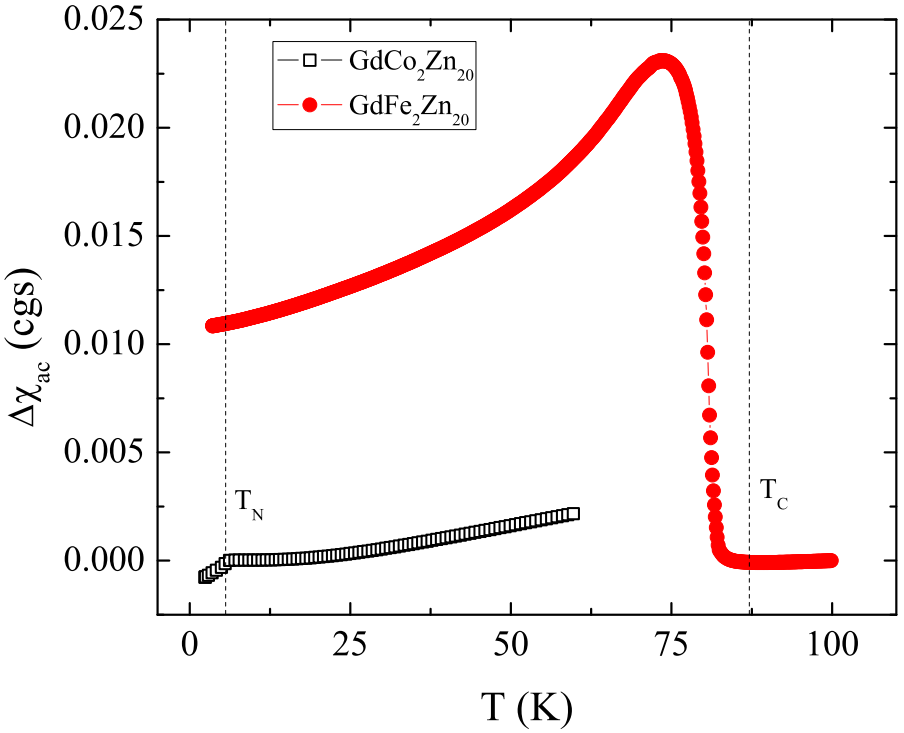

Figure 5.1 Comparison of $\Delta\chi_{TDR}$ vs. T for $GdCo_2Zn_{20}$ (hollow symbols) and $GdFe_2Zn_{20}$ (solid symbols). Dotted lines mark published T_N and T_C for the cobalt and iron compounds respectively.

ferromagnets whereas the behavior of the high temperature maximum is consistent with local moment ferromagnets. This may be expected since $GdFe_2Zn_{20}$ is proposed to be a material with local moment Gd embedded in a nearly ferromagnetic Fermi liquid.

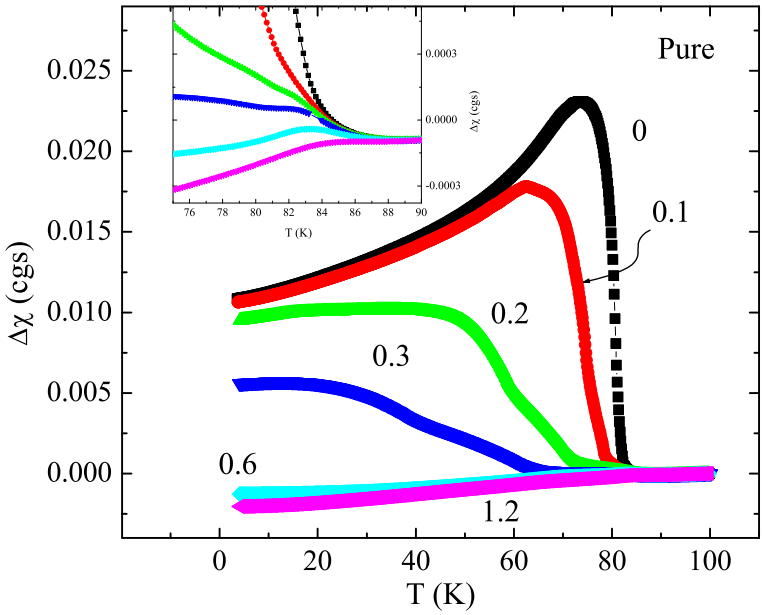

Figure 5.2 Field dependent change in $\chi_{TDR}(T)$ for $GdFe_2Zn_{20}$. The inset is a detail in the vicinity of the phase transition. Numbers indicate magnetic field in kOe.

5.2.2 Cobalt doping

Figure 5.3 presents the change in χ vs. temperature for five different samples with differing cobalt concentrations. It is seen that as cobalt concentration increases, the magnetic ordering temperature decreases. The amplitude of the low T peak in χ_{TDR} first increases then decreases with increasing cobalt concentration. Application of a static magnetic field suppresses the change in susceptibility for all samples (Fig. 5.4). In some concentrations the application of magnetic field also uncovers other features. This is most evident in the 50% cobalt doped

sample where in fields of 0.6–1.1 kOe a well–defined peak in χ is observed in the vicinity of 20 K. Previous TDR rf susceptibility studies on other magnetic materials have shown that the presence of a well defined peak is indicitative of the onset of local moment ferromagnetic order [Vannette et al. (2008d), Vannette et al. (2008a), Vannette and Prozorov (2008)]. As the introduction of cobalt ions into the parent $GdFe_2Zn_{20}$ lattice has been shown to suppress the itinerant component of the magnetism, the observation of features strongly associated with local moment magnetic order is not surprising. The sharpness of the peak in the 75% cobalt doped sample is strongly suggestive of a transition from itinerant to local moment behavior.

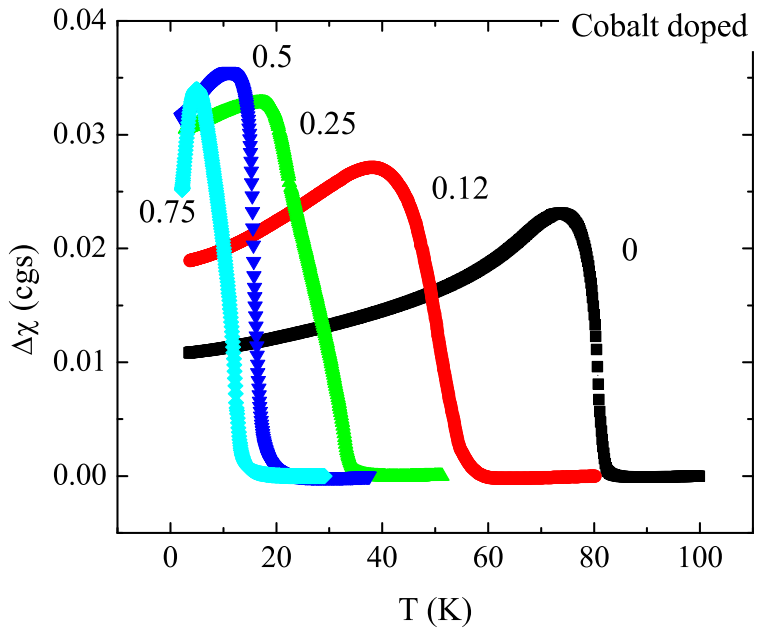

Figure 5.3 Change in the measured susceptibility vs. temperature for five cobalt concentration ranging from x =0-0.75 in $Gd(Fe_xCo_{1-x})_2Zn_{20}$.

The sharp features seen in the 12% and 50% cobalt doped samples show very little temperature dependence on applied field. There is a very slight increase in the temperature of the peak which is likely due to the change in the FM ordering temperature in applied field.

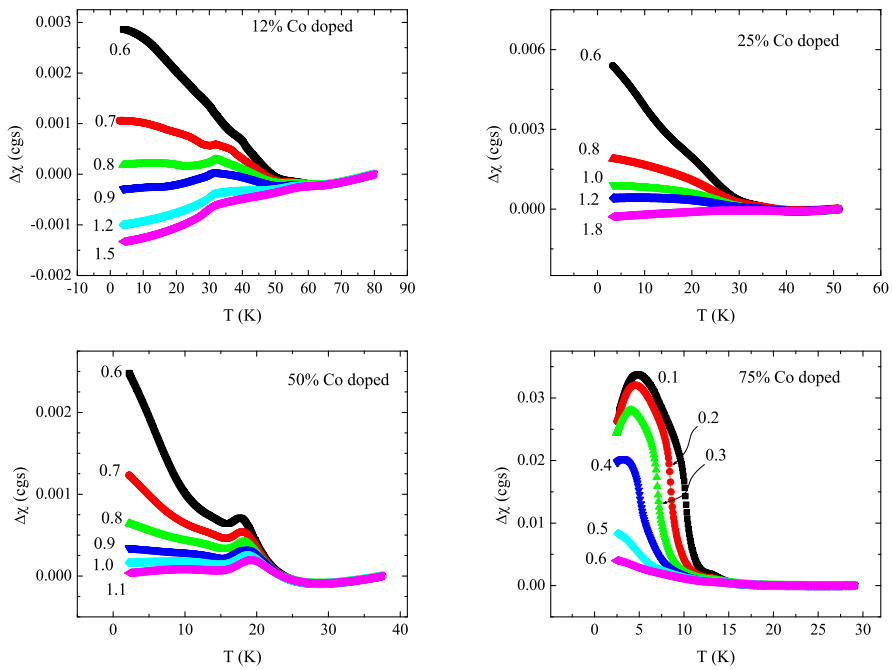

Figure 5.4 χ vs. T in different fields for the four Co concentrations studied here. Numbers next to each trace indicate the applied field in kOe. Strong local moment peaks are observed in all samples except for the 50% doping.

Conversely, the sharp feature in χ observed in the 75% doped sample shows a negative temperature dependence on applied field. Published static moment measurements suggest that the ordering in $x = 0.75$ $Gd(Fe_xCo_{1-x})_2Zn_{20}$ is not conventional FM order [Jia et al. (2008)].

5.2.3 Aluminum doping

For comparison, a series of aluminum doped $GdFe_2Zn_{20}$samples was measured. Figure 5.5 presents zero field χ_{TDR} vs. T curves for several concentrations of aluminum ions. Ni et al. (2008) have shown that the magnetic transition temperature is suppressed with increasing aluminum concentration in a manner similar to the temperature suppression seen in the cobalt doped case. This will be explored further below.

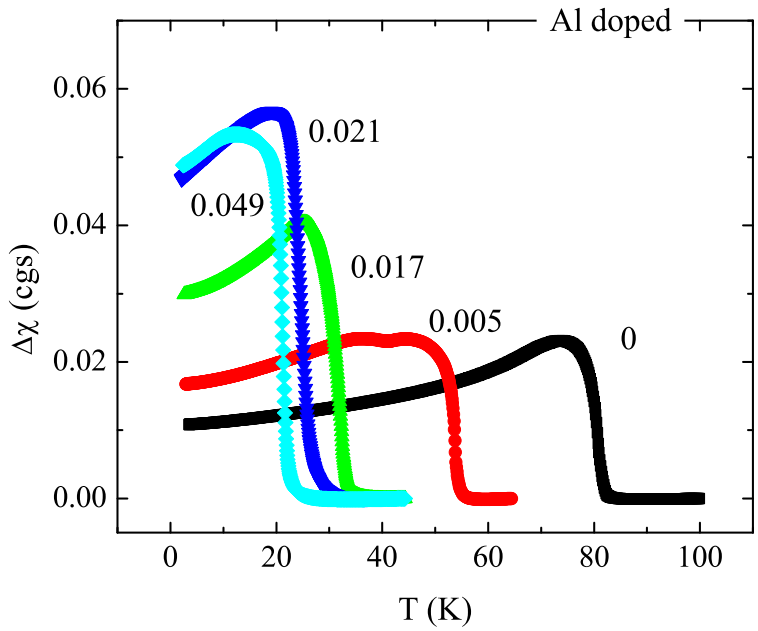

Figure 5.5 Magnetic susceptibility vs. temperature for five aluminum concentrations ranging from 0-4.9%.

As shown in Fig. 5.6, χ_{TDR} vs. T for the lowest aluminum doping studied reveals a small

dip near $T = 40$ K. Application of a static field does not change the temperature of this dip appreciably. However, by applying a field of 0.4 kOe the dip is suppressed. Such a dip in χ_{TDR} is not seen in other aluminum dopings. All other aluminum concentrations studied have χ_{TDR}–T curves similar to pure $GdFe_2Zn_{20}$, the main difference being the magnetic transition is shifted lower in temperature. The absence of additional features associated with local moment magnetism suggests that the effect of aluminum doping is not equivalent to that of cobalt doping. Cobalt substitution directly affects the magnetic sublattice while aluminum doping only affects the conduction band.

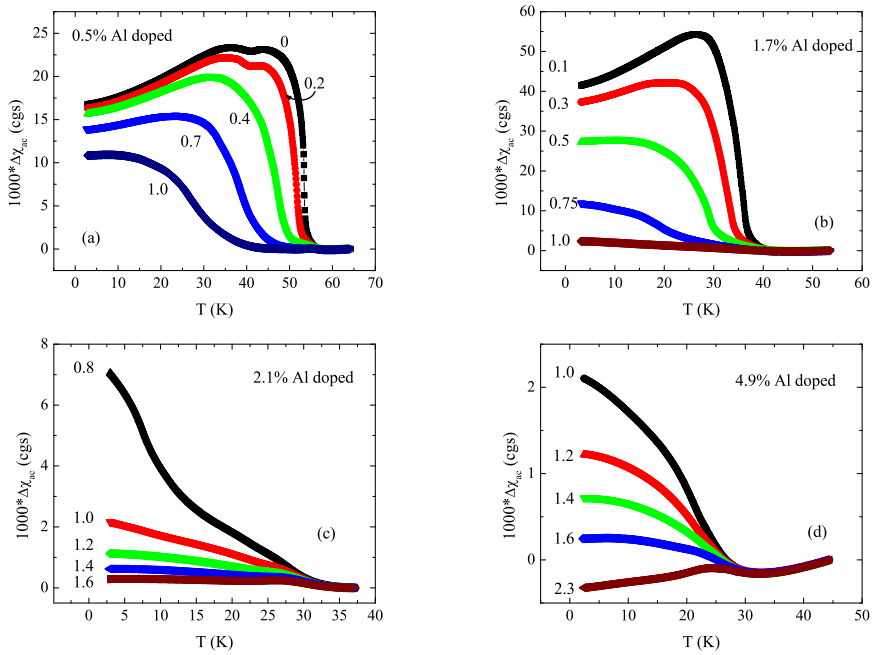

Figure 5.6 χ_{TDR} vs. T in applied DC fields for the four Al doped samples studied. Only the 0.5% and 4.9% Al dopings show well–defined additional features. Numbers next to each trace indicate the applied field in kOe.

5.2.4 Discussion

Figure 5.7 compares published magnetic ordering temperatures for $Gd(Fe_xCo_{1-x})_2Zn_{20}$ vs. extra electron per formula unit [Jia et al. (2007)] with temperatures determined by three different criteria for zero field χ_{TDR} data on $GdFe_2Zn_{20}$, $Gd(Fe_xCo_{1-x})_2Zn_{20}$, and $GdFe_2(Zn_yAl_{1-y})_{20}$. The lowest temperature is the temperature of the maximum in χ_{TDR} for each sample, T_{peak}. The temperature of the maximum negative slope for $T > T_{peak}$ defines the slope criterion. This temperature was determined by a sharp, negative peak in $d\chi_{TDR}/dT$. The highest temperature for each sample was determined by an onset criterion, taken as a zero derivative for $T > T_{peak}$.

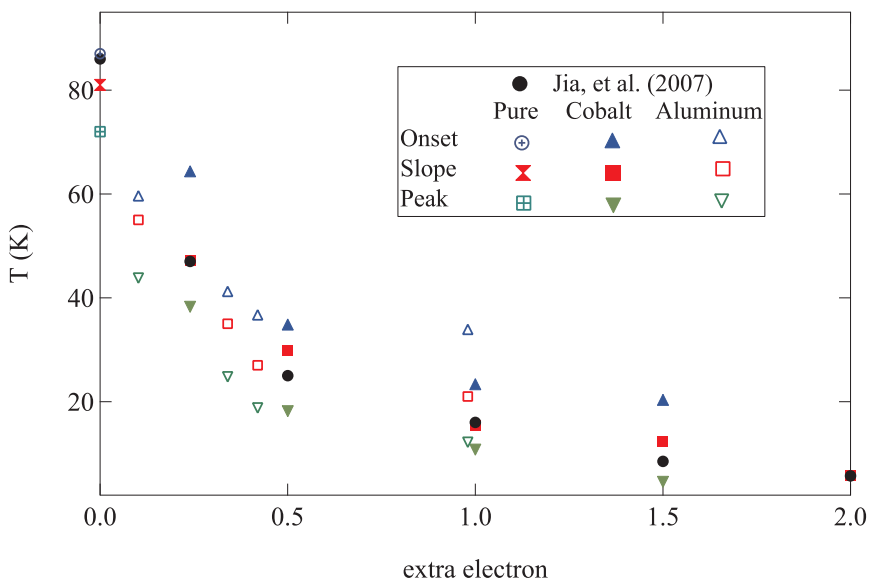

Figure 5.7 Comparison of published ordering temperatures (solid circles) with temperatures derived from χ_{TDR} data using three different criteria. Onset criteria is determined by a zero derivative in $\chi_{TDR}(T)$ for T greater than T of the large maximum. Slope criteria is determined by the maximum in $d\chi_{TDR}/dT$. Peak criterion is determined by finding the maximum in χ_{TDR}.

For pure $GdFe_2Zn_{20}$ the onset criterion compares favorably with the published T_C, with slope and peak temperatures falling well below 87 K. However, as electron number increases,

the onset criterion diverges from the published magnetic ordering temperatures in favor of a maximum slope criterion. At still higher extra electron number published ordering temperatures fall between the slope and peak temperatures. This may be indicative of the crossover from mixed local/itinerant to strongly local moment magnetism. Choosing the proper ordering temperature selection criterion is problematic, especially in the absence of data showing strong features. The TDR data do not provide a clear path to a solution, however, when combined with other techniques it may provide a means to quantify the degree of itineracy in a mixed system. More work is needed to understand what useful role the TDR might play in studying magnetic transitions general.

Complete replacement of cobalt for iron changes the ferromagnetic ordering of the gadolinium moments to antiferromagnetic. Based on the TDR data presented here, it seems that the transition is not smooth, with the ferromagnetic state persisting to high concentrations of cobalt. These findings are consistent with static measurements on the same compounds [Jia et al. (2008)]. While high field, static measurements show that conduction band spin fluctuations are smoothly suppressed with increasing cobalt concentration [Jia et al. (2007)], the low field, rf data presented here suggest that considerable fluctuations persist up to at least 50% cobalt substitution. This should not be too surprising as there is little reason to suppose that the low field, dynamic response of material should be equivalent to the high field, static response.

Based on the evidence provided by rf susceptibility, it seems ferromagnetic order persists up to at least 75% cobalt substitution and 5% aluminium substitution. This conclusion is supported by the observed increase in χ_{TDR} below the magnetic ordering temperature seen in all ordered compounds except for $GdCo_2Zn_{20}$. The true nature of the magnetic order of the gadolinium moments in the compounds $Gd(Fe_xCo_{1-x})_2Zn_{20}$ and $GdFe_2(Zn_yAl_{1-y})_{20}$ is still open, however. Neutron scattering would normally be the ideal technique for determining this conclusively, but the small scattering cross–section for a natural distribution of Gd isotopes presents a particularly difficult obstacle. It is possible that magnetic x–ray scattering would provide information regarding how the magnetic structure evolves from ferro– to antiferromag-

netic with increasing cobalt concnetration. Magnetic x–ray scattering could also allow for a determination of the magnetic order in $GdFe_2(Zn_yAl_{1-y})_{20}$ as the compound $GdFe_2Al_{20}$ does not exist.

5.3 Summary

Nine different chemical dopings on the mixed local moment/itinerant ferromagnet $GdFe_2Zn_{20}$ as well as $GdCo_2Zn_{20}$, YFe_2Zn_{20}, and YCo_2Zn_{20} have been studied via rf susceptibility. The observed difference in the measured susceptibilities of YFe_2Zn_{20} and YCo_2Zn_{20} supports previous conclusions that the Fe containing compound exhibits dramatic Stoner enhancement of the conduction band while the Co containing compound does not. The data on $GdCo_2Zn_{20}$ strongly support the conclusion that this compound orders antiferromagnetically at $T_N \approx 5.7$ K. Looking across both cobalt and aluminum dopings in $GdFe_2Zn_{20}$, the data show that increasing the valence electron population decreases the magnetic transition temperature and increases the change in χ_{TDR} through ordering. Whereas the change in ordering temperature is independent of the nature of the electron doping, dopants which affect the magnetic iron site have a smaller effect on the change in χ_{TDR} than dopants on the non–magnetic zinc site. Whereas previous high field static results show that the Stoner enhancement of the magnetic susceptibility in the conduction band is gradually reduced, the low field radio–frequency results show that band fluctuations in the ordered state persist through at least 75% cobalt doping. These data suggest that the transition from ferromagnetic $GdFe_2Zn_{20}$ to antiferromagnetic $GdCo_2Zn_{20}$ does not proceed gradually. Rather an abrupt change in magnetic order apparently occurs with complete replacement of cobalt for iron.

CHAPTER 6. Conclusion and Future Directions

Sensitive measurements of the rf susceptibility have been shown to be of use in many areas in magnetically active samples. Here the TDR has been extended to magnetic systems in a first attempt at a broad survey of ferromagnetic materials. It has been shown that the TDR is sensitive to magnetic ordering in ferromagnets as well as antiferromagnets. It also has been demonstrated that precise measurements of the rf susceptibility distinguish between local moment and itinerant ferromagnets.

Clearly more work is required to understand the nature of rf susceptibility in magnetically ordered compounds. As employed here, the TDR might be considered a sensitive inductance meter, since the changes in resonant frequency of the tank circuit are related to changes in inductance. It was shown that the changes in L can be related to changes in χ in a sample. However, it remains unclear what a measure of χ in a magnetically ordered state actually means. The dynamics of the critical fluctuations associated with the phase transition should be probed using frequency resolved measurements in addition to studying other, well–characterized materials. Finally, the physical reason underpinning the observed difference in χ_{TDR} between local moment and itinerant ferromagnets needs to be studied. The model presented in Ch. 4 represents a first attempt at understanding what might be happening, and it is by no means definitive. This work focused on measurements of ferromagnets and lightly touched on antiferromagnets. Other physical phenomena can be explored with this technique. Preliminary work has been carried out for spin glasses, superparamagnetic powders, and multiferroic compounds. Studies on materials manifesting other types of phase transitions will require more work toward understanding what χ_{TDR} data truly means.

In the course of this work, the primary technological development to occur for the TDR was

in increasing the upper bound on the temperature. Such measurements had been performed prior to this work, but not pursued in any manner, serious or otherwise. There are other technological developments that may be explored.

The scaling behavior seen in the local moment systems studied here may actually be a finite frequency effect. The analysis of the peaks in χ_{TDR} seen in $CeAgSb_2$, $YTiO_3$ and GdPtIn (Ch. 3) suggests that for some samples the dynamics of the ordering may occur on the time scale implied by the tens of MHz regime. The only way to sort this out is to perform the measurements over 1-1.5 orders of magnitude in frequency. The issues with constructing such a setup are manifold, however.

First, the condition for resonance is that the impedance of the tank circuit be less than or equal to the impedance of the tunnel diode. This condition can be met only for a fairly small range of the product LC. The limitation can be overcome by simultaneously varying the inductance and the capacitance. The obstacle here is that for stability the components must be held at a constant temperature and in fairly close proximity to the tank coil to limit noise introduced by thermal gradients, vibration, etc. in long leads. By extension, the components must be at low temperature. It is very difficult to adjust both L and C at or near base temperature without introducing extra heat and noise in the resonance. In the development of the TDR as an NMR, Aslam and Weyhmann (1973) suggest using varactor diodes. These are diodes that are designed to have variable capacitance as the voltage drop across them varies. The drawback noted by Aslam and Weyhmann is that below about 100 K the change in capacitance of a varactor with applied voltage becomes almost zero. Further, since the resonant frequency depends on the square root of LC, a small change in f requires a fairly large change in the tank circuit parameters (one order of magnitude change in f requires two orders change in LC) . Still, it is possible to construct a set of circuits that span the frequency range from 1 MHz to 1 GHz in discrete steps. The upper bound on the switching speed for the tunnel diode is on the order of 5 GHz, and the low GHz range in the TDR has been obtained by other groups [Martin et al. (2005)]. The major drawback to the array of circuits approach is that the filling factor for each sample will likely change as the coil size will have to change

to accommodate the varying capacitor. One might suggest going to differently sized samples to keep the filling factor constant. What may happen then is in certain materials the smaller samples may not be skin depth limited while the larger may. Even within the skin depth limited regime, as the frequency varies, the skin depth varies as well. Again, the variation in δ is $1/\sqrt{f}$, so a large change in frequency is required to substantially change the skin depth. Regardless of the magnitude, it must be remembered that the change would present.

To maintain a constant filling factor, an array of TDR's, such as that mentioned above, should have a common tank coil. It is not unreasonable to consider varying the tap coil inductance (see Appendix A), as it contributes to the resonant frequency. This would allow the tank coil to remain constant while simultaneously varying the total L keeping the circuit properly tuned on resonance. This variation in the tap coil inductance must be achieved without recourse to physically changing the coil. As was shown in Ch. 1, resoldering even one connection can change the resonant frequency by 5-10%.

A very useful measurement would be to adapt the TDR back to Van Degrift's setup and measure ϵ as functions of T, H, and E. The obvious immediate application of such a system is to the multiferroics (Appendix D) in an attempt to clarify the mutual effect of the coexisting orders. This could be useful in examining systems that exhibit orbital ordering, as in $YTiO_3$ or Ba_2NaOsO_6 as well.

APPENDIX A. Design and Materials Considerations for the TDR

Three different TDRs were used to collect data for this work. The first is mounted on a closed cycle ^{3}He cryostat with a temperature range from 0.5-100 K operating at a frequency of 13 MHz. To minimize any drifts in the signal due to varying circuit properties, the circuit temperature is stabilized at 5 K. The actual temperature to hold the circuit at is not as important as the fact that the temperature is held stable. The circuit mounting block is anchored to the helium bath, with a nominal base temperature of 4.2 K. $T = 5$ K was chosen for convenience as it requires low heating power output from the temperature controller.

The sample is mounted on a sapphire rod approximately 25 mm long and 1 mm in diameter with a small amount of Apezion low temperature grease. The opposite end of the sapphire is mounted in a small copper cylinder (approximately 4 mm in diameter and 10 mm long) with Stycast 1266 epoxy. Wound around this copper cylinder is a length of doubled over and twisted nichrome wire (room temperature resistance $\approx$75 Ω) which acts as a heater. A Cernox thermometer (Lakeshore SD package) is glued to a flat milled on the heater block between the heater coil and the sapphire with a thin layer of GE-varnish. The heater block is epoxied to a macor ceramic rod, which is mounted to a larger copper cylinder. The larger cylinder makes handling the sample holder easier and provides a place to attach a heat link and feed wires to the heater and thermometer. Figure A.1 shows the basic design of the sample holder. The sample end of the sapphire is inserted into the coil of the LC tank circuit. The entire apparatus (circuit and sample) are placed in a vacuum can that is pumped to a typical pressure of 10^{-5}-10^{-6} torr. This pressure is sufficiently low to allow for separate control of the sample and circuit temperatures. Based on thermal hysteresis runs (ramping sample temperature up and down), there is little thermal lag between the sample and the thermometer. Comparison

of transition temperatures in $CeVSb_3$ [Sefat et al. (2008)], $CeAgSb_2$ [Myers et al. (1999a)], and GdPtIn [Morosan et al. (2005)] determined from TDR measurements with published values show that the agreement between the thermometer temperature and the sample temperature is within the published uncertainty.

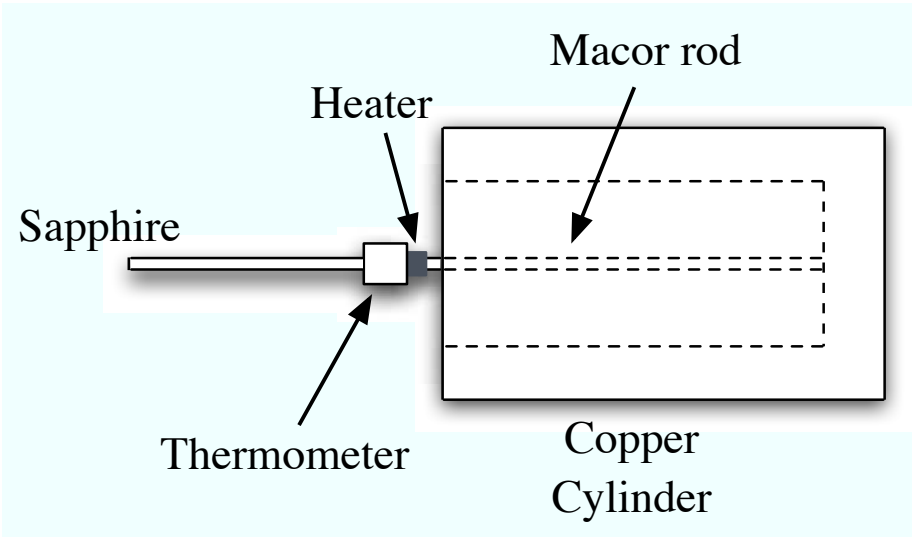

Figure A.1 Schematic of the basic design of the sample holder. Note this is not to scale. Heater and thermometry wires feed through the right end of the copper cylinder.

A major drawback of the ^{3}He system is that the circuit elements, in particular the tunnel diode, are placed in the magnetic field. This introduces a sizeable field induced background due to the field dependent properties of the diode. Fortunately, this background is very reproducible within a single run. Low temperature magnetoresistance of the thermometer can pose a problem. However, at the low fields and relatively high temperatures here it is safe to neglect this error. Further, if one can reasonably assume that the only shift in resonance at high temperatures is due to the circuit itself, then the temperature swept data can be shifted so that high temperature portions overlap. This may or may not be a reasonable assumption. It is expected that for the fields of interest in this work ($H \leq 10$ kOe, and often $H \leq 2.5$ kOe) this assumption should be valid.

Two other systems were constructed for this work. They were modeled on the ^{3}He system,

however it was possible to make certain modifications to permit collection of field swept data at constant temperature and allow access to higher temperatures. The first new system is mounted on a ^{4}He cryostat constructed with a low temperature pot, colloquially referred to as a 1 K pot. Mounted on this 1 K pot is a superconducting magnet and persistent switch as well as the sample holder and centering rig. The large amount of material anchored to the 1 K pot limits the practical lower bound on the temperature to 1.7 K. The ^{4}He sample temperature range of 2-300 K operating at a frequency of 28 MHz. Heat sinking of the leads and coaxial cables running from the room temperature in this system is less effective than in the ^{3}He system. The high heat load brought to the circuit from the leads keeps the base temperature of the circuit at approximately 7 K. Consequently, the circuit temperature is stabilized at 7.5 K. A major difference between the ^{3}He and ^{4}He systems is that the circuit in the former is mounted below the sample whereas it is above the sample in the latter. There is a coaxial cable that transmits the rf signal from the tank circuit to the rest of the low temperature elements.

The sample holder in the ^{4}He system is modeled very closely on the ^{3}He sample holder. The main difference is that the sapphire is approximately 35 mm long and 2 mm in diameter. This allows for larger samples to be studied, but requires more care in heating the sample. One way to compensate for the larger overall sapphire mass is to use a larger heater block, which was employed here. The rationale is that the heat capacity of the heater block needs to be large enough that the temperature rises slowly enough to keep both ends of the sapphire in near thermal equilibrium. A check on this condition is to sweep the temperature up and down through a second order phase transition. If there is significant thermal lag, then there will be artificial hysteresis in the temperature sweeps. If such hysteresis is present, a slower temperature ramp rate can be used. Exceptionally high temperatures ($T \geq 250$ K) pose additional problems. Even by ramping up to room temperature over the course of 2 hours (≈ 2.5 K/min) thermal lag is still observed. Ramping much slower than this is not reasonable in the ^{4}He system as constructed because the 1K pot on which the sample and superconducting magnet are mounted is not able to maintain a low enough temperature to prevent the magnet from transitioning to the normal state. It does not have enough cooling power. This undesirable

situation results in a loss of magnetic field and a wasted run. Therefore, temperatures near 250 K and higher are to be considered approximate and no quantitative assessment of transition temperatures should be made. A newer cryostat with similar design was recently purchased, and it has a larger 1K pot. This new version should provide enough cooling power to keep a conductively cooled magnet in the superconducting state even while heating the sample up to and above room temperature. Also, the sample holder could be redesigned to allow for these higher temperatures.

The long sapphire rod, which is the source of many thermal problems, is needed because a superconducting magnet was made in house to mount inside the vacuum can for this system. This allows for the application of magnetic field on the sample while keeping the circuit in a relatively field–free region. Therefore, the ^{4}He system permits field swept data to be collected. Further, the ^{4}He system has an *in situ* extraction mechanism that allows for the removal of the sample from the coil at base temperature. This permits an estimate of the absolute value of χ_{TDR}. To account for the contribution of the sapphire, empty holder runs including extraction were conducted. It was assumed that the rf susceptibility of the sapphire rod combined additively with the sample. Such an estimate is useful in making comparisons of the band component of the ferromagnetism in cobalt and aluminum doped $GdFe_2Zn_{20}$ presented herein. This also allows for an estimate of the absolute value of the penetration depth in superconductors, which is necessary for a determination of the superfluid density [Prozorov et al. (2000), Prozorov and Giannetta (2006)].

The third system is a high temperature version christened the Inferno. The circuit temperature is allowed to float near room temperature. This system allows access to temperatures as high as 800 K, and operates at a frequency of approximately 36 MHz. The sample holder is a single copper rod (100 mm long and 5 mm initial diameter) with one end turned down to a diameter of approximately 3 mm. A flat surface is milled on one side of the turned diameter. While the ^{3}He and ^{4}He systems are constructed with a vertical geometry, the high temperature resonator was set up horizontally. Samples are secured to the stage with sliver paste which is allowed to cure for two hours at room temperature before heat curing with the sample holder

itself. Heat is applied through two filaments from 100 W incandescent bulbs wired in parallel and wrapped around the larger diameter of the copper rod. The heater filaments are secured with Resbond 940 LE potting compound, a two part silica based adhesive commonly found sealing the bases of incandescent bulbs. It is rated to 1370°C, and designed to very nearly match the thermal expansion of fused silica. Sample temperature is monitored with a platinum resistance thermometer (Lakeshore PT-103) mounted in groove milled in the copper rod. To permit changes in the thermometry, should such need arise, the thermometer sits in a copper sleeve that is attached to the rod with the same potting compound used to attach the heater. The vacuum chamber for this system is a 30 cm long KF-25 nipple. The coil is mounted in a hollow drilled out of one end of a 6.35 mm diameter copper rod. Both the coil and the sample holder are in the vacuum chamber and the circuit is in air.

An obvious improvement to the Inferno would be to actively stabilize the circuit temperature. A passive stabilization is done by gluing the circuit board to an aluminum table ($61\times61\times2$ cm^3 top plate). The drift introduced by not stabilizing the circuit temperature is overwhelmed by the drift caused by the sample holder. For the low temperature versions, sapphire is used as the sample mounting surface because it is a diamagnetic (in the absence of impurities) insulator but has high thermal conductivity at low temperature. The thermal conductivity drops as temperature increases because it is mediated by phonons. Using a metal allows the thermal conductivity to stay fairly high because it can be mediated by the conduction electrons. The tradeoff is that the metal shows a changing ac susceptibility due to its changing resistance. Again, this background signal is largely reproducible. The irreproducible part likely comes from the thermal cycling of the coil.

The specifics of our systems are summarized in Table A.1. This table repeats the information provided in Table 1.2.

Table A.1 TDR Specifics

System	**Coil Volume (mm^3)**	f_{res} **(MHz)**	**Temp. Range (K)**
^{3}He	31	14	0.5-100
^{4}He	33	28	2-200
Inferno	250	36	293-800

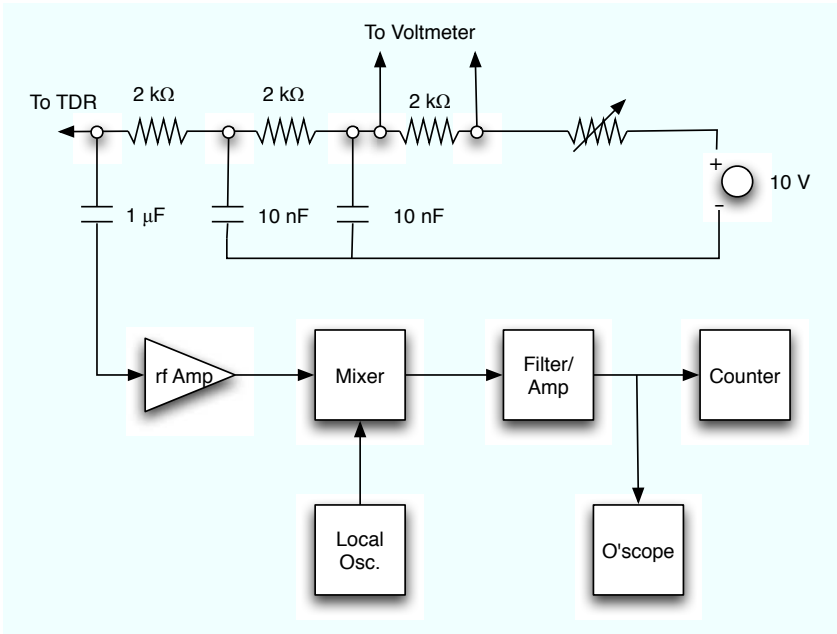

Figure A.2 Room temperature electronics for the tunnel diode.

Figure A.2 is a circuit diagram of the biasing supply and a block diagram of the room temperature electronics used in collecting the TDR data. This is a simplified version of the bias supply, as it omits an op-amp that may be used to further stabilize the voltage. However, with such a circuit, it is possible to obtain the highest sensitivity as VanDegrift showed [VanDegrift (1975b)]. The 10 nF capacitors in conjunction with the 2 kΩ resistors act as low pass filters, shunting frequencies on the order of 50 kHz and greater to ground. If more stringent ac filtering is required, a π-filter (an inline inductor with each end capacitively connected to ground) can be used. A voltmeter can be employed to monitor the bias voltage being applied to the TDR. The 1 μF capacitor acts as a high pass filter, shunting the rf signal from the low temperature circuit to an amplifier. The amplified signal is fed into a mixer where it is subtracted from a fixed local oscillator frequency. The resulting mixed frequency is in the kHz band. This kHz signal is filtered and amplified before being sent to a counter and an oscilloscope. In principle the oscilloscope is not necessary, as the information is extracted from the frequency of the oscillations. What the oscilloscope offers is the chance to observe the waveform and assure

oneself that there are no or few harmonics mixed into the main signal. The actual instruments used in these experiments are listed in Table A.2.

Table A.2 Commercial electronics used in this work

Instrument	**Use**	**Specifications**
MITEQ AU-1494	rf Amplifier	1-200 MHz, 58 dB
MiniCircuits ZX05-1-S+	Mixer	0.5-500 MHz input, 7dB drop
Agilent 33250A	Local Oscillator	0-80 MHz, 0.01-10 V
SRS 560	Filter & Preamp	variable BP filter DC-1 MHz, up to 5×10^4 amplifier
Agilent 53131A	Counter	up to 225 MHz input frequency
Agilent 54622A	Oscilloscope	100 MHz dual channel

APPENDIX B. Thermal Response of Materials to the rf Probe Field

Introduction

As was stated in Ch. 1, the energy scales associated with the rf excitation field are very small – both the amplitude and the frequency contributions being ≤ 1 mK in thermal equivalent units. However, in the cobalt doped $GdFe_2Zn_{20}$ samples it was noticed, quite by accident, that at base temperature as the magnetic field was swept up, the temperature of the sample dropped by approximately 100 mK. This temperature shift precisely correlates to the susceptibility of the sample, as shown in the blue curve of Fig. B.1. This behavior was seen in the aluminum doped samples as well. From Fig. B.2, where the temperature of an aluminum doped sample is plotted versus time as the rf field is turned on and off, it is evident that this effect is related to the presence of the rf excitation field. Given the obvious dependence of sample temperature on (a) the magnitude of the susceptibility and (b) the presence of the rf excitation field it was decided to try pin down the specific source of this effect. There are two possibilities.

First, the thermal effect (TE) could be associated with the power dissipated by the shielding currents induced in the skin-depth layer. Jackson (1998) shows that the time averaged power per volume associated with this effect is

$$P_{res} = \mu \pi f H_0^2 e^{-2z/\delta}. \tag{B.1}$$

H_0 is the magnitude of the rf field, f is the frequency of oscillation, μ is the magnetic permeability of the sample, and δ is the skin depth. z represents the depth to which the oscillating field penetrates the sample. In the case of a long thin rod with the excitation field parallel to the long axis, the power dissipated per length is proportional to $\mu \rho f$. For a sphere, after integrating by parts and assuming that the power density dissipated follows the form of Eq. B.1

throughout predicts that the total power dissipated should be

$$P^T = \frac{1}{2} A_s H_0^2 \sqrt{\pi \rho \mu f}. \tag{B.2}$$

In the above, A_s is the surface area of the sphere. An important prediction is that the power dissipated should vary like the square of the amplitude of the rf field and the square root of the magnetic permeability. As the static field is increased the AC permeability drops, and the power dissipated drops. If we assume the magnetic permeability is inversely proportional to the applied field, then the power dissipated should increase in as the field is lowered, so this is a feasible scenario.

The second possibility is that the remagnetization of the magnetic moments in response to the rf field has a large decrease in entropy associated with it. The magnetic moments release this entropy to the lattice, resulting in an effective heating of the sample. As the static field is increased, the ac susceptibility decreases and the remagnetization process is inhibited. This leads to a drop in entropy released to the lattice and a decrease in the heating. Invoking this mechanism requires considerable coupling between the spins and the lattice. It also requires the spins to have time to relax before the rf field changes direction. Samples with a large magnetic susceptibility at a given frequency satisfy this requirement. In this scenario the rate of change of entropy should be directly proportional to the frequency of the rf field, therefore the change in temperature should also be directly proportional to the frequency. The entropy should also be directly proportional to the magnitude of the rf field. Finally, the change in entropy (and power dissipated) should vary like $1/H_{static}$. It can be expected that the temperature would vary like $1/H_{static}$ as well.

The true test, then, for which mechanism is responsible for the heating is a frequency resolved measurement coupled with a varying rf amplitude. A slightly simpler test is to take a metal with no magnetic order and turn the rf excitation on and off to see if there is an effect on the temperature. Further, an insulating ferromagnet with a field dependent susceptibility will allow one to discriminate if the magnetic moments do play a direct role in the observed TE or if the effect seen in the doped $GdFe_2Zn_{20}$ samples is due only to the effect of the permeability on the skin depth.

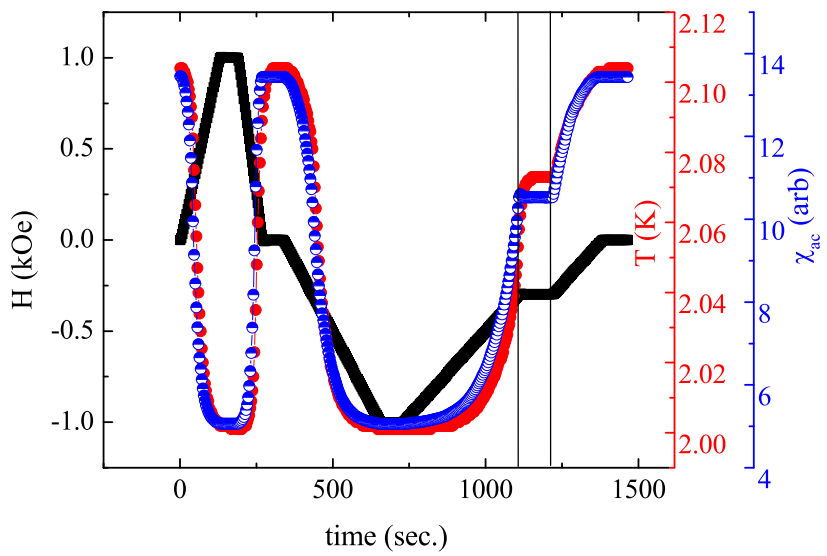

Figure B.1 Magnetic field (solid line, left axis), sample temperature (filled circles, right axis), and magnetic susceptibility (half-filled pentagons, far right axis) vs. time for $Gd(Fe_{0.5}Co_{0.5})_2Zn_{20}$. The correlation between the sample temperature and susceptibility is clear. Vertical bars near 1250 seconds denote the time period where the field was held at a non-zero, constant value.

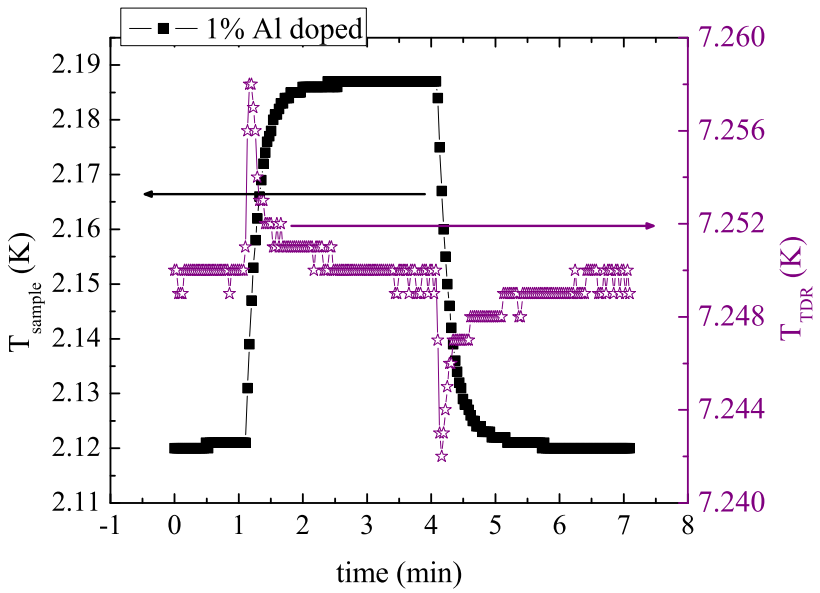

Figure B.2 Sample temperature (left axis, solid symbols) and TDR temperature (right axis, open symobls) vs. time for 1% Al doping in $GdFe_2Zn_{20}$. Initially the rf excitation field was off. At approximately 1 minute the circuit was set resonating and the temperature was allowed to reach a steady state. The rf field was turned off again at 4 minutes, and the temperature relaxed to the time=0 value.

Regardless of the source of the power (whether magneto-caloric or skin depth heating), the data on the doped $GdFe_2Zn_{20}$ systems demonstrate that the magnetic permeability is a key player. Further, for the TE to be observable the material must have a low heat capacity, C. If C is large then the extra heat deposited into the system will go to changing the entropy rather than the temperature. Therefore, the effect should not be visible at higher temperatures. Another consideration is the proximity to a second order phase change. If the sample in question undergoes a para- to ferromagnetic phase change close to the measurement temperature, the heat capacity of the sample will be large and the magnitude of the TE is expected to be small. The final consideration is the size of the sample relative to the sample holder. If the sample is small it may not generate enough heat to measurably affect the sapphire and heater block used in this experiment. In this sense, a better way to perform the experiment is to mount the sample directly to a thermally isolated thermometer and then apply the rf and static fields. Still, it is evident that the TE discussed herein is measurable in some materials with the current equipment.

Experimental Details

Six materials were chosen for this experiment in an attempt to unambiguously identify the source of the TE: $GdFe_2(Zn_{0.979}Al_{0.021})_{20}$, $CeVSb_3$, $YTiO_3$, GdPtIn, YFe_2Zn_{20} and Cu. The first is seen to have a large and strongly field dependent χ at low temperatures. Further, it is believed to have a band magnetism component. $CeVSb_3$ is a metallic local moment ferromagnet with almost zero low temperature field dependence in χ. Field dependent χ measurements suggest there is an aspect of the magnetism with considerable fluctuation. $YTiO_3$ is an insulating ferromagnet, but due to orbital ordering, the susceptibility remains large at low temperatures. It also has a similar field dependence in χ when compared to an itinerant compound for low temperatures. If the TE is related to the remagnetization, then the $YTiO_3$ might be expected to show it as well. If, however, it is only related to the joule heating from the shielding currents the Cu sample will show the effect. GdPtIn is a local moment ferromagnet, and the field dependent data suggests that it is pure local with little or no band

enhancement. YFe_2Zn_{20} is the non-magnetically ordered parent compound of $GdFe_2Zn_{20}$. It exhibits a large Stoner enhancement of its conduction band as discussed in Ch. 5. All samples were approximately 0.75 mm^3 in volume. With the exception of copper, all samples were single crystals. The copper sample was cut with a shear from a plate purchased from McMaster-Carr. This original purpose of the plate was to build a stage on which the ^{4}He circuit was mounted. The cut piece of copper was washed in ethanol and acetone separately to remove any residual grease and/or oil from the cutting process. After a rinse in distilled water, the sample was etched with a 1:1 mixture of nitric acid and distilled water three times in an attempt to remove any surface impurities resulting from the cutting. After each etching, the sample was washed throughly in distilled water. When magnetic order was present, the magnetic easy axis was aligned with the rf field.

Results and Discussion

The TE observed in the doped $GdFe_2Zn_{20}$ is not seen in any serious or conclusive way in Cu, $YTiO_3$, or GdPtIn. (Figs. B.3, B.4, and B.5). Based solely on the energy considerations from Ch. 1 the size of the temperature shift seen in Cu is consistent with expectations given the relatively low permeability expected for this material. Further, the weak effect seen in the $YTiO_3$ suggests that the TE is not just from remagnetization processes. This is a much weaker conclusion, though, because it is difficult to estimate the absolute value of the moment change from the rf field due to a lack of knowledge of the precise value of the rf amplitude. However, this amplitude, and the subsequent moment change, should be quite small.

That the effect is not connected with magnetic order is evident from YFe_2Zn_{20}. The heating effect is seen quite obviously in Fig. B.6. Cycling the rf field on and off induces a 20 mK temperature change. This is somewhat smaller than that seen in the doped $GdFe_2Zn_{20}$, however it is substantially larger than what is seen in either Cu, $YTiO_3$ and GdPtIn.

The results of $CeVSb_3$ are more interesting. Even though the compound exhibits strong local moment behavior and the low temperature susceptibility is not strongly field dependent, the effect on temperature of the rf field is obvious. This suggests that the TE discussed herein

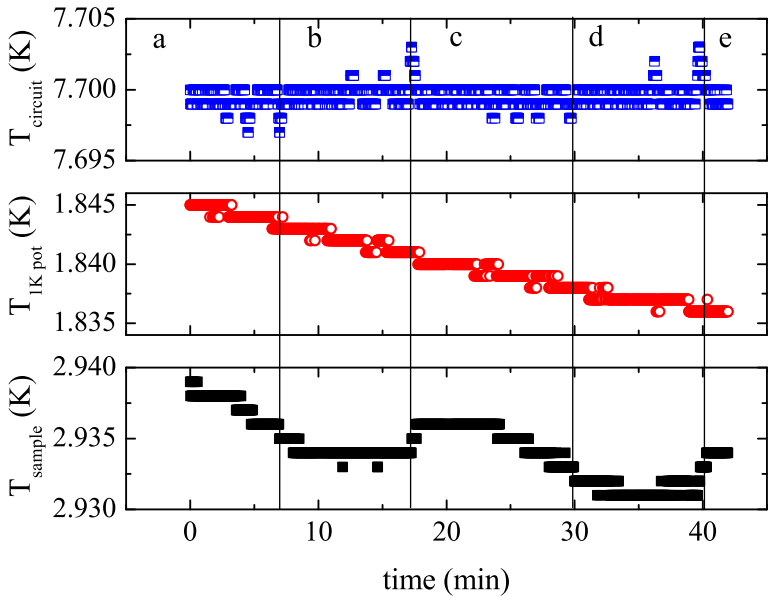

Figure B.3 Circuit, 1-K pot, and sample temperature vs. time for a copper sample as the rf excitation field was cycled on and off. At time=0 the rf field was on. From a-e the rf field cycled between on, off, on, off, and on. Initial tests suggested the effect was small, so to mitigate any possible change in heat load due to the changing power dissipated in the circuit itself, the bias voltage on the diode was change very slowly.

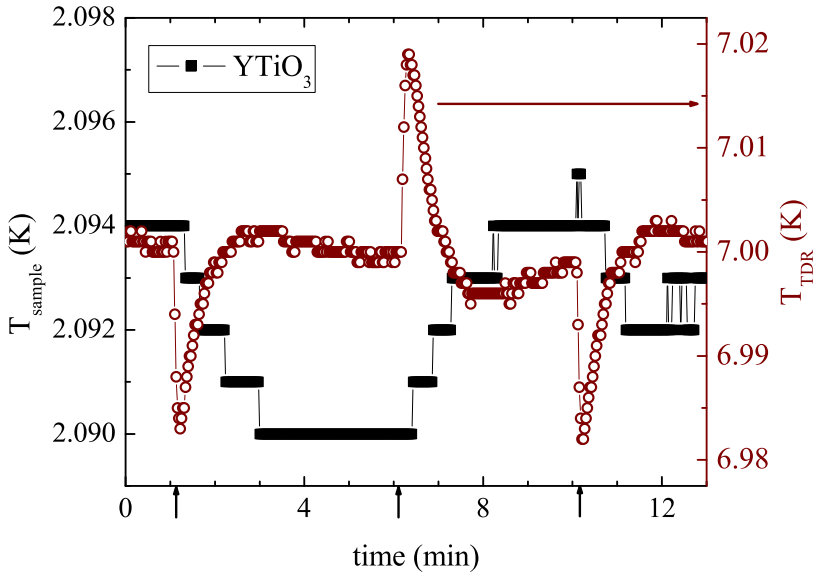

Figure B.4 Response of the temperature of $YTiO_3$ with the rf field cycled between on-off-on (left axis, solid symbols) and the TDR temperature (right axis, open symbols). The effect is quite small, even with the heat pulse from rapidly changing the bias on the circuit.

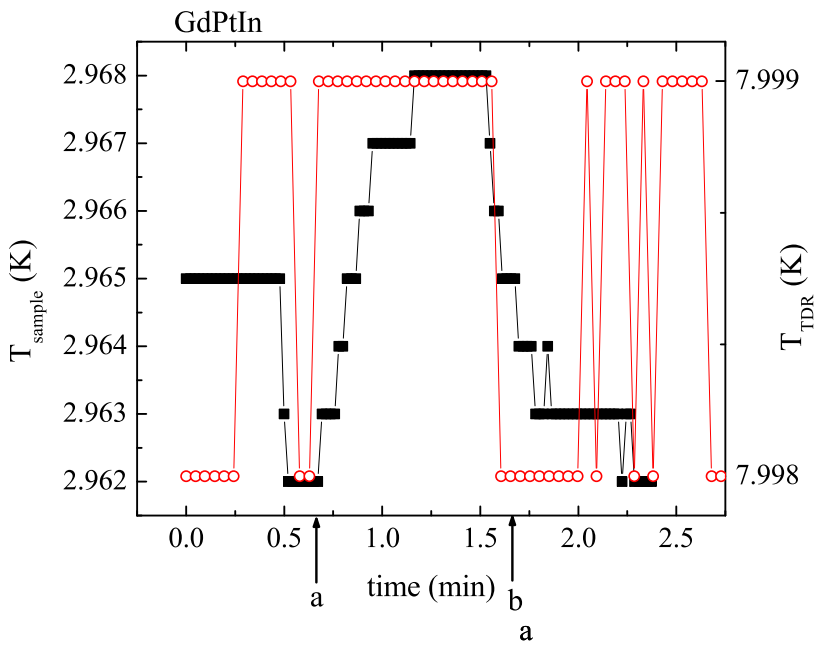

Figure B.5 Temperatures of GdPtIn (left axis, solid squares) and the circuit (right axis, open circles) vs. time as the bias voltage was increased. At the time marked 'a' the circuit began resonating. At 'b' the resonance switched off due to overbiasing.

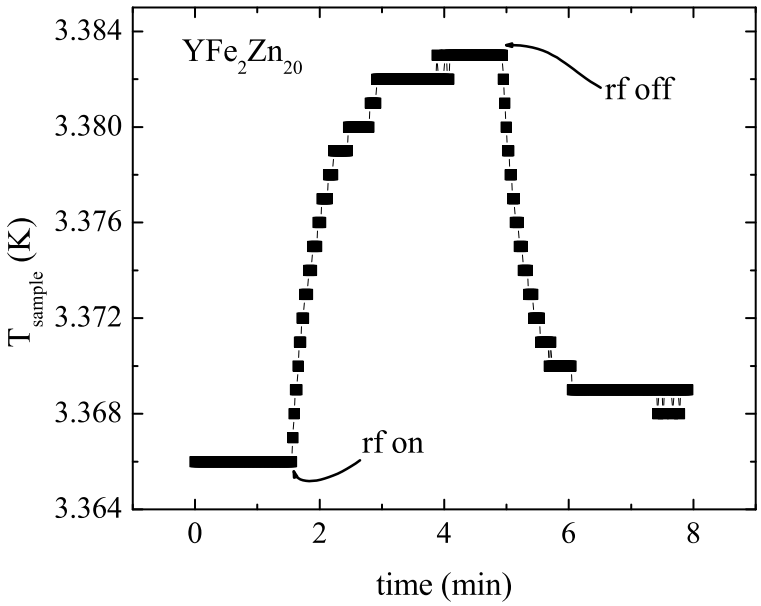

Figure B.6 Sample temperature vs. time for YFe_2Zn_{20} as the rf field was cycled on and off.

is due to the presence of ferromagnetic order in a metal.

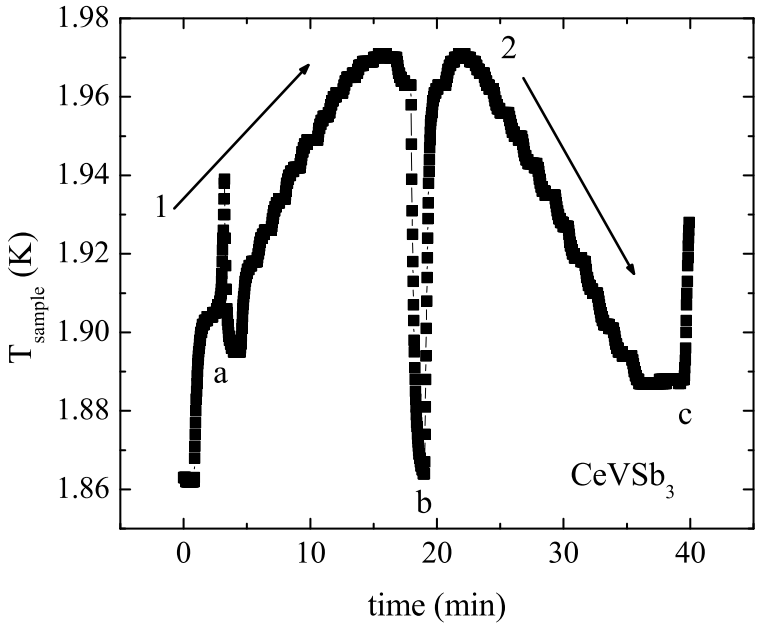

Figure B.7 Sample temperature for a 1 mm^3 single crystal of $CeVSb_3$ vs. time as the bias voltage is adjusted. The arrows labeled 1 and 2 are for increasing and decreasing bias voltages, respectively. The rf field was off at time=0.

Figure B.7 presents the temperature of the sample versus time as the bias voltage is adjusted. Initially the rf field was off due to under biasing the circuit. The peak at 'a' indicates the resonance turned on. The bias was then reduced to bring it to a minimum value. Biasing was increased in approximately 100 mV steps until the resonance turned off at the negative peak 'b.' A frequency dependent measurement was attempted for this material over a very narrow window. By changing the bias voltage on the tunnel diode it is possible to change the resonant frequency by a small amount. Even with this small change in f, there is a correlation between f and ΔT, as shown in Fig. B.8. It is not strictly linear in f nor is it even monotonic. Such non-monoticity can be accounted for by realizing that as the bias point moves along the

$I - V$ curve (Fig. 1.2) the amplitude of the rf field also changes. The rf amplitude might be expected to be very nearly constant over most of the range of suitable bias values. At the extremes the absolute value of the slope of the $I - V$ curve decreases. If the voltage oscillation about the bias point is of fixed amplitude for all bias points, then for lower slopes a smaller ΔI results. It is this change in the passed current that accounts for the amplitude of the radio frequency field. Therefore, at the extreme bias voltages, the amplitude of the rf field may be expected to decrease. Through the middle of the bias voltages, though, one is tempted to assume the rf field maintains a fixed peak to peak amplitude.

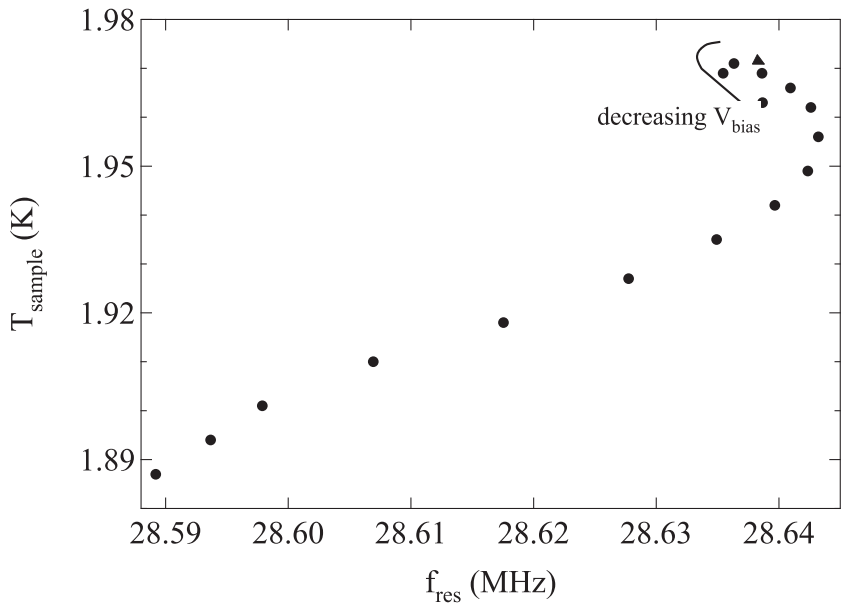

Figure B.8 Sample temperature vs. resonant frequency for $CeVSb_3$. The arrow indicates the direction of decreasing bias voltage.

However, this appears not to be the case. The sample temperature is directly proportional to the bias voltage, only becoming non-monotonic at the highest bias values (Fig. B.9). These points on the temperature downturn correspond to resonances that were especially unstable, changing as much as 500 Hz in a matter of seconds, a consequence of being marginally biased. It might be argued that since the bias voltage is increasing more power is being dissipated in the other circuit elements as well as the coil itself. This argument is laid to rest by noting that

once the resonance is shifted off, either by over or under biasing, the temperature of the sample drops (Fig. B.7). Referring to Fig. 1.2, the curvature of the TD $I - V$ plot is much greater near the peak current when compared to the valley at higher bias voltages. This can account for the continued monotonic behavior down to the lowest resonating biases as the crossover from negative to positive slope occurs over a much smaller voltage window.

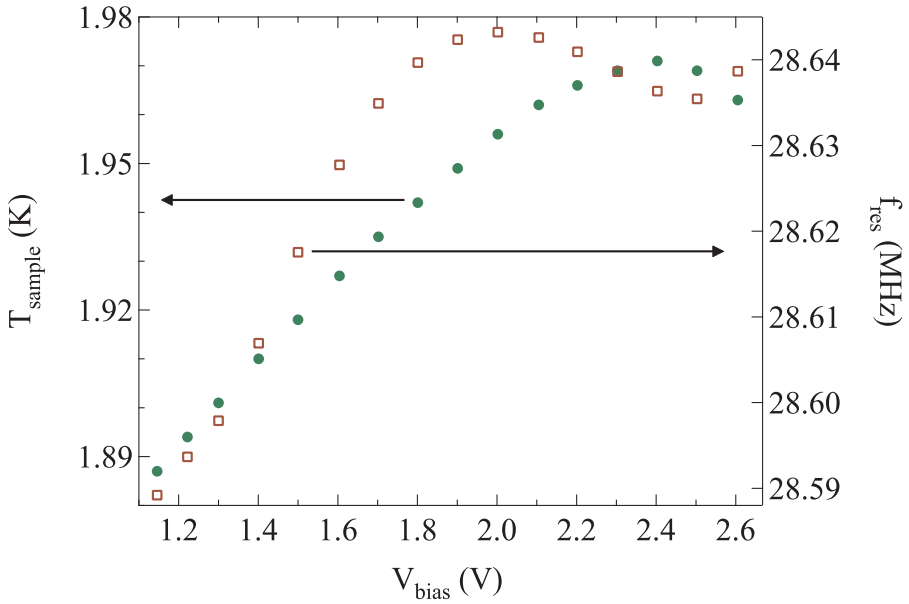

Figure B.9 Sample temperature (left axis, filled circles) and resonant frequency (right axis, hollow squares) vs. bias voltage for $CeVSb_3$. The lower and upper voltage points denote the resonance window.

Conclusions

Magnetically soft, highly permeable metals show a pronounced thermal effect in response to an rf field. The ferromagnetic insulator $YTiO_3$ does not manifest this effect even though it is a highly polarizable material at low temperatures. This effect is due to the Joule heating from the screening of the rf field by the conduction band electrons. A comparison of the heat dissipated in copper and YFe_2Zn_{20} as the rf field is cycled on and off shows that the

conduction band must have a high polarizability for the effect to be observable. Given the very small amplitude of the rf field ($\leq$ 6 mOe, estimated) the polarizability requirement is not too surprising.

All these observations taken together suggest that for the rf heating to be manifest in the TDR measurements the conduction band electrons must have a fairly large polarizability. These data suggest that $CeVSb_3$ has a highly polarizable conduction band, even though the magnetism is strongly localized on the cerium sites. In a manner similar to the cobalt and aluminum doped $GdFe_2Zn_{20}$ the conduction band may be polarizable in low fields, but show saturation in somewhat larger fields. Therefore, static measurements may mask the low field, dynamic response of the materials under consideration. Even though the measured Stoner enhancement is low, the materials are still dynamically very active for sufficiently low H.

Given the requirement of passive heating to observe this effect coupled with the varying heat link and base temperature from run to run, it is difficult to make any systematic comparison between different samples. Still, the fortuitous discovery of the rf heating may offer another avenue to explore the nature of the differences between band and local moment magnetism. An experimental system optimized to passively heat the sample to a certain temperature would allow for a better estimate of the power dissipated in a given sample. From a series of such measurements on differently sized samples it may be possible to determine the amplitude of the rf field which would allow for a second method to determine the magnetic permeability in a sample. Such a study would be very valuable for determining how band magnetism behaves.

APPENDIX C. Shubnikov-de Haas Oscillations in Ce- & $SmAgSb_2$

Measurements of quantum oscillations in the resistivity, Shubnikov-de Haas (SdH) oscillations, are among the primary techniques to study the geometry of the Fermi surface in metals. Electron transport depends on the density of states and the scattering rates. The density of states is modulated by the Landau quantization. Within the standard theory [Shoenberg (1984)] for a three-dimensional Fermi surface the amplitude of the rth harmonic oscillatory part of the resistivity is given by

$$\alpha_r \propto \frac{m_c S_{extr} B^{1/2}}{|S''|_{extr}^{1/2}} R_T(r) R_D(r) R_S(r) \tag{C.1}$$

where m_c is the cyclotron mass, S_{extr} is the extremal cross section of the Fermi surface (FS) perpendicular to the applied field, $|S''|_{extr} = (\partial^2 S/\partial p_B^2)_{extr}$ is a measure of the FS curvature along $\mathbf{B}$ at the extremal cross section, and the damping factors R_T, R_D, and R_S are caused by finite temperature, scattering, and Zeeman splitting respectively. The corresponding fundamental frequency is

$$f = \frac{S_{extr}}{he}. \tag{C.2}$$

Such oscillations are generally difficult to measure in three-dimensional metals, especially if the metal is highly conducting. Conventional four–probe resistivity measurements on a highly conducting metal require relatively high currents to generate measurable voltages. If contact resistance, i. e. the resistance across the joint connecting the current lead wires to sample, is large, the increased current will lead to sample heating. The problem is exacerbated for small crystals where attaching contacts is not an easy task. Further issues arise in materials with a small cyclotron mass, giving rise to a reduced amplitude of the SdH signal. The TDR allows for a contactless measurement of the resistivity and changes therein by probing the skin depth (Eqs. 1.1 and 1.17).

In large magnetic fields far from any possible ordering effects, where $\mu \approx 1$, the magnitude of the skin depth at 13 MHz can be estimated by

$$\delta[\mu\text{m}] = 15\sqrt{\rho[\mu\Omega \text{ cm}]}. \tag{C.3}$$

For crystals with a typical size $R = 500$ μm, the upper limit of the resistivity that the TDR used here can probe can be estimated by equating $\delta = R$. This gives $\rho_{max} \approx 1000$ $\mu\Omega$ cm. The lower bound on resistivity is reached when the skin depth becomes smaller than the mean free path, l, and the local Ohm's law is no longer valid. This is the anomalous skin effect. An estimate on this lower bound can be made using a Drude approximation where l is given by

$$l = \frac{(3\pi^2)^{1/3}\hbar}{n^{2/3}e^2\rho}. \tag{C.4}$$

n is the electron density and e is the electron charge. Combining equations 1.1 and C.4 one obtains

$$\rho_{min} = \left(\frac{\mu f \pi^{7/3} 3^{2/3}\hbar^2}{n^{4/3}e^4}\right)^{1/3} \approx 8.6 \times \frac{(\mu f)^{1/3}}{n^{4/9}}. \tag{C.5}$$

For a typical nonmagnetic metal with $n = 5 \times 10^{28}$ m^{-3} and $f = 10^7$ Hz, $\rho_{min} \approx 0.03$ $\mu\Omega$ cm. Therefore, a direct quantitative study of the contactless resistivity in small crystals in the range 0.03-1000 $\mu\Omega$ cm is possible. This range covers most metallic materials of interest. In the regime of a highly conducting metal, the measured susceptibility is expressed by the linearized form of Eq. 1.17,

$$4\pi\chi_{TDR} = \frac{\mu\delta}{2R} - 1. \tag{C.6}$$

Agreement between the resistivity in $SmAgSb_2$ derived from skin depth and that measured via a direct 4-probe technique is very good, as seen in Fig. C.1. Under the assumption that $\mu = constant$, Eq. 1.17 can be recast as

$$4\pi\chi_{TDR} = G\sqrt{\rho} - 1. \tag{C.7}$$

For this experiment the constant G was determined by comparing χ_{TDR} at two temperatures ($T_1 \approx 0.5$ K and $T_2 \approx 12$ K) with ρ determined from conventional measurements. A single G was then used to convert the TDR data to resistivity. This procedure was employed because the ^{3}He system did not have an extraction mechanism when these data were collected.

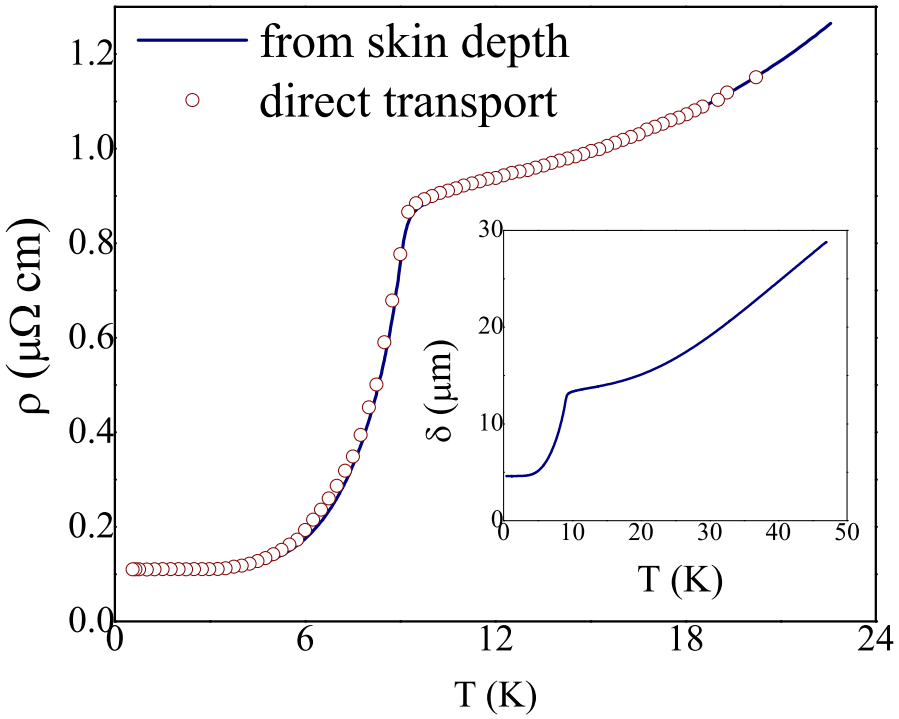

Figure C.1 Comparison of temperature dependent resistivity derived from skin depth (solid line) and 4–probe (hollow circles) in $SmAgSb_2$. *Inset:* Skin depth vs. temperature as measured by the TDR.

Presented here is field dependent data at different temperatures from slab shaped samples of Ce- and $SmAgSb_2$. Both crystals are tetragonal intermetallic compounds. $CeAgSb_2$ orders ferromagnetically at 9.8 K, whereas $SmAgSb_2$ orders antiferromagnetic ordering at 9.5 K. These materials, along with the other rare earth members of the family, has been studied before [Brylak et al. (1995), Sologub et al. (1995), Myers et al. (1999b), Myers et al. (1999a), Jobiliong et al. (2005)]. Direct measurements of SdH oscillations have been reported previously [Myers et al. (1999a)].

The technique is best suited to measurements of changes in χ_{TDR}, and by extension ρ. Observation of SdH oscillations is still sensitive to the residual resistivity in that if there is significant scattering in the sample, then the quantum oscillations will be suppressed. However, in terms of measuring small changes in ρ which are less than a few percent of the background, the TDR possesses another advantage, illustrated here. The amplitude of the measured resistivity oscillations is on the order of a few nΩ cm (see Fig. C.3), whereas the absolute value of the background resistivity is on the order of 100's of nΩ cm (as determined by conventional 4-probe transport measurements). Resolving changes on the order of 1% or less of the background signal can be difficult using normal techniques. This is especially evident as the temperature of the samarium sample is raised. Thermal scattering decreases the amplitude of the oscillations (Eq. C.1). This is coupled with an increase in the resistivity of the sample. The net result is a greatly diminished signal to noise ratio. However, the TDR measurement detects high field oscillations up to 9.5 K.

The power spectra obtained from a Fourier transform of the oscillations is relatively simple for the cerium compound with only one major frequency evident. Conversely, the samarium compound exhibits many frequencies associated with the extremal Fermi surfaces as seen in Fig. C.5. The main peaks are identified by the Greek letters α, β, and γ'. The orbit identified as γ' was first observed with the TDR. These results agree with Myers et al. (1999a) and detect the new orbit. This serves to further demonstrate the utility of the TDR in the study of metallic samples.

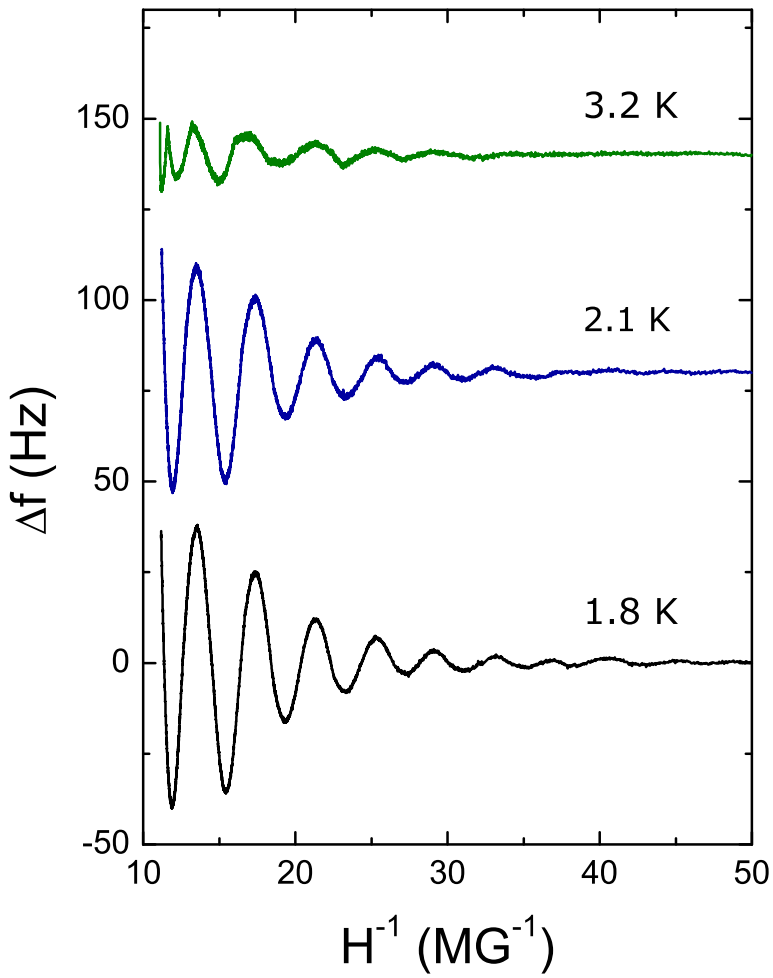

Figure C.2 Temperature variation of the resonant frequency oscillation amplitude in $CeAgSb_2$.

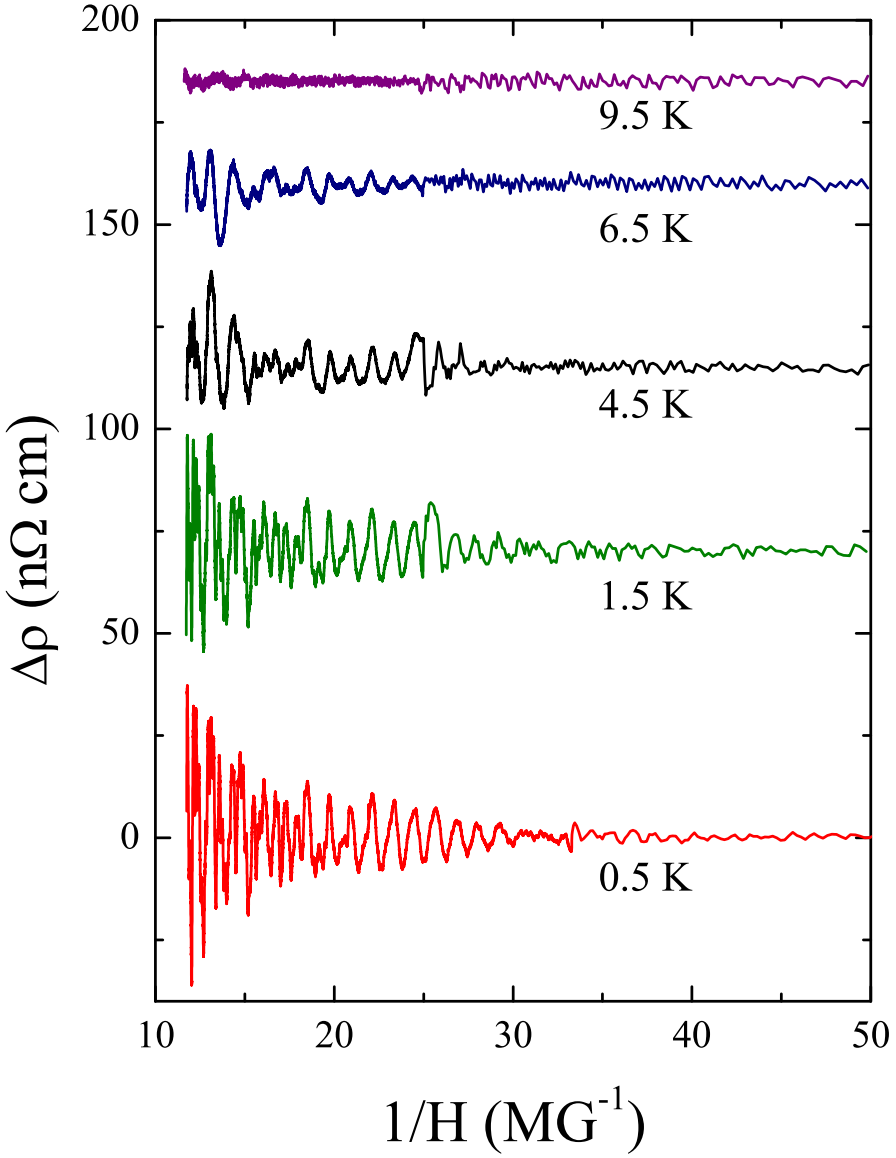

Figure C.3 Temperature variation of the oscillation amplitude in $SmAgSb_2$. Note the scale of $\Delta\rho$.

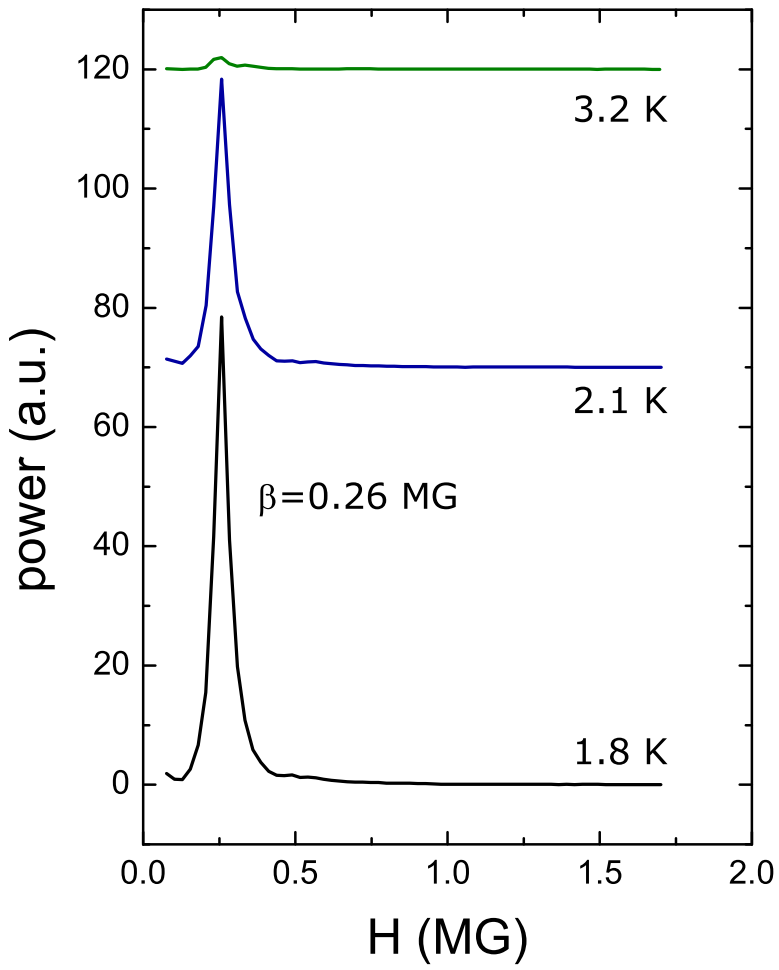

Figure C.4 Power spectrum of resistivity oscillations at three temperatures for $CeAgSb_2$.

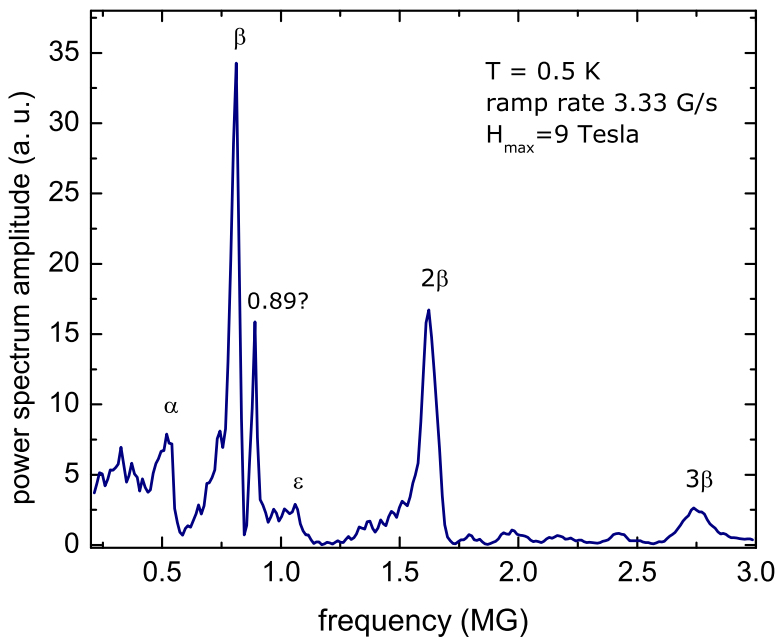

Figure C.5 Power spectrum of the resistivity oscillations at 0.5 K for $SmAgSb_2$. The peak at 0.89 MG derives from a newly observed hole orbit.

APPENDIX D. Multiferroic Compounds

Introduction

Recent years have seen a resurgence in the interest in magnetoelectric multiferroics (materials exhibiting simultaneous magnetic order and electric polarization) [Spaldin and Fiebig (2005)]. The possibility of controlling the magnetic subsystem via an electric field or vice versa could have significant implications for the field of information storage. Candidate materials that conclusively exhibit these properties are few in number, making detailed study of the physics involved rather difficult. One family of materials that is high on the list of potentials is the hexagonal rare earth system RMnO$_3$ (R=Ho-Yb).

The full rare earth series exists in either a hexagonal or an orthorhombic structure depending on the pressure and/or rare earth ion. The heavier, smaller rare earths (Ho-Lu) along with yttrium favor the hexagonal phase while the lighter and larger (La-Tb) tend toward the orthorhombic phase [Yakel et al. (1963)]. Normally, symmetry conditions would prevent the hexagonal phase from showing a linear magnetoelectric effect (ME), wherein an electric (magnetic) field can control the magnetic (electrical) properties of the system [Lottermoser et al. (2004)], however it has been demonstrated that hexagonal HoMnO$_3$ shows evidence of strong magnetodielectric coupling [Yen et al. (2005)].

An interesting aspect of HoMnO$_3$ is its rich $H-T$ phase diagram [Fiebig et al. (2002b) Lorenz et al. (2005)]. Frustration in the Mn sublattice has been cited as one reason for this richness. Fiebig et al. (2002b) claim that the other hexagonal RMnO$_3$ compounds with partially filled $4f$ shells exhibit phase diagrams comparable to HoMnO$_3$ as determined from second harmonic generation. That there are multiple phase transitions is presented by Fiebig et al. (2002a) and Fiebig et al. (2003). However, published magnetization, magnetic susceptibility,

and dielectric constant data [Yen et al. (2005)] seem to contradict this statement . It may be that the latter measurements lacked sufficient sensitivity to detect the phase changes. Fiebig et al. (2002a) label one of the phase transitions in $ErMnO_3$ as "hidden," hinting at its aversion to detection. It has been speculated that the large Ho^{3+} moment better couples to the Mn^{3+} moments and may thus provide some explanation for the differences in diagram complexity and detectability of the transitions [Fiebig et al. (2002b)].

Unlike the other hexagonal members of this family, $DyMnO_3$ has received little attention. This member is usually encountered in the orthorhombic structure, but it can also be synthesized in the hexagonal [Kamegashira et al. (2004), Ivanov et al. (2006)]. Dy^{3+} with an even larger free ion moment than Ho^{3+} may be expected to manifest properties similar to holmium if the coupling between the Mn-$3d^4$ and $R-4f^n$, where n represents the filling of the f shell, moments is driven mainly by the size of the moment. The $H-T$ phase diagram for the orthorhombic structure has been mapped [Kimura et al. (2005)], and the properties extensively studied [Goto et al. (2004), Laverdière et al. (2006), Feyerherm et al. (2006), Prokhnenko et al. (2007)]. Therefore, the dysprosium compound offers a stage on which the effects of structural differences and rare earth moment size on the magnetic order and any ME can be explored.

Single crystal samples of hexagonal Dy- and $HoMnO_3$ were grown via a floating zone method [Ivanov et al. (2006)]. Samples were first cut into plates with a wire saw and orientation was verified via Laue diffraction. From the oriented plates smaller pieces were cut with a blade for the resonator samples. The holmium sample was a planar right triangle with dimensions of $0.7\times0.7\times0.06$ mm^3 while the dysprosium sample was a rectangular plate with dimensions of $1\times0.75\times0.3$ mm^3. The smaller sample was mounted on one end of a 20 mm long by 1 mm diameter sapphire rod with low temperature grease. The opposite end of the sapphire was secured in a copper heater block where temperature was monitored with a negative temperature coefficient resistance thermometer. Sample and sapphire were then inserted into the coil of the LC tank circuit of the TDR mounted on a ^{3}He cryostat. The entire low temperature part of the setup was enclosed in a vacuum can permitting independent control of the circuit and sample temperatures. The cryostat was placed in the bore of a superconducting magnet.

The static bias and rf excitation fields both were aligned parallel to the c-axis. All data was collected as temperature sweeps in constant field.

Phase Diagrams for Hexagonal $HoMnO_3$ and $DyMnO_3$

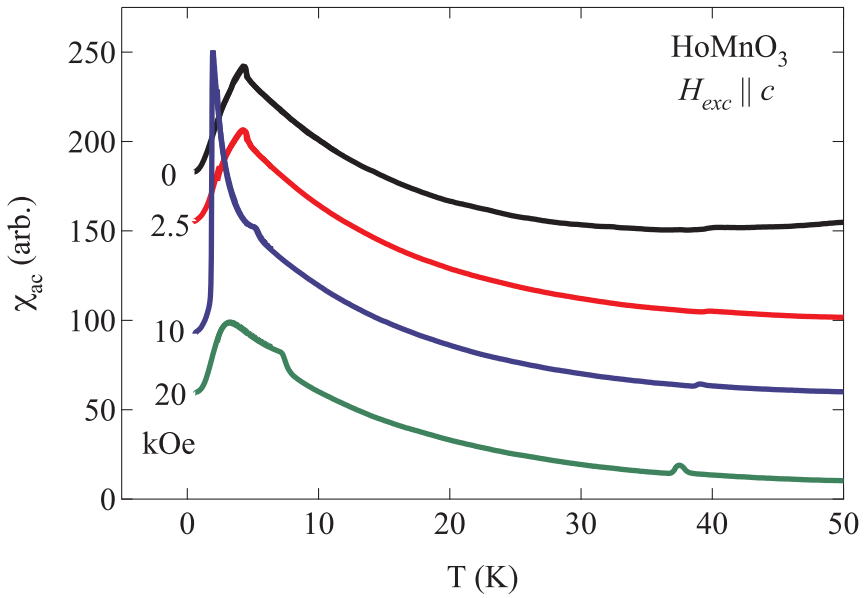

Figure D.1 AC susceptibility of $HoMnO_3$ measured parallel to the c-axis in different static magnetic fields. Curves are offset for clarity.

Figure D.1 presents the magnetic susceptibility versus temperature for $HoMnO_3$ in four applied static fields. The zero field curve shows an obvious phase change near 4.5 K and a weaker feature near 40 K. Application of a modest field (2.5 kOe) does not appreciably change the temperature dependent susceptibility. As the static field is further increased, more features of different types become evident. Each feature is associated with a change in the magnetic order of either the holmium or manganese spins or both.

Previous works have used an onset criterion for delineating phase boundaries in this material [Lorenz et al. (2005), Yen et al. (2005)]. Here a different set of criteria is used, as illustrated in Fig. D.2. When a well-defined peak is present, the temperature of that peak is taken as the critical temperature for the phase transition (T_4). In the absence of an obvious peak,

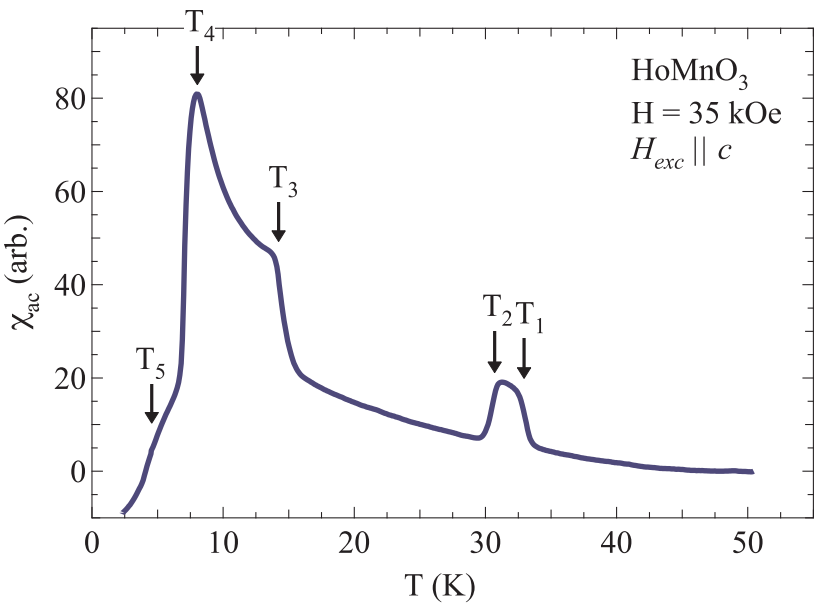

Figure D.2 35 kOe temperature sweep for $HoMnO_3$ along the c-axis with features associated with phase changes marked by $T_1 - T_5$.

linear extrapolation of the $\chi - T$ curves on either side of the transition is done ($T_1 - T_3$). The intersection of these extrapolated curves is taken as the critical temperature. Inflection points marking a change from an increasing to a decreasing slope (T_5) are also identified as being associated with changes in magnetic structure. The difference between these two sets of criteria do not affect the conclusions of this work.

Figure D.3 is the $H-T$ phase diagram for $HoMnO_3$ as determined via TDR measurements. For comparison the phase diagrams from Lorenz et al. (2005) and Yen et al. (2005) have been digitized and added. Figure D.4 is an expanded view of the low temperature region of Fig. D.3. The similarities between the TDR phase diagram and the published versions is striking. The difference in the high temperature lines is ascribed to differences in sample quality. What is intriguing about the low temperature region is that certain magnetic susceptibility points detected by the TDR more closely correspond to anomalies previously detected via dielectric constant measurements (bowties in Figs. D.3 and D.4). To be sure, not every feature seen via dielectric measurements is present in the TDR, but that may be due to selection criteria. It is

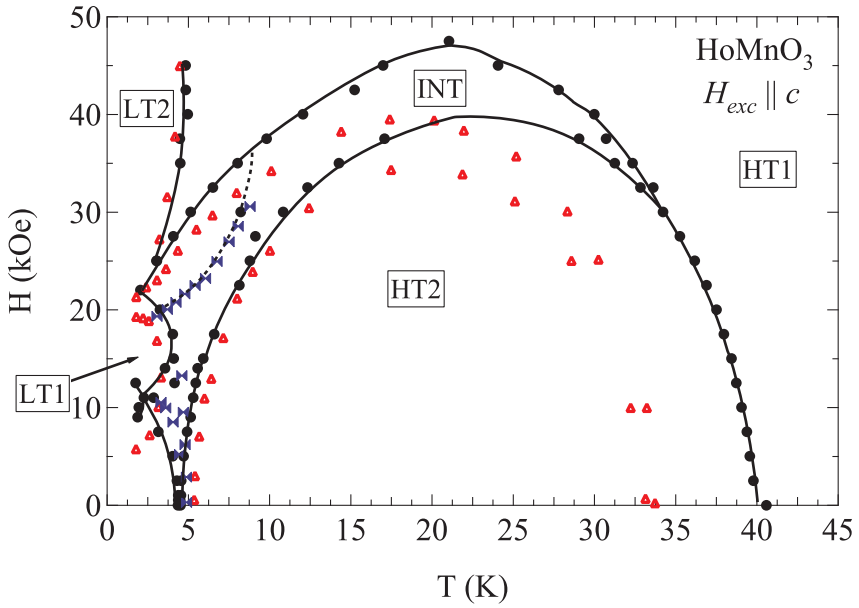

Figure D.3 Phase diagram for $HoMnO_3$ measured along the c-axis. Solid circles are phase changes detected with the TDR. Open red triangles are defined phase transitions digitized from Lorenz et al. (2005). Blue bowties are anomalies in dielectric constant digitized from Yen et al. (2005). Lines are guides to the eye, and labeled phases follow the convention of Lorenz et al. (2005).

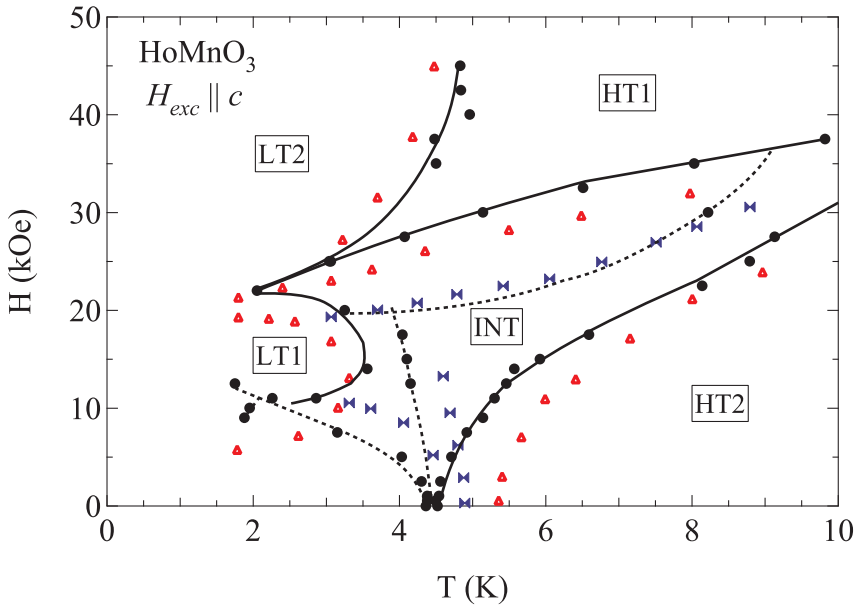

Figure D.4 Low temperature detail of the phase diagram show in Fig. D.3.

evident, though, that the TDR is quite capable of detecting the many phase changes seen in $HoMnO_3$.

Fig. D.5 presents the $H - T$ phase diagram from $HoMnO_3$ with the static and rf fields applied in the basal plane. No intermediate phase transition is observed as for the c axis data. The high temperature transition evolve with field in a manner quite different from the perpendicular orientation, however comparison with Fig. D.7 shows that there are some similarities between $DyMnO_3$ and $HoMnO_3$ phase diagrams.

Fig. D.6 presents χ versus T data for hexagonal $DyMnO_3$ in five applied static fields. The zero field similarity between the dysprosium compound and the holmium analogue is obvious. The features in the Dy system are more subtle, however they can be picked out. As the static field increases more phase transitions are revealed. Using the same criteria as was used for the holmium, the phase diagram for hexagonal $DyMnO_3$ was created and is presented in Fig. D.7. The only previously published line [Ivanov et al. (2006)] is marked with open triangles. Dotted lines are through points that show a weak local maximum and may be associated with

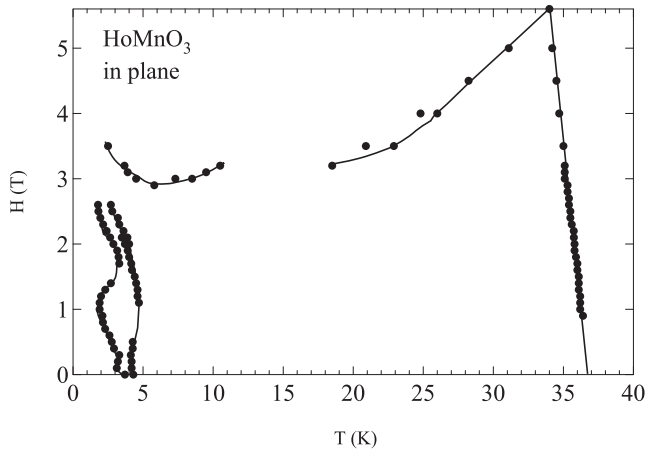

Figure D.5 Full phase diagram for $HoMnO_3$ measured in the basal plane.

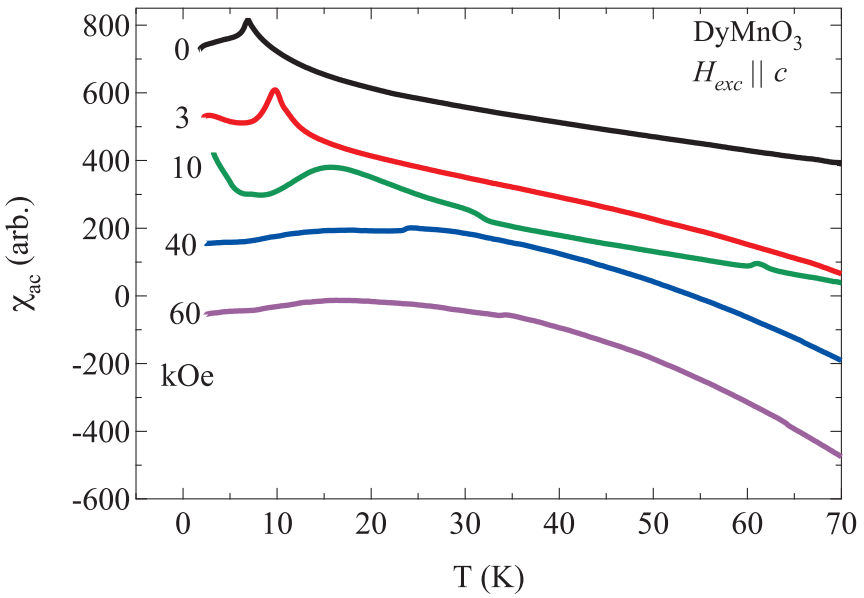

Figure D.6 χ vs. T for $DyMnO_3$ in five applied fields. The similarities between this compound and the holmium analogue are obvious.

a gradual reorientation of the magnetic moments rather than an abrupt phase change. This argument was put forth to explain similar soft features seen in $HoMnO_3$ [Yen et al. (2007)].

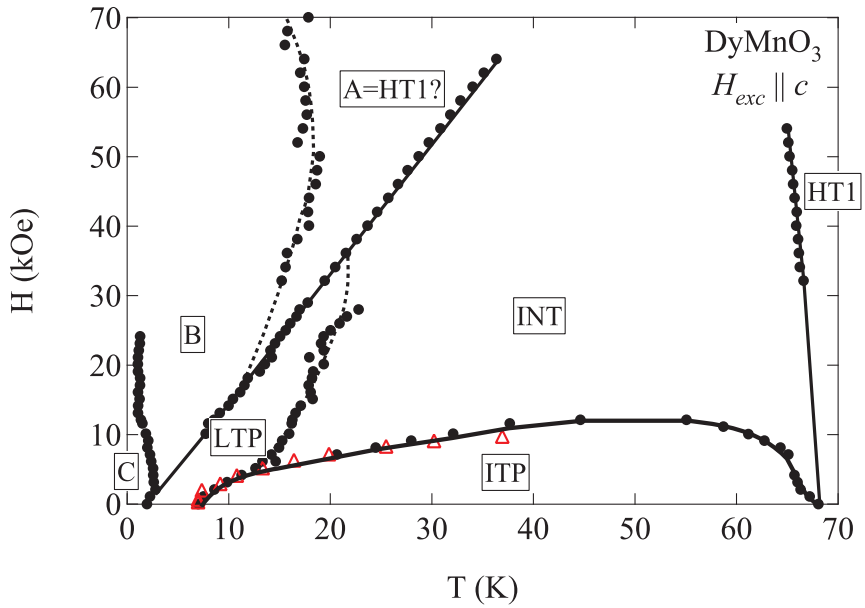

Figure D.7 Phase diagram for hexagonal $DyMnO_3$. Filled black circles are TDR data and open red triangles are from Ivanov et al. (2006). Phases ITP and LTP are named following Nandi et al. (2008). Phases HT1 and INT are labeled as such under the assumption that they are similar to the other hexagonal rare earth manganites.

Interpretation of the Results

Interpretation of the TDR data in magnetically ordered samples is subtle. It is known that for local moment ferromagnets at the Curie temperature, zero field χ goes through a very narrow maximum provided the magnetic easy axis coincides with the rf coil axis. It is also known that magnetocrystalline anisotropy manifests at T_C as a decrease in the growth of χ through T_C when measured perpendicular to the easy axis as compared with parallel (see Ch. 2). Further, in antiferromagnetic metals [Prozorov et al. (2006)] no maximum in χ is seen at the Nèel temperature, T_N, when the ordering axis is aligned with the rf coil axis.

This can be understood once the amplitude of the rf field is considered. Such a small field is not able to overcome the AFM exchange interaction. If a given moment responds to the probe field, the magnetic coupling between it and its neighbors leads to a compensation of the induced moment. Therefore, there is no bulk change in the magnetization of the sample and the measured susceptibility shows no large response. This may be considered some zero field limit of the low temperature behavior of $\chi_{||}$. The situation in metals is further complicated by the fact that a magnetic field in the rf is screened from the bulk of the metal, thereby reducing the effective sample volume probed. Therefore, it is unclear what sort of response to expect from an antiferromagnetically ordered sample probed perpendicular to the ordering axis. Fortunately for the current work the rf screening is not a problem.

The magnetic symmetries of many of the phases of $HoMnO_3$ have been determined via second harmonic generation experiments [Fiebig et al. (2002b)]. For the hexagonal rare earth manganites the rare earth ions occupy two distinct lattice sites within the $P6_3cm$ space group (2a and 4b) [Kamegashira et al. (2004)]. Each site may order differently from the other, depending on the temperature and field. Referring to Fig. D.3, phase HT1 has been identified as $P\underline{6_3}\underline{c}m$ wherein the 2a Ho ions are free and the 4b ions exhibit AFM order along the c-axis. In HT2, all rare earth spins are in an AFM structure still aligned with the c axis. The phase labeled INT has been identified as $P\underline{6_3}$ where all the spins are antiferromagnetically aligned in the basal plane Yen et al. (2007). Phase LT2 has been identified as $P6_3\underline{cm}$ with all rare earth moments ordered parallel to the c axis [Yen et al. (2007)]. The magnetic structure of phase LT1 has not been identified.

With the previously published magnetic symmetries at hand, we can begin to understand the TDR data. Referring to Fig. D.2, between temperatures T_1 and T_2 there is an obvious enhancement of the c axis susceptibility. This is also the INT phase. On either side the moments order aligned parallel to the c axis. With the moments ordering in the basal plane, as occurs in INT, the rf field is inducing a coherent deflection, and hence a larger susceptibility results. At T_3 the system reenters the INT phase and at T_4 there is a return to c axis ordering in the phase HT1. Down to T_4 the transitions are superimposed on a Curie-like background.

For temperatures less than T_4, however, there is a rapid decrease in χ. This would normally be associated with a fully ordered system. Based on the magnetic symmetry of the HT1 phase (which is presumed to exist in this region) there should be two free Ho moments. Normally these two spins would contribute significantly to χ. What can be inferred is that the impending full ordering of moments at T_5 leads to a slowing of the response of the free moments via exchange interactions.

Recent XRMS work on hexagonal $DyMnO_3$ has allowed the phases labeled ITP and LTP in Fig. D.7 have been assigned the magnetic symmetries of $P\underline{6_3}c\underline{m}$ and $P6_3\underline{cm}$ respectively [Nandi et al. (2008)]. The TDR data agrees with the XRMS data in the sense that both compounds exhibit similar features in χ on crossing similar phase boundaries. The phase changes seen in the Dy compound are much more subtle than those from the Ho. This suggests that the moment size is not as critical in determining the interaction between the rare earth ion and the underlying lattice. Phase C has been identified in Er- and $YbMnO_3$. In both of those compounds, as well as in the Ho version, this phase has the magnetic symmetry $P6_3cm$. In both the Er and Yb compounds the C phase is stable up to fields of approximately 0.5 kOe while in the Ho it exists all the way up to 10 kOe. If the Dy C phase has the same symmetry as the other members, then the low T, low H behavior is closer to Ho than Er or Yb. The transitions from INT to LTP and A to B are associated with weak maxima in χ. These may be more evident in dielectric measurements. The well defined phases observed in $DyMnO_3$ are qualitatively similar to the other RMnO$_3$ [Yen et al. (2007)].

BIBLIOGRAPHY

Ashcroft, N. W. and Mermin, N. D. (1976). *Solid State Physics*. W. B. Saunders.

Aslam, J. and Weyhmann, W. (1973). A tunnel diode NMR spectrometer. *Rev. Sci. Inst.*, 44(1):71.

Bartholin, H., Florence, D., Tcheng-Si, W., and Vogt, O. (1975). Magnetic properties of CeSb. *Phys. Stat. Solidi (a)*, 29:275.

Blundell, S. (2001). *Magnetism in Condensed Matter*. Oxford University Press.

Borca, C. N., Komesu, T., Jeong, H.-K., Dowben, P. A., Ristoiu, D., Hordequin, C., Nozières, J. P., Pierre, J., Stadler, S., and Idzerda, Y. U. (2001). Evidence for temperature dependent moments ordering in ferromagnetic nimnsb (100). *Phys. Rev. B*, 64:052409.

Boucherle, J. X., Givord, F., Lapertot, G., noz, A. M., and Schweizer, J. (1995). The magnetic structures of Ce_3Al_{11}: a single crystal study. *J. Mag. Mag. Mat*, 148:397–408.

Brylak, M., Moeller, M. H., and Jeitschko, W. (1995). Ternary arsenides ACuAs$_2$ and ternary antimonides AAgSb$_2$ (A=rare-earth elements and uranium) with HfCuSi$_2$-type structure. *J. Solid State Chem.*, 115:305.

Clover, R. B. and Wolf, W. P. (1970). Magnetic susceptibility measurements with a tunnel diode oscillator. *Rev. Sci. Inst.*, 41(5):617.

Coffey, T., Bayindir, Z., DeCarolis, J. F., Bennett, M., Esper, G., and Agosta, C. C. (2000). Measuring radio frequency properties of materials in pulsed magnetic fields with a tunnel diode oscillator. *Rev. Sci. Inst.*, 71(12):4800.

de Groot, R. A., Mueller, F. M., van Engen, P. G., and Buschow, K. H. J. (1983). New class of materials: Half-metallic ferromagnets. *Phys. Rev. Lett.*, 50(25):2024.

Drobac, D. (1996). Critical exponents from high-precision AC susceptibility data. *J. Magn. Magn. Mat.*, 159:159–165.

Engelhardt, L., Gass, I. A., Milos, C. J., Brechin, E. K., Murrie, M., Prozorov, R., Vannette, M. D., and Luban, M. (2007). Heisenberg model of an [Fe8]-cubane cluster. *Phys. Rev. B*, 76:172406.

Esaki, L. (1976). Discovery of the tunnel diode. *IEEE Trans. Elec. Dev.*, ED-23:644.

Escorne, M., Mauger, A., Ravot, D., and Achard, J. C. (1981). Transport properties of CeSb. *J. Phys. C: Solid State Phys.*, 14:1821.

Feyerherm, R., Dudzik, E., Aliouane, N., and Argyriou, D. N. (2006). Commensurate Dy mangetic ordering associated with incommensurate lattice distortion in multiferroic $DyMnO_3$. *Phys. Rev. B*, 73:180401(R).

Fiebig, M., Degenhardt, C., and Pisarev, R. V. (2002a). Interaction of frustrated magnetic sublattices in $ErMnO_3$. *Phys. Rev. Lett.*, 88:027203.

Fiebig, M., Degenhardt, C., and Pisarev, R. V. (2002b). Magnetic phase diagram of $HoMnO_3$. *J. App. Phys.*, 91:8867.

Fiebig, M., Lottermoser, T., and Pisarev, R. V. (2003). Spin-rotation phenomena and magnetic phase diagrams of hexagonal $RMnO_3$. *J. App. Phys.*, 93:8194.

Fisher, M. E. (1967). The theory of equilibrium critical phenomena. *Rep. Prog. Phys.*, 30(2):615–730.

Fox, J. N. and Trefay, J. U. (1975). Experiments using a tunnel diode oscillator. *Am. J. Phys.*, 43(7):622–625.

Garrett, J. D., Greedan, J. E., and MacLean, D. A. (1981). Crystal growth and magnetic anisotropy of $YTiO_3$. *Mat. Res. Bull.*, 16:145–148.

Gordon, R. T., Ni, N., Martin, C., Tanatar, M. A., Vannette, M. D., Kim, H., Samolyuk, G., Schmalian, J., Nandi, S., Kreyssig, A., Goldman, A. I., Yan, J. Q., Bud'ko, S. L., Canfield, P. C., and Prozorov, R. (2008a). Unconventional London penetration depth in $Ba(Fe_{0.93}Co_{0.07})_2As_2$ single crystals. submitted. preprint available at arXiv:0810.2295.

Gordon, R. T., Vannette, M. D., T., and Prozorov, R. (2008b). Itinerant magnetism and superconductivity in Y_9Co_7. in progress.

Goto, T., Kimura, T., Lawes, G., Ramirez, A. P., and Tokura, Y. (2004). Ferroelectricity and giant magnetocapacitance in perovskite rare-earth manganites. *Phys. Rev. Lett.*, 92:257201.

Habbal, F., Watson, G. E., and Elliston, P. R. (1975). Simple cryostat for measuring rf susceptibility from 4.2 to 300 K. *Rev. Sci. Inst.*, 46(2):192–195.

Ho, S. C., Maartense, I., and Williams, G. (1981). AC susceptibility and resistivity of the ferromagnetic phase of PdMn. *J. Phys. F*, 11:699–710.

Ivanov, V. Y., Mukhin, A. A., Prokhorov, A. S., Balbashov, A. M., and Iskhakova, L. D. (2006). Magnetic properties and phase transitions in hexagonal $DyMnO_3$ single crystals. *Phys. Solid State*, 48:1726.

Jackson, J. D. (1998). *Classical Electrodynamics*. John Wiley & Sons, Inc.

Jia, S. (2008). *Magnetic properties of RT_2Zn_{20}, R = rare earth, T = Fe, Co , Ru, Rh , Os and Ir*. PhD dissertation, Iowa State University.

Jia, S., Bud'ko, S. L., Samolyuk, G. D., and Canfield, P. C. (2007). Nearly ferromagnetic fermi-liquid behaviour in YFe_2Zn_{20} and high-temperature ferromagnetism of $GdFe_2Zn_{20}$. *Nature Physics*, 3:334–338.

Jia, S., Ni, N., Samolyuk, G. D., Sefat, A. S., Dennis, K., Ko, H., Miller, G. J., Bud'ko, S. L., and Canfield, P. C. (2008). Variation of the magnetic ordering in GdT_2Zn_{20} (T=Fe, Ru, Os, Co, Rh, and Ir) and its correlation with the electronic structure of isostructural YT_2Zn_{20}. *Phys. Rev. B*, 77:104408.

Jobiliong, E., Brooks, J. S., Choi, E. S., Lee, H., and Fisk, Z. (2005). Magnetization and electrical-transport investigaion of the dense kondo system $CeAgSb_2$. *Phys. Rev. B*, 72:104428.

Kadanoff, L. P., Gotze, W., Hamblen, D., Hecht, R., Lewis, E. A. S., Palciauskas, V. V., Rayl, M., Swift, J., Aspenes, D., and Kane, J. (1967). Static phenomena near critical points: Theory and experiment. *Rev. Mod. Phys.*, 39(2):395–431.

Kamegashira, N., Satoh, H., and Ashizuka, S. (2004). Synthesis and crystal structure of hexagonal $DyMnO_3$. *Mater. Sci. Forum*, 449-452:1045.

Kimura, T., Lawes, G., Goto, T., Tokura, Y., and Ramirez, A. P. (2005). Mangetoelectric phase diagrams of orthorhombic RMnO$_3$ (R= Gd, Tb and Dy). *Phys. Rev. B*, 71:224425.

Kunkel, H. P., Roshko, R. M., and Williams, G. (1988). Field-dependent susceptibility of a paramagnet. *Phys. Rev. B*, 37(10):5880.

Landau, L. D. (1937). *Phys. Z. Sowjetunion*, 11:26.

Laverdière, J., Jandl, S., Mukhin, A. A., Ivanov, V. Y., Ivanov, V. G., and Iliev, M. N. (2006). Spin-phonon coupling in orthorhombic RMnO$_3$ (R=Pr, Nd, Sm, Eu, Gd, Tb, Dy, Ho, Y): A Raman study. *Phys. Rev. B*, 73:214301.

Lebech, B., Clausen, K., and Vogt, O. (1980). First-order transitions and the magnetic phase diagram of CeSb. *J. Phys. C: Solid State Phys.*, 13:1725.

Lonzarich, G. G. and Taillefer, L. (1985). Effect of spin fluctuations on the magnetic equation of state of ferromagnetic or nearly ferromagnetic metals. *J. Phys. C: Solid State Phys.*, 18:4339.

Lorenz, B., Yen, F., Gospodinov, M. M., and Chu, C. W. (2005). Field-induced phases in $HoMnO_3$ at low temperatures. *Phys. Rev. B*, 71:014438.

Lottermoser, T., Lonkai, T., Amann, U., Hohlwein, D., Ihringer, J., and Fiebig, M. (2004). Mangetic phase control by an electric field. *Nature*, 430:541.

Martin, C., Agosta, C. C., Tozer, S. W., Radovan, H. A., Palm, E. C., Murphy, T. P., and Sarro, J. L. (2005). Evidence for the Fulde-Ferrell-Larkin-Ovchinnikov state in $CeCoIn_5$ from penetration depth measurements. *Phys. Rev. B*, 71:020503.

Martin, C., Vannette, M. D., Gordon, R. T., Karpinski, J., Zhigaldo, N. D., and Prozorov, R. (2008). Effect of C and Li doping on the rf magnetic susceptibility in MgB_2 single crystals. in press, Phys. Rev. B. preprint available at arXiv:0807.3098v1.

Matthias, B. T. and Bozorth, R. M. (1958). Ferromagnetism of a zirconium-zinc compound. *Phys. Rev.*, 109:604–605.

McManus, I. C. (1976). Scrotal asymmetry in man and in ancient sculpture. *Nature*, 259:426.

Meier, G., Fischer, P., Halg, W., Lebech, B., Rainford, B. D., and Vogt, O. (1978). Magnetic phase transtions in CeSb. II. Effects of applied magnetic fields. *J. Phys. C: Solid State Phys.*, 11:1173.

Mohn, P. (2003). *Magnetism in the Solid State*. Springer.

Moriya, T. (1985). *Spin Fluctuations in Itinerant Electron Magnetism*. Springer-Verlag.

Moriya, T. and Kawabata, A. (1973). Effect of spin fluctuations on itinerant electron ferromagnetism. *J. Phys. Soc. Jap.*, 34(3):639.

Morosan, E., Bud'ko, S. L., and Canfield, P. C. (2005). Magnetic ordering and effects of crystal electric field anisotropy in the hexagonal compounds RPtIn (R=Y, Gd-Lu). *Phys. Rev. B*, 72:014425.

Morrish, A. H. (2001). *The Physical Principles of Magnetism, Reissue*. IEEE Press. Original edition 1965 published by John Wiley & Sons.

Myers, K. D., Bud'ko, S. L., Antropov, V. P., Harmon, B. N., and Canfield, P. C. (1999a). de haas-van alphen and shubnikov-de haas oscillations in RAgSb$_2$ (R= Y, La-Nd, Sm). *Phys. Rev. B*, 60:13 371.

Myers, K. D., Bud'ko, S. L., Fisher, I. R., Islam, Z., Kleinke, H., Lacerda, A. H., and Canfield, P. C. (1999b). Systematic study of anisotropic transport and magnetic properties of $RAgSb_2$ (R=Y, La-Nd, Sm, Gd-Tm). *J. Magn. Magn. Mat.*, 205:27–52.

Nandi, S., Kreyssig, A., Yan, J. Q., Vannette, M. D., Lang, J. C., Tan, L., Kim, J. W., Prozorov, R., Lograsso, T. A., McQueeny, R. J., and Goldman, A. I. (2008). Magnetic structure of Dy^{3+} in hexagonal multiferroic $DyMnO_3$. *Phys. Rev. B*, 78:075118.

Nasch, T., Jeitschko, W., and Rodewald, U. C. (1997). Ternary rare earth transition metal zinc compounds RT_2Zn_{20} with T=Fe,Ru, Co, Rh, and Ni. *Z. Naturforsch. B*, 52:1023.

Ni, N., Jia, S., Bud'ko, S. L., and Canfield, P. C. (2008). unpublished.

Pathria, R. K. (1996). *Statistical Mechanics, Second Edition*. Elsevier.

Prokhnenko, O., Feyerherm, R., Dudzik, E., Landsgesell, S., Aliouane, N., Chapon, L. C., and Argyriou, D. N. (2007). Enhanced ferroelectric polarization by induced Dy spin order in multiferroic $DyMnO_3$. *Phys. Rev. Lett.*, 98:057206.

Prozorov, R. and Giannetta, R. W. (2006). Magnetic penetration depth in unconventional superconductors. *Supercond. Sci. Tech.*, 19:R41–R67.

Prozorov, R., Giannetta, R. W., Carrington, A., and Araujo-Moreira, F. M. (2000). Meissner-London state in superconductors of rectangular cross section in a perpendicular magnetic field. *Phys. Rev. B*, 62(1):115.

Prozorov, R., Kogan, V. G., Vannette, M. D., Bud'ko, S. L., and Canfield, P. C. (2007). Radio-frequency magnetic response of vortex lattices undergoing structural transformations. *Phys. Rev. B*, 76:094520.

Prozorov, R., Vannette, M. D., Gordon, R. T., Martin, C., Bud'ko, S. L., and Canfield, P. C. (2008a). Coexistence of long-range magnetic order and superconductivity from Campbell penetration depth measurements. submitted.

Prozorov, R., Vannette, M. D., Law, S. A., Bud'ko, S. L., and Canfield, P. C. (2008b). Coexistence of ferromagnets and superconductivity in $errh_4b_4$ single crystals probed by dynamic magnetic susceptibilitiy. *Phys. Rev. B*, 77:100503(R).

Prozorov, R., Vannette, M. D., Samolyuk, G. D., Law, S. A., Bud'ko, S. L., and Canfield, P. C. (2006). Contactless measurements of Shubnikov-de Haas oscillations in the magnetically ordered state of $CeAgSb_2$ and $SmAgSb_2$ single crystals. *Phys. Rev. B*, 75:014413.

Rastogi, A. K. and Coles, B. R. (1985). The magnetic character of Y_9Co_7. *J. Phys. F: Met. Phys.*, 15:1165.

Rhodes, P. and Wohlfarth, E. P. (1963). The effective curie-weiss constant of ferromagnetic metals and alloys. *Proc. Roy. Soc. Lond. A*, 273(1353):247–258.

Roussat-Mignod, J., Burlet, P., Bartholin, H., Vogt, O., and Lagnier, R. (1980). Specific heat analysis of the magnetic phase diagram of CeSb. *J. Phys. C: Solid State Phys.*, 13:6318.

Saitoh, E., Miyajima, H., Yamaoka, T., and Tatara, G. (2004). Current-induced resonance and mass determination of a single magnetic domain wall. *Nature*, 432:203.

Sarkissian, B. V. B. and Grover, A. K. (1982). The hybrid state of the magnetic superconductor Y_9Co_7. *J. Phys. F: Met. Phys.*, 12:L107.

Schroder, C., Prozorov, R., Kögerler, P., Vannette, M. D., Fang, X., Luban, M., Matsuo, A., Kindo, K., Muller, A., and Todea, A. M. (2008). Multiple nearest-neighbor exchange model for the frustrated Keplerate magnetic molecules $\{Mo_{72}Fe_{30}\}$ and $\{Mo_{72}Cr_{30}\}$. *Phys. Rev. B*, 77:224409.

Sefat, A. S., Bud'ko, S. L., and Canfield, P. C. (2008). Magnetization, resistivity and heat capacity of the anisotropic $RVSb_3$ crystals (R=La-Nd, Sm, Gd-Dy). *J. Magn. Magn. Mat.*, 320(3-4):120.

Shoenberg, D. (1984). *Magnetic oscillations in metals.* Cambridge University Press.

Singh, Y., Niazi, A., Vannette, M. D., Prozorov, R., and Johnston, D. C. (2007). Superconducting and normal state properties of the layered diboride osb_2. *Phys. Rev. B*, 76:214510.

Sologub, O., Noeel, H., Leithe-Jasper, A., Rogl, P., and Bodak, O. I. (1995). Ternary compounds REAgSb$_2$, RE=Y, La, Ce, Pr, Nd, Sm, Gd, Tb, Dy, Ho, Er, Tm: Magnetism and crystal structure. *J. Solid State Chem.*, 115:441.

Spaldin, N. (2003). *Magnetic Materials, Fundamentals and Device Applications*. Cambridge University Press.

Spaldin, N. A. and Fiebig, M. (2005). The renaissance of mangetoelectric multiferroics. *Science*, 309:391.

Spinu, L., Srikanth, H., Gupta, A., Li, X. W., and Xiao, G. (2000). Probing magnetic anisotropy effects in epitaxial CrO_2 thin films. *Phys. Rev. B*, 62:8931.

Stanley, H. E. (1999). Scaling, universality, and renormalization: Three pillars of modern critical phenomena. *Rev. Mod. Phys.*, 71:358.

Stoner, E. C. (1938). Collective electron ferromagnetism. *Proc. Roy. Soc. Lond. A*, 165(922):372.

Sznajd, J. (2001). Field dependence of the susceptibility maximum temperature in ferromagnets. *Phys. Rev. B*, 64:052401.

Vannette, M. D., Bud'ko, S. L., Canfield, P. C., and Prozorov, R. (2008a). Distinguishing local moment vs. itinerant ferromagnetism: Dynamic magnetic susceptibility. *J. Appl. Phys.*, 103:07D302.

Vannette, M. D., Nandi, S., Kreyssig, A., Goldman, A., and Prozorov, R. (2008b). $h-t$ phase diagram of hexagonal RMnO$_3$ (R=Ho, Dy) from radio-frequency magnetic susceptibility. in progress.

Vannette, M. D. and Prozorov, R. (2008). Field dependent AC susceptibility of itinerant ferromagnets. *J. Phys.: Condens. Matt.*, 20:475208.

Vannette, M. D., Schmalian, J., Bud'ko, S. L., Canfield, P. C., and Prozorov, R. (2008c). Characteristic fields and critical scaling in single crystals of ferromagnetic Ce VSb_3 and Ce Ag Sb_2. unpublished.

Vannette, M. D., Sefat, A. S., Jia, S., Law, S. A., Lapertot, G., Bud'ko, S. L., Canfield, P. C., Schmalian, J., and Prozorov, R. (2008d). Precise measurements of radio-frequency magnetic susceptibility in ferromagnetic and antiferromagnetic materials. *J. Magn. Magn. Mat.*, 320:354.

Vannette, M. D., Yeninas, S., Morosan, E., and Prozorov, R. (2008e). Unusual domain behavior in $Fe_{1/4}TaS_2$ studied via magneto-optical visualization and rf magnetic susceptibility. in progress.

VanDegrift, C. T. (1975a). Tunnel diode oscillator for 0.001 ppm measurements at low temperatures. *Rev. Sci. Inst.*, 48(5):599–607.

VanDegrift, C. T. (1975b). *Tunnel diode oscillator for 0.001 ppm measurements at low temperatures.* PhD dissertation, Univeristy of California, Irvine.

Wiener, T. A. and Canfield, P. C. (2000). Magnetic phase diagram of flux-grown single crystals of CeSb. *J. Alloys Compd.*, 303-304:505–508.

Wohlfarth, E. P. (1968). Very weak itinerant ferromagnets; Application to $ZrZn_2$. *J. App. Phys.*, 39:1061.

Yakel, H. L., Koehler, W. C., Bertaut, E. F., and Forrat, E. F. (1963). On the crystal structure of the manganese (iii) trioxides of the heavy lanthanides and yttrium. *Acta Cryst.*, 16:957.

Yamaguchi, Y., Nishihara, Y., and Ogawa, S. (1984). Magnetization study of itinerant-electron ferromagnet Y_9Co_7. *J. Phys. Soc. Jpn.*, 53:3985.

Yelland, E. A., Yates, S. J. C., Taylor, O., Griffiths, A., Hayden, S. M., and Carrington, A. (2005). Ferromagnetic properties of $ZrZn_2$. *Phys. Rev. B*, 72:184436.

Yen, F., dela Cruz, C. R., Lorenz, B., Galstyan, E., Sun, Y. Y., Gospodinov, M., and Chu, C. W. (2007). Magnetic phase diagram of multiferroic hexagonal RMnO$_3$ (R=Er, Yb, Tm, and Ho). *J. Mater. Res.*, 22:2163.

Yen, F., dela Cruz, C. R., Lorenz, B., Sun, Y. Y., Wang, Y. Q., Gospodinov, M. M., and Chu, C. W. (2005). Low-temperature dielectric anomalies in HoMnO$_3$: The complex phase diagram. *Phys. Rev. B*, 71:180407(R).

Zong, X., Das, S., Borsa, F., Vannette, M. D., Prozorov, R., Schmalian, J., and Johnston, D. C. (2008). ^{7}Li NMR study of heavy fermion LiV$_2$O$_4$ containing magnetic defects. *Phys. Rev. B*, 77:144419.

Zuev, Y. L., Kuznetsova, V. A., Prozorov, R., Vannette, M. D., Lobanov, M. V., Christen, D. K., and Thompson, J. R. (2007). s-wave superconductivity in non-centrosymmetric Re$_3$W probed by magnetic penetration depth. *Phys. Rev. B*, 76:132508.